

(NASA-CR-171577) THE UTILIZATION OF
SATELLITE DATA AND DYNAMICS IN UNDERSTANDING
AND PREDICTING GLOBAL WEATHER PHENOMENA
Final Report, 15 Aug. 1980 - 31 Mar. 1985
(Pennsylvania State Univ.) 390 p

N86-11749
THRU
N86-11756
Unclass
22139

G3/47

NASA CONTRACTOR
REPORT

NASA CR-171577

THE UTILIZATION OF SATELLITE DATA AND DYNAMICS
IN UNDERSTANDING AND PREDICTING GLOBAL WEATHER PHENOMENA

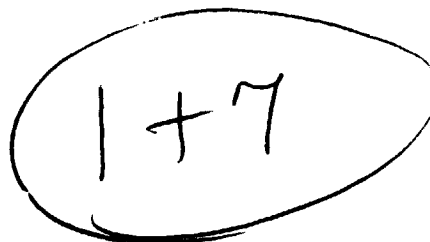
Department of Meteorology
The Pennsylvania State University
University Park, PA 16802

May 1985

Prepared for

NASA-George C. Marshall Space Flight Center
Marshall Space Flight Center, Alabama 35812

Final Report




1. REPORT NO. NASA CR- 171577	2. GOVERNMENT ACCESSION NO.	3. RECIPIENT'S CATALOG NO.	
4. TITLE AND SUBTITLE The Utilization of Satellite Data and Dynamics in Understanding and Predicting Global Weather Phenomena		5. REPORT DATE May 1985	
		6. PERFORMING ORGANIZATION CODE	
7. AUTHOR(S) Edited by Hampton N. Shirer and John A. Dutton		8. PERFORMING ORGANIZATION REPORT #	
9. PERFORMING ORGANIZATION NAME AND ADDRESS Department of Meteorology The Pennsylvania State University University Park, PA 16802		10. WORK UNIT NO.	
		11. CONTRACT OR GRANT NO. NAS8-33794	
12. SPONSORING AGENCY NAME AND ADDRESS National Aeronautics and Space Administration Washington, D.C. 20546		13. TYPE OF REPORT & PERIOD COVERED Contractor Report August 15, 1980-March 31, 1985 Final Report	
		14. SPONSORING AGENCY CODE OSSA, NASA Hdqts.	
15. SUPPLEMENTARY NOTES Prepared for the Atmospheric Sciences Division, System Dynamics Lab., Marshall Space Flight Center, AL., 35812. Technical Monitors: Mr. John W. Kaufman and Dr. George H. Fichtl			
16. ABSTRACT <p>A two-layer spectral quasi-geostrophic model is used to simulate the effects of topography on the equilibria, the stability, and the long-term evaluation of incipient unstable waves. The flow is forced by latitudinally dependent radiational heating. The nature of the form-drag instability of high-index equilibria is investigated. It is shown that the proximity of the equilibrium shear to a resonant value is essential for the instability, provided the equilibrium occurs at a slightly stronger shear than resonance. The properties of the steady Hadley and Rossby required for a thermally-forced rotating fluid on a sphere are further explained. An objective parameterization technique is developed for general nonlinear hydrodynamical systems. The typical structure is one in which the rates of change of the dependent variables depend on homogeneous quadratic and linear forms, as well as on inhomogeneous forcing terms.</p> <p>Also documented is a steady, axisymmetric model of the general circulation developed as a basis for climate stability studies. The model includes the effects of heating, rotation, and internal friction, but neglects topography. Included is further research on cloud street phenomena. Orientation angles and horizontal wavelengths of boundary layer rolls and cloud streets are determined from an analysis of a truncated spectral model of three-dimensional shallow moist Boussinesq convection in a shearing environment is further explained. Relatively broadly spaced roll clouds have orientations for which the Fourier component of the roll-perpendicular shear is nearly zero, but the second corresponds to narrowly spaced rolls having orientations for which the Fourier coefficients of both the perpendicular and the parallel components of the shear are nearly equal. Also included is the physical relationship between steady axisymmetric flows that might be observed in the atmosphere and in laboratory vessels, theoretically.</p>			
17. KEY WORDS Geosciences Global-Scale Processes Atmospheric Models Cloud Structure Global Weather		18. DISTRIBUTION STATEMENT  G. F. McDonough Director, Systems Dynamics Lab. Unclassified-Unlimited	
19. SECURITY CLASSIF. (of this report) Unclassified	20. SECURITY CLASSIF. (of this page) Unclassified	21. NO. OF PAGES 391	22. PRICE NTIS

Table of Contents

	Page
1. Introduction	1
2. The Effect of Topography on the Evolution of Unstable Disturbances in a Baroclinic Atmosphere (John H. E. Clark) . .	19
3. The Hadley and Rossby Regimes in a Spherical Atmosphere (Steven B. Feldstein and John H. E. Clark)	69
4. A Parameterization Technique for Nonlinear Spectral Models (Ronald Gelaro and Hampton N. Shiner)	109
5. A Numerical Study of Global Axisymmetric States and Their Stability to Quasi-Geostrophic Disturbances (Harry W. Henderson and John A. Dutton)	167
6. On Cloud Street Development in Three Dimensions: Parallel and Rayleigh Instabilities (Hampton N. Shiner)	223
7. Cloud Streets During KonTur: A Comparison of Parallel/ Thermal Instability Modes with Observations (Hampton N. Shiner, Burghard Brümmer and Alan Grant)	291
8. On the Nonlinear Characteristics of the Axisymmetric Flow Regime: Cylindrical and Hemispherical Systems (R. Wayne Higgins, John A. Dutton and Hampton N. Shiner) . . .	319

Chapter 1

Introduction

In this chapter we first present in Sections 1.1-1.7 the abstracts of the individual papers that form the remaining 7 chapters of this report. Each paper, which is in the form of a manuscript for publication in a technical journal, has been written by one or more members of our research group. Most of these manuscripts are being reviewed, and their final forms will be different than those presented here.

In Sections 1.8-1.10, we briefly review the work that was under way during the contract, but which has not progressed sufficiently for the writing of summarizing manuscripts. One of the projects, "On Cloud Street Development from the Inflection Point Instability" is the MS thesis topic for Mr. Dave Stensrud and another one, "Wavenumber and Amplitude Vacillation Arising from Time-Dependent Flows" is the PhD thesis topic for Mr. Steven Feldstein. The last study, "Modeling the Index Cycle Variations" is a postdoctoral project for Dr. Harry Henderson. The reports summarizing these studies will be included in the final report for the present contract, NAS6-36150.

amt

1.1 The Effect of Topography on the Evolution of Unstable Disturbances in a Baroclinic Atmosphere

A two-layer spectral quasi-geostrophic model is used to simulate the effects of topography on the equilibria, their stability, and the long-term evolution of incipient unstable waves. The flow is forced by latitudinally dependent radiative heating. Dissipation is in the form of Rayleigh friction.

An analytical solution is found for the propagating finite-amplitude waves which result from baroclinic instability of the zonal winds when topography is absent. The appearance of this solution for wavelengths just longer than the Rossby radius of deformation and disappearance of ultra-long wave-lengths is interpreted in terms of the Hopf bifurcation theory of Marsden and McCracken (1976). Simple dynamic and thermodynamic criteria for the existence of periodic Rossby solutions are presented. A Floquet stability analysis shows that the waves are neutral.

One result of the introduction of topography is multiple steady solutions for certain values of external parameters. Metastable high index equilibria are especially prominent when the zonal wind shear is close to resonance.

The nature of the form-drag instability of high-index equilibria is investigated. It is shown that the proximity of the equilibrium shear to a resonant value is essential for the instability, provided the equilibrium occurs at a slightly stronger shear than resonance.

The baroclinically unstable waves with topography evolve with increasing radiative forcing via a series of period doublings, as opposed to Hopf bifurcations, to an aperiodic state. A Floquet stability analysis of the successive periodic solutions facilitated an accurate determination of the critical heatings. Feigenbaum's asymptotic relation was closely followed.

ant

Preliminary calculations with less severe spectral truncations suggest that Feigenbaum's relation holds independently of the truncation.

omit

1.2 The Hadley and Rossby Regimes in a Spherical Atmosphere

The properties of the steady Hadley and Rossby regimes for a thermally-forced rotating fluid on a sphere are studied. The two-layer modified geostrophic model of Lorenz (1960) is employed which allows for thermal advection by the divergent wind and time dependent static stability. Heating processes are parameterized using the Newtonian approximation and Rayleigh friction is accounted for. The equations are transformed to spectral form using spherical harmonics and then truncated retaining a simple axisymmetric state and initially one wave.

A time independent Hadley circulation is obtained which is neutral to axisymmetric disturbances but unstable to wave-like perturbations for intermediate values of the meridional temperature gradient indicating the existence of both an upper and lower symmetric Hadley regime. An analytical solution for the steady Rossby circulation is determined for values of the meridional temperature gradient where the Hadley regime is unstable. Linear perturbation theory is used to show that within the steady Rossby regime two or more waves cannot exist simultaneously. This implies that the transition from one wavenumber to another occurs abruptly as the meridional temperature gradient is varied in contrast to the finding of Lorenz (1962) for the rotating dishpan. For small values of dissipation and forcing, the steady Rossby regime is replaced by a doubly periodic time dependent circulation consisting of both amplitude vacillation and wave propagation. Also, there is very good agreement between the wavenumber of maximum instability for the steady Hadley regime and the wavenumber observed in the steady Rossby regime.

omit

1.3 A Parameterization Technique for Nonlinear Spectral Models

An objective parameterization technique is developed for general nonlinear hydrodynamical systems. The typical structure of these hydrodynamical systems, regardless of their complexity, is one in which the rates of change of the dependent variables depend on homogeneous quadratic and linear forms, as well as on inhomogeneous forcing terms. As a prototype of the generic problem containing this typical structure, we apply the parameterization technique to various three-component subsets of a five-component nonlinear spectral model of forced, dissipative quasi-geostrophic flow in a channel. The results obtained here lead to specification of the necessary data coverage requirements for applying the technique in general.

The emphasis of the parameterization approach is on preserving the behavior of the steady states by incorporating in the parameterized models information concerning the topological structure of the original solutions. The parameterized spectral components are expressed as power series involving the retained components, and it is found that the optimum parameterization is obtained when these series are terminated at quadratic terms. The values of the coefficients in these series are determined from the moments of the original set of spectral components over some range of forcing.

For testing convenience, the moments are computed using the steady solutions to the original five-component model as data. This is accomplished by assuming that the values of the zonal forcing rate obey some standard statistical distributions. In regions of phase space in which multiple steady solutions occur, the likelihood of the occurrence of any one solution may be weighted according to its stability. Thus, the data sets can be viewed as simulating either idealized data, in which both stable and unstable solutions

omit

are permitted, or observational data, in which only stable solutions are permitted. Special attention is paid to the sensitivity of the parameterization to data coverage requirements, and to the relation of these requirements to the general structure of the solution surfaces. Significantly, it is shown that with sufficient data coverage, a successful parameterization may be obtained even in the more restrictive case when only stable (observable) solutions are used as data.

omit

1.4 A Numerical Study of Global Axisymmetric States and Their Stability to Quasi-Geostrophic Disturbances

A steady, axisymmetric model of the general circulation is developed as a basis for climate stability studies. The model includes the effects of heating, rotation, and internal friction, but neglects topography. It is assumed that the axisymmetric flow may be modeled by making the Boussinesq and deep convection approximations. The hydrostatic assumption is not made, thus permitting the advective terms to be included in the vertical equation of motion. The initial set of five primitive equations is reduced to three equations in terms of the zonal velocity, meridional streamfunction, and the potential temperature perturbation.

The three dependent variables are assumed to satisfy appropriate spectral expansions, and the three equations are then arranged into a Galerkin representation. The number of degrees of freedom retained in the expansions is restricted to eight waves or less, which places the model in the class of highly truncated spectral models.

The motions are forced by a specified heating distribution and dissipated through an eddy mixing coefficient formulation. The specified heating distribution is an idealized pattern based upon the observed net heating field. The eddy mixing coefficients are chosen to be representative of the observed circulation.

The axisymmetric circulation is tested for stability to quasi-geostrophic disturbances. The original set of five primitive equations is reduced to a single equation governing the evolution of quasi-geostrophic potential vorticity. This equation is linearized about the axisymmetric state, and the stability of the disturbances is found by examining the eigenvalues

omit

associated with each disturbance. The longitudinal resolution is truncated beyond the 15th longitudinal wave.

The application of the Boussinesq, deep convection, and quasi-geostrophic assumptions limits the ranges of the heating and rotation rates. For values not too far from typical atmospheric values, the model produces a stability boundary separating Hadley from Rossby flow. The boundary is characterized by a particular value of vertical wind shear, which suggests that baroclinic instability is the primary mechanism for the loss of stability. The initial growth rates are largest for longitudinal waves 4-7, also in agreement with studies of baroclinic instability.

1.5 On Cloud Street Development in Three Dimensions: Parallel and Rayleigh Instabilities

Expected orientation angles and horizontal wavelengths of boundary layer rolls or cloud streets are determined from an analysis of a truncated spectral model of three-dimensional shallow moist Boussinesq convection in a shearing environment. The nonlinear secondary circulations are organized into two-dimensional forms by the height-dependent wind field, and these rolls may develop from the combined effects of thermal stratification and mean wind shear. The associated thermal and parallel instability mechanisms are shown to be special cases of a single one. Only one mode is found when the stratification is unstable or neutral, but a second one is possible when the stratification is weakly stable. The first corresponds to relatively broadly spaced rolls having orientations for which the Fourier component of the roll-perpendicular shear is nearly zero, but the second corresponds to relatively narrowly spaced rolls having orientations for which the Fourier coefficients of both the perpendicular and the parallel components of the shear are nearly equal.

omT.

1.6 Cloud Streets During KonTur: A Comparison of Parallel/Thermal Instability Modes with Observations

Estimates of cloud street geometry produced by a model of the parallel/thermal instability modes of shallow convection (Shirer, 1985) are compared with observations obtained during the 1981 KonTur experiment (Brümmer and Grant, 1985). Good agreement between the modeled and observed orientation angles, wavelengths and Reynolds numbers are found when the streets are assumed to derive their energy from the average shear and the lowest order sine terms of a Fourier expansion of the mean wind profile (or equivalently from the lowest order cosine terms of the mean shear profile). The modes associated with the cosine terms of the wind profile (or the sine terms of the wind shear profile) do not agree well with the observations. These results suggest that the boundary layer rolls observed during KonTur might have developed owing to a combined parallel/thermal instability originating primarily from the cosine terms of the ambient roll-parallel wind shear.

1.7 On the Nonlinear Characteristics of the Axisymmetric Flow Regime:

Cylindrical and Hemispheric Systems

The physical relationship between steady axisymmetric flows that might be observed in the atmosphere and in laboratory vessels is investigated theoretically. This is accomplished by comparing both the nonlinear structure and the thermal forcing mechanisms in two truncated spectral models of flow in the atmosphere and the rotating laboratory cylinder respectively. Under statically stable conditions, the response of the internally-forced spherical model (which is developed here from a set of new orthonormal basis functions) exhibits steady behavior different from that in the externally forced cylindrical model. Two regions of multiple steady solutions occur in the cylindrical model, under stable conditions, that are not found in the spherical one. The possible physical relevance of these multiple solutions is investigated by determining their location in parameter space with respect to the classical Hadley-Rossby transition curve. The results suggest that the wave flow regime, in an annulus, might develop catastrophically when an upper symmetric flow ceases to exist. Further examination of each model reveals that steady behavior is linked to the hydrostatic assumption and so to the aspect ratio and basis functions of each system. The results suggest that the manner by which regime transitions occur in externally forced vessels might differ from those for the internally (and externally) forced atmosphere. Significantly, internally forced laboratory vessels are found to have the greatest utility for studies of large-scale axisymmetric flow regimes in the atmosphere.

omit

1.8 On Cloud Street Development from the Inflection Point Instability

The inflection point instability as a formation mechanism for cloud streets in a neutral atmosphere is studied with a low-order spectral model. Since one vertical wavenumber is not sufficient to capture the inflection point instability (Shirer, 1985 and Chapter 6), we develop two versions of the model: one with two vertical wavenumbers, and the other with three vertical wavenumbers. The linear stability analysis for both model versions yields a single polynomial in the squared critical Reynolds number (Re_c^2) that depends on the Fourier coefficients of the wind profile. Solving for the minimum acceptable value of Re_c^2 ($Re_c^2 > 0$) yields the preferred values of the orientation angle (θ) and the aspect ratio (A), and hence gives the preferred geometry of the streets.

To test the model results, we use several idealized wind profiles as well as several observed wind profiles; their Fourier coefficients determine the minimum value of Re_c . In previous studies, the Ekman profile has been used primarily to examine the inflection point instability, and orientation angles θ and aspect ratios A have been calculated (Lilly, 1966; Assi and Nakasugi, 1973). In the present model, the preferred values of θ and A associated with the Ekman profile agree well with these previous results.

The observed wind profiles are taken from the 1981 KonTur experiment (Brümmer and Grant, 1985). KonTur was a West German convection experiment in which high resolution wind data was collected by aircraft flying through the boundary layer. We find that the preferred values of θ and A given by the KonTur data on days containing cloud streets agree with the observed values. Indeed, the two wavenumber version of the model does very well in determining the preferred orientation angles and aspect ratios, although greater confidence is maintained with the three wavenumber version.

One form of low vertical resolution data that is routinely available is radiosonde data for which the wind observations are given every 1000 ft. This data is, in general, too coarse to produce reliable preferred values of θ and A during cloud street outbreaks. However, it may be possible to use a cubic spline to enhance the data and adjust the preferred values of θ and A . In this way the boundary layer wind profile can be improved by using the spline profile that yields the observed values of θ and A on days containing cloud streets. This hypothesis is currently under investigation and the initial results are indefinite.

omit

1.9 Wavenumber and Amplitude Vacillation Arising from Time-Dependent Flows

The finite-amplitude stability of planetary scale waves is being studied to show that synoptic scale amplitude and wavenumber vacillation can develop from the instability of the planetary waves. A two-layer quasi-geostrophic midlatitude β -plane model is used. Both forced and free planetary scale basic state waves are being considered.

An asymptotic series expansion is used to study the weakly nonlinear finite amplitude evolution of synoptic scale perturbations. When the planetary wave is forced, the synoptic scale perturbations experience a slow amplitude vacillation cycle. On the other hand, when the planetary wave is free, the weakly nonlinear theory breaks down due to an explosive finite amplitude instability of the perturbation.

The weakly nonlinear theory is then used to specify a truncation for a completely nonlinear spectral model. Both the lower and higher order modes of the weakly nonlinear solutions are retained in the spectral model. This is because the higher order modes are found to play a crucial role in the evolution of the lower order modes.

The spectral model results for the forced planetary wave case are similar to those of the weakly nonlinear theory. When the planetary wave is free, the results are quite different. The synoptic scale modes underwent a slow, regular wavenumber vacillation cycle that was possible only due to the explosive instability of the basic wave.

Presently, we are studying these two vacillation cycles in detail and we are trying to understand why the forced and free basic wave cases are so different.

omit

1.10 Modeling the Index Cycle Variations

Initially we expected that a forecast model of the index cycle could be built from the empirical orthogonal functions (EOF) of the 500 mb height field, but this has not proved to be the case for two reasons. First, the EOF's could readily describe the blocking situations, but no obvious choice of EOF's seemed to be adequate in describing the high index (zonal) flows. The second obstacle was centered about the problem of errors introduced into the interaction coefficients that were derived from the EOF fields. The domain area of the study was the NMC octagon, and the only feasible way to obtain the horizontal derivatives of the EOF's (which are necessary for the calculation of the interaction coefficients) was to use finite differencing. This in turn introduced errors into the interaction coefficients. No explosive instabilities occur with these errors, as the errors cancel each other in the mean kinetic energy and vorticity equations, but errors in phase speeds did occur. It did not seem fruitful to pursue this approach, as tests made with a very low order model confirmed the decay in predictability solely due to errors in the interaction coefficients.

Instead, we turned our efforts to studying the barotropic vorticity equation. This model is based on the divergent form of the quasi-geostrophic model, as used by Charney and DeVore (1979). However, the model has been recast in spherical harmonics for use over the Northern Hemisphere. This will allow comparisons between observations and forecasts. A higher number of degrees of freedom have been incorporated--there are 15 modes available (wavenumbers 1-5 in both the meridional and zonal directions), along with direct forcing of each mode and all possible terrain modes for this truncation. The model was tested for accuracy in conserving energy and vorticity, and found to be ready for use with analyzed data.

omit

The very low order barotropic results were in agreement with those of Charney and DeVore (1979) and also Hart (1979). There were regions of multiple solutions, but the steady solutions that were analogous to high and low index patterns were stable to perturbations. Stable periodic solutions are probably present, but were not found (similar to Hart's results). It has been proposed by both Charney and Hart that baroclinic instability is necessary to provide the instability that moves the atmospheric state between index patterns. Accordingly, some work was done to seek an appropriate low order model that includes baroclinic instability. There seems to be such a suitable model developed by Lorenz (1984), although it is still being refined. It is two-level and incorporates parameterized diabatic effects.

The next step will be to run the barotropic model for extended periods, and to look at the behavior of the index. Oscillations will probably not be present, as these states may be stable. The same modeling approach as that used with the Lorenz two-level model should yield oscillations.

References

- Asai, T. and I. Nakazuji, 1973: On the stability of Ekman boundary layer flow with thermally unstable stratification. J. Meteor. Soc. Japan, 51, 29-42.
- Brümmer, B. and A. Grant, 1985: Structure, dynamics and energetics of boundary layer rolls from KonTur aircraft observations. Beitr. Phys. Atmos., 58, in press.
- Charney, J.G. and J.G. DeVore, 1979: Multiple flow equilibria in the atmosphere and blocking. J. Atmos. Sci., 36, 1205-1216.
- Hart, J., 1979: Barotropic quasi-geostrophic flow over anisotropic mountains. J. Atmos. Sci., 36, 1736-1746.
- Lilly, D.K., 1966: On the stability of Ekman boundary flow. J. Atmos. Sci., 23, 481-494.
- Lorenz, E.N., 1960: Energy and numerical weather prediction. Tellus, 12, 364-373.
- Lorenz, E.N., 1962: Simplified dynamic equations applied to the rotating basin experiments. J. Atmos. Sci., 19, 39-51.
- Lorenz, E.N., 1984: Irregularity: A fundamental property of the atmosphere. Tellus, 36A, 98-110.
- Marsden, J.E. and M. McCracken, 1976: The Hopf Bifurcation and Its Applications. Applied Mathematical Sciences, 19, Springer-Verlag, 408 pp.
- Shirer, H.N., 1985: On cloud street development in three dimensions: Parallel and Rayleigh instabilities. Submitted to Beitr. Phys. Atmos. for review.
- mit

DI

19

CHAPTER 2

N86-11750

The Effect of Topography on the Evolution
of Unstable Disturbances in a Baroclinic Atmosphere

John H. E. Clark
The Pennsylvania State University
University Park, PA 16802

PRECEDING PAGE BLANK NOT FILMED

1. Introduction

A great deal of attention has been devoted, in recent years, to the conditions under which mathematical fluid dynamical models exhibit a transition from deterministic to stochastic behaviour in response to a changing external parameter. Models of phenomena as diverse as the development of turbulence, Ruelle and Takens (1971), two-dimensional incompressible flow, Franceschini and Tetaldi (1979), and the evolution of marginally unstable planetary waves, Pedlosky and Frenzen (1980), demonstrate the evolution of the flows via a series of period doublings to a chaotic or aperiodic state. If the time evolution of the solution is regarded as the trajectory of a point in an n -dimensional phase space whose coordinates represent the amplitudes of a set of orthogonal functions used to represent the solution, then the trajectories become erratic in the vicinity of a region called a strange attractor.

Feigenbaum (1978), using a first-order difference equation, found that there is a universal relationship between the values of the external parameter at which each period doubling occurs that seemed to be independent of the detailed nature of the equation. Collet and Eckman (1980) show how the long-term evolution of a multi-dimensional system under certain conditions can be governed by Feigenbaum's relation.

A long-held belief among atmospheric dynamicists is that an important process giving rise to the finite-amplitude propagating and stationary planetary scale waves at mid and high latitudes is baroclinic instability of the zonally-averaged westerlies. Indeed, steady axisymmetric or Hadley solutions to the Navier-Stokes equations whose existence with weak external heating has been proven by Dutton and Kloeden (1983) are believed to break

down with increased heating mainly by the process of baroclinic instability into the meandering asymmetric flow patterns characteristic of mid and high latitudes. Pedlosky (1970, 1972) has shown analytically how incipient marginally unstable disturbances to a vertically sheared flow can evolve to either steady or oscillating waves depending upon the intensity of dissipation. An additional instability mechanism giving rise to finite-amplitude waves is form-drag instability associated with wavelike topographic features at the base of a barotropic or baroclinic atmosphere, Charney and Devore (1979) and Charney and Straus (1980). The instability arises when the model atmosphere is close to a state of resonance such that the frequency of a free mode coincides with the frequency associated with the topographic forcing (usually zero). The resonant growth of infinitesimal wavelike disturbances has previously been suggested as the mechanism for the establishment of blocking patterns, Lindzen and Tung (1979a, b). A unique feature of the form-drag instability is that non-linear wave-mean flow interactions are able to lock the system in a quasi-resonant state long after the initial linear growth period thus facilitating the eventual equilibration of the wave at amplitudes substantially above those predicted from a purely linear theory, Plumb (1979, 1981). Charney and Straus (1980) suggest that low index equilibrium states in a truncated spectral model arise from the nonlinear resonant growth of an initially linearly unstable mode in a baroclinic model with topography. The energy source of the growing wave is the available potential energy of the mean sheared flow just as for a baroclinically unstable disturbance.

It appears that topography has the potential for strongly modifying the long-term behavior of an incipient unstable wave by allowing the atmosphere to

remain locked in a quasi-resonant configuration. The purpose of this study is to assess that potential with a truncated, two-layer quasi-geostrophic model.

Under the impetus provided by the pioneering effort of Lorenz (1960) on the design of spectral models, a large number of studies have followed providing valuable insight into the non-linear dynamics of forced, dissipative planetary-scale motions. Some of the more recent studies are those of Vickroy and Dutton (1979), Charney and Devore (1979), Charney and Strauss (1980), Mitchell and Dutton (1981), and Boville (1981). These models reveal a rich variety of behavior arising from the non-linearities such as multiple stationary solutions, bifurcations from stationary to periodic solutions, amplitude vacillations, and hysteresis.

We shall initially account for nonlinear wave-mean flow interactions by neglecting wave-wave interactions and by representing only the gravest mode in the north-south direction and a single wave in the east-west direction. No restrictions on the wave amplitude will be imposed. This is to be contrasted to the approach of Pedlosky (1970, 1972, 1980) and Plumb (1979, 1980) who assumed a priori the nonlinearities are weak and thus wave-wave interactions are negligible at least for the leading order solution. We shall be particularly interested in whether period-doublings can occur in response to changing external forcing and whether they are predicted by the Feigenbaum formula.

In section 2, the model is developed and in section 3 the long-term evolution of a baroclinically unstable disturbance without topography is considered. The effects of topography are considered in section 4.

2. Theory

The domain of interest will be a mid-latitude β -plane channel of width π/l where l is the north-south wavenumber of the gravest mode. The wave amplitude will be constrained to attain a single maximum at the middle of the channel and to fall off to zero at the sides. Vertical structures of the quasi-geostrophic stream function ψ and the vertical velocity ω will be represented in the two-layer model of Fig. 1. The thickness of each layer is 500 mb. The variables ψ and ω are accounted for at the levels shown. The upper boundary condition where the pressure is zero is $\omega = 0$ for the vertical motion associated with the wave. The boundary condition at 1000 mb is

$$\omega_0 = -g_0 \vec{v}_g \cdot \vec{\nabla} h_s \quad (1)$$

where we have assumed that the 1000 mb surface deviates in height so little from the terrain that $\omega_0 = w_s = \vec{v}_g \cdot \vec{\nabla} h_s$, where h_s is the terrain height.

The quasi-geostrophic equations are, see Holton (1972),

$$\frac{\partial}{\partial t} \nabla^2 \psi + \vec{v}_g \cdot \vec{\nabla} (\nabla^2 \psi + f) = f_0 \frac{\partial \omega}{\partial p} - d \nabla^2 \psi \quad (2)$$

$$\frac{\partial}{\partial t} \left(\frac{\partial \psi}{\partial p} \right) + \vec{v}_g \cdot \vec{\nabla} \left(\frac{\partial \psi}{\partial p} \right) + \frac{\sigma}{f_0} \omega = - \frac{J}{\rho f_0 c_p T} - d \left(\frac{\partial \psi}{\partial p} \right) \quad (3)$$

where ψ is the geostrophic stream function, i.e. $\vec{v}_g = \hat{k} \times \vec{\nabla} \psi$, f the Coriolis parameter ($f = f_0 + \beta y$), J is the radiative heating rate per unit mass (in Joules $\text{kg}^{-1}\text{s}^{-1}$), c_p the specific heat of air at constant pressure, and σ a constant stability parameter. Turbulent viscous dissipation of kinetic energy

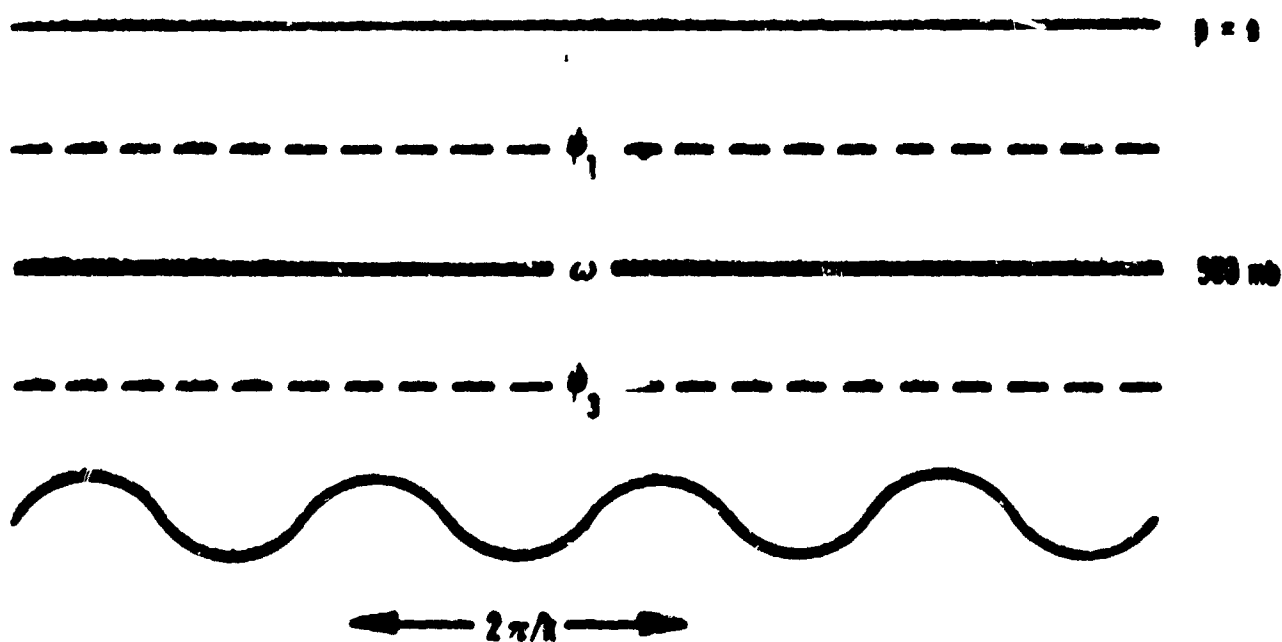


FIG. 1 The two-level model.

has been accounted for with a Rayleigh friction term in vorticity equation (2). The dissipative time constant, d^{-1} , was chosen to be 5 days. The flow will be forced by external radiative heating that is linearly dependent upon the deviation of the zonally-averaged temperature from a specified radiative equilibrium field.

A thermal dissipation term has also been included in (3). It will be assumed to act only on the wave-like part of the temperature pattern and its form is the same as that of Rayleigh friction term.

The subscripts 1 and 3 will denote the levels shown in Fig. 1 at which the stream function will be represented. The spectral expansions are

$$\psi_{1,3} = -U_{1,3}g_0(y) + A_{1,3}g_1(x, y) + B_{1,3}g_2(x, y) \quad (4)$$

$$\omega = \omega_0g_0(y) + \omega_Ag_1(x, y) + \omega_Bg_2(x, y) \quad (5)$$

where

$$\begin{aligned} g_0(y) &= y \\ g_1(x, y) &= \cos(ly) \sin(kx) \\ g_2(x, y) &= \cos(ly) \cos(kx) \end{aligned} \quad (6)$$

This choice of functions differs from that of Charney and Straus (1980) and in some ways is simpler. They represent the zonally-averaged portion of the stream function as a $\cos(ly)$. The choice of a linear field in y was made to facilitate a more representative thermal forcing field with cooling in the northern portion of the channel and warming to the south. A sinusoidal heating field is unrealistic and since radiative forcing plays a crucial role in the model it makes sense to model it accurately. The above expansion also satisfies the necessary lateral boundary conditions for the channel, namely:

The geostrophic flow vanishes at $y = \pm \pi/2l$ and $\frac{\partial}{\partial t} \int_c (\vec{\nabla} \psi \cdot \vec{n}) dl = 0$ for all z where c is a closed horizontal curve including the walls at $y = \pm \pi/2l$ and portions one to east-west wave apart connecting the walls. \vec{n} is normal to c .

The wave is constrained to have its ridge and trough lines oriented north-south and thus barotropic wave-mean flow interactions are precluded. For simplicity, the undulation of the lower boundary will be expressed as $g_1(x, y)$, i.e., the height h_g is

$$h_g = h_A g_1(x, y) / (-g p_0) \quad (7)$$

Thus at 1000 mb

$$\omega = \frac{3kl^2}{\pi^2} B_3 h_A g_0(y) + kh_A U_3 g_2(x, y) \quad (8)$$

Use has been made of the orthogonality of g_0 , g_1 , and g_2 over the region R defined by $0 \leq x \leq 2\pi/k$, $-\pi/2l \leq y \leq +\pi/2l$. Also note that

$$\iint_R g_0^2(y) dx dy = \frac{\pi^4}{6kl^3} \quad , \quad \iint_R \{g_1^2(x, y), g_2^2(x, y)\} dx dy = \frac{\pi^2}{2kl} \quad (9)$$

If the vorticity equation (3) is averaged over the interval $0 \leq x \leq 2\pi/k$, we find that $\partial \omega_0 / \partial p = 0$ at levels 1 and 3. Thus the zonal mean vertical motion field must be equal to $3kl^2 B_3 h_A y / \pi^2$ at all levels and from continuity the mean ageostrophic meridional flow, \bar{v}_{ag} , will be independent of y . The mean flows U_1 and U_3 can thus change in response to the Coriolis torque acting on \bar{v}_{ag} . There are no Reynolds stresses to accelerate the mean flow.

The spectral equations are derived by substituting Eqs. (1) and (2) into (3) and (4) making use of (6), (7), and (8).

It is convenient to separate the stream function and mean wind fields into vertically - averaged barotropic and sheared or baroclinic components.

Let

$$(U_1, U_3) = (U + \Delta U, U - \Delta U),$$

$$(A_1, A_3) = (A + \Delta A, A - \Delta A), \quad (10)$$

and

$$(B_1, B_3) = (B + \Delta B, B - \Delta B),$$

The vorticity Eq. (2) can then be rewritten

$$-\kappa^2 \dot{A} = -\kappa^2 (UB + \Delta U \Delta B) + k\beta B + d\kappa^2 A, \quad (11)$$

$$-\kappa^2 \dot{\Delta A} = -\kappa^2 (U \Delta B + B \Delta U) + k\beta \Delta B + f_o \omega_A / P + d\kappa^2 \Delta A, \quad (12)$$

$$-\kappa^2 \dot{B} = \kappa^2 (UA + \Delta U \Delta A) - k\beta A + f_o kh_A (U - \Delta U) / 2P + d\kappa^2 B, \quad (13)$$

$$-\kappa^2 \dot{\Delta B} = \kappa^2 (U \Delta A + A \Delta U) - k\beta \Delta A + f_o \omega_B / P - f_o kh_A (U - \Delta U) / 2P + d\kappa^2 \Delta B, \quad (14)$$

The thermodynamic Eq. (3) becomes

$$\Delta \dot{U} = 3k\epsilon^2 (B \Delta A - A \Delta B) / \pi^2 - 3k\epsilon^2 \sigma P (B - \Delta B) h_A / (2f_o \pi^2) - R J_o / (2f_o c_p), \quad (15)$$

$$\Delta \dot{A} = k(U \Delta B - B \Delta U) + \sigma P \omega_A / 2f_o - d \Delta A, \quad (16)$$

and

$$\Delta \dot{B} = k(A \Delta U - U \Delta A) + \sigma P \omega_B / 2f_o - d \Delta B. \quad (17)$$

R is the gas constant for air, $\kappa^2 \equiv k^2 + l^2$, $J = J_y$ and time derivatives are denoted with a dot. Reference to the vertical motion field can be suppressed by eliminating ω_A and ω_B between (12), (14), (16), and (17). These four equations can then be replaced by

$$-(\kappa^2 + \lambda^2)\Delta\dot{A} = -k(\kappa^2 + \lambda^2)U\Delta B - k(\kappa^2 - \lambda^2)B\Delta U + d(\kappa^2 + \lambda^2)\Delta A \quad (18)$$

and

$$\begin{aligned} -(\kappa^2 + \lambda^2)\Delta\dot{B} = & k(\kappa^2 + \lambda^2)U\Delta A + k(\kappa^2 - \lambda^2)A\Delta U - f_0 k h_A (U - \Delta U)/2P \\ & + d(\kappa^2 + \lambda^2)\Delta B \end{aligned} \quad (19)$$

where

$$\lambda = \left(\frac{2f_0^2}{\sigma P^2} \right)^{1/2} \quad (20)$$

is $2\pi/L_R$. L_R is the Rossby radius of deformation (about 4350 km).

It is convenient to non-dimensionalize the equations by rescaling dependent and independent variables. Table I shows the variables and corresponding scales, where ψ_0 and U_0 are arbitrary amplitudes.

TABLE I SCALING OF VARIABLES

<u>VARIABLE</u>	<u>SCALE</u>
$A, \Delta A, B, \Delta B$	ψ_0
$U, \Delta U$	U_0
t	$1/(kU_0)$

A number of dimensionless parameters arise from this process. They are

$$H_1 \equiv 3 \left(\frac{\lambda \psi_0}{\pi U_0} \right)^2$$

$$d_0 \equiv \frac{d}{kU_0}$$

$$U_c \equiv \frac{\beta}{\kappa^2 U_0}$$

$$b_0 \equiv \frac{f_0 h_A}{2F\kappa^2 \psi_0}$$

(21)

$$H_2 \equiv b_0 \left(\frac{\kappa}{\lambda} \right)^2 H_1$$

$$r_0 \equiv \frac{r}{kU_0}$$

$$R \equiv \frac{\kappa^2 - \lambda^2}{\kappa^2 + \lambda^2}$$

$$U_c^* \equiv U_c \frac{\kappa^2}{\kappa^2 + \lambda^2}$$

$$b_0^* \equiv b_0 \frac{\kappa^2}{\kappa^2 + \lambda^2}$$

The zonally-symmetric heating term in (15) will be expressed as $RJ_0/2f_0 = r(\Delta U - \Delta U_e)$, where ΔU_e is an equilibrium mean wind shear which through the thermal wind equation can be related to a meridional temperature gradient ΔT_e .

With these definitions the following set of spectral equations results:

$$\dot{A} = (U - U_c)B + \Delta U \Delta B - d_0 A \quad (22)$$

$$\dot{B} = - (U - U_c)A - \Delta U \Delta A - b_0 (U - \Delta U) - d_0 B \quad (23)$$

$$\Delta \dot{U} = - H_1 (A \Delta B - B \Delta A) - H_2 (B - \Delta B) - r(\Delta U - \Delta U_e) \quad (24)$$

$$\Delta \dot{A} = (U - U_c^*) \Delta B + R \Delta U - d_0 \Delta A \quad (25)$$

$$\Delta \dot{B} = - (U - U_c^*) \Delta A - R \Delta U + b_0^* (U - \Delta U) - d_0 \Delta B \quad (26)$$

3. Topography - free model

When h_A is zero, the coefficients b_0 , b_0^* , and H_2 in (22) to (26) are zero. Although it is not immediately obvious, the resulting equations actually only have 4 degrees of freedom instead of 5. In the Appendix, Eqs. (22) to (26) are written explicitly in terms of the amplitude and phase of the barotropic and baroclinic waves. It is then shown how one phase is arbitrary and the remaining 4 coefficients are independent of it as first shown by Baer (1970). This reduction in degrees of freedom is not possible with topography and we have our first indication of the fundamentally different nature of the topographic and non-topographic models.

One solution to the time-independent equations without topography is $A = B = \Delta A = \Delta B = 0$ and $\Delta U = \Delta U_e$. There is no wave present and the mean wind shear assumes the equilibrium value. The vertically averaged mean wind U is arbitrary. This will be called the Hadley solution. It is appropriate to examine its stability to infinitesimal perturbations whose time dependence is of the form $e^{\omega t}$. The problem reduces to the form

$$(\tilde{M} - \omega I) \tilde{S} = 0$$

where

$$\tilde{M} = \begin{pmatrix} -d_0 & U - U_c & 0 & \Delta U_e & \Delta B \\ -(U - U_c) & -d_0 & -\Delta U_e & 0 & -\Delta A \\ 0 & R\Delta U_e & -d_0 & U - U_c^* & RB \\ -R\Delta U_e & 0 & -(U - U_c^*) & -d_0 & -RA \\ -H_1\Delta B & H_1\Delta A & H_1B & -H_1A & -r \end{pmatrix} \quad (27)$$

\tilde{S} is the column matrix $(A', B', \Delta A', \Delta B', \Delta U')$, where the primes denote perturbations from the Hadley solution. For the present case $A, B, \Delta A$, and ΔB are zero in (27). There are five eigenfrequencies of \tilde{M} , one of which is $-r$ by inspection. The other four occur as conjugate pairs with negative real parts for $\kappa^2 > \lambda^2$, i.e., for a disturbance wavelength shorter than the Rossby radius of deformation. For larger wavelengths, the Hadley solution can become baroclinically unstable as evidenced by the fact that one pair of eigenvalue crosses the imaginary axis with non-zero speed from negative to positive $\text{Re}(\omega)$. A Hopf bifurcation has occurred, Marsden and McCracken (1976), as the steady Hadley solution loses its stability to a new periodic Rossby solution. For even longer wavelengths, the Hadley solution can regain its stability as the same conjugate pair recrosses the imaginary axis. The wavenumber at which these transitions occur depends upon the equilibrium wind shear ΔU_e but is independent of the mean wind U . The transition between the Hadley and the Rossby solution is shown in Fig. 2 as well as the e-folding time in days associated with the instability of the Hadley solutions. The transition or Hopf bifurcation curve is associated with an infinite e-folding time.

So far we have mostly reworked the two-layer baroclinic instability model of Phillips (1954). We shall now examine the nature of the Rossby solution that evolves as a result of the instability and also determine its stability to infinitesimal disturbances.

Assume the periodic solution consists of a constant amplitude propagating wave. The frequency is ω , and ΔU is held constant. Let

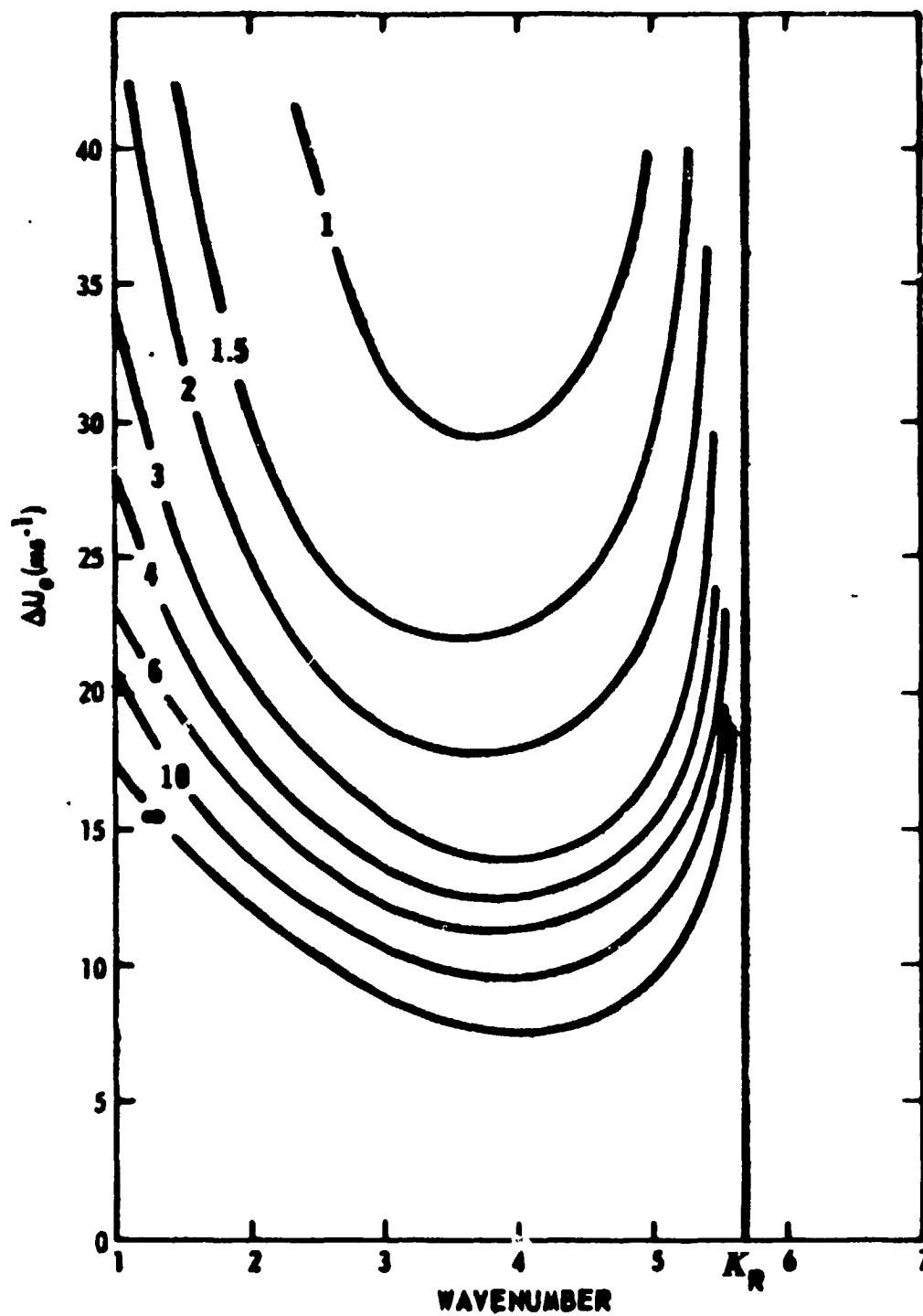


FIG. 2 Stability analysis without topography. Curves are labeled in e-folding time (days).

$$\begin{pmatrix} \dot{A} \\ \dot{B} \\ \dot{\Delta A} \\ \dot{\Delta B} \end{pmatrix} = \omega \begin{pmatrix} -B \\ A \\ -\Delta B \\ \Delta A \end{pmatrix}, \quad (28)$$

then (22) to (26) become a set of coupled algebraic equations. They are solved by first expressing A and B in terms of ΔA , ΔB , and ΔU using (22) and (23). Define

$$D \equiv d_o^2 + (U - U_c + \omega)^2$$

$$c_1 = -(U - U_c + \omega)/D \quad (29)$$

and

$$c_2 = d_o/D.$$

Then

$$\left. \begin{aligned} A &= c_1 \Delta U \Delta A + c_2 \Delta U \Delta B \\ B &= -c_2 \Delta U \Delta A + c_1 \Delta U \Delta B \end{aligned} \right\} \quad (30)$$

If (30) is substituted into (25) and (26), we find

$$\begin{pmatrix} -d_o - c_2 \Delta U^2 & U - U_c + \omega + c_1 \Delta U^2 \\ -(U - U_c + \omega) - c_1 \Delta U^2 & -d_o - c_2 \Delta U^2 \end{pmatrix} \begin{pmatrix} \Delta A \\ \Delta B \end{pmatrix} = 0 \quad (31)$$

Because of the special form of the coefficient matrix, non-trivial solution for ΔA and ΔB can exist only if all the elements are zero. If the definitions of R , c_1 , and c_2 are used, then

$$\omega + U = 0.5 U_c (2\kappa^2 + \lambda^2)/(\kappa^2 + \lambda^2) , \quad (32)$$

and

$$\Delta U^2 = D (\kappa^2 + \lambda^2)/(\lambda^2 - \kappa^2) . \quad (33)$$

Thus both the mean shear and the Doppler-shifted frequency of the periodic solution are determined. The wave amplitude is found from the thermodynamic equation (24). Note from (30) that the amplitudes of the baroclinic component, $(\Delta A^2 + \Delta B^2)^{1/2}$, and barotropic component, $(A^2 + B^2)^{1/2}$, are related by

$$A^2 + B^2 = \Delta U^2 (\Delta A^2 + \Delta B^2)/D \quad (34)$$

The baroclinic wave amplitude squared is, using (24),

$$\Delta A^2 + \Delta B^2 = \tau \frac{(\Delta U_e - \Delta U)}{c_2 H_1 \Delta U} \quad (35)$$

Two conditions emerge for the existence of the periodic Rossby solution:

- i. $\lambda/\kappa > 1$ such that ΔU is real in (33)
- ii. $0 < \Delta U < \Delta U_e$ such that $\Delta A^2 + \Delta B^2$ is real in (35)
assuming ΔU_e is positive, i.e., cold air to the north in the radiative equilibrium state.

Condition i restricts the east-west wavelength to be greater than the Rossby radius of deformation; however it is not sufficient to insure that the

periodic solution exists. For wavelengths a little longer than the radius of deformation ΔU is very large, condition ii is violated, and the thermodynamic equation is not satisfied. The wave cannot transport heat northward fast enough to counter radiative heating at low latitudes and cooling at high latitudes. Thus there is both a dynamical constraint, condition i, and a thermodynamical constraint, condition ii, that must be satisfied for a steady propagating Rossby wave to exist. These points are illustrated in Fig. 3 where $\Delta A^2 + \Delta B^2$ is shown as a function of horizontal wavenumber by the solid line. The range of wavenumbers over which the Rossby solution exists coincides exactly with the range over which the Hadley solution is unstable. The wind shear, shown by the dashed line, is less than ΔU_0 for these wavelengths.

Fig. 4 shows the amplitude of the propagating nonlinear Rossby wave in the unstable region. For a given equilibrium shear ΔU_0 , the most unstable wavenumber in Fig. 2 does not achieve the maximum amplitude in Fig. 4. The longer wavelengths, typically, achieve larger amplitudes in spite of the fact that their initial growth rates are not as large as the shorter more unstable wavelengths. This results from the fact that the longer wavelengths do not reduce the wind shear, ΔU , as much below ΔU_0 as the shorter more unstable waves, see Fig. 3. They thus have more available potential energy to tap and eventually achieve a larger amplitude. Figs. 5 and 6 show the time-evolution of wavenumber 4 kinetic energy and associated mean shear, ΔU , for an initially small disturbance to the unstable Hadley solution when $\Delta U_0 = 20 \text{ ms}^{-1}$. In this and all subsequent numerical integrations the algorithm of Lorenz (1963) was used. Large and slowly damped oscillations in the energy and shear occur as they approach the propagating Rossby wave solution. The oscillations are 180°

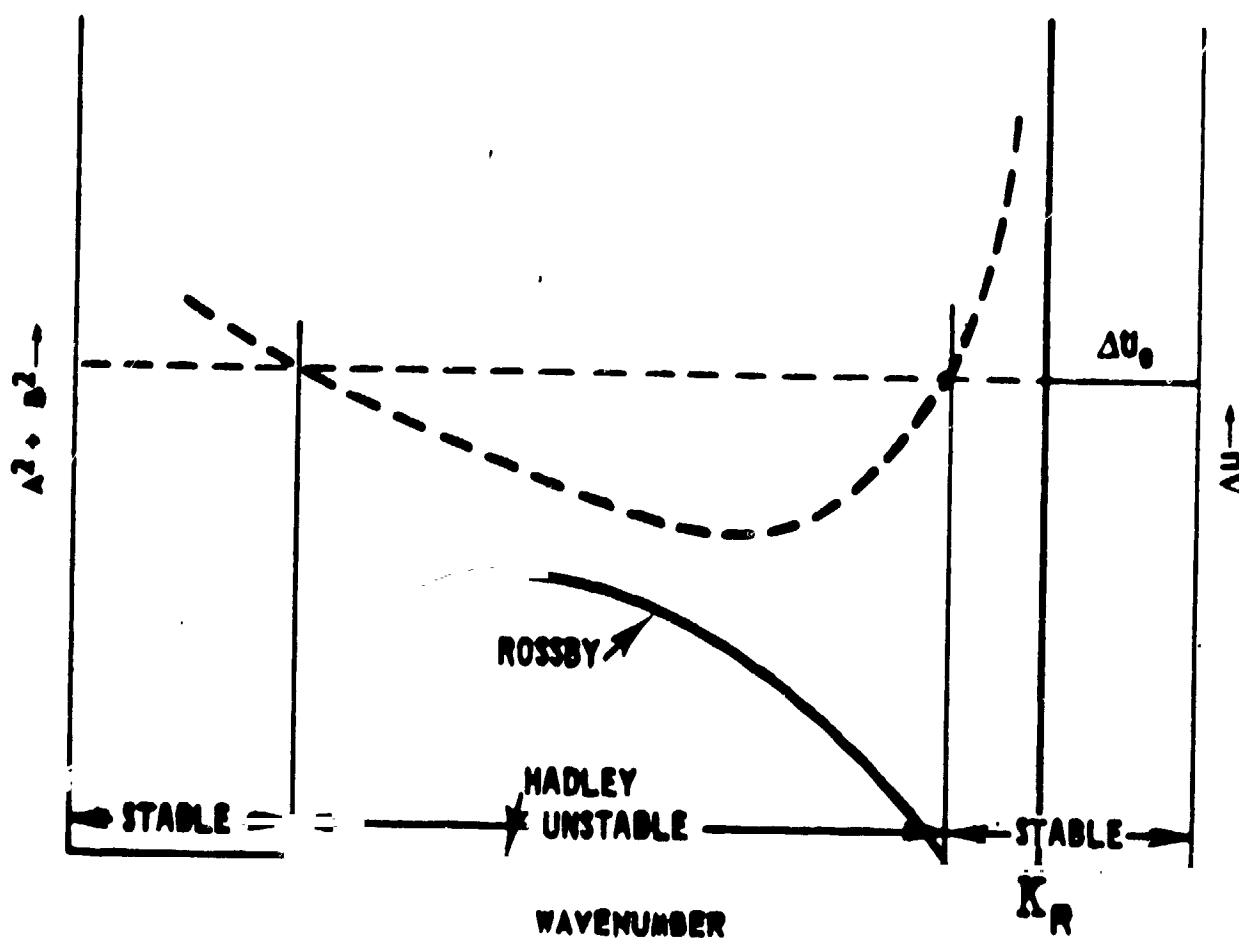


FIG. 3 Hadley and Rossby solutions without topography. Solid curve is amplitude of Rossby solution, $\Delta A^2 + \Delta B^2$, and dashed curve is the shear, ΔU . Rossby solution exists if $\Delta U < \Delta U_0$. K_R is wavenumber of Rossby radius of deformation.

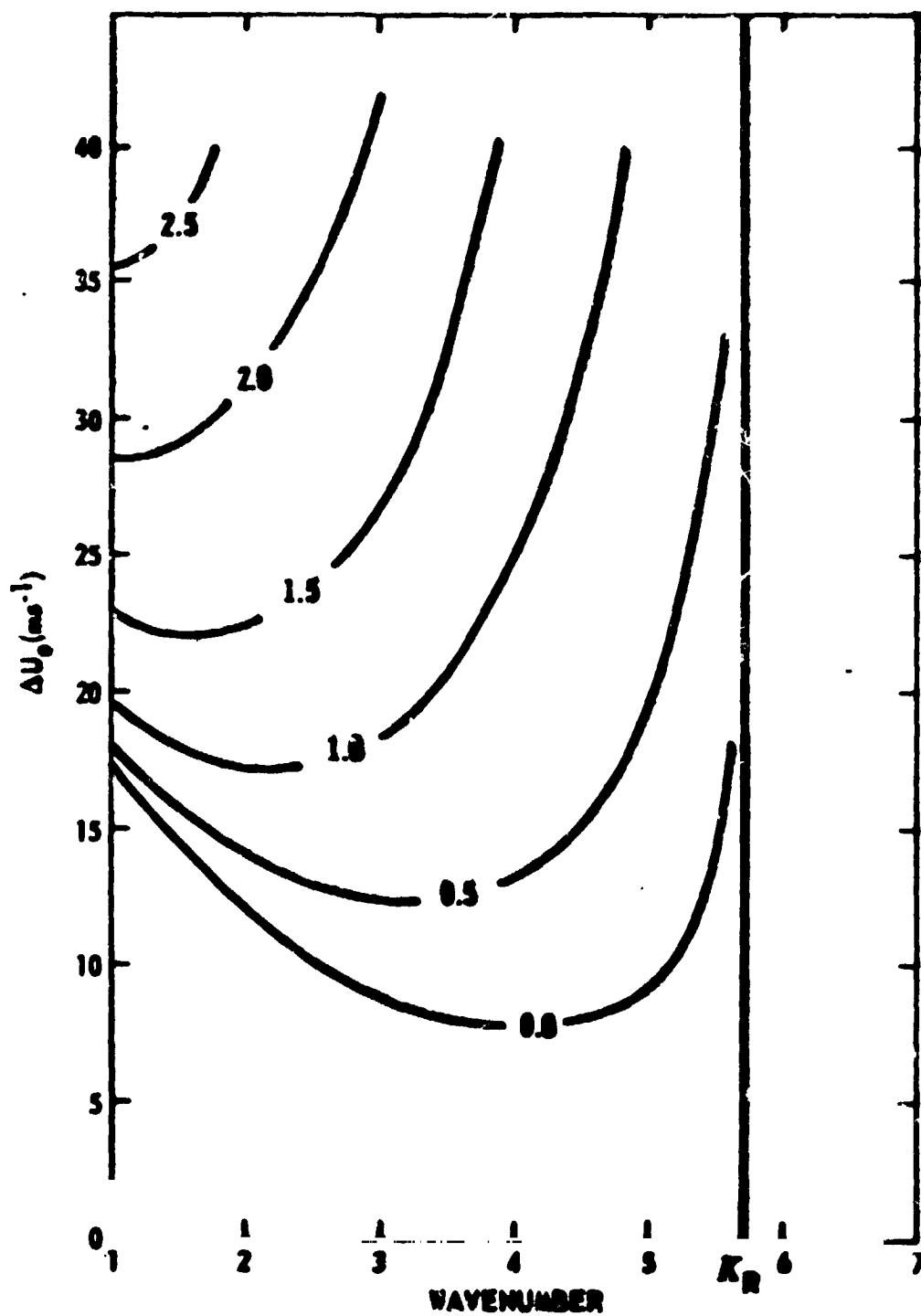


FIG. 4 Amplitude (dimensionless) of Rossby solution without topography.

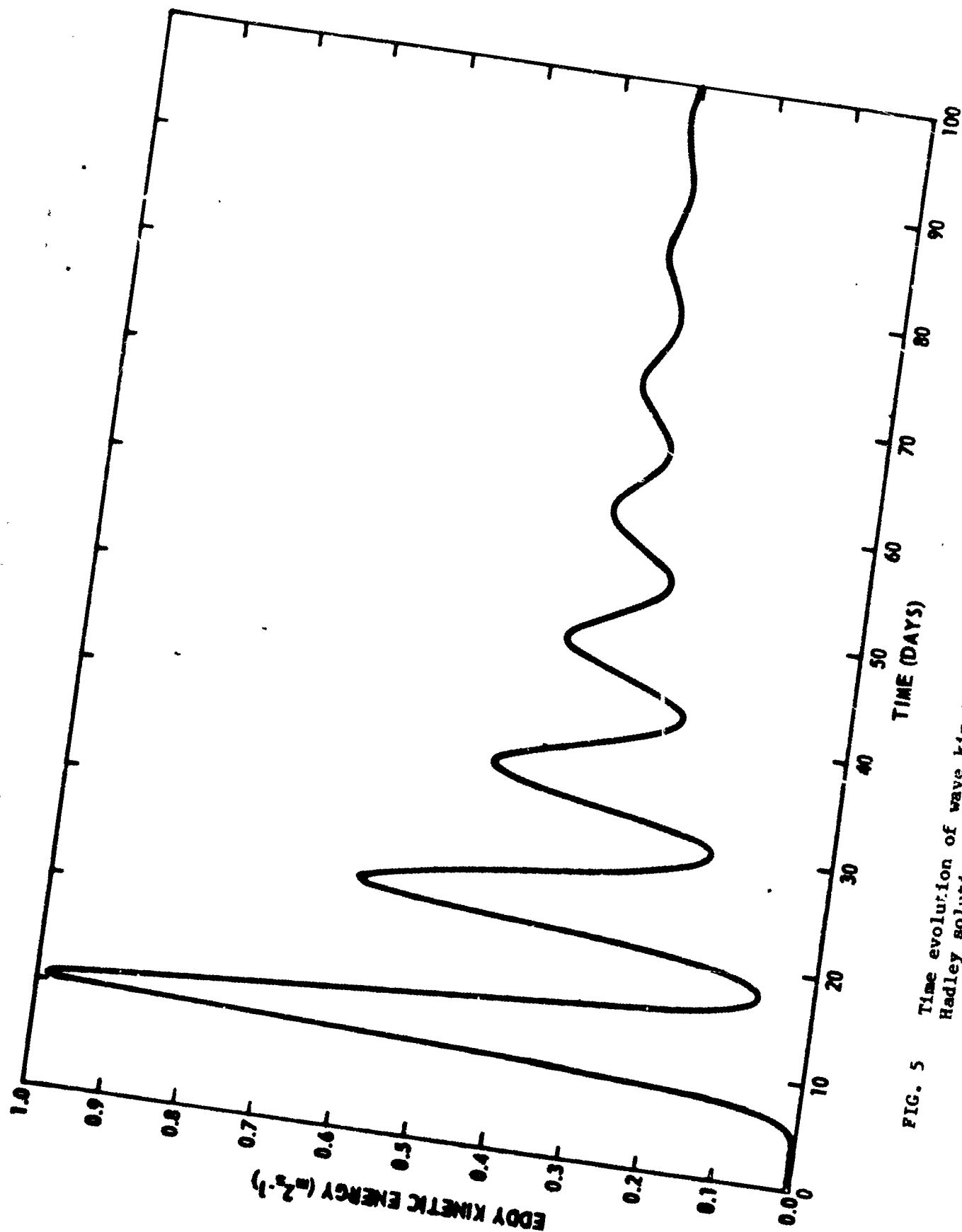


FIG. 5 Time evolution of wave kinetic energy from unstable perturbation to Hadley solution to steady Rossby solution.

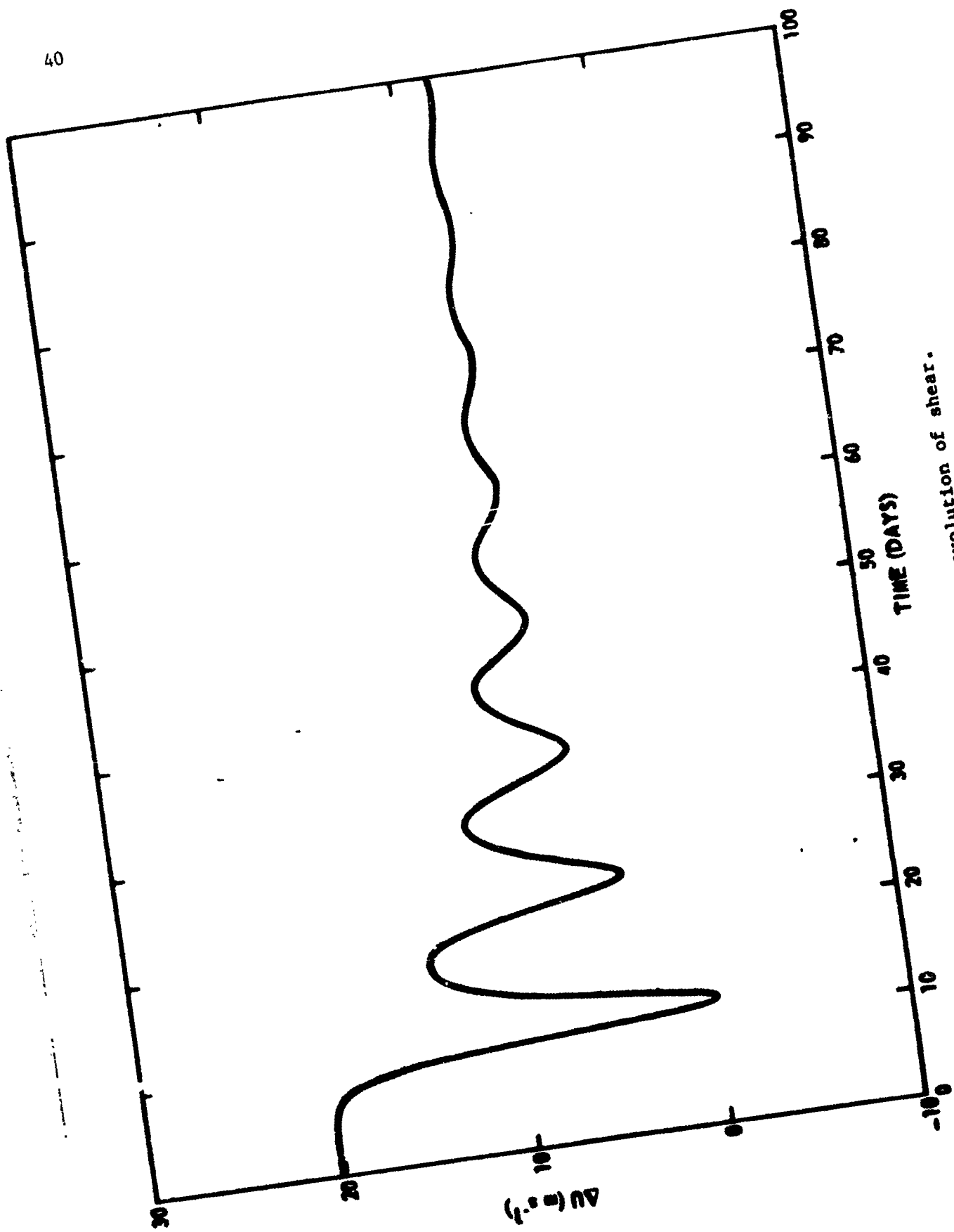


FIG. 6 Time evolution of shear.

out of phase with each other as wave and mean flow interact via the wave heat transport and associated mean meridional vertical motion field.

Our analysis of the topography - free model will be completed by examining the stability of the periodic Rossby solution to infinitesimal perturbations. This step is complicated by the fact that the coefficients of the resulting perturbation equations are time dependent. Let the subscript R be used to denote a variable associated with the Rossby solution. According to (28), we can let

$$\left. \begin{aligned} A_R &= A_S \sin(\omega t) + A_C \cos(\omega t) \\ B_R &= -A_S \cos(\omega t) + A_C \sin(\omega t) \\ \Delta A_R &= \Delta A_S \sin(\omega t) + \Delta A_C \cos(\omega t) \\ \Delta B_R &= \Delta A_S \cos(\omega t) + \Delta A_C \sin(\omega t) \end{aligned} \right\} \quad (36)$$

Let \tilde{S}_R be a column matrix representing the infinitesimal disturbance to the Rossby wave. Then

$$\dot{\tilde{S}}_R = \tilde{M}_R \tilde{S}_R, \quad (37)$$

where \tilde{M} is given by (27) but with A, B, ΔA , and ΔB replaced by the right sides of Eqs. (36).

Consider the change in \tilde{S} over a period, $T \equiv 2\pi/\omega$, associated with the propagating Rossby wave. Floquet theory, Iooss and Joseph (1980), deals with the linear stability of time periodic states and the object is to find the complex Floquet multipliers M_i , $i = 1, \dots, n$. For the present problem,

$n = 5$. If the modulus of each M_1 is less than unity, the basic state is stable. If at least one is greater than unity, it is unstable. Marsden and McCracken (1976) presented a simple numerical technique to find M_1 . Integrate the equation $\dot{\tilde{A}} = \tilde{M}_T \tilde{A}$, where \tilde{A} is $n \times n$, numerically from an initial state given by the unity matrix over exactly one period.

The eigenvalues of the resulting monodromy matrix \tilde{A} are the multipliers. Marsden and McCracken (1976) show that one multiplier will always be $+1$ and thus the stability is found from the moduli of the remaining four. This technique is particularly attractive since it can be applied to periodic solutions which are determined analytically or numerically. When topography is included in the model, we shall find that simple analytical periodic solutions are no longer available.

The periodic Rossby wave solution was stable under all conditions. In fact, the Floquet multipliers are all independent of U the mean zonal wind speed. Rossby waves have been shown to be unstable under certain conditions either due to a Rayleigh type of instability of the mean flow, Lorenz (1972), or to resonant interactions between the disturbance and the Rossby wave in the weak interaction limit, Gill (1974) and Clark (1978). Both of these mechanisms are precluded from this study.

4. Effect of Topography

In this section we shall investigate how topography affects the steady solutions, their stability, and the long-term evolution of initially baroclinically unstable disturbances.

A solid lower boundary can exert two kinds of drag on the atmosphere. One is a frictional drag due to tangential stress at the boundary. The second is a form drag or normal stress due to pressure differences across undulations in the lower boundary. In this model the former stress does not occur since internal viscosity is not allowed for while the latter can occur with topography. Consider the form drag exerted on the fluid in the x -direction averaged over a wavelength: $\int p_s (\partial h_s / \partial x) dx$, where p_s is the surface pressure. When this is integrated by parts it becomes proportional to $\int h_s v_g dx$. If Eqs. (4), (7), and (10) are used, the integral can be evaluated and it is clear that we can interpret the term $H_2(B - \Delta B)$ in Eq. (24) as the tendency of the form drag to change the mean shear. As we shall see, the topography permits new time independent equilibria aside from Hadley solution of the previous section. We can now have solutions consisting of stationary finite-amplitude waves and associated mean zonal flows. A new form of instability of these equilibria called form-drag instability by Charney and Straus (1980), hereafter referred to as CS, can occur. The instability results if an increase (decrease) of mean shear, ΔU , from an equilibrium is associated with a decrease (increase) in the form-drag leading to an amplifying disturbance.

CS were also able to demonstrate that form-drag instability is closely related to a resonant state being approximated where the mean flow configuration is such that a Rossby wave disturbance to a Hadley circulation

is close to being stationary. Growth of the wave ensues as long as its wavelength is the same as that of the topography.

An appropriate question here is whether these two views of form-drag or topographic instability are mutually exclusive or is a comprehensive understanding of the phenomenon to be gained only by considering both mechanisms. CS do not clarify this point.

Fig. 7 shows the solution to Eqs. (22) to (26) obtained by setting all time derivatives equal to zero. A single equation in ΔU is formed which is solved numerically. U and ΔU_0 are set equal to 20 ms^{-1} . For certain values for the horizontal wavelength of the topography and the associated stationary wave, multiple solutions are possible. The Hadley solution shown by the horizontal line has $\Delta U = 20 \text{ ms}^{-1}$ and, of course, is independent of wavelength. It is stable for wavelengths smaller than the Rossby radius of deformation (λ_R) and becomes baroclinically unstable for wavelengths larger than about 5500 km. A Hopf bifurcation, Marsden and McCracken (1976), occurs at the critical wavelength as a pair of eigenvalues of the stability matrix crosses the imaginary axis. An analytical form for the periodic solution could not be found and thus all inferences about its behavior were obtained from numerical solutions.

At ultra-long wavelengths corresponding to zonal wavenumbers 1 to 3 and short wavelengths for wavenumber 7 or greater, a pair of stationary Rossby solutions appears. The high index solution (with relatively small wave amplitude) is unstable (except at very small wavelengths where it exchanges instability with the Hadley solution) and the low index solution is stable. The instability of the high index mode is evidenced by a single eigenvalue of the stability matrix having a positive real part. The amplifying disturbance

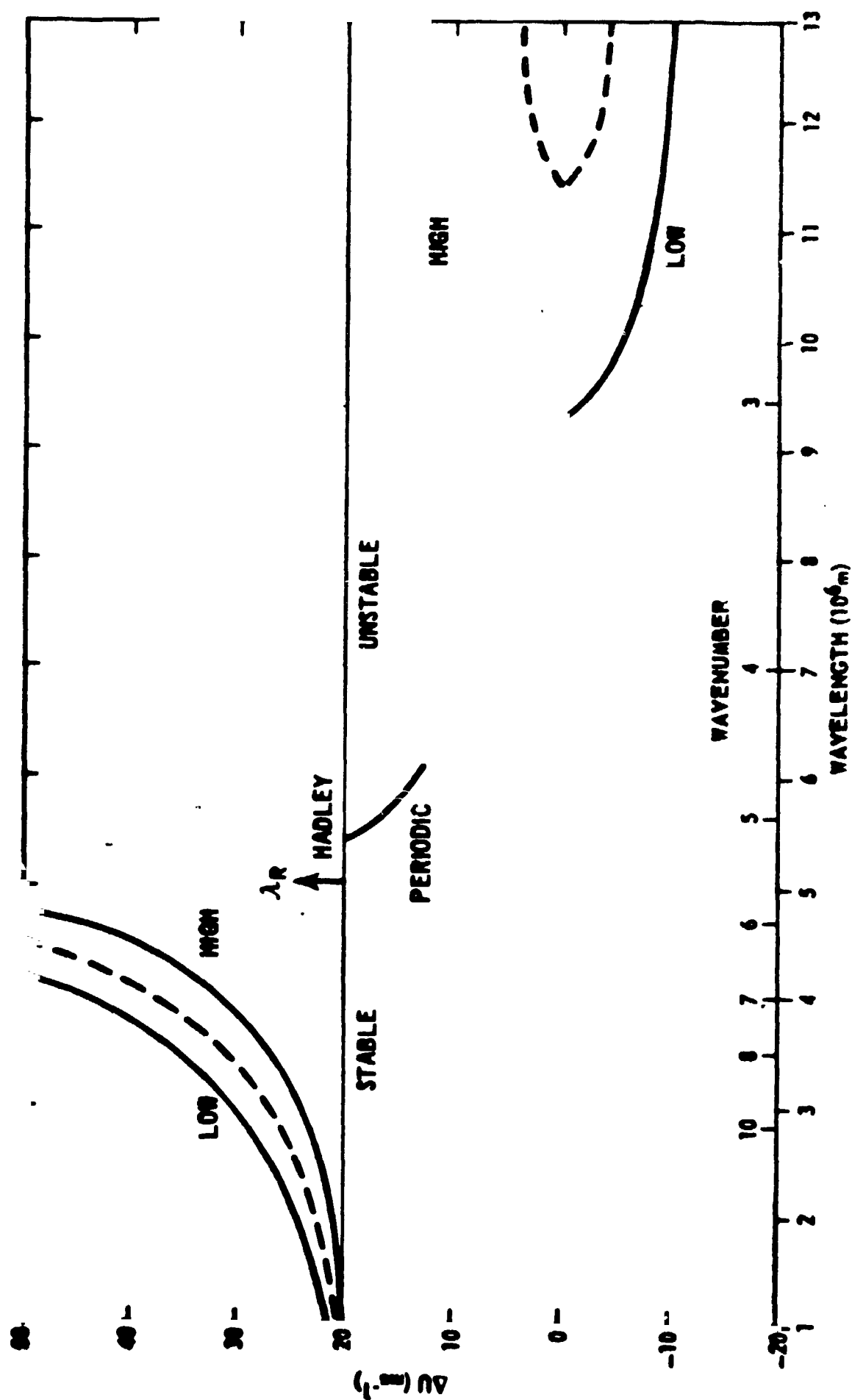


FIG. 7 Steady solutions with topography (amplitude 500 m). λ_R is Rossby radius of deformation. Dashed curve are resonant shears.

is thus stationary and the growth is related to the form-drag associated with the topography.

The dashed lines in Fig. 7 indicate the shear, ΔU , for which a resonant response to topographic forcing would occur. In the absence of dissipation and if $\Delta U_e = \Delta U$, the time-independent solution to Eqs. (22) to (26) is $B = \Delta B = 0$ (the topography varies as $\sin(kx)$) and A , ΔA , and Δ' are determined from

$$\begin{pmatrix} U - U_c & \Delta U_e \\ R\Delta U_e & U - U_c^* \end{pmatrix} \begin{pmatrix} A \\ \Delta A \end{pmatrix} = (U - \Delta U_e) \begin{pmatrix} b_o \\ b_o^* \end{pmatrix}. \quad (38)$$

An unbounded response to the topography occurs when ΔU attains that value for which the determinant is zero:

$$\Delta U_e = \Delta U = \pm [(U - U_c)(U - U_c^*)/R]^{1/2} \equiv \Delta U_R \quad (39)$$

A finite-amplitude stationary wave is excited by the topography for $\Delta U_e \neq \Delta U_R$ provided the mean flow in the lower layer, $U - \Delta U$, is nonzero. The dashed lines in Fig. 7 show the resonant shear and both the high and low index modes are associated with shears that are close to resonance.

The time-independent solutions to the model depend strongly on the radiative forcing. Fig. 8 shows the Hadley, low index, and high index modes as functions of ΔU_e when $U = 20 \text{ ms}^{-1}$. A Hadley solution strictly exists only when the wave amplitudes are zero. This can occur when $\Delta U = \Delta U_e = U = 20 \text{ ms}^{-1}$ since the zonal flow in the lower layer will be zero. The label Hadley will still apply to those solutions for which $\Delta U \sim \Delta U_e$ even though a weak wave is excited by the topography. The model can catastrophically transform from a

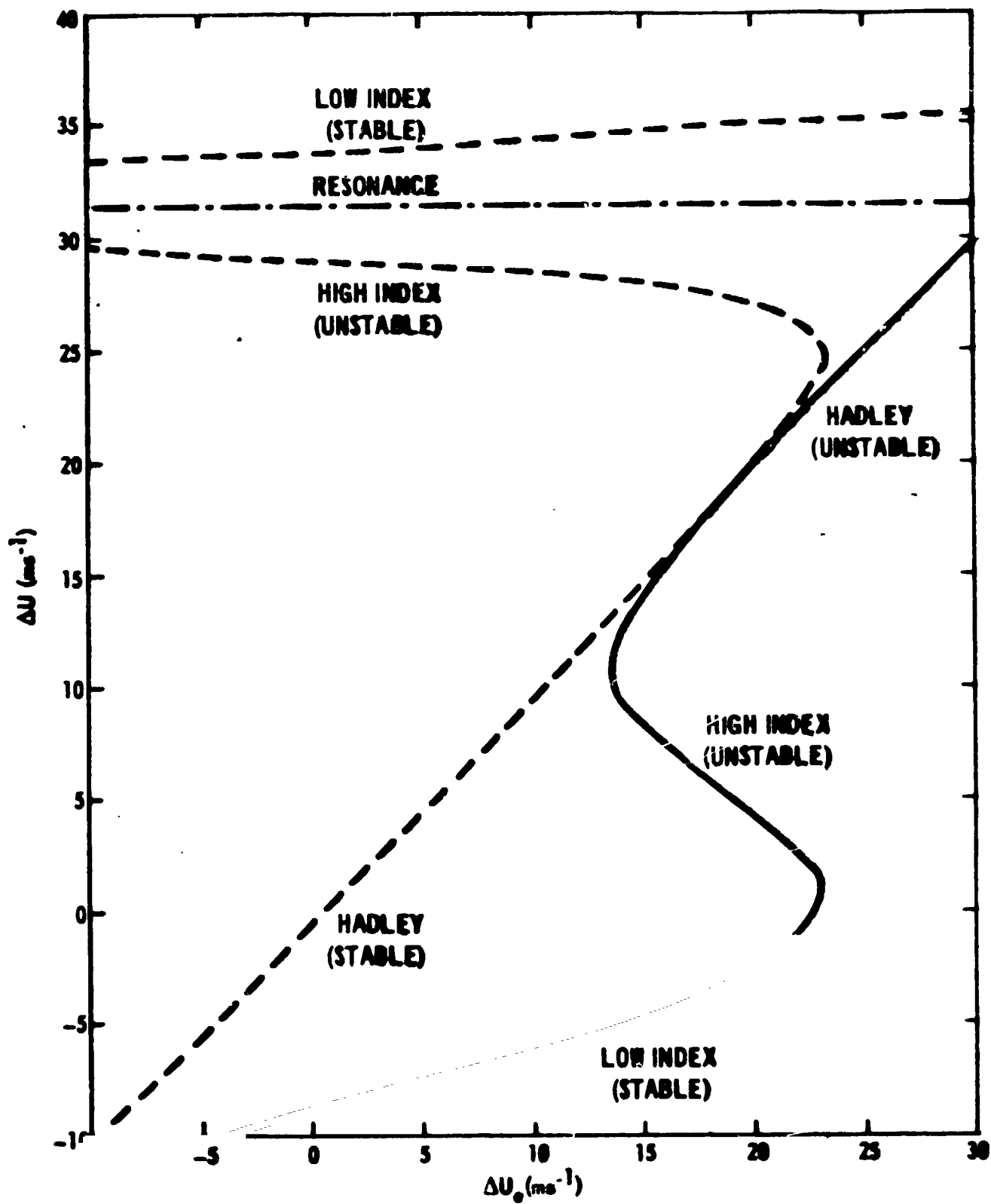


FIG. 8 Steady topographic solutions. Solid line - wavenumber 3, dashed line - wavenumber 8.

Hadley configuration to a low index or blocking configuration for small changes in ΔU_e for both the short and long wavelengths. Furthermore the blocking pattern can be highly stable to further changes in ΔU_e irrespective of their direction.

Fig. 9 illustrates the nature of the instability of the high index flow at wavenumber 3. The tendency of ΔU is plotted against ΔU by solving Eq. (24) assuming \dot{A} , \dot{B} , $\dot{\Delta A}$, and $\dot{\Delta B}$ are zero in (22), (23), (25), and (26) respectively. Baroclinic instability of the Hadley solution is thus suppressed. The low index solution is meta-stable. Only very large positive departures of ΔU beyond the value for the high index equilibrium can amplify with time. The high index equilibrium is clearly unstable with positive (negative) departures in shear tending to approach the Hadley (low index) equilibrium. The variation of the form-drag, $-H_2(B - \Delta B)$, with ΔU is illustrated by the dashed line. Maximum westward drags are achieved at shears close to resonant values of Eq. (39) shown by the heavy arrows. The resonant shear must lie to the right of the low index equilibrium to render it unstable since positive (negative) departures of ΔU decrease (increase) the eastward drag. The high index mode is stable by similar reasoning.

The proximity of a resonant configuration to an equilibrium is thus necessary but not sufficient for it becoming unstable. Note however that the coincidence of an equilibrium with resonance would not render it unstable. The growth of a quasi-resonant disturbance to a finite-amplitude wave equilibrium is only guaranteed if the resonant shear is to the right of the critical shear in Fig. 9.

This relationship is further illustrated in Fig. 10 where the wave amplitude is shown as a function of the equilibrium shear, ΔU_e , for wavenumber

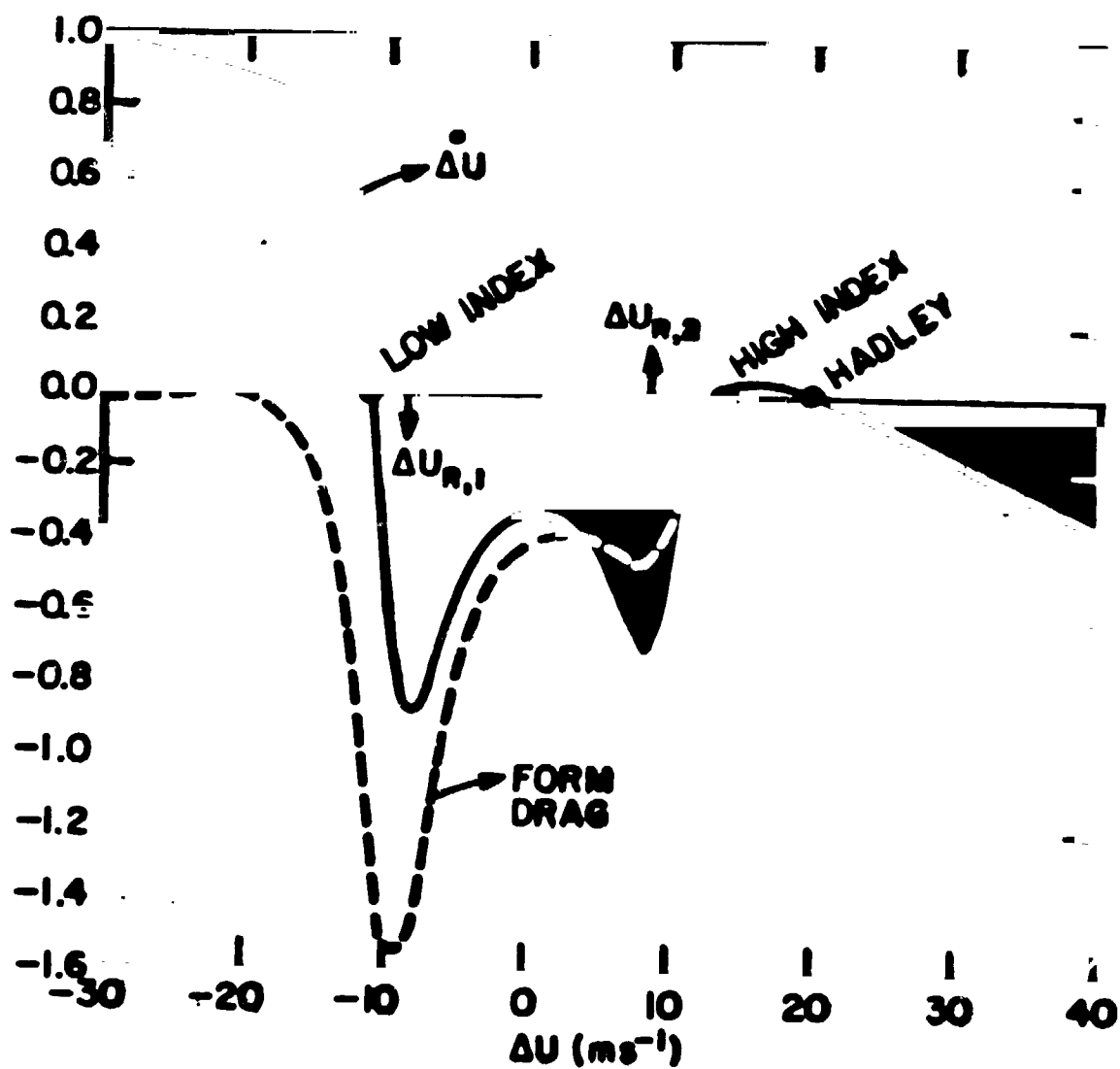


FIG. 9 Shear tendency ($\dot{\Delta U}$) and form-drag, both dimensionless, for wavenumber 2. $\Delta U_0 = 20 \text{ ms}^{-1}$. ΔU_R indicates resonant shear.

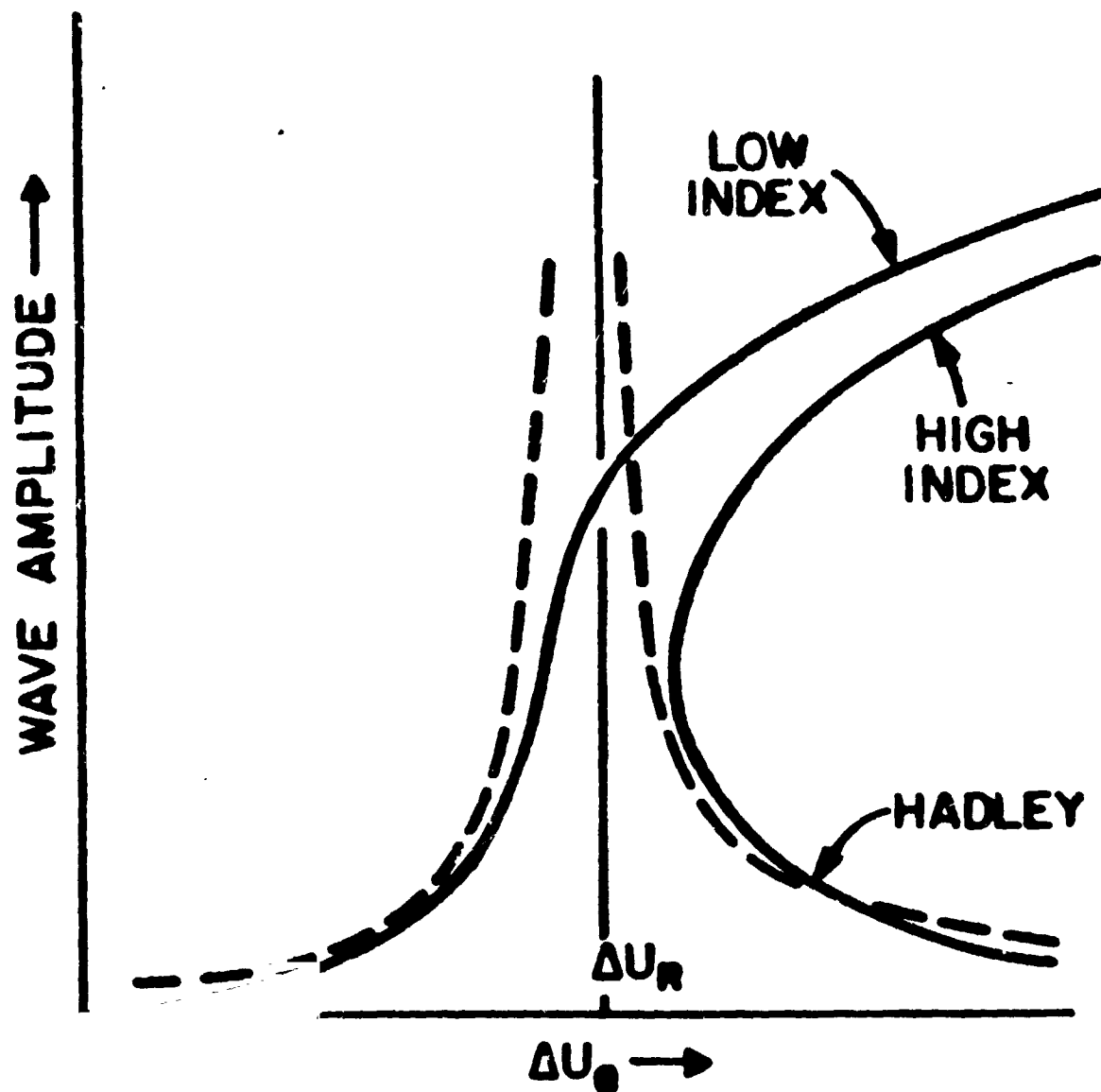


FIG. 10 Dissipative (solid line) and dissipation free (dashed) steady solutions. ΔU_R is resonant shear for dissipation free case. Zonal wavenumber is 3.

3. Without dissipation an unbounded amplitude appears as the resonant shear ΔU_R given by Eq. (39) is approached. With dissipation, as shown by the solid lines, three equilibria are possible for $\Delta U_0 > \Delta U_R$. The low index and high index shears ΔU (not shown) for wavenumber 3 are on either side of the resonant shear. The presence of dissipation is this indispensable to multiple equilibria in the steady state model.

The primary purpose of this section is to study the effects of topography on the baroclinically unstable disturbances to the Hadley equilibrium in Fig. 7. The results of a stability analysis of the Hadley equilibrium are shown in Fig. 11. The dashed lines are the shear, ΔU , of the Hadley solution which is smaller than ΔU_0 with topography (without topography they are equal). If this figure is compared with Fig. 2, it is seen that the topography stabilizes the Hadley solution for small ΔU_0 , whereas for large ΔU_0 the e-folding times are roughly equal for wavenumbers 3 to 5 but are increased for wavenumbers 1 and 2. The ultra-long waves are stabilized with large radiative forcing because the topography reduces the shear via the form-drag and thus the store of energy for the wave to feed upon.

A series of numerical integrations have been carried out to determine the long-term evolution of wavenumber 5 unstable disturbances (the topography has the same wavenumber). Runs with forcing, ΔU_0 , just above the onset of instability (a little less than 13 ms^{-1}) evolve into singly-periodic solutions. The period (about 5 days) can be anticipated from the imaginary part of the pair of eigenvalues that cross the imaginary axis at the Hopf bifurcation. Fig. 12 shows the wave kinetic energy and shear from day 50 to 150 for $\Delta U_0 = U = 20 \text{ ms}^{-1}$. They oscillate 180° out of phase with each other. The solution consists of a eastward propagating finite-amplitude wave whose

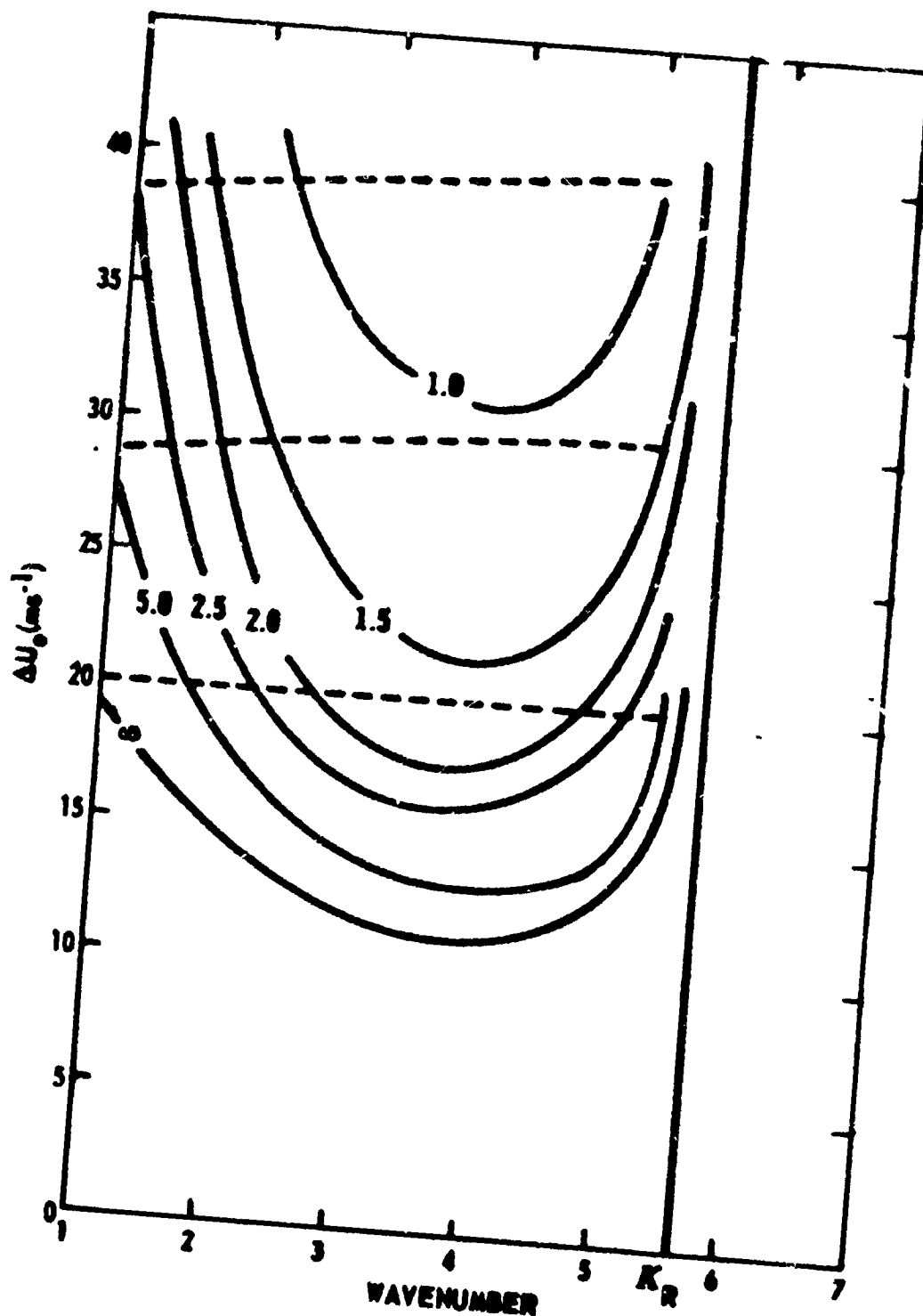


FIG. 11 Stability analysis with topography. Curves are labelled in e-folding time (days). Dashed lines show shear, ΔU , for $\Delta U_0 = 20$, 30, and 40 ms⁻¹.

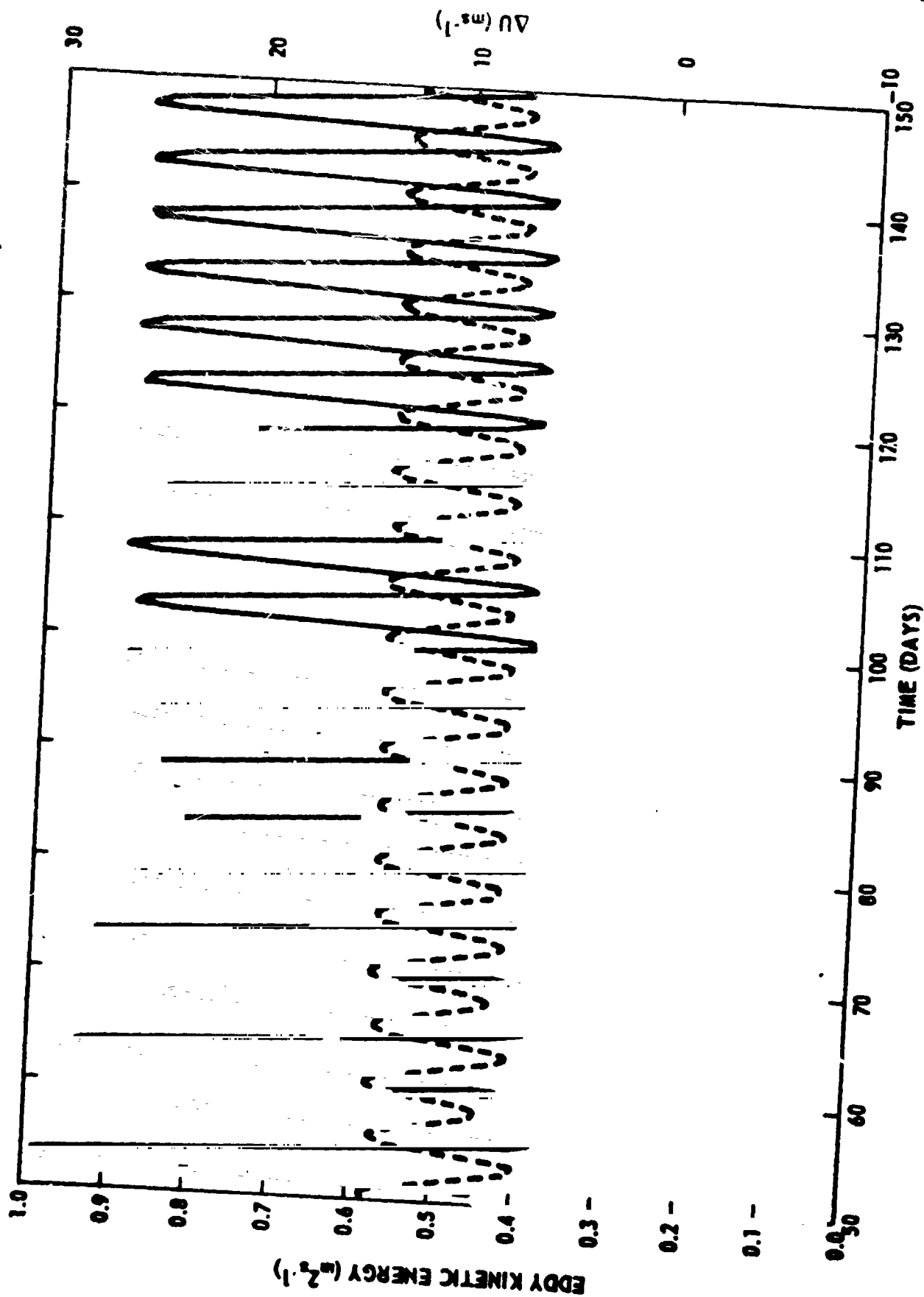


FIG. 12 Singly-periodic solution, wavenumber 5. Solid line - wave kinetic energy, dashed line - shear. $U = \Delta U_e = 20 \text{ ms}^{-1}$.

amplitude modulates as it comes into and out of phase with the topography. The period of the modulation is thus the same as the wave period. The baroclinic conversion of zonal available potential energy also influences the wave amplitude but both effects (baroclinicity and topography) are in phase. Fig. 13 shows the baroclinic, topographic, and radiative generation of zonal available energy as well as the shear (proportional to the zonal mean temperature gradient) over a period. Both the baroclinic and topographic energy sources lead the shear by about 90° .

When the forcing exceeds 23.53 ms^{-1} , a doubly periodic solution appears, see Fig. 14, with the fundamental period of 5 days still present but with a harmonic with period 10 days appearing. The modulated finite-amplitude wave still propagates eastward with a period of about 5 days and thus the form drag oscillates at the fundamental frequency. The baroclinic and topographic energy conversions are still in phase, see Fig. 15, but the baroclinic conversion has the fundamental as well as the first harmonic. An increase of the forcing beyond 24.36 ms^{-1} induces an additional subharmonic of the fundamental with a 20-day period. A 40-day period appears beyond 24.54 ms^{-1} and the solution becomes aperiodic when ΔU_e exceeds 24.6 ms^{-1} . These findings are summarized in Fig. 16.

A Floquet stability analysis of the singly or doubly periodic solution in the vicinity of the points where the new harmonics first appear can help determine the values of ΔU_e at the points and also verify that indeed a subharmonic bifurcation has occurred, i.e., that the singly periodic solution has exchanged stability with a doubly periodic one. Let E_1 be the Floquet exponent related to the multiplier M_1 by the formula

$$M_1 = e^{E_1 T}, \quad (40)$$

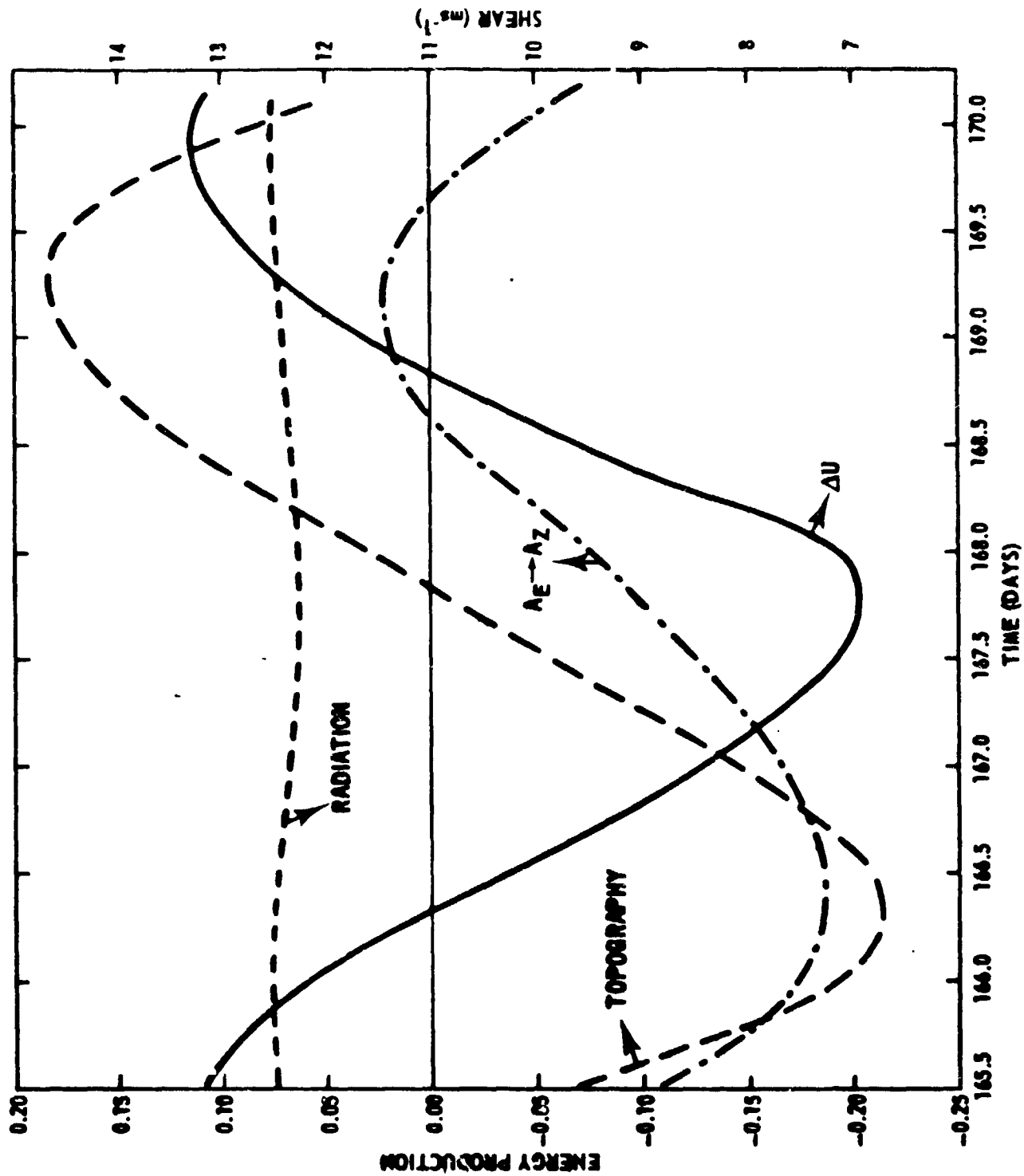


FIG. 13 Diagnosis of singly-periodic solution of Fig. 12.

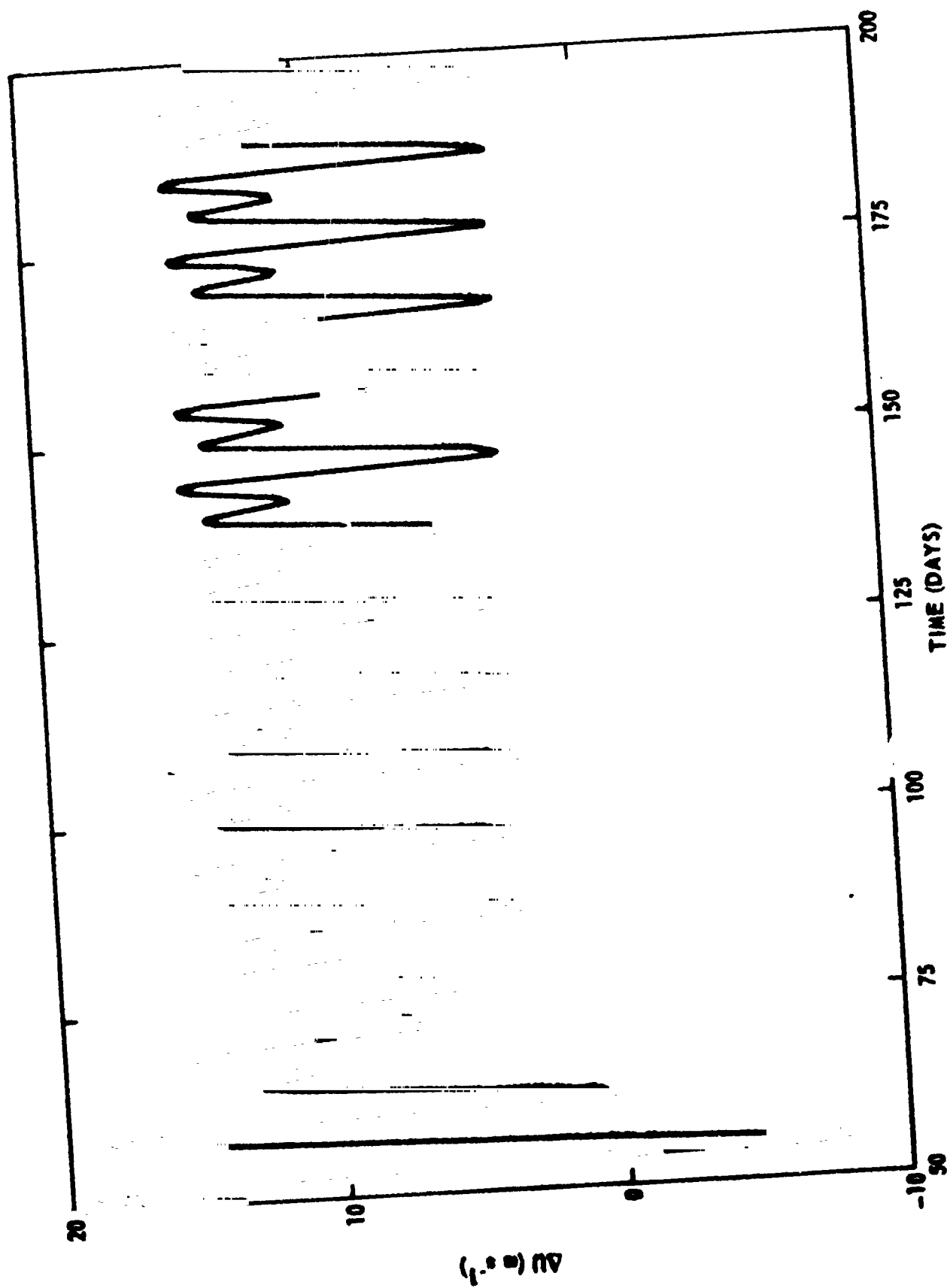


FIG. 14 Doubly-periodic solution, wavenumber 5. $U = 20 \text{ ms}^{-1}$, $\Delta U_e = 24 \text{ ms}^{-1}$.

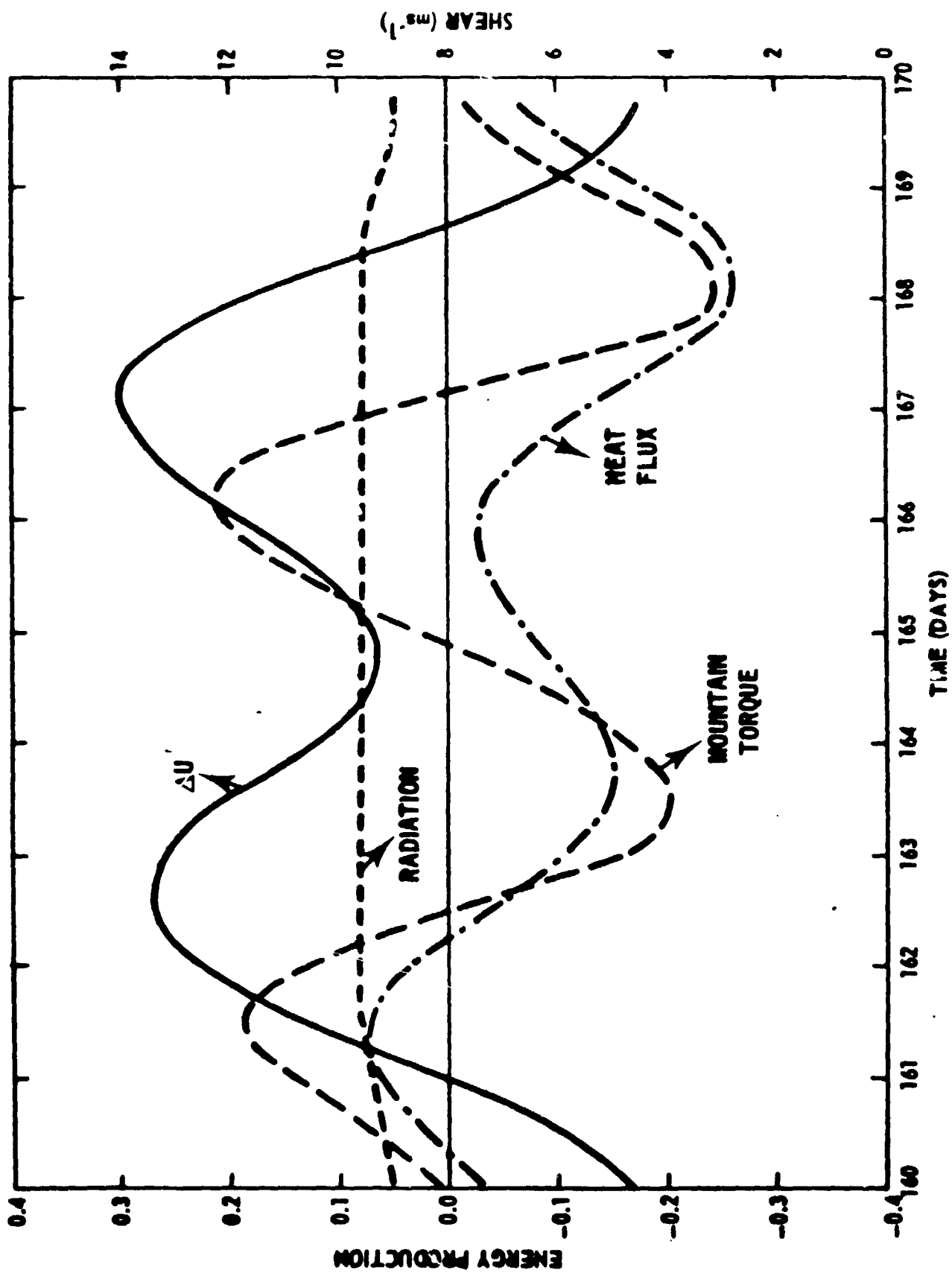


FIG. 15 Diagnosis of doubly-periodic solution of Fig. 14.

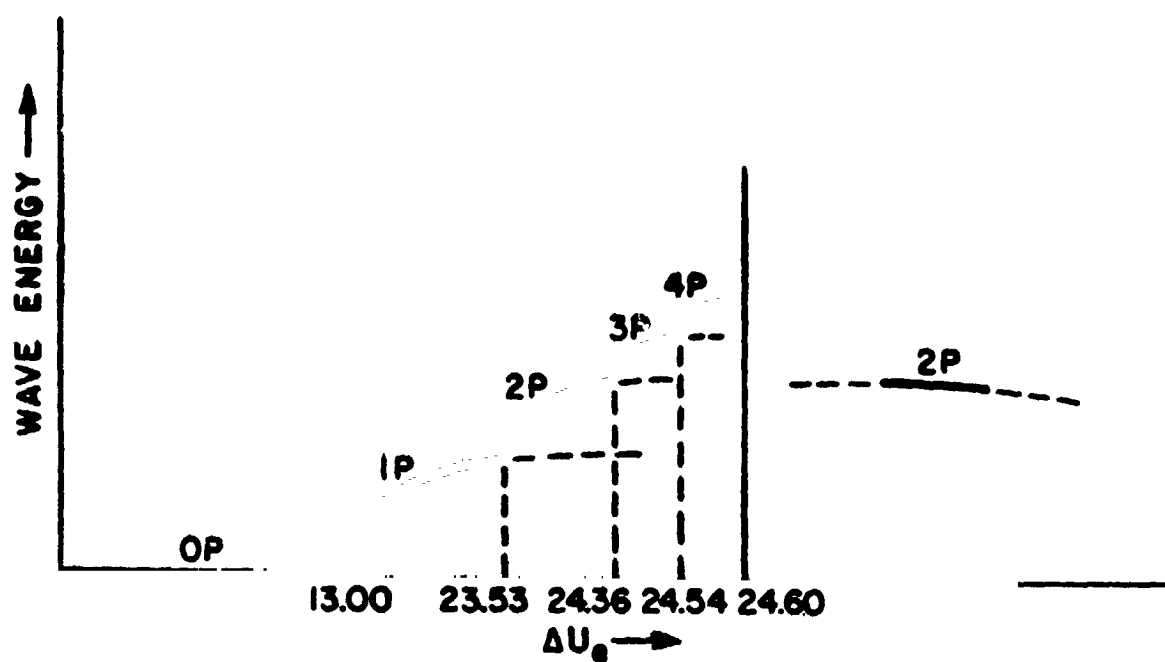


FIG. 16 Bifurcation diagram. Wavenumber 5, $U = 20 \text{ ms}^{-1}$.

Iooss and Joseph (1980). If a solution of period $2T$ appears at the bifurcation point then $E_1 = 2\pi i/2T$ and thus $M_1 = -1$. A subharmonic bifurcation occurs at that value of ΔU_e for which the modulus of this multiplier is unity. This can be used as a means of finding the precise location of a bifurcation point. Visual inspection of the solutions yields only very rough estimates of the critical forcing ΔU_e . One of the multipliers of the monodromy matrix will still be $+1$. It is possible, but unlikely, that two of the multipliers could simultaneously cross through -1 at the bifurcation point but this would almost certainly yield a new solution whose period is not an integral multiple of the fundamental. This behavior is not often observed in geophysical models.

An interesting side benefit of the Floquet analysis is that it permitted the period of the fundamental or doubly periodic solution to be precisely determined as the forcing changed. It is only when the numerical integration to determine the monodromy matrix is carried over an exact period that one of the $M_1 = +1$. Both periods increased slightly with increased forcing. For instance the fundamental period increased from 4.96 days to 5.03 days from $\Delta U_e = 13$ to 23.53 ms^{-1} .

A sequence of subharmonic bifurcations leading to a chaotic or aperiodic solution for a baroclinically unstable initial mean flow has been found. In this model the presence of a sinusoidally varying solid lower boundary was necessary to stimulate the multi-periodic solutions. Only constant amplitude waves evolve in the topography-free model. The topography is not always necessary however, for multi-periodic solutions. Pedlosky and Penzen (1980) developed an asymptotic two-layer nonlinear model for marginally baroclinically unstable waves without topographic forcing. In response to

varying dissipation, harmonics of the fundamental frequency can evolve just as in this model.

The intriguing aspect of this study is that the values of the forcing, ΔU_e , at which the subharmonic bifurcations occur closely follow the hypothesis of Feigenbaum (1978), namely, if $\Delta U_{e,n}$ is the n^{th} bifurcation value,

$$\Gamma_n \equiv \frac{\Delta U_{e,n} - \Delta U_{e,n+1}}{\Delta U_{e,n+1} - \Delta U_{e,n+2}} \rightarrow 4.6692 \text{ for } n \text{ large.} \quad (41)$$

Pedlosky (1981) did not obtain such close agreement.

Feigenbaum considered one-dimensional smooth mappings of a closed interval upon itself with a single maximum. It seems unreasonable to expect that the hypothesis should work for a multi-dimensional differential system like ours and yet it does.

An appropriate question with a severely truncated model like this one is how sensitive the results are to the degree of truncation. Is the sequence of period doublings in response to changing external forcing merely a feature unique to low order models? All the runs with initially baroclinically unstable disturbances were repeated, but with two additional modes in the north-south direction in addition to the gravest mode, i.e., $\cos(ly)$, $\cos(2ly)$, and $\cos(3ly)$ modes were included. One wavenumber in the x-direction was only represented. A similar sequence of bifurcations of the periodic solutions were obtained leading to aperiodic behavior beyond a critical forcing. Feigenbaum's formula was reasonably satisfied again.

An interesting phenomenon occurs as ΔU_e is increased well beyond the value for the onset of aperiodic flow. A region of doubly-periodic flow appears in the chaotic region, see Fig. (16). Possibly a reversed bifurcation

process has occurred, Lorenz (1980). A similar phenomenon was found by Pedlosky and Frenzen (1980).

DISCUSSION

Topography has affected the steady solutions, their stability, and the long-term evolution of baroclinically unstable waves in a fundamental way. It has provided an additional degree of freedom to the model that has enabled multi-periodic and aperiodic solutions exist. Calculations with smaller but finite amplitudes for the topography reveal a similar sequence of subharmonic bifurcations with increasing radiative forcing. And yet, with no topography this behavior is entirely absent. Is the transition from the singly-periodic non-topographic behavior to the multi-periodic, bifurcating behavior gradual or sudden? Both the non-topographic and topographic models exhibit singular behavior at the value of forcing for which the Rossby and Hadley solutions exist. Part of the problem with the topography-free model is that the behavior of the Rossby solution near the singularity is not properly described because of too few external parameters. Shirer and Wells (1982) outline a technique to add terms to the polynomial in ΔU describing the steady state to fully unfold the singularity by expressing it in the most general form. Their procedure can identify what parameters should be added to the non-topographic model and indeed determine whether topography properly unfolds the singularity. Once that procedure has been completed, a proper evaluation of the role of topography can be made. Suffice it to say now that the topography-free model does not appear to be a generic one.

Another geophysical system has been found where temporal behavior evolves via a series of sub-harmonic bifurcations to an aperiodic state, in this case, under the influence of increasing zonally-symmetric heating. The preliminary indications are that this behavior is not altered by the degree of truncation

of the present spectral model. Equally intriguing is the fact that the prediction of Feigenbaum (1978) for the positions of the bifurcation points is apparently verified for a baroclinic model of arbitrary dimension. The fact that his formula is derived from a one-dimensional mapping of a closed interval upon itself suggests that the long-term behavior of many geophysical models tends to become one or two dimensional. Collet and Eckmann (1980) suggest how the time evolution of multi-dimensional systems in the vicinity of periodic solutions can be reduced in dimension by constructing a sequence of Poincaré maps onto hyperplanes of dimension $n - 1$ in n -dimensional spaces.

A frustrating aspect of this study was the apparent inaccessibility of analytic solutions for the propagating multi-periodic solutions with topography in spite of the simplicity of the spectral equations. The Lyapunov-Schmidt method, Iooss and Joseph (1980), could yield useful information about the singly-periodic solution near the bifurcation point at which the Hadley solution becomes baroclinically unstable in Fig. 7. It will give the initial terms in a regular perturbation expansion of the solution about this point.

APPENDIX

The purpose of this section is to show that the 5-coefficient system without topography reduces to a 4-coefficient system. Introduce the amplitude and phase of the barotropic wave, $|A|$ and ϕ respectively, and the same for the baroclinic wave, $|B|$ and α , such that

$$\begin{aligned} A &= |A| \cos \phi & B &= |A| \sin \phi \\ \Delta A &= |B| \cos \alpha & \Delta B &= |B| \sin \alpha \end{aligned} \quad (A1)$$

Eq. (22) and (23) can be transformed to

$$\dot{|A|} = \Delta U |B| \sin(\alpha - \phi) - d_0 |A| - b_0 (U - \Delta U) \sin \phi \quad (A2)$$

$$\dot{\phi} = - (U - U_c) - [\Delta U |B| \cos(\alpha - \phi) - b_0 (U - \Delta U) \cos \phi] / |A| \quad (A3)$$

similarly (25) and (26) becomes

$$\dot{|B|} = R \Delta U |A| \sin(\phi - \alpha) - d_0 |B| + b_0^* (U - \Delta U) \sin \alpha \quad (A4)$$

$$\dot{\alpha} = - (U - U_c^*) - [R \Delta U |A| \cos(\alpha - \phi) - b_0^* (U - \Delta U) \cos \alpha] / |B| \quad (A5)$$

If the topographic terms are dropped and the phases

$$\theta_d \equiv \alpha - \phi \quad (A6)$$

$$\theta_s \equiv \alpha + \phi$$

are introduced (A2) to (A6) become

$$\dot{|A|} = \Delta U |B| \sin \theta_d - d_o |A| , \quad (A7)$$

$$\dot{|B|} = - R \Delta U |A| \sin \theta_d - d_o |B| , \quad (A8)$$

$$\dot{\theta}_s = - (2U - U_c - U_c^*) - \Delta U \left\{ \frac{|B|}{|A|} + R \frac{|A|}{|B|} \right\} \cos \theta_d , \quad (A9)$$

and

$$\dot{\theta}_d = (U_c^* - U_c) + \Delta U \left\{ \frac{|B|}{|A|} - R \frac{|A|}{|B|} \right\} \cos \theta_d . \quad (A10)$$

The set is completed with the thermodynamic equation (24):

$$\dot{\Delta U} = - H_1 |A| |B| \sin \theta_d - r(\Delta U - \Delta U_e) , \quad (A11)$$

where the form-drag has been omitted.

The equations have an appealing simplicity when expressed in this form. The important feature is that $|A|$, $|B|$, θ_d , and ΔU evolve independently of θ_s and thus (A9) can be ignored rendering a 4-coefficient system. As soon as topography is introduced, these 4 coefficients are no longer independent of θ_s .

ACKNOWLEDGEMENTS

This work was supported by NASA Contract NAS8-33794. The author is indebted to Dr. Peter Koeden, Murdoch University, Australia, and Drs. John Dutton and Hampton Shirer of The Pennsylvania State University for their interest and helpful suggestions.

REFERENCES

- Baer, F., 1970: Analytical solutions to low-order spectral systems. Arch. Met. Geoph. Biokl., Ser. A., 19, 255-282.
- Boville, B.A., 1981: Amplitude oscillation on a β -plane. J. Atmos. Sci., 38, 609-618.
- Charney, J.G. and J.G. Devore, 1979: Multiple flow equilibria in the atmosphere and blocking. J. Atmos. Sci., 36, 1205-1216.
- Charney, J.G. and D.M. Straus, 1980: Form-drag instability, multiple equilibria and propagating waves in baroclinic, orographically forced planetary wave systems. J. Atmos. Sci., 37, 1157-1176.
- Clark, J.H.E., 1978: The stability of ultra-long waves on a mid-latitude β -plane. Quart. J. Roy. Meteor. Soc., 104, 429-445.
- Collet, P. and J.P. Eckman, 1980: Iterated Maps on the Interval as Dynamical Systems. Birkhäuser, Boston, 248 pp.
- Dutton, J.A. and P.E. Kloeden, 1983: The existence of Hadley convective regimes of atmospheric motion. J. Austral. Math. Soc., (Series B), 24, 318-338.
- Feigenbaum, M., 1978: Quantitative universality for a class of nonlinear transformations. J. Stat. Phys., 19, 25-52.
- Franceschini, V. and C. Tebaldi, 1979: Sequences of infinite bifurcations and turbulence in a five-mode truncation of the Navier Stokes equation. J. Stat. Phys., 21, 707-726.
- Gill, A.E., 1974: The stability of planetary waves on an infinite beta-plane. Geophys. Fluid Dynam., 6, 29-47.
- Holton, J.R., 1972: An Introduction to Dynamic Meteorology. Academic Press, 319 pp.
- Iooss, G. and D.D. Joseph, 1980: Elementary Stability and Bifurcation Theory. Springer - Verlag, 286 pp.
- Lindzen, R.S. and K.K. Tung, 1979a. A theory of stationary long waves. Part I: A simple theory of blocking. Mon. Weath. Rev., 107, 714-734.
- Lindzen, R.S. and K.K. Tung, 1979b. A theory of stationary long waves. Part II: Resonant Rossby Waves in the presence of realistic vertical shears. Mon. Weath. Rev., 107, 735-750.
- Lorenz, E.N., 1963: Deterministic nonperiodic flow. J. Atmos. Sci., 20, 130-141.

- Lorenz, E.N., 1972: Barotropic instability of Rossby wave motion. J. Atmos. Sci., 29, 258-264.
- Lorenz, E.N., 1980: Noisy periodicity and reverse bifurcation. Ann. New York Acad. Sci., 357, 282-291.
- Marsden, J.E. and M. McCracken, 1976: The Hopf Bifurcation and its Applications. Springer - Verlag, 408 pp.
- Mitchell, K.E. and J.A. Dutton, 1981: Bifurcation from stationary to periodic solutions in a low-order model of forced, dissipative barotropic flow. J. Atmos. Sci., 38, 690-715.
- Pedlosky, J., 1970: Finite amplitude baroclinic waves. J. Atmos. Sci., 27, 15-30.
- Pedlosky, J., 1972: Limit cycles and unstable baroclinic waves. J. Atmos. Sci., 29, 53-63.
- Pedlosky, J. and C. Frenzen, 1980: Chaotic and periodic behavior of finite - amplitude baroclinic waves. J. Atmos. Sci., 37, 1177-1196.
- Pedlosky, J., 1981: The effect of β on the chaotic behavior of unstable baroclinic waves. J. Atmos. Sci., 38, 717-731.
- Phillips, N.A., 1954: Energy transformations and meridional circulations associated with simple baroclinic waves in a two-level, quasi-geostrophic model. Tellus, 6, 273-286.
- Plumb, R.A., 1979: Forced waves in a baroclinic shear flow. Part 1: Undamped evolution near the baroclinic instability threshold. J. Atmos. Sci., 36, 205-216.
- Plumb, R.A., 1981: Forced waves in a baroclinic shear flow. Part 2: Damped and undamped response to weak near-resonant forcing. J. Atmos. Sci., 38, 1856-1869.
- Ruelle, D. and F. Takens, 1971: On the nature of turbulence. Commun. Math. Phys., 20, 167-192.
- Shirer, H.N. and R. Wells, 1982: Improving spectral models by unfolding their singularities. J. Atmos. Sci., 39, 610-621.
- Vickroy, J.G. and J.A. Dutton, 1979: Bifurcation and catastrophe in a simple forced, dissipative quasi-geostrophic flow. J. Atmos. Sci., 36, 42-52.

22

CHAPTER 3

N86-11751

The Hadley and Rossby Regimes
in a Spherical Atmosphere

Steven B. Feldstein

and

John H. E. Clark
Department of Meteorology
The Pennsylvania State University
University Park, PA 16802

1. Introduction

During the past thirty years several laboratory experiments on thermally-forced rotating liquids have been performed. They used a rotating annulus, Hide (1953, 1958) or rotating dishpan, Fultz (1953, 1959), with an imposed radial temperature gradient. Even though the sphericity of the earth could not be accounted for, many properties similar to those of the real atmosphere were observed. These experiments produced a symmetric single-celled meridional circulation pattern both for small and large radial temperature gradients, known as the lower and upper symmetric Hadley regimes, respectively. For intermediate temperature gradients, a wave-like asymmetric circulation appeared in both experiments, and, especially for the rotating annulus, a simple pattern with one or two waves was present. Furthermore, the wavenumber decreased as the radial temperature gradient increased. However, in the rotating dishpan, as distinct from the rotating annulus, a more complicated changing wave structure resembling the atmospheric circulation was observed.

Lorenz (1962) presented a detailed theoretical investigation of the rotating dishpan experiment. The liquid was thermally-forced with an externally imposed radial temperature gradient on the lower surface. He used a two layer model with a modified form of the quasi-geostrophic approximation. A highly truncated series expansion in terms of Fourier-Bessel functions for the dependent variables was used, and both the Hadley and Rossby regimes showed remarkable similarities to those observed experimentally, especially Hide's rotating annulus.

One serious limitation of the laboratory experiments is that they did not simulate the spherical geometry of the earth. This study will examine the question of the existence and the properties of the Hadley and Rossby regimes

for a spherical atmosphere. Lorenz's modified geostrophic model (1960) is used which is the same as the quasigeostrophic model but with the additional effects of a time varying static stability and thermal advection by the divergent wind. The model consists of two spherical layers around the earth and the flow is thermally driven by radiative heating. A Newtonian approximation expresses the heating as the difference between the actual temperature and a specified equilibrium temperature. The dependent variables are expanded in a truncated series of spherical harmonics that retains enough terms to allow a detailed analysis of the properties of the Hadley and Rossby regimes. The main topics of interest are the basic properties of the transitions between the Hadley and Rossby regimes, and the transitions between wavenumbers within the Rossby regime. We shall emphasize the distinct features introduced by the sphericity and shall contrast our findings with those of Lorenz (1960) for the rotating dishpan.

In Section 2 a detailed description of the model will be given. Following this, in Section 3, the properties of the steady Hadley regime and its stability both to axisymmetric and wave perturbations will be studied. In Section 4 the equations for the steady Rossby regime are first solved analytically when one wave is present. Then after showing that only one steady wave can exist, linear perturbation theory is used to determine the transition conditions between wavenumbers within the steady Rossby regime. Finally, the structure of the steady Hadley and Rossby regimes for various rotation rates is obtained.

2. Description of the Model

Since we are interested in the fundamental properties of the Hadley and Rossby regimes which are sensitive to thermal advection by the divergent wind and variations in the static stability, the modified geostrophic model of Lorenz (1960) is used.

Thermal forcing is parameterized with a Newtonian heating approximation. A simple linear turbulent friction representation will be employed where the drag at the interface separating the two layers is proportional to their velocity difference, and the drag due to the solid surface below is proportional to the velocity of the lower layer. A diagram of this model is shown in Fig. 1 where $p = 500$ mb. The stream function for the nondivergent wind has the value $\psi + \tau$ in the upper layer and $\psi - \tau$ in the lower layer. The potential temperature in the upper and lower layers is $\theta + \sigma$ and $\theta - \sigma$, respectively. The fifth independent variable is the velocity potential which has a value $-\chi$ in the upper layer and χ in the lower layer to satisfy the conditions that $\omega = 0$ at the pressure levels 0 and $2p$.

The baroclinic and barotropic vorticity equations are

$$\frac{\partial}{\partial t} \nabla^2 \psi = J(\psi, \nabla^2 \psi) - J(\tau, \nabla^2 \tau) - k_2 \nabla^2 \psi + k_2 \nabla^2 \tau - \beta \frac{\partial \psi}{\partial x} \quad (1)$$

$$\begin{aligned} \frac{\partial}{\partial t} \nabla^2 \tau = & -J(\psi, \nabla^2 \tau) - J(\tau, \nabla^2 \psi) + \nabla \cdot f \nabla \chi - (k_2 + 2k_1) \nabla^2 \tau \\ & + k_2 \nabla^2 \psi - \beta \frac{\partial \tau}{\partial x} \end{aligned} \quad (2)$$

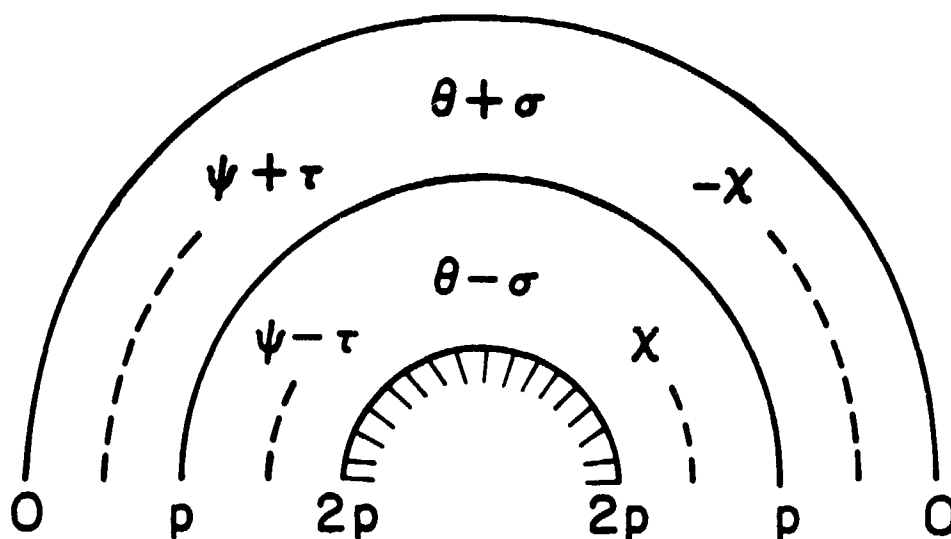


Figure 1 Arrangement of layers and discrete data surfaces for the model. Refer to text for the explanation of the symbols.

where $\beta = \frac{df}{dy}$ and k_1 and $2k_2$ are the coefficients of friction between the upper and lower layer and between the lower layer and the underlying surface, respectively. The Jacobian operator J has the property that

$$J(f, g) = \frac{\partial f}{\partial x} \frac{\partial g}{\partial y} - \frac{\partial f}{\partial y} \frac{\partial g}{\partial x}.$$

The two thermodynamic energy equations are

$$\frac{\partial \theta}{\partial t} = -J(\psi, \theta) - J(\tau, \sigma) + \sigma \nabla^2 \lambda - g_1 (\theta - \theta^*) \quad (3)$$

$$\frac{\partial \sigma}{\partial t} = -J(\psi, \sigma) - J(\tau, \theta) + \nabla \lambda \cdot \nabla \theta - g_1 (\sigma - \sigma^*) \quad (4)$$

where θ^* and σ^* represent equilibrium temperature fields and g_1 is the Newtonian heating coefficient.

The system of equations is completed with the linear balance equation

$$f \nabla^2 \tau + \beta \frac{\partial \tau}{\partial y} = g_3 \nabla^2 \theta \quad (5)$$

where

$$g_3 = \frac{C_p (1/2)^\kappa}{2} [(3/2)^\kappa - (1/2)^\kappa]$$

and

$$\kappa = \frac{R}{C_p}$$

The five independent variables are all expanded in a truncated series of spherical harmonics. The model is chosen to be weakly nonlinear in the sense that all wave-wave interactions will be neglected but wave-mean flow interactions are accounted for.

The spectral expansions are

$$\frac{\psi}{a} = \psi_1^0 P_1^0 + \psi_3^0 P_3^0 + \psi_{n+1}^n P_{n+1}^n e^{in\lambda} + \psi_{n+1}^{-n} P_{n+1}^{-n} e^{-in\lambda},$$

$$\frac{\tau}{a} = \tau_1^0 P_1^0 + \tau_3^0 P_3^0 + \tau_{n+1}^n P_{n+1}^n e^{in\lambda} + \tau_{n+1}^{-n} P_{n+1}^{-n} e^{-in\lambda},$$

$$\frac{\lambda}{a} = \chi_2^0 P_2^0 + \chi_n^n P_n^n e^{in\lambda} + \chi_n^{-n} P_n^{-n} e^{-in\lambda}, \quad (6)$$

$$\theta = \theta_0^0 P_0^0 + \theta_2^0 P_2^0 + \theta_n^n P_n^n e^{in\lambda} + \theta_n^{-n} P_n^{-n} e^{-in\lambda},$$

$$\sigma = \sigma_0^0 P_0^0,$$

and

$$\sigma^* = \sigma_0^{0*} P_0^0,$$

where a is the earth's radius.

Properties of Legendre polynomials are reviewed in the Appendix.

The complex spectral coefficients must satisfy the relation

$$\psi_{n+1}^{n*} = (-1)^n \psi_{n+1}^{-n}, \quad \theta_n^{n*} = (-1)^n \theta_n^{-n},$$

which is necessary for ψ and θ to be real variables.

The stream function is chosen to be antisymmetric across the equator to yield a symmetric nondivergent velocity field. The potential temperature and divergent velocity component are chosen to be symmetric across the equator.

The meridional structure for the wave is chosen to be the mode with the largest growth rate, i.e., the gravest mode.

If the above expansions are used, then (1) to (5) become:

$$-C_1 \frac{d\psi_1^0}{dt} = k_2 C_1 \psi_1^0 - k_2 C_1 \tau_1^0 \quad (7)$$

$$-C_3 \frac{d\psi_3^0}{dt} = k_2 C_3 \psi_3^0 - k_2 C_3 \tau_3^0 \quad (8)$$

$$\begin{aligned} -C_{n+1} \frac{d\psi_{n+1}^n}{dt} = & i(C_{n+1} - C_1) \psi_{n+1}^n \psi_1^0 L_{n+1,n+1,1}^{n,n,0} \\ & + i(C_{n+1} - C_3) \psi_{n+1}^n \psi_3^0 L_{n+1,n+1,3}^{n,n,0} \\ & + i(C_{n+1} - C_1) \tau_{n+1}^n \tau_1^0 L_{n+1,n+1,1}^{n,n,0} \\ & + i(C_{n+1} - C_3) \tau_{n+1}^n \tau_3^0 L_{n+1,n+1,3}^{n,n,0} \\ & + k_2 C_{n+1} \psi_{n+1}^n - k_2 C_{n+1} \tau_{n+1}^n - 12\Omega n \psi_{n+1}^n \end{aligned} \quad (9)$$

$$- C_1 \frac{d\tau_1^0}{dt} = -6\Omega \epsilon_2^0 \chi_2^0 + (k_2 + 2k_1) C_1 \tau_1^0 - k_2 C_1 \psi_1^0 \quad (10)$$

$$- C_3 \frac{d\tau_3^0}{dt} = -16\Omega \epsilon_3^0 \chi_2^0 + (k_2 + 2k_1) C_3 \tau_3^0 - k_2 C_3 \psi_3^0 \quad (11)$$

$$\begin{aligned} - C_{n+1} \frac{d\tau_{n+1}^n}{dt} = & 1(C_{n+1} - C_1) \psi_{n+1}^n \tau_1^0 L_{n+1, n+1, 1}^{n, n, 0} \\ & + 1(C_{n+1} - C_3) \psi_{n+1}^n \tau_3^0 L_{n+1, n+1, 3}^{n, n, 0} \\ & + 1(C_{n+1} - C_1) \tau_{n+1}^n \psi_1^0 L_{n+1, n+1, 1}^{0, n, n, 0} \\ & + 1(C_{n+1} - C_3) \tau_{n+1}^n \psi_3^0 L_{n+1, n+1, 3}^{0, n, n, 0} \\ & - 2\Omega n(n+1) \epsilon_{n+1}^n \chi_n^n + (k_2 + 2k_1) C_{n+1} \tau_{n+1}^n \\ & - 2\Omega n \epsilon_{n+1}^n \chi_n^n - k_2 C_{n+1} \psi_{n+1}^n \\ & - 12\Omega n \tau_{n+1}^n \end{aligned} \quad (12)$$

$$\frac{d\theta_0^0}{dt} = -g_1(\theta_0^0 - \theta_0^{0*}) \quad (13)$$

$$\begin{aligned} \frac{d\theta_2^0}{dt} = & 1 \psi_{n+1}^n \theta_n^n L_{n+1, 2, n}^{n, 0, -n} + 1 \psi_{n+1}^n \theta_n^n L_{n+1, 2, n}^{-n, 0, n} \\ & - \frac{\sigma_0^0}{\sqrt{2}} C_2 \chi_2^0 - g_1(\theta_2^0 - \theta_2^{0*}) \end{aligned} \quad (14)$$

$$\begin{aligned} \frac{d\theta_n^n}{dt} = & i \psi_1^0 \theta_n^n L_{1,n,n}^{0,n,n} + i \psi_3^0 \theta_n^n L_{3,n,n}^{0,n,n} \\ & - i \psi_{n+1}^n \theta_{n+1,n,2}^0 L_{n+1,n,2}^{n,n,0} - \frac{\sigma_0^0}{\sqrt{2}} C_n \chi_n^n \end{aligned} \quad (15)$$

$$\begin{aligned} \frac{d\sigma_0^0}{dt} = & - \chi_n^n \theta_n^n I_{n,0,n}^{n,0,n} / C_n - \chi_n^n \theta_n^n I_{n,C,n}^{n,0,n} / C_n \\ & - \chi_2^0 \theta_2^0 I_{2,0,2}^{0,0,0} / C_2 - g_1 (\sigma_0^0 - \sigma_0^{0*}) \end{aligned} \quad (16)$$

$$3\Omega \epsilon_2^0 \tau_1^0 + 8\Omega \epsilon_3^0 \tau_3^0 = \frac{3g_3}{a} \theta_2^0 \quad (17)$$

$$2\Omega n(n+2) \tau_{n+1}^n = \frac{g_3 C_n}{a^2} \theta_n^n \quad (18)$$

where

$$\epsilon_n^n = \frac{(n^2 - \frac{1}{2})}{(4n^2 - 1)}$$

$$C_n = n(n+1)$$

and Ω is the earth's angular velocity. The factors $L_{\alpha\gamma\beta}$ and $I_{\alpha\gamma\beta}$ are interaction coefficients and their properties are reviewed in the Appendix. Since for each given zonal wavenumber there is only one meridional mode, the ridge and trough axes will be parallel to meridians of longitude thus preventing meridional transport of momentum and suppressing barotropic wave mean flow interactions. Similarly, the trough and ridge axes of the temperature wave

are oriented north-south. There is, however, no restriction on the phase difference between the stream function and the isotherms; thus, baroclinic conversions of available potential energy to kinetic energy can occur.

Merilees (1968) showed that a truncated spectral model will conserve the sum of kinetic energy and available potential energy as the original partial differential equations do in the absence of external energy sources and sinks. Furthermore, Lorenz (1960) proved that the sum of kinetic and available potential energy, in the absence of forcing and dissipation, will be constant for the system of equations chosen for this model with the following definitions for kinetic energy, K , and available potential energy, A :

$$K = \frac{p_0}{2g} \int_{-\pi/2}^{\pi/2} \int_0^{2\pi} (\nabla\psi \cdot \nabla\psi + \nabla\tau \cdot \nabla\tau) a^2 \cos\phi d\lambda d\phi \quad (19)$$

and

$$A = \frac{g_3 p_0}{g} \int_{-\pi/2}^{\pi/2} \int_0^{2\pi} [(\sigma^2 + \theta'^2)^{1/2} - \sigma] a^2 \cos\phi d\lambda d\phi \quad (20)$$

where

$$\theta' = \theta - [\theta]$$

and $[]$ denotes a horizontal average over an isobaric surface.

3. Steady Hadley Regime

a. Properties of the steady Hadley regime

A straightforward solution of these equations is that for a time independent axisymmetric flow. Due to the severe truncation in the axisymmetric terms, only a single-celled Hadley circulation is possible.

The solution is obtained by setting all the spectral coefficients associated with wave disturbances and all the terms involving time derivatives equal to zero in (7) to (18). The resulting 8 nonlinear equations can be reduced to one equation in θ_2^0 ,

$$(\theta_2^0)^3 + \frac{g_1 + 3\sqrt{2} E \sigma_0^{0*}}{3 \sqrt{2} E F} \theta_2^0 - \frac{g_1 \theta_2^{0*}}{3\sqrt{2} E F} = 0 \quad (21)$$

where

$$E = \frac{1/2 k_1^2 g_3}{Da^2}, \quad D = k_1 \Omega^2 [108(\epsilon_2^0)^2 + 128(\epsilon_3^0)^2],$$

and

$$F = \frac{g_1 3\sqrt{2} E}{g_1^2 - g_2^2}.$$

Note that θ_2^{0*} must be negative if the equilibrium temperature is higher in the tropics than in the polar regions.

Once θ_2^0 is known, the other seven variables defining the steady Hadley regime can be found. The equations for σ_0^0 , θ_0^0 , and χ_2^0 are

$$\sigma_0^0 = \sigma_0^{0*} + \frac{3\sqrt{2} E}{g_1} (\theta_2^0)^2 \quad (22)$$

$$\theta_0^0 = \theta_0^{0*} \quad (23)$$

and

$$\lambda_2^0 = \frac{72 k_1^2 \epsilon_3}{Da^2} \quad (24)$$

Any real root of (21) must satisfy $\theta_2^0 < 0$ implying that the temperature decreases poleward. Equation (21) also requires that $\theta_2^{0*} < \theta_2^0 < 0$ implying that the meridional temperature gradient is less than the equilibrium meridional temperature gradient. This is physically reasonable since the external forcing continuously strives to increase the observed temperature gradient against the effect of a poleward heat transport which reduces the atmosphere's meridional temperature gradient. Also, (22) indicates that $\sigma_0^0 > \sigma_0^{0*} > 0$ implying that the Hadley cell circulation is always statically stable since σ_0^{0*} is always positive.

The structure of the meridional circulation can be seen in the sign of λ_2^0 . From (24), λ_2^0 must be negative and since the divergent wind is proportional to $\frac{\partial \chi}{\partial y}$ and the vertical velocity is proportional to $\frac{\partial^2 \chi}{\partial y^2}$ a direct meridional circulation is implied.

The stream functions have the form

$$\psi_1^0 = \tau_1^0 = \frac{108 \Omega \epsilon_2^0 k_1 g_3 \theta_2^0}{Da^2} \quad (25)$$

$$\psi_3^0 = \tau_3^0 = \frac{48 \Omega \epsilon_3^0 k_1 g_3 \theta_2^0}{Da^2} \quad (26)$$

and therefore the zonal velocity in the lower layer must vanish.

Figs. 2,3, and 4 illustrate the potential temperature and wind field structure of the steady Hadley circulation for typical atmospheric conditions. The time constants for both Newtonian heating and dissipation were chosen to be 10 days. Typical values of θ_0^{0*} , σ_0^{0*} and θ_2^{0*} for the observed winter circulation of the northern hemisphere are

$$\theta_0^{0*} = 435.6, \sigma_0^{0*} = 22.6, \text{ and } \theta_2^{0*} = -25.0.$$

A direct circulation is evident with warm tropical air rising and cold polar air sinking. The meridional divergent wind is poleward in the upper layer and equatorward in the lower layer. The zonal velocity in the upper layer is zero at the equator and pole and reaches a maximum at 55°N. The variables v_2 and ω_2 are not shown but they can be readily obtained noting that $v_2 = -v_1$ and $\omega_2 = \omega_1$.

b. Stability of the Steady Hadley Regime

We shall now examine the stability of our analytical Hadley solution. The system of 8 equations, i.e., (7), (8), (10), (11), (13), (14), (16), and (17), representing the axisymmetric part of the flow can be reduced to a system of 7 prognostic equations by eliminating χ_2^0 using (17). When the steady Hadley solution is used as a basic state, these 7 equations determine the stability of the Hadley circulation to axisymmetric disturbances. Over a wide range of values for θ_2^{0*} , six stable eigenvalues are obtained. There is always one neutral or zero eigenvalue indicating that there is an unknown parameter and associated process which has been incorrectly omitted from the model. We plan to deal with this problem in a future study.

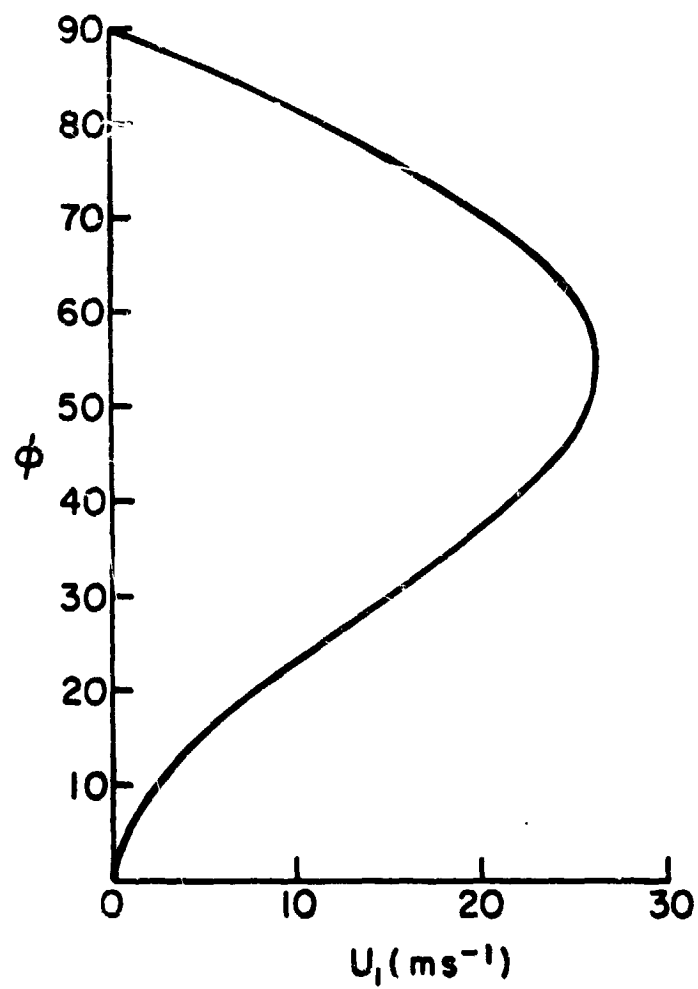


Figure 2 Upper layer zonal velocity profile for the steady Hadley regime for $\theta_2^{0*} = -25 \text{ ms}^{-1}$.

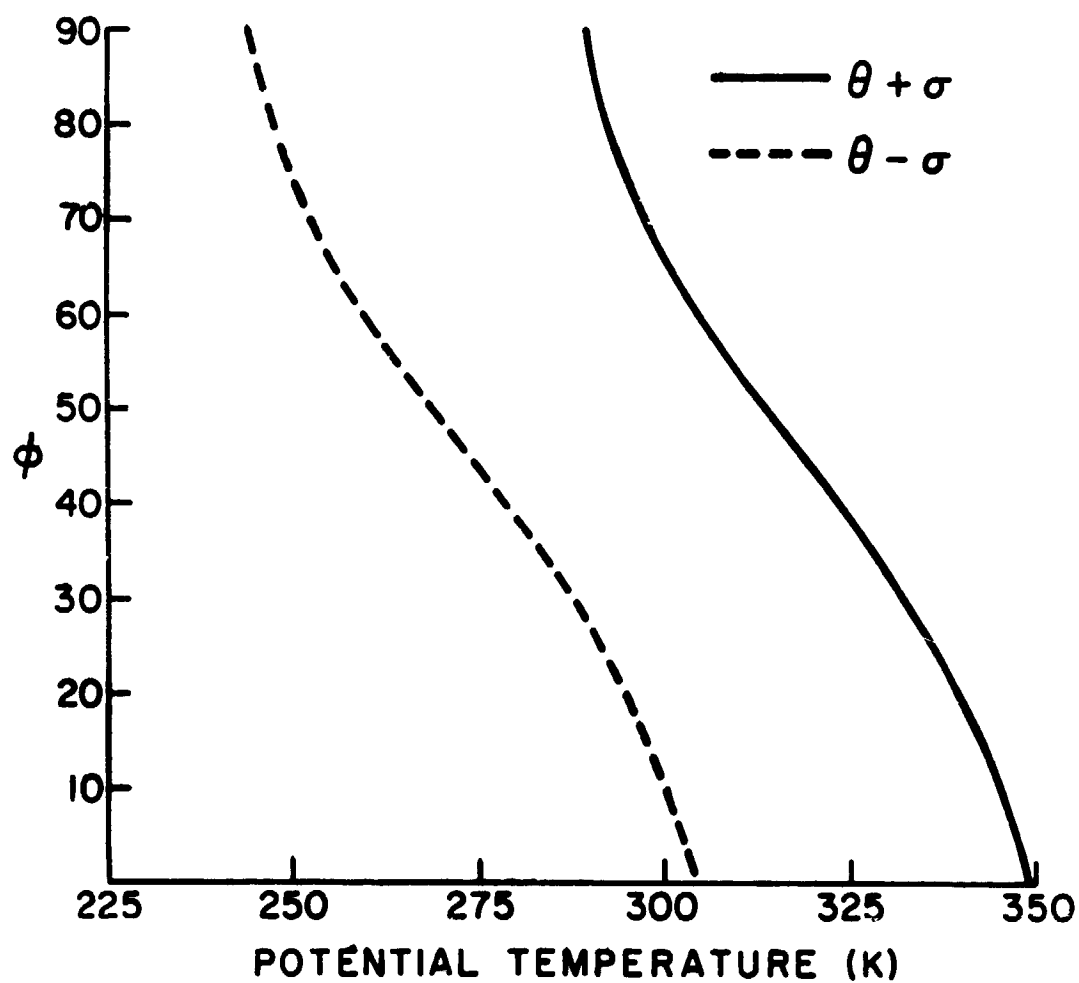


Figure 3 Potential temperature profile for the steady Hadley regime for $\theta_2^{0*} = -25 \text{ ms}^{-1}$.

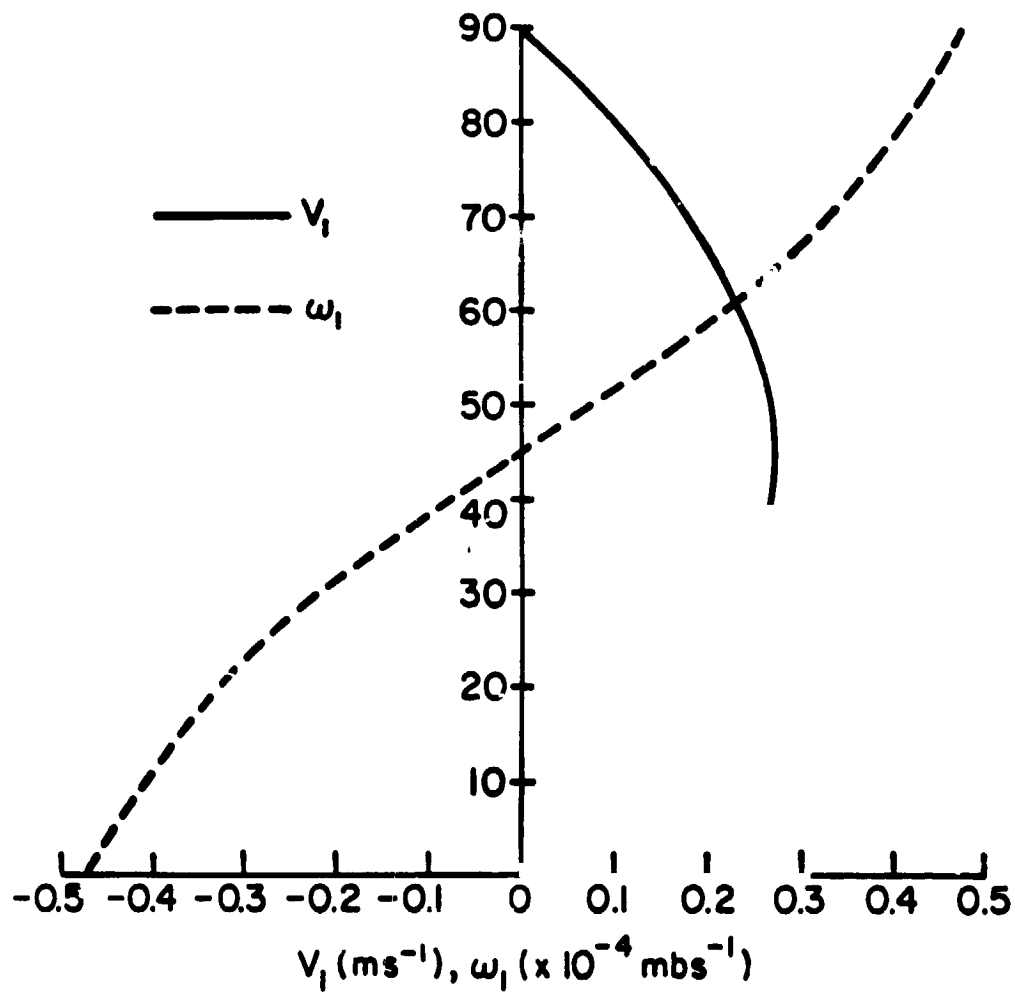


Figure 4 Meridional and vertical velocity profile for the steady Hadley regime for $\theta_2^{0*} = -25 \text{ ms}^{-1}$.

The stability analysis of the steady Hadley regime is completed by considering both the axisymmetric perturbations discussed above and wave-like perturbations. The stability matrix can be partitioned into separate axisymmetric and wave submatrices. Therefore, the stability of the steady Hadley regime to wave perturbations can be determined independently from that of the axisymmetric perturbations.

The wave stability analysis can be reduced to the following equation

$$\begin{vmatrix} \dot{\psi}_{n+1}^n \\ \dot{\theta}_n^n \end{vmatrix} = \begin{vmatrix} B_{1,n} & B_{2,n} \\ B_{3,n} & B_{4,n} \end{vmatrix} \begin{vmatrix} \psi_{n+1}^n \\ \theta_n^n \end{vmatrix}, \quad (27)$$

where

$$B_{1,n} = [i(C_{n+1} - C_1) \psi_1^0 L_{n+1,n+1,1}^{n,n,0} + i(C_{n+1} - C_3) \psi_3^0 L_{n+1,n+1,3}^{n,n,0} + k_2 C_{n+1} - i2\Omega n] \left(\frac{-1}{C_{n+1}} \right), \quad (28)$$

$$B_{2,n} = [i(C_{n+1} - C_1) \tau_1^0 L_{n+1,n+1,1}^{n,n,C} + i(C_{n+1} - C_3) \tau_3^0 L_{n+1,n+1,3}^{n,n,0} - k_2 C_{n+1}] \left(\frac{-\beta_n}{C_{n+1}} \right), \quad (29)$$

$$B_{3,n} = \left\{ \frac{\sigma_0^0 C_n}{\sqrt{2} \gamma_n} [i(C_{n+1} - C_1) \psi_1^0 L_{n+1,n+1,1}^{n,n,0} + i(C_{n+1} - C_3) \tau_3^0 L_{n+1,n+1,3}^{n,n,0} - k_2 C_{n+1}] + i\sigma_2^0 L_{n+1,n,2}^{n,n,Q} \right\} \left(1 - \frac{\sigma_0^0 C_n C_{n+1} \beta_n}{\sqrt{2} \gamma_n} \right)^{-1}, \quad (30)$$

$$\begin{aligned}
B_{4,n} = & \left\{ \frac{\sigma_0^0 C_n \beta_n}{\sqrt{2} \gamma_n} [1(C_{n+1} - C_1) \psi_1^0 L_{n+1,n+1,1}^{n,n,0} \right. \\
& + 1(C_{n+1} - C_3) \psi_3^0 L_{n+1,n+1,3}^{n,n,0} \\
& + (k_2 + 2k_1) C_{n+1} - 12\Omega n] + i\psi_1^0 L_{1,n,n}^{0,n,n} \\
& \left. + i\psi_3^0 L_{3,n,n}^{0,n,n} \right\} \left(1 - \frac{\sigma_0^0 C_n C_{n+1} \beta_n}{\sqrt{2} \gamma_n} \right)^{-1},
\end{aligned} \tag{31}$$

where

$$\beta_n = \frac{g_3 C_n}{a^2} \frac{1}{2\Omega n (n+2) \epsilon_{n+1}^n},$$

and

$$\gamma_n = -2\Omega n (n+2) \epsilon_{n+1}^n.$$

Solutions of the form

$$\psi_{n+1}^n = \psi_{n+1,0}^n e^{\mu t} \quad \text{and} \quad \theta_n^n = \theta_{n,0}^n e^{\mu t}$$

can be found, where $\mu = \mu_r + i\mu_i$, if

$$\mu^2 - (B_{1,n} + B_{\psi,n}) \mu + (B_{1,n} B_{4,n} - B_{2,n} B_{3,n}) = 0 \tag{32}$$

The findings of the Hadley regime stability analysis appear in Figs. 5 and 6. For a disturbance of given east-west wavenumber,

- i. instability obtained for a range of equilibrium temperature gradients, θ_2^{0*} , bounded above and below, i.e., the Hadley regime is stable for small and large θ_2^{0*} , see Fig. 5,
- ii. maximum e-folding times on the order of a day are achieved for an intermediate θ_2^{0*} , and
- iii. the growing disturbance tends to propagate westward for the small θ_2^{0*} , (or small equilibrium vertical shear) and eastward for large θ_2^{0*} , see Fig. 6.

For comparison, the stability analysis of the traditional Phillip's two-layer, quasi-geostrophic β -plane model appears in Fig. 7. The stabilization accompanying large θ_2^{0*} or vertical shear is clearly related to the high static stability produced in the Hadley circulation. Northward advection of warm air in the upper layer and southward advection of cold air in the lower layer by the divergent component of the flow will eventually suppress the baroclinic instability associated with the vertical shear.

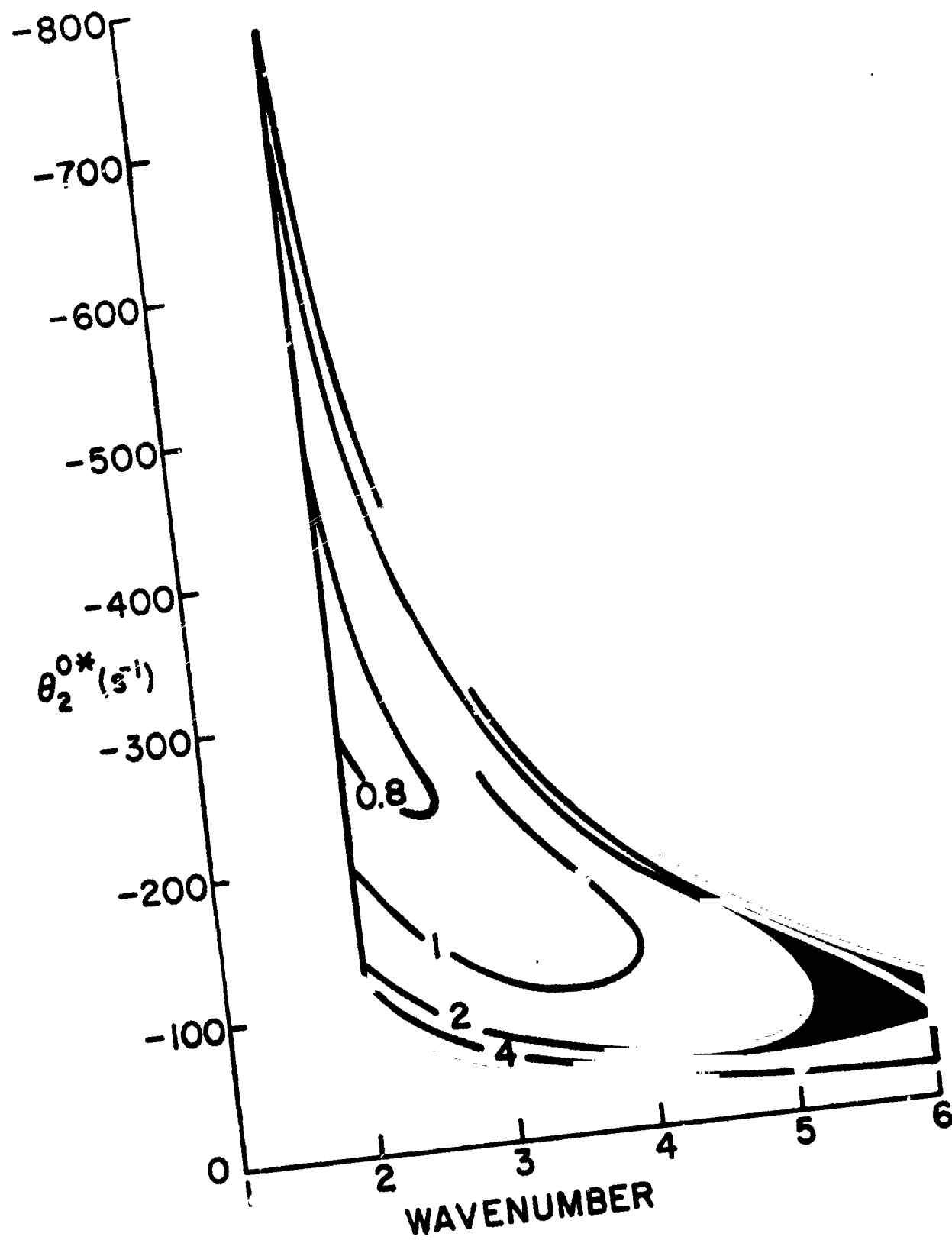


Figure 5 The e-folding times (days) for the unstable steady Hadley regime.

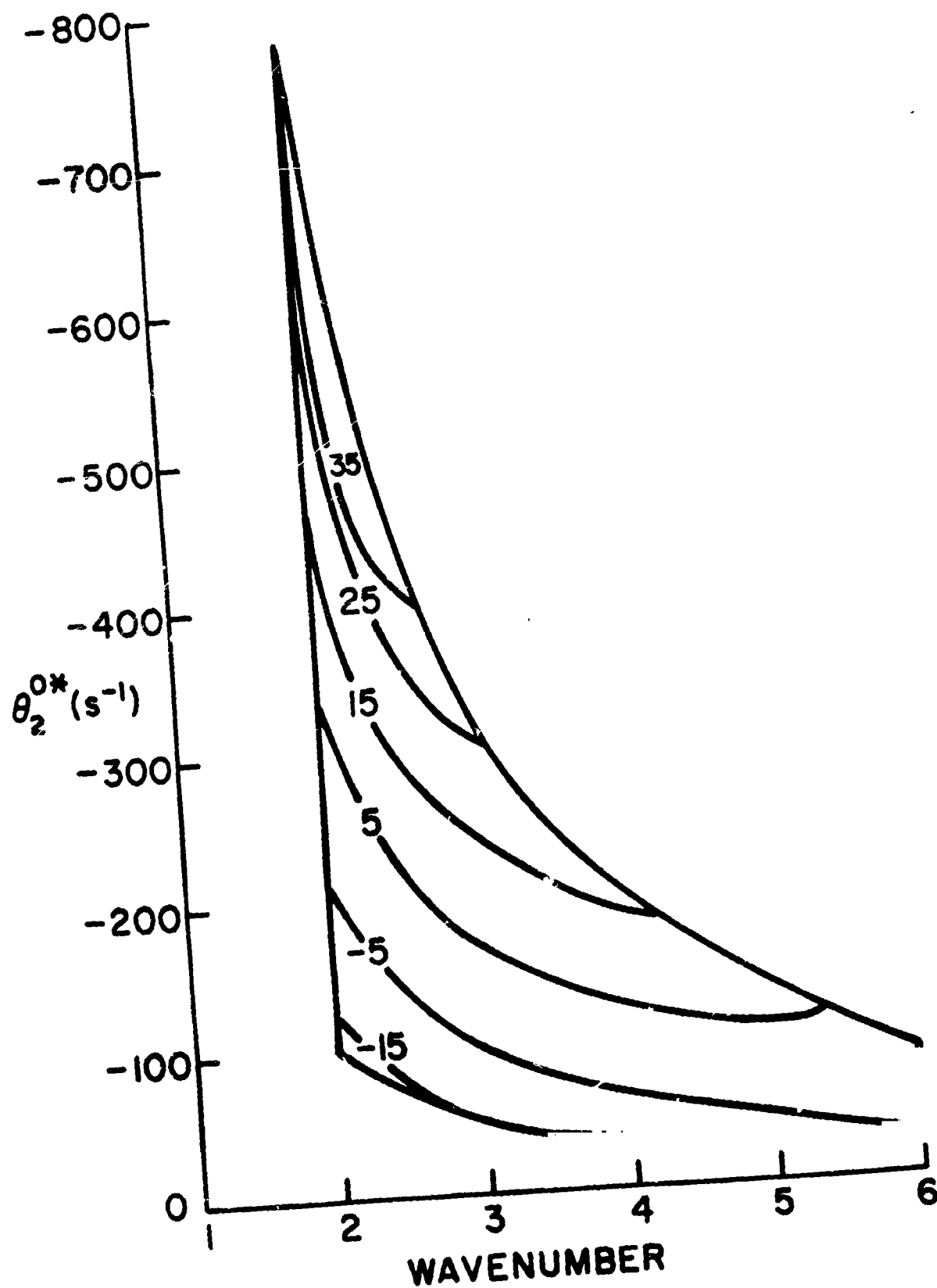


Figure 6 Phase velocities (ms^{-1}) for the unstable steady Hadley regime.

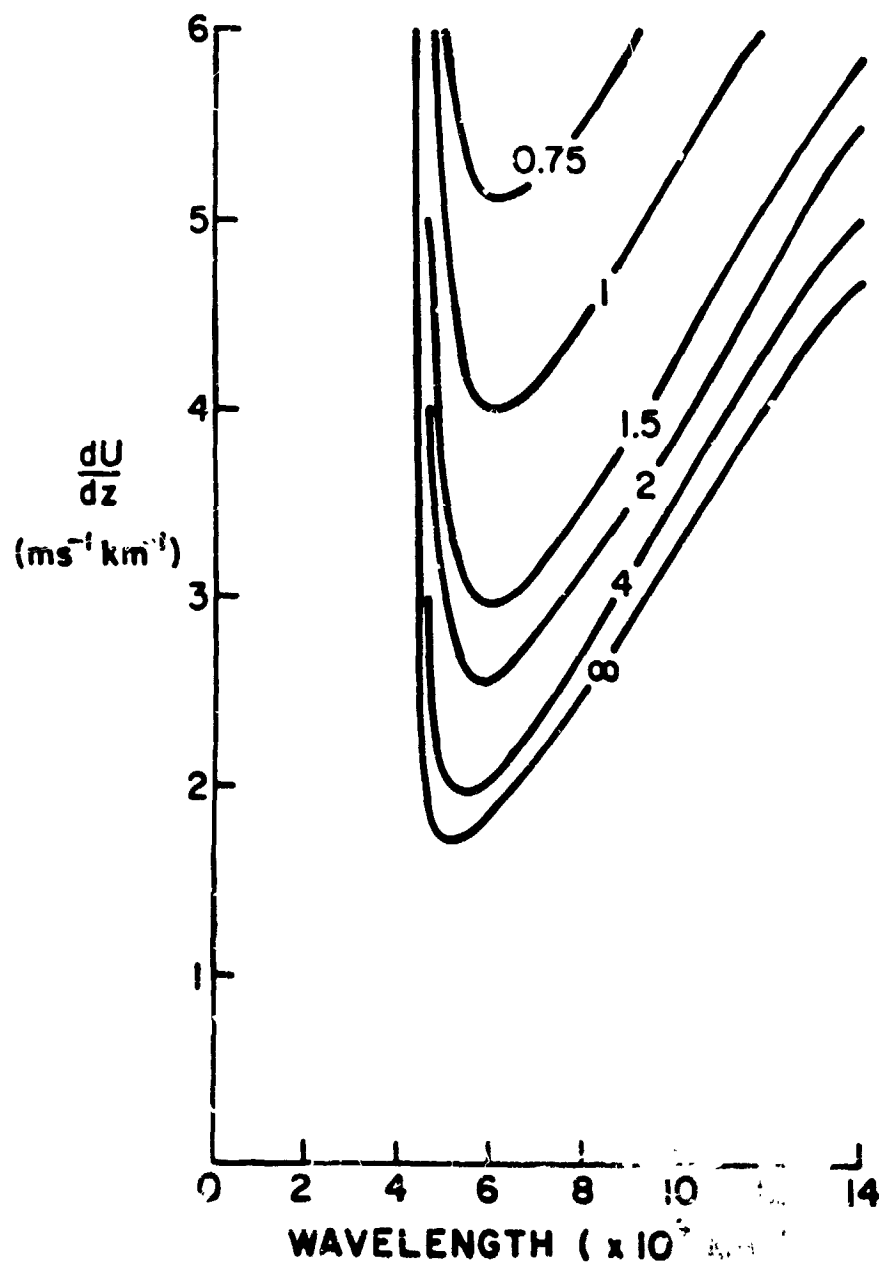


Figure 7 The time in days required for an unstable wave in the two-level model to double its amplitude, given as a function of the vertical wind shear in the basic current and the wavelength. After Phillips (1954).

4. Steady Rossby Regime

a. Properties of the Steady Rossby Regime

In the previous section the Hadley circulation and its stability were studied. A wave-like disturbance can grow and at the same time alter the axisymmetric part of the flow. It is expected that eventually a new type of steady regime will be attained characterized by uniformly propagating waves of constant amplitude and a time independent axisymmetric flow.

We will first look at the steady Rossby circulation with just one wave present. Consideration of more than one wave coexisting at the same time will be postponed until later.

The steady Rossby circulation is determined by setting the time derivatives of the axisymmetric terms in (6) to (17) equal to zero. The axisymmetric coefficients ψ_1^0 , ψ_3^0 , τ_1^0 , τ_3^0 , τ_2^0 , and θ_0^0 , are each specified by the same equations as for the steady Hadley regime.

Next a procedure will be developed to express the wave part of the flow, i.e., ψ_{n+1}^n , τ_{n+1}^n , θ_n^n , and λ_n^n , in terms of θ_2^0 and σ_0^0 . We will later derive two nonlinear equations in the two unknowns in θ_2^0 and σ_0^0 , whose solution will completely specify the steady Rossby circulation. By the same technique used to study the stability of the Hadley circulation, (9), (12), (15), and (18) can be combined into the two equations:

$$\frac{d\psi_{n+1}^n}{dt} = B_{1,n}(\theta_2^0)\psi_{n+1}^n + B_{2,n}(\theta_2^0)\theta_n^n \quad (33)$$

and

$$\frac{d\theta_n^n}{dt} = B_{3,n}(\theta_2^0, \sigma_0^0)\psi_{n+1}^n + B_{4,n}(\theta_2^0, \sigma_0^0)\psi_n^n \quad (34)$$

Since these are linear, they have the general solution

$$\psi_{n+1}^n = \psi_{n+1,A}^n e^{\mu_1 t} + \psi_{n+1,B}^n e^{\mu_2 t} \quad (35)$$

and

$$\theta_n^n = \theta_{n,A}^n e^{\mu_1 t} + \theta_{n,B}^n e^{\mu_2 t} \quad (36)$$

where

$$\mu_1 = \frac{1}{2} (B_{1,n} + B_{4,n} + \sqrt{(B_{1,n} + B_{4,n})^2 - 4(B_{1,n}B_{4,n} - B_{2,n}B_{3,n})}) \quad (37)$$

$$\mu_2 = \frac{1}{2} (B_{1,n} + B_{4,n} - \sqrt{(B_{1,n} + B_{4,n})^2 - 4(B_{1,n}B_{4,n} - B_{2,n}B_{3,n})}) \quad (38)$$

and

$$\theta_{n,A}^n = \frac{\mu_2 - B_{1,n}}{B_{2,n}} \psi_{n+1,A}^n \quad (39)$$

$$\theta_{n,B}^n = \frac{\mu_1 - B_{1,n}}{B_{2,n}} \psi_{n+1,B}^n \quad (40)$$

The latter equations specify the phase relationships between the 500 mb stream function and temperature patterns.

It was shown earlier that $\text{Re}(\mu_2) < 0$ and, therefore, the wave solution corresponding to μ_2 will decay to zero for large time. Therefore, for large time, only the first expression on the right side of (35) and (36) need be retained. The requirement that the steady Rossby waves have constant amplitude implies that

$$\text{Re}(\mu_1) = 0 \quad . \quad (41)$$

With

$$q \equiv \frac{\mu_1 - B_{1,n}}{B_{2,n}} \quad , \quad (42)$$

Eq. (14) can be written

$$iq^* \psi_{n+1}^n \psi_{n+1}^{-n} L_{n+1,2,n}^{n,0,-n} + \psi_{n+1}^n \psi_{n+1}^{-n} L_{n+1,2,n}^{-n,0,n} - \frac{\sigma_0^0}{\sqrt{2}} c_2 x_2^0 - g_1 (\theta_2^0 - \theta_2^{0*}) = 0 \quad (43)$$

where q^* denotes the complex conjugate of q . Using the properties

$$L_{n+1,2,n}^{n,0,-n} = -L_{n+1,2,n}^{-n,0,n}$$

and

$$\psi_{n+1}^{-n} = (-1) \psi_{n+1}^{n*} \quad ,$$

it follows that

C-2

$$\left| \psi_{n+1}^n \right|^2 = \frac{(-1)^n}{2 L_{n+1,2,n}^{n,0,-n} \operatorname{Im}(q)} \left(\frac{\sigma_0^0}{\sqrt{2}} c_2 x_2^0 + g_1 (\theta_2^0 - \theta_2^{0*}) \right) \quad (44)$$

The wave amplitude is thus determined. Its phase, however, is arbitrary.

The characteristic equation for μ_1 is also (32) and is of the general form

$$Ax^2 + (B + E)x + (C + F) = 0 \quad (45)$$

where A,B,C,E,F are all real and A,B are positive. If we follow the same procedure as Lorenz (1962), we find that (45) has one root with a zero real part if

$$AF^2 - B(BC + EF) = 0 \quad (46)$$

Matching corresponding terms in (45) with (32) requires

$$\begin{aligned} & [\operatorname{Im}(B_{1,n} B_{4,n} - B_{2,n} B_{3,n})]^2 \\ & - \operatorname{Re}(B_{1,n} + B_{4,n}) [\operatorname{Re}(B_{1,n} + B_{4,n}) \operatorname{Re}(B_{1,n} B_{4,n} - B_{2,n} B_{3,n}) \\ & + \operatorname{Im}(B_{1,n} + B_{4,n}) \operatorname{Im}(B_{1,n} B_{4,n} - B_{2,n} B_{3,n})] = 0 \end{aligned} \quad (47)$$

Another equation involving θ_2^0 and σ_0^0 can be derived by solving for χ_n^n in (15) and substituting into (16). If the properties

$$\begin{aligned} \psi_{n+1}^{-n} &= (-1)^n \psi_{n+1}^{n*}, & \theta_n^{-n} &= (-1)^n \theta_n^{n*}, \\ \operatorname{Re}(\mu_1) &= 0, & I_{n,0,n}^{n,0,-n} &= I_{n,0,n}^{-n,0,n} \end{aligned}$$

are used, it can be shown that

$$\begin{aligned} & \frac{\sqrt{2}}{\sigma_0} \frac{I_{n,0,n}^{n,0,-n}}{C_n^2} \theta_2^0 |\psi_{n+1}^n|^2 (-1)^n \text{Im}(q) L_{n+1,n,2}^{n,n,0} \\ & + \chi_2^0 \theta_2^0 I_{2,0,2}^{0,0,0}/C_2 + \frac{(g_1^2 - g_2^2)}{\varepsilon_1} (\sigma_0^0 - \sigma_0^{0*}) = 0 \end{aligned} \quad (48)$$

Eqs. (47) and (48) were solved for θ_2^0 and σ_0^0 numerically, after which the wave part of the solution and the phase velocity were found.

Fig. 8 shows the phase velocity of the finite amplitude steady Rossby solution. Outside the region shown, $|\psi_{n+1}^n|^2 < 0$ implying that the calculated solutions of (47) and (48) are not solutions to the entire system. Since these equations are nonlinear, there exists the possibility of other solutions which are far away from the initial guess made in the numerical iterative technique. We could not find any such solutions and it is assumed that ours are the only acceptable ones. One significant point is that the boundary in Fig. 8 exactly matches the boundary for the stability of the steady Hadley regime demonstrating that whenever the Hadley regime is unstable to a perturbation of a given wavenumber, a steady Rossby circulation will exist at that wavenumber. If Figs. 6 and 8 are compared, we find similar values of phase velocity for large n , whereas there are two differences for smaller wavenumbers. First, both the maximum westward and eastward speeds are significantly larger in Fig. 8 and second, the stationary finite amplitude wave with zero phase speed occurs at a larger equilibrium temperature gradient than for the infinitesimal growing wave.

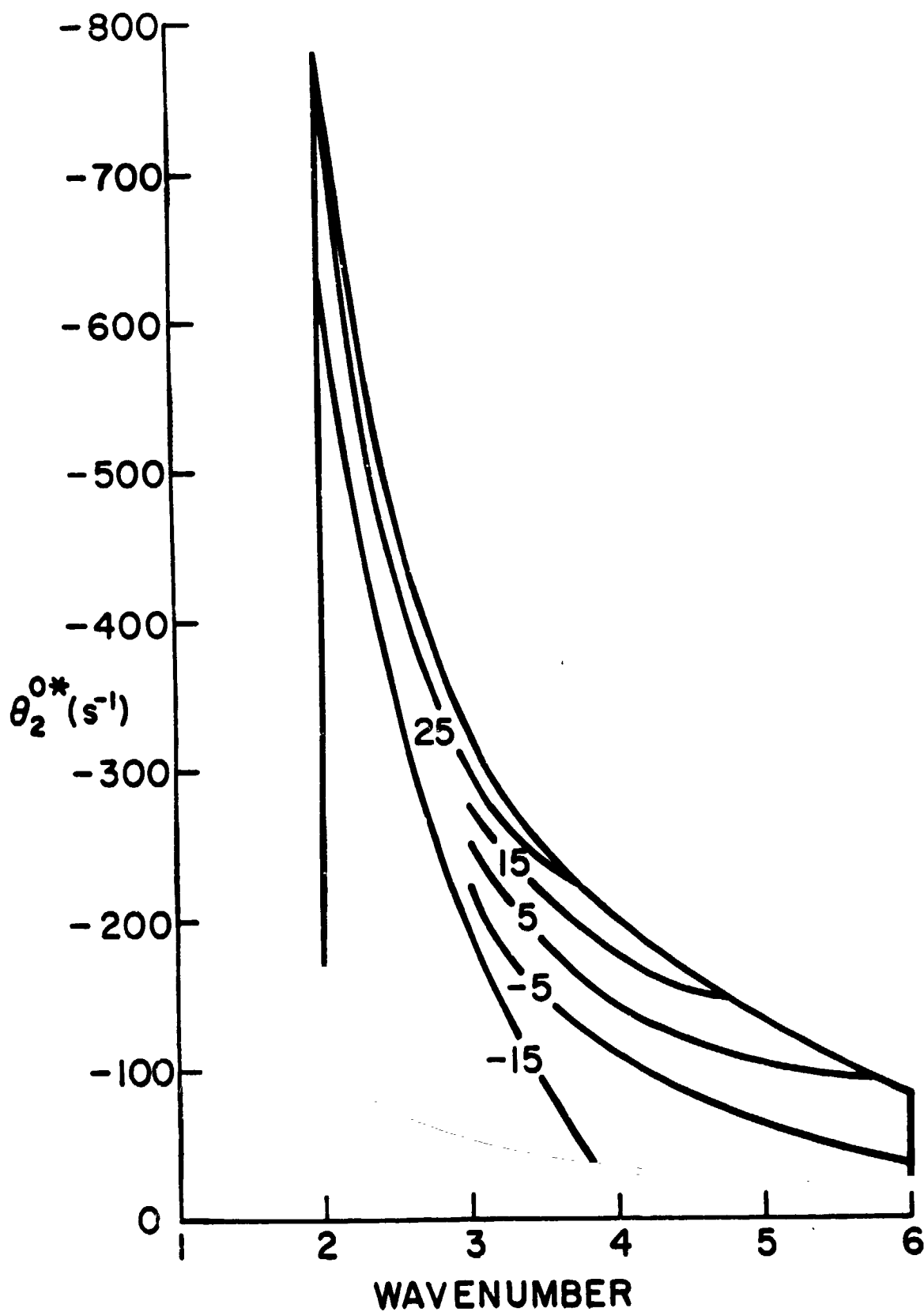


Figure 8 Phase velocities (ms^{-1}) for the steady Rossby regime.

Throughout this section only the situation with one wave present at a time was considered. If two waves with wavenumbers m and n coexist, both propagating with constant amplitude, (41) must apply for both wavenumbers separately. After calculating θ_2^0 and σ_0^0 , it was found that either $|\psi_{n+1}^n|^2$ is positive and $|\psi_{m+1}^m|^2$ negative or vice versa for all values of θ_2^{0*} when the steady Hadley circulation is unstable. Furthermore since (41) would have to apply for each wave, there would be more equations than unknowns and no solution for θ_2^0 and σ_0^0 could be obtained. Therefore, our steady Rossby circulation can exist only when one wave is present.

b. Stability of the Steady Rossby Regime

Consider now the stability of the steady Rossby circulation. The steady Rossby circulation for a given wavenumber will be initially perturbed with a wavelike disturbance of another wavenumber. As in the previous stability analysis of the steady Hadley regime, the perturbation equations can be separated into axisymmetric and wave parts. Since all waves are independent of each other, the same equations for the stability analysis of the steady Hadley circulation are retained except for the fact that the axisymmetric terms are for the steady Rossby circulation at a given wavenumber. The axisymmetric perturbation equations yielded six stable eigenvalues and one neutral eigenvalue as was found earlier. The wave perturbation equations are

$$\frac{d \psi_{m+1}^m}{dt} = B_{1,m}(\theta_2^0) \psi_{m+1}^m + B_{2,m}(\theta_2^0) \theta_m^0 \quad (49)$$

and

$$\frac{d \theta_m^m}{dt} = B_{3,m} (\theta_2^0, \sigma_0^0) \psi_{m+1}^m + B_{4,m} (\theta_2^0, \sigma_0^0) \theta_m^m \quad (50)$$

where m is the wavenumber of the perturbation and θ_2^0 and σ_0^0 are the values for a steady Rossby circulation of wavenumber n .

When the wavenumber of the perturbation is the same as that of the steady Rossby circulation, the stability analysis becomes much more complicated because the stability equations have time dependent coefficients. In this situation the stability was determined by integrating in time the complete system of spectral equations from a state far from equilibrium and seeing if it converged to the steady Rossby circulation. These integrations indicated that the steady Rossby circulation is stable to a perturbation of the same wavenumber if it is also stable to perturbations at all other wavenumbers.

These results are summarized in Fig. 9. The abscissa is θ_2^{0*} and the ordinate n . The solid line indicates where the wavenumber n steady Rossby circulation is stable to perturbations of all other wavenumbers and the dashed line where it is unstable to at least one other wavenumber. The steady Rossby circulation allows the presence of only one wave at a time, and as $|\theta_2^{0*}|$ increases the wavenumber observed decreases from six to two. Also, it can be seen that the transition from one wave to another occurs abruptly, and that for all transitions including that between the lower and upper symmetric Hadley regime there exists no hysteresis effect, i.e., the solution for the steady Rossby circulation does not depend on whether or not θ_2^{0*} was increasing or decreasing as the transition occurred.

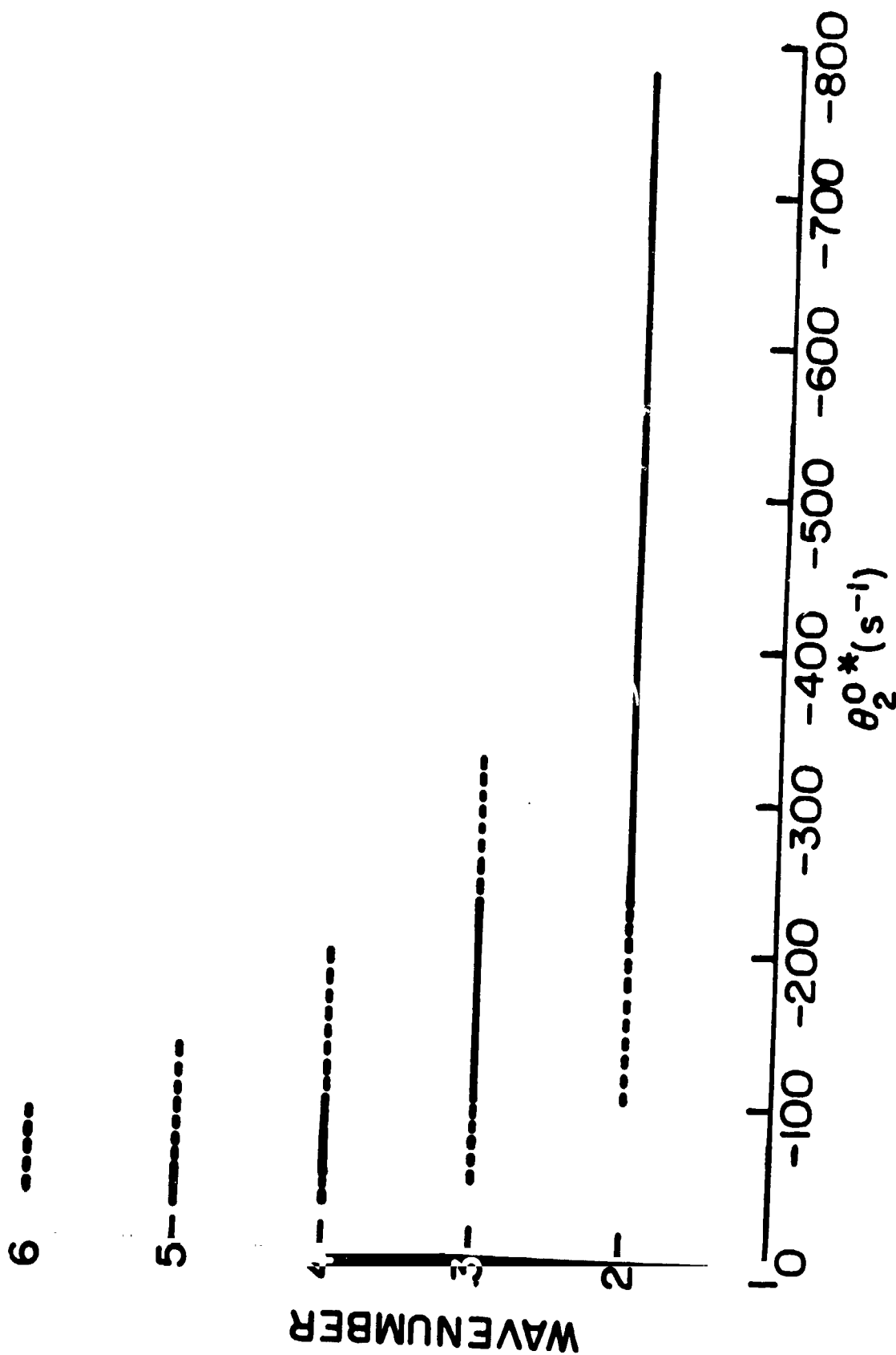


Figure 9 Steady Rossby regime. Solid lines indicate where a particular wavenumber is stable, dashed where it is unstable.

We also found an excellent correspondence between the wavenumber of the stable observed wave of the steady Rossby circulation and that of the most unstable wave of the steady Hadley circulation. This correspondence holds for all values of θ_2^{0*} except very near the transition boundary between wavenumbers 2 and 3, i.e., the wavenumber predicted for the steady Rossby regime is not the most unstable wave for the Hadley solution in this narrow region. However, in general the wave that is initially most unstable will also eventually be the wave that is observed in the steady Rossby regime.

The time scales for Newtonian heating and dissipation also play an important role in the Rossby circulation. It was found that for heating and dissipation time scales of 50 days or greater, a disturbance to the steady Rossby solution would evolve into a vacillating or periodic state. This circulation is doubly periodic characterized by an amplitude vacillation whose period is roughly 2.5 times that associated with the wave propagation. The energetics of this vacillation consisted of zonal available potential to eddy available potential to eddy kinetic energy conversions followed by the reverse cycle with the period of the amplitude vacillation.

So far, the rotation rate of the earth, Ω , has been kept constant; however, Ω is varied in many laboratory experiments. It would be interesting to vary the rotation rate and then compare results with those for the f-plane. Fig. 10 shows both the steady Hadley and Rossby regimes as a function of the rotation rate, Ω , and θ_2^{0*} . The boundary between the steady Hadley regime and the steady Rossby regime is shown by the dark curve. This boundary is quite similar in shape to that obtained by Lorenz (1962) for the rotating dishpan experiment indicating that sphericity plays a secondary role. For fixed values of θ_2^{0*} , the stable wavenumber observed in the steady Rossby regime increases with Ω . Also, as in Lorenz (1962), the steady Rossby regime

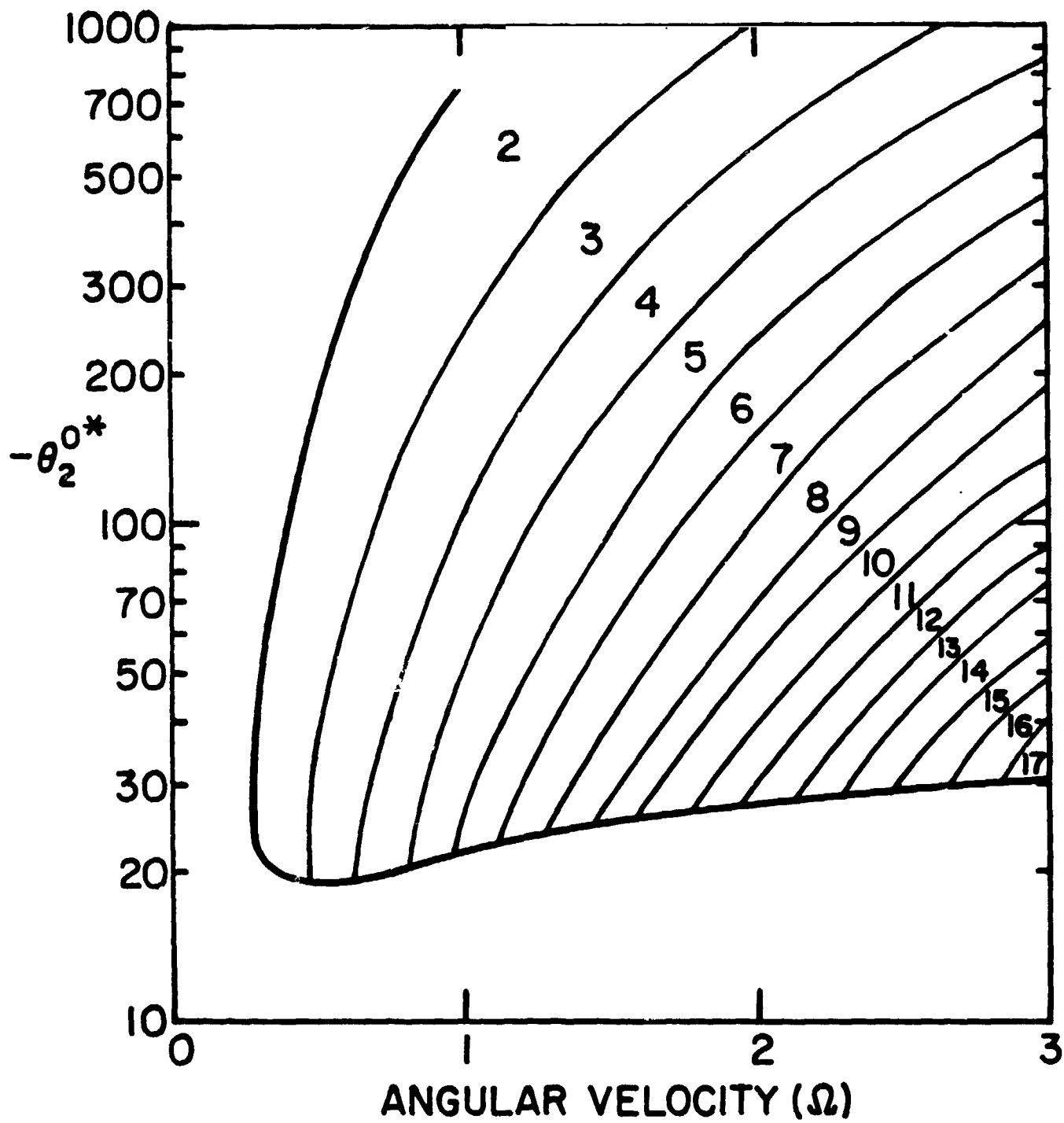


Figure 10 Stable wavenumbers for the steady Rossby regime.

does not exist for wavenumber one. This is most likely a result of our choice of eigenfunctions. All the transitions between wavenumbers still occur abruptly for all values of Ω tested.

5. Conclusions

We have found that for all imposed meridional temperature gradients a steady Hadley circulation exists in our two layer spherical model. The stability of this circulation to axisymmetric and wave perturbations was then examined. The axisymmetric perturbations always had one neutral eigenvalue but never grew. The Hadley regime for intermediate values of the meridional temperature gradient, was baroclinically unstable to wavelike disturbances, whereas for higher and lower meridional temperature gradients it remained stable. We thus have confirmed the existence of an upper and lower symmetric Hadley regime on the sphere.

The steady Rossby circulation for the sphere was shown to have two significant differences with that found by Lorenz (1962) for the rotating dishpan. Lorenz found a hysteresis effect between the steady Rossby regime and the upper symmetric Hadley regime. Our spherical model showed that the transition between the steady Rossby regime and the upper symmetric Hadley regime occurs at the same meridional temperature gradient irrespective of the direction of change. Also, Lorenz found that transitions between wavenumbers in the Rossby regime do not take place suddenly but rather there exists a region in between where two waves can exist together. In our model these transitions always occurred abruptly.

For very small values of heating and dissipation it was shown that the steady Rossby regime was unstable and evolved into a time varying circulation. This new flow was doubly periodic with a longer period amplitude vacillation and a shorter period associated with the propagation of the wave.

A comparison was made between the most unstable wavenumber of the steady Hadley regime and the wavenumber that is ultimately seen in the steady Rossby regime for the same value of the equilibrium meridional temperature gradient. The correspondence was very good and showed that almost always whichever wave had the largest initial growth rate would be the steady wave that is eventually observed.

Acknowledgements

This research was supported by NASA under contract NAS8-33794.

Appendix

Properties of the Associated Legendre Polynomials and Interaction Coefficients

The normalized associated Legendre polynomial can be defined as

$$P_n^m = \left[\frac{(2n+1)}{2} \frac{(n-m)!}{(n+m)!} \right]^{1/2} \frac{(1-\mu^2)^{m/2}}{2^n n!} \frac{d^{n+m}}{d\mu^{n+m}} (\mu^2-1)^n \quad (A-1)$$

where $\mu = \sin\phi$, and ϕ is the latitude. The spherical harmonic can then be defined as $Y_n^m = P_n^m e^{im\lambda}$ where m is the zonal wavenumber and $|n-m|$ is the number of zeros along a meridian of longitude. It will be simpler to follow the notation of Platzman (1962) by defining a complex wave vector $\gamma = n+im$. Some of its properties are

$$\nabla^2 Y_\gamma = -n(n+1)Y_\gamma \quad (A-2)$$

$$\text{and} \quad \int_0^{2\pi} \int_{-\pi/2}^{\pi/2} Y_\alpha^* Y_\beta \cos\phi d\phi d\lambda = 2\pi \delta_{\alpha\beta} \quad (A-3)$$

where $\delta_{\alpha\beta}$ is the Kronecker delta, and $*$ denotes complex conjugate.

The two interaction coefficients are

$$L_{\alpha\gamma\beta} = \int_{-\pi/2}^{\pi/2} P_\gamma [m_\beta P_\beta \frac{dP_\alpha}{d\phi} - m_\alpha P_\alpha \frac{dP_\beta}{d\phi}] d\phi \quad (A-4)$$

$$I_{\alpha\gamma\beta} = \int_{-\pi/2}^{\pi/2} P_Y \left[\frac{m_\alpha m_\beta P_\alpha P_\beta}{\cos^2 \phi} \frac{dP_\alpha}{d\phi} \frac{dP_\beta}{d\phi} \right] \cos \phi d\phi \quad (A-5)$$

The interaction coefficients follow several selection rules summarized in Merilees (1968). $L_{\alpha\gamma\beta} = 0$ if any of the following conditions are not satisfied.

$$m_\alpha + m_\beta = m_\gamma$$

$$|n_\alpha - n_\beta| < n_\gamma < n_\alpha + n_\beta$$

$$n_\alpha + n_\beta + n_\gamma = \text{odd}$$

$$m_\alpha^2 + m_\beta^2 \neq 0$$

$I_{\alpha\gamma\beta} = 0$ if any of the following conditions are not satisfied:

$$m_\alpha + m_\beta = m_\gamma$$

$$|n_\alpha - n_\beta| < n_\gamma < n_\alpha + n_\beta$$

$$n_\alpha + n_\beta + n_\gamma = \text{even}$$

$$n_\alpha + n_\beta \neq 0$$

REFERENCES

- Fultz, D., 1953: A survey of certain thermally and mechanically driven fluid systems of meteorological interest. Fluid models in geophysics. Proc. 1st Sympos. on the Use of Models in Geophys. Fluid Dynamics, Baltimore, 27-63.
- Fultz, D., R. R. Long, G. V. Owens, W. Rohan, R. Kaylor, and J. Weil, 1959: Studies of thermal convection in a rotating cylinder with some applications for large-scale atmospheric motions. Meteor. Monographs, Amer. Meteor. Soc., 104 pp.
- Hide, R., 1953: Some experiments on thermal convection in a rotating liquid. Quart. J. R. Met. Soc., 79, 161.
- Hide, R., 1958: An experimental study of thermal convection in a rotating liquid. Phil. Trans. Roy. Soc. London, (A), 250, 441-478.
- Lorenz, E. N., 1960: Energy and numerical weather prediction. Tellus, 12, 364-373.
- Lorenz, E. N., 1962: Simplified dynamic equations applied to the rotating basin experiments. J. Atmos. Sci., 19, 39-51.
- Merilees, P. E., 1968: The equations of motion in spectral form. J. Atmos. Sci., 25, 736-743.
- Phillips, N. A., 1954: Energy transformations and meridional circulations associated with simple baroclinic waves in a two-level, quasi-geostrophic mode. Tellus, 6, 273-286.
- Platzman, G. W., 1962: The analytical dynamics of the spectral vorticity equation. J. Meteor., 17, 635-644.

CHAPTER 4

N86-11752

A Parameterization Technique for Nonlinear Spectral Models

Ronald Gelaro

and

Hampton N. Shirer

Department of Meteorology
The Pennsylvania State University
University Park, PA 16802

1. Introduction

A fundamental characteristic of atmospheric motions on all scales is that the exchange of energy between various wavelengths is accomplished via nonlinear interactions. Accordingly, it is essential that mathematical models of atmospheric motion retain this nonlinear behavior as completely as possible. This is difficult owing to the fact that, in general, mathematical models are necessarily finite-dimensional, while the governing systems (such as the Navier-Stokes equations) are infinite-dimensional. As a result, the use of models that are based on systems of ordinary differential equations forces the modeler to truncate both implicitly and explicitly. Thus, the parameterization of certain variables is a necessary feature of all models. For example, this is an important step in the development of global forecast models of the index cycle, in which only certain scales of motion are emphasized.

In view of the requirement for parameterization in numerical models of all types, it is necessary to ensure that these operations are accomplished with maximum efficiency regarding the techniques employed and the scales of the motions that are parameterized. It is reasonable to assume that the structure of the solutions to the derived systems themselves should provide a basis for developing parameterization methods that would preserve more accurately the nonlinear properties of these dynamical systems. In particular, we refer to the topological structure of solutions as a means of describing them in terms of their critical parameter values, branching behavior and stability. We propose that a knowledge of the topological structure of the solutions to a dynamical system is essential for developing an efficient parameterization technique, and, that this technique will provide insight into ways of properly truncating all mathematical models of

atmospheric flow. Moreover, because even low-order models contain terms that are analogous to those that appear in the original partial differential equations, it is likely that a successful treatment of these models will be relevant in a general sense.

For the purposes of demonstrating this parameterization technique conveniently, we use the quasi-geostrophic equation because it has the advantage of being easily represented in spectral form (e.g., Vickroy and Dutton (1979), Charney and DeVore (1979), Wiin-Nielsen (1979)). Thus, as a prototype, we consider a truncated spectral model based on the forced, dissipative quasi-geostrophic equation developed by Dutton (1976a) for flow in a channel. The channel is centered at middle latitudes, has rigid lateral boundaries and is cyclic in the zonal direction. The stream function $\psi(x,t)$ is represented by a Fourier expansion. Newtonian heating is used to model the thermal forcing, and a direct dissipation mechanism is employed via an eddy viscosity coefficient.

The use of severely truncated spectral models has made it possible to study various properties of atmospheric flow by, among others, Lorenz (1960, 1963), Vickroy and Dutton (1979), Charney and DeVore (1979), Wiin-Nielsen (1979), and later by Lorenz (1980), Shirer (1980), Mitchell and Dutton (1981) and Shirer and Wells (1983). A significant advantage of working with severely truncated spectral models is that many of their properties may be studied analytically. In particular, steady solutions are made easily tractable in models of this type. The occurrence of multiple steady solutions in a forced, dissipative system is a manifestation of the fact that, upon eliminating the temporal derivatives of the spectral components, we can express the model as a system of nonlinear algebraic equations. These equations often can be expressed as a polynomial of odd degree in terms of only a single component.

The steady solutions to the model represent balances between the rates of forcing and dissipation, and they are obtained by solving this polynomial for its real roots. New solutions to the dynamical system tend to be born in pairs, and this is reflected by the fact that the real roots of the polynomial occur in odd numbers. The stabilities of the solutions are of interest; physically, stable solutions are states that might be observable. Points in phase space at which two or more steady solutions meet, known as steady bifurcation points, indicate transitions in the flow from one regime to another as the magnitudes of certain external forcing parameters are varied. It has been shown by Shirer and Wells (1982) that these transitions may be smooth or sudden depending on the general form of the solution surface, and on which forcing parameter is varied. The loss of stability of a steady state at the bifurcation point is a crucial factor in determining which of the available flow regimes might represent observable solutions to the system. In more recent work, Shirer and Wells (1983) point out that the topological form of the solution surface depends, in general, on a polynomial of lower order than the complete one, further demonstrating the relevance of results obtained from the study of severely truncated models. In addition, Dutton and Wells (1984) have examined the attractors of similar hydrodynamical flows and have found that the dimensions of the spaces in which these solutions reside are likely to be finite.

However, it is clear that the truncation process also results in the omission of energy exchanges between the scales in the model and the ones outside the truncated set. This is particularly significant for large-scale flow, owing to the importance of the transfer of enstrophy from the smaller waves to the ultralong waves and to the zonal flow. Thus, we seek an objective method for representing the effects of these interactions in which

we reduce, or at least maintain, the length of the original truncation. If we parameterize those interactions involving components outside the truncated set, then the nonlinearity inherent in a large model with many components may be represented accurately in a smaller model involving fewer nonlinear equations. This can be accomplished by expressing the omitted components as functions of those retained in the truncated set of the smaller model. The parameterized components appear in the truncated set as a result of the structure of the nonlinear and linear terms in the model, which derive from analogous forms in the original set of partial differential equations. In a parameterized model, those components that originate outside the truncated set are expressed as polynomials involving the retained components. The coefficients of these polynomials are referred to here as parameterization functions and they portray the effects of interactions between the retained and parameterized components of the flow. In an operational setting, the values of these parameterization functions would be computed using observed data. In the present study, we will test this scheme by creating data sets obtained from the solutions to a larger spectral model.

In this article, we are concerned with parameterizing steady behavior, and, with preserving the information it reveals about the transitions exhibited by hydrodynamical flows. The development of this scheme is presented in a way that facilitates its application to spectral models of all sizes. However, it should also be noted that the concept of utilizing data sets as a device for parameterization may be applied to numerical models of all types.

2. Spectral model of quasi-geostrophic flow

We consider the forced, dissipative quasi-geostrophic equation discussed by Vickroy and Dutton (1979)

$$\frac{\partial}{\partial t} (\nabla_H^2 \Psi) + J(\Psi, \nabla_H^2 \Psi) + \beta \frac{\partial \Psi}{\partial x} - \nu \nabla_H^4 \Psi = H \quad , \quad (2.1)$$

which contains the standard quadratic, linear and inhomogeneous forms found in all models. Here, J is the Jacobian operator, Ψ is a dimensionless stream function, and we use the β -plane approximation $f = f_0 + \beta y$. A direct dissipation mechanism is employed that is proportional to $\nu \nabla_H^4 \Psi$, in which ν is a dimensionless eddy viscosity coefficient. Theoretical supporting arguments for using an eddy viscosity in models of large-scale flow are presented in Dutton (1982). The inhomogeneous term H in (2.1) represents some simple forcing and derives from an approximate form of the thermodynamic equation (e.g. Dutton, 1976b) that is applicable to quasi-geostrophic motion. Here, we interpret H as a form of thermal forcing. However, other interpretations exist such as those of Egger (1978, 1979) and Charney and DeVore (1979) who derive analogous terms to represent topographical forcing.

To apply (2.1) to flow in a channel with a maximum westerly current located at the middle latitude, we select the domain

$$\underline{x} = \{x: 0 \leq x \leq 2\pi; \quad y: -\frac{\pi}{2} \leq y \leq \frac{\pi}{2}\} \quad .$$

Appropriate boundary conditions on Ψ are 1) periodicity in the zonal direction,

2) the meridional velocity component v vanishes at the northern and southern boundaries of the channel, and 3) the Phillips (1954) constraint, which prohibits the development of a circulation around the boundaries.

Because (2.1) contains the horizontal Laplacian of the stream function, we solve $\nabla_H^2 \psi = -\lambda_n \psi$ to determine the eigenvalues λ_n and the eigenfunctions ψ_n which we use to write

$$\psi(\underline{x}, t) = \sum_{n=1}^N A_n(t) \psi_n(\underline{x}) \quad (2.2)$$

To obtain the spectral representation of (2.1), we substitute (2.2) into (2.1) and then multiply each term by its conjugate $\bar{\psi}_n$. Because the eigenfunctions are orthogonal, we can integrate over the entire spatial domain \underline{x} for each $n=1, 2, \dots, N$ to produce the Fourier transformation

$$\dot{A}_n = - \sum_{k=1}^N \sum_{m=1}^N D_{p \ k \ m} A_k A_m + \beta \sum_{r=1}^N C_{q \ r} A_r - \nu \lambda_n A_n + H_n \quad (2.3)$$

in which D_p and C_q are interaction coefficients which we define in the Appendix. The eigenvalues are $\lambda_n = l^2 + n^2$, in which l and n are the horizontal wave numbers in the zonal and meridional directions respectively. To obtain a simple spectral model with a maximum in the westerly velocity component $u(y)$ that is located at the center of the channel, and that interacts nonlinearly with the disturbance components, we choose the five-component expansion

$$\begin{aligned} \psi(x, t) = & A_1(t) \sin(y) + A_2(t) \cos(kx) \cos(y) + A_3(t) \sin(kx) \cos(y) \\ & + A_4(t) \cos(kx) \cos(3y) + A_5(t) \sin(kx) \cos(3y) \end{aligned} \quad (2.4)$$

Because we are interested primarily in the steady solutions a to the model, we define $A(t) = a + \underline{a}(t)$, and set $\underline{a}(t) = 0$. With this condition, and with (2.4) to represent the stream function $\psi(x, t)$, we obtain from (2.3) the five-component steady spectral system

$$\begin{aligned} -D_{134} a_1 + D_{125} a_2 - V_{11} a_1 &= h_1 \\ -D_{213} a_1 - D_{315} a_2 + B_{23} a_3 - V_{22} a_2 &= h_2 \\ D_{212} a_1 + D_{314} a_2 - B_{32} a_3 - V_{33} a_3 &= h_3 \\ -D_{413} a_1 - D_{515} a_2 + B_{45} a_4 - V_{44} a_4 &= h_4 \\ D_{412} a_1 + D_{514} a_2 - B_{54} a_4 - V_{55} a_5 &= h_5 \end{aligned} \quad (2.5)$$

in which D_n , V_n , B_n and h_n are defined in the Appendix. The parameterization technique developed in the sequel will be applied to subsets of (2.5).

It can be shown algebraically that the determinant of the left side of (2.5) does not vanish. Thus, assuming a_1 is known, we can use Cramer's Rule to solve the last four equations in (2.5), which are linear in a_2, \dots, a_5 . Substituting these solutions into the first equation in (2.5), we obtain a ninth-degree polynomial in a_1 of the form

$$P(a_1) = p_9 a_1^9 + p_8 a_1^8 + \dots + p_0 = 0 \quad (2.6)$$

whose real roots are the steady solutions to the spectral equations (2.5). Because (2.6) is of odd degree and the coefficients p_n are real, complex roots must occur in conjugate pairs and the existence of at least one real root is guaranteed.

Owing to different balances between the rates of forcing and dissipation, (2.6) will often have several real solutions. Thus, the stabilities of these solutions are of interest. The fact that a stable solution relates physically to an observable state is discussed formally in Minorsky (1962), while other discussions on the relevance of bifurcation and stability to hydrodynamical systems may be found in Shirer and Dutton (1979) and Vickroy and Dutton (1979). In general, the stability of a stationary point a_n may be examined by linearizing the system about that point and then computing the eigenvalues γ of the linearized problem, which has solutions of the form $q(t) = \hat{q} \exp[\gamma t]$. Thus, a stationary solution a_n is stable to a small perturbation $q_n(t)$ provided that $\text{Re}\{\gamma\} < 0$ for every eigenvalue γ . The point at which stability changes and a new steady solution bifurcates from the first is, in general, given by $\text{Re}\{\gamma\} = 0$. For real eigenvalues, the critical point is given by simply $\gamma = 0$ for some γ . Bifurcations that indicate the appearance of a temporally periodic solution are known as Hopf bifurcations and these occur when $\text{Re}\{\gamma\} = 0$, $\text{Im}\{\gamma\} \neq 0$. Although in the present study we consider only preservation of the steady state structure of the solutions to the larger model, clearly the parameterization technique will need to be extended sufficiently so that the stability of the solutions is preserved as well. This is a topic of future research.

3. Development of the parameterization scheme

Analogous to (2.3), the steady spectral model (2.5) can be written in the general form

$$\sum_{k=1}^N \sum_{m=1}^N D_{p,km} a_k a_m - \sum_{r=1}^N B_{q,r} a_r + V_n a_n - h_n = 0, \quad n=1, \dots, N \quad (3.1)$$

However, if we wish to reduce the number of equations in (3.1) to some number $L < N$, then in a retained a_i -equation we lose the contribution of the terms

$$T_L = \left\{ \sum_{k=1}^L \sum_{m=L+1}^N + \sum_{m=1}^L \sum_{k=L+1}^N + \sum_{k,m=L+1}^N \right\} D_{p,km} a_k a_m - \sum_{r=L+1}^N B_{q,r} a_r \quad (3.2)$$

where, for simplicity, we have chosen to omit the last $L+1, \dots, N$ equations although any L -component subset may be used. To retain in the spectral model information concerning T_L , we parameterize its terms in the remaining L equations. If we denote the omitted spectral components by a_n and the retained spectral components by a_i , then the parameterization of (3.2) is achieved by representing the coefficients a_n that appear in the nonlinear terms of the remaining equations as functions of the coefficients a_i . We will assume that the general form of the relationship between the parameterized and retained components is given by the infinite series

$$a_n = F_{n0} + \sum_{i=1}^L F_{ni} a_i + \sum_{i=1}^L \sum_{m=1}^L F_{nim} a_i a_m + \sum_{i=1}^L \sum_{m=1}^L \sum_{p=1}^L F_{nimp} a_i a_m a_p + \dots, \quad (3.3)$$

in which the quantities F_{α} are parameterization functions that must be determined from a data set. In this study, we let the values of F_{α} depend on the moments of the spectral components which result from particular choices for the rates of forcing, rotation and dissipation. Thus the F_{α} contain information concerning the interactions between the retained components a_i and the parameterized components a_n . It will be shown in Section 4 that selecting a suitable termination level for (3.3) depends primarily on the characteristics of the data set.

To determine how the values of F_{α} are obtained, we consider in the following example a linear approximation of the parameterized spectral components; in this case (3.3) becomes simply

$$\bar{a}_n = F_{n0} + \sum_{i=1}^L F_{ni} a_i \quad (3.4)$$

In Section 4 we show that the use of a nonlinear approximation of (3.3) proceeds analogously. Using (3.4) so that the components a_n are approximated by \bar{a}_n , we require that the values of F_{α} are those for which the parameterization of (3.2) satisfies the relation

$$E \left[\left(F_{n0} + \sum_{i=1}^L F_{ni} a_i \right) - a_n \right]^2 = \epsilon_n, \quad n = 1, \dots, L \quad (3.5)$$

Here, E and ϵ_n denote the expected value and minimum mean square error respectively, which apply over an ensemble of responses that depend on the

forcing rate h_l . The parameterization functions F_{n0} and F_{nl} that satisfy (3.5) are given by

$$\bar{a}_n = F_{n0} + \sum_{l=1}^L F_{nl} \bar{a}_l \quad (3.6)$$

$$\overline{a_n a_k} = F_{n0} \bar{a}_k + \sum_{l=1}^L F_{nl} \overline{a_l a_k}, \quad k = 1, \dots, L$$

which is a linear, inhomogeneous set of equations in F_{nl} provided that the barred quantities are known. Here the tildes have been dropped and $\bar{\phi}$ denotes the moment of ϕ . Therefore, the quantities $\overline{a_n a_k}$ and $\overline{a_l a_k}$ represent the correlation coefficients between the spectral components. Obviously, a nonlinear approximation of (3.3) will yield higher-order moments in addition to those appearing in (3.6). In Section 3a, we discuss a procedure for obtaining the necessary data from (2.5).

Substituting the linear approximation (3.4) into the spectral model (3.1) and adjusting the subscripts, we obtain the parameterized steady spectral model

$$\sum_{k=1}^L \sum_{m=1}^L D_p a_k a_m - \sum_{r=1}^L B_q a_r + V_l a_l - h_l + \sum_{k=L+1}^N \sum_{m=1}^L D_p \bar{a}_k a_m \quad (3.7)$$

$$+ \sum_{k=1}^L \sum_{m=L+1}^N D_p a_k \bar{a}_m + \sum_{k,n=L+1}^N \sum_{m=L+1}^N D_p \bar{a}_k \bar{a}_m - \sum_{r=L+1}^N B_q \bar{a}_r = 0,$$

$$l=1, \dots, L$$

in which the terms after h_2 in (3.7) include the effects of the parameterized spectral components. Because (3.4) is a linear approximation, (3.7) contains no terms of higher order than quadratic, which is a form similar to that of the original spectral equations (3.1). However, the use of a nonlinear approximation for the parameterized components will introduce higher-order nonlinearities which may alter the form of the steady polynomial for the parameterized model. This will be discussed in Section 4.

a. Application and testing techniques

In the absence of observed data, an alternative procedure is needed to produce the data sets required to compute the values of the moments that appear in (3.6). A simple method for creating these data is to use the steady solutions to the original five-component model for various test cases. The use of solutions to (2.5) as data has the virtue of being mathematically simple because the values of a_2, \dots, a_5 can be computed algebraically once the roots of (2.6) are found. In addition, the steady solutions to (2.5) provide examples with which the solutions to the parameterized models may be compared. A standard depiction of the steady states is a one-dimensional cross-section through phase space, in which we plot the magnitude of the zonal component a_1 versus a single forcing rate. In this study, we choose to compute the steady solutions a_1 for various values of the zonal forcing rate h_1 , while the magnitudes of the remaining parameters remain fixed. Thus, the moments of the spectral components, and consequently, the values of the parameterization functions F_{α} will depend only on the value of h_1 .

For a discrete number k of values of h_1 , the moments are given by

$$\overline{f(h_1)} = \sum_{i=1}^k f(h_1)_i p[f(h_1)_i] \quad , \quad (3.8)$$

in which $f(h_1)$ can be any function of the spectral components, while the summand is the i^{th} value of $f(h_1)$ multiplied by the probability that $f(h_1)$ equals that value. In this study we consider both uniformly and normally distributed values of h_1 .

With the uniform distribution we assume $p[f(h_1)_i]$ has density $1/(h_{1a}, h_{1b})$ over some finite interval $[h_{1a}, h_{1b}]$, and use randomly generated values of h_1 to produce the data points $f(h_1)_i$. In this case, (3.8) reduces to a simple average.

If instead we assume that the values of h_1 are distributed normally with mean \bar{h}_1 and standard deviation σ_1 , then (3.8) can be written in the form

$$\overline{f(h_1)} = \int_{-\infty}^{\infty} f(h_1) p(h_1) dh_1 \quad (3.9)$$

in which $p(h_1)$ is the normal probability density function of h_1 . An advantage of using the normal distribution is that, in the proper form, (3.9) can be evaluated easily using a Hermite polynomial approximation. For example, by making the appropriate substitution in (3.9), we would obtain the correlation

$$\overline{a_n a_m} = \int_{-\infty}^{\infty} a_n a_m \exp[-x^2] dx = \sum_{i=1}^k w_i a_{ni} a_{mi} \quad (3.10)$$

in which the quantities w_i are weighting factors corresponding to the zeros x_i of the Hermite polynomial (Abramowitz and Stegun, 1964). Here relatively few data points are required compared with the number used with the uniform distribution. In this study, we use $k=200$ random values of h_1 with the uniform distribution, while in (3.10), the value of $k=16$ corresponds to a distance from the mean for which $w_i \sim 1 \times 10^{-10}$.

Finally, a weighting procedure must be employed when, for a particular value of h_1 , (2.6) has multiple steady solutions a_1 , which correspond to multiple solutions for each component a_2, \dots, a_5 . For comparison, we will consider two weighting procedures. The first is useful for determining the general form of the parameterized expansions; with it, the solutions are weighted equally regardless of stability. In the second approach, we simulate the use of observed data; one stable solution is selected at random. These procedures will be discussed in Section 4.

b. Effects on stability

The preservation of bifurcation and stability properties in the parameterized models is of concern. However, because the values of F_a depend only on the moments of the spectral components, they contain no explicit information concerning the stabilities of the steady solutions. However, one might expect fold points such as those in the cross-section in Fig. 1 to be preserved by the parameterization provided that an optimum number of terms is retained in (3.3). The preservation of these points will ensure that the number of steady solutions produced by the parameterized models agree with that of the original. However, as permitted by linear stability theory, the parameterization may reproduce the original cross-section, but reverse the stabilities of the solutions. In this case, the signs of some of the eigenvalues are reversed.

Hopf bifurcations, which denote the appearance of temporally periodic solutions (Marsden and McCracken, 1976), may result in a loss of stability at a point on a steady solution other than a fold, or turning, point (Fig. 1). Although Hopf bifurcations may still appear in the solutions to the parameterized models, the likelihood of preserving their locations cannot be assured owing to the exclusion of information concerning temporal solutions in

computing the values of F_{α} . As a result, an optimum parameterization based on (3.3) may produce solutions whose cross-sections in phase space are similar to those of the original solutions, but whose qualitative behavior may differ owing to changes in stability. Because this is a feasibility study, and modeling steady bifurcations is the primary interest, no effort has been made to account for stability changes due to Hopf bifurcations. However, we will see evidence in Section 4 that, in some cases, a proper treatment of steady behavior may increase the likelihood of preserving the temporal behavior of the solutions.

c. Truncation types

The parameterization technique developed in this section will be applied to two subsets of (2.5), each containing three components. In each parameterized subset we retain the zonal component a_1 and two of the remaining disturbance components. In this way, any three-component subset of (2.5) can be categorized as belonging to one of two qualitatively different classes of truncations.

We will parameterize a representative of each class. The two classes of truncations are revealed upon inspection of the spectral expansion for $\psi(x,t)$ given by (2.4). The basis functions associated with A_2 and A_3 correspond to wave number $n=1$, while those for A_4 and A_5 correspond to $n=3$. The members of each pair differ only in phase in the zonal direction. We consider the truncations in Class I to be those in which both components of either wave number are retained, while the effects of the remaining wave number are parameterized. The members of this class are the subsets $\{1,2,3\}$ and $\{1,4,5\}$. In the Class II truncations, we retain one component of each wave number resulting in the choices $\{1,2,4\}$, $\{1,2,5\}$, $\{1,3,4\}$ and $\{1,3,5\}$. The subsets $\{1,2,4\}$ and $\{1,3,5\}$ represent special cases whose properties are discussed in Section 4.

From Class I we consider the subset {1,2,3} in which the effects of wave number $n=3$ are parameterized:

$$\begin{aligned}
 -D_1 a_3 a'_4 + D_1 a_2 a'_5 - V_1 a_1 &= h_1 \\
 -D_2 a_1 a_3 - D_3 a_1 a'_5 + B_2 a_3 - V_2 a_2 &= h_2 \\
 D_2 a_1 a_2 + D_3 a_1 a'_4 - B_3 a_2 - V_3 a_3 &= h_3
 \end{aligned} \tag{3.16}$$

In (3.16), a'_4 and a'_5 are expressed as functions of a_1 , a_2 and a_3 based on (3.3). The use of (3.16) is founded on a philosophy commonly employed to parameterize small or sub-grid-scale processes whose effects need to be incorporated into the large-scale components of the model. A typical example is the parameterization of surface heat fluxes in operational synoptic-scale finite difference models used to forecast the large-scale flow of the middle latitudes.

As a representative of Class II, we consider the subset {1,2,5}:

$$\begin{aligned}
 -D_1 a'_3 a'_4 + D_1 a_2 a'_5 - V_1 a_1 &= h_1 \\
 -D_2 a_1 a'_3 - D_3 a_1 a'_5 + B_2 a'_3 - V_2 a_2 &= h_2 \\
 D_4 a_1 a_2 + D_5 a_1 a'_4 - B_5 a'_4 - V_5 a_5 &= h_5
 \end{aligned} \tag{3.17}$$

This subset differs physically, although not mathematically, from (3.16). In (3.16) we might expect to represent the behavior of the smaller wave number

components more accurately while representing implicitly downscale energy transfers. This concept is analogous to the creation of an eddy viscosity in which we parameterize the cascade of energy from small to large wave numbers (Dutton, 1976a). In general, these small wave number components contain a large percentage of the total energy of the original system. Conversely, in (3.17) we retain a higher wave number (and generally less energetic) component of the flow in lieu of a more complete representation of the larger scale. Thus, in (3.17) we represent explicitly one avenue of downscale transfer at the expense of a complete explicit representation of transfers between large-scale components.

4. Optimum parameterization

To apply the parameterization scheme, we must select a termination level for the series (3.3). It is reasonable to assume that an optimum parameterization can be obtained by retaining only the m terms in the series that are necessary to describe, to some desired accuracy, the steady behavior of the original solutions. To find the m terms, we terminate (3.3) at some number $M \geq m$ of terms and, proceeding as from (3.4) to (3.6), we generate M linearly independent equations whose coefficients are the moments $\overline{f(h_1)}$. The optimum parameterization is determined by the m significant terms in the solution F_2 to the resulting system of equations. It will be shown that the maximum permissible value of M for which a linearly independent system of equations can be generated depends significantly on the data coverage. Moreover, we observe that, for this study, the data coverage requirements are controlled, in part, by the topological forms of the steady solutions to the five-component model.

In all nonlinearly interacting flows, there are certain disturbance components between which no exchange of energy occurs via nonlinear interactions. In the five-component model (2.5), we observe no nonlinear terms containing the products a_2a_4 or a_3a_5 , which lead to the special subsets $\{1,2,4\}$ and $\{1,3,5\}$ noted in Section 3c. An advantage of studying these special cases is that simple analytical solutions can be obtained from (2.5) for the omitted spectral components in each subset. These solutions are expressed as functions of the three remaining components; thus, they are of a form which is similar to that of the parameterized expansions obtained from (3.3). As a first guess for any model, we might expect a reasonable termination level M for (3.3) to be determined by the highest-degree terms

that appear in the solutions to its special cases. For example, if we assume that the values of a_1 , a_3 and a_5 are known, then from (2.5) we obtain

$$a_2 = \frac{1}{V_2} [-D_2 a_1 a_3 - D_3 a_1 a_5 + B_2 a_3 - h_2] \quad (4.1)$$

and

$$a_4 = \frac{1}{V_4} [-D_4 a_1 a_3 - D_5 a_1 a_5 + B_4 a_5 - h_4] \quad (4.2)$$

Expressions similar to (4.1) and (4.2) result for the coefficients a_3 and a_5 in the other special case. By inspecting the right sides of (4.1) and (4.2), we might infer that an optimum parameterization would involve expansions that contain no terms of degree higher than quadratic. Moreover, because the forms of the equations in (2.5) are typical of those found in hydrodynamical systems regardless of the severity of the truncation, (4.1) and (4.2) are likely to be representative of the optimum parameterized expansions for any model of this type.

Accordingly, we terminate (3.3) so that the parameterized spectral components are approximated by

$$a_n = F_{n0} + \sum_{l=1}^L F_{nl} a_l + \sum_{l=1}^L \sum_{m=1}^L F_{nlm} a_l a_m, \quad (4.3)$$

from which we generate $M \leq 1 + L(L+3)/2$ linearly independent equations, depending on the data coverage. Because $M \geq n$ terms are required in (4.3) to obtain the correct values of F_n , we will begin with the complete quadratic expansion. Analogous to the linear example in Section 3, the values of the

parameterization functions F_{α} are the solutions to the system

$$\bar{a}_n = F_{n0} + \sum_{l=1}^L F_{nl} \bar{a}_l + \sum_{l=1}^L \sum_{m=1}^l F_{nlm} \overline{a_l a_m}$$

$$\sum_{p=1}^L [\overline{a_n a_p} = F_{n0} \overline{a_p} + \sum_{l=1}^L F_{nl} \overline{a_l a_p} + \sum_{l=1}^L \sum_{m=1}^l F_{nlm} \overline{a_l a_m a_p}] \quad (4.4)$$

$$\sum_{p=1}^L \sum_{q=1}^p [\overline{a_n a_p a_q} = F_{n0} \overline{a_p a_q} + \sum_{l=1}^L F_{nl} \overline{a_l a_p a_q} + \sum_{l=1}^L \sum_{m=1}^l F_{nlm} \overline{a_l a_m a_p a_q}]$$

For $L = 3$, (4.4) becomes a set of ten linear inhomogeneous equations provided that the moments are known. For example, in the subset $\{1,2,5\}$, we would parameterize a_3 according to (4.3) and obtain

$$a_3 = F_{30} + F_{31} a_1 + F_{32} a_2 + F_{35} a_5 + F_{311} a_1^2 + F_{312} a_1 a_2 + F_{315} a_1 a_5$$

$$+ F_{322} a_2^2 + F_{325} a_2 a_5 + F_{355} a_5^2, \quad (4.5)$$

which corresponds to the first equation in (4.4). The remaining nine equations in (4.4) are produced by multiplying (4.5) by the functions $f(h_1)$ in each term on its right side, and then averaging to produce the moments.

a. Data Types

We now investigate procedures for creating the data necessary to compute the values of the moments that appear in (4.4). Several types of data will be considered. For each data type, we employ one of the two statistical distributions discussed in Section 3a, and a weighting procedure that determines the probability that a particular steady solution results when the response to a value of the forcing is not unique. The data also will be classified according to stability in two ways. We refer to a data set in which all solutions are permitted regardless of stability as being a complete-data set,

and one in which only stable solutions are permitted as being an observable-data set (Table 1).

Considering the preceding criteria, we will select four types of data and examine their effects on the values of the parameterization functions F_Q . For convenience, we denote each data type by the first letter describing its stability class (Observable, Complete), subscripted by the first letter describing the statistical distribution of the zonal forcing values (Uniform, Normal). Thus, the first data type in Table 1, which consists of observable solutions that are uniformly distributed, is referred to as type O_U . Each data type fulfills a specific testing purpose which we now discuss briefly.

Type O_U data are intended to simulate observed data in the simplest manner. In this case, the values of h_1 are assumed to be uniformly distributed and only stable solutions are considered. When multiple stable solutions occur, we select one solution at random and assume that only this solution contributes to the calculation of the moments for the corresponding forcing value. This is consistent with the fact that, with observed data, the occurrence of any one state might be as equally likely as another. Here, the moments are computed using (3.9).

Type C_U data differs from type O_U in that the complete set of steady solutions from each test case may be used as data. By using a similar distribution and weighting procedure as for type O_U data, we permit the occurrence of unstable solutions to be as equally likely as stable ones when multiple solutions result. Type C_U data will be used to determine whether the inclusion of unstable solutions as data in the parameterization scheme is crucial for reproducing the complete forms of the steady states.

Data types C_N and O_N represent special cases of the previous data types, in which we assume that the values of the zonal forcing rate obey a normal

Table 1.

Data types used for calculating the values of
the parameterization functions F_g .

	Stability class	Stat. distribution	Weighting	Applications
Type O_U	Observable	Uniform	1 Random	Observations
Type C_U	Complete	Uniform	1 Random	Research
Type C_N	Complete	Normal	1/r	Research
Type O_N	Observable	Normal	1/s	Research/ Observations

distribution. While actual observed data may obey a more specialized distribution than the uniform one employed in types O_U and C_U , we do not propose that a normal distribution for h_1 would be more physically representative than any of the other standard distributions. Because relatively few data points are required to calculate the moments with the Hermite approximation, we employ a different weighting procedure with these data types, as shown in Table 1. When multiple solutions occur, all permissible ones are weighted equally. Thus, with type C_N data, we weight equally each of the combined total number r of both stable and unstable solutions, while with type O_N data, we only weight equally each of the number s of stable solutions. We have verified that these procedures are analogous to using a randomly selected, fully weighted solution (as in types O_U and C_U) when many normally distributed data points are used.

Because the data coverage in a particular test case may depend significantly on the data type used, we expect that the maximum value of M for which (4.4) yields a linearly independent system of equations also will depend on the data type. However, we can determine beforehand the number of linearly dependent equations in (4.4) by computing the eigenvalues of its complete right side. A vanishing eigenvalue (and thus, a vanishing determinant) indicates a linearly dependent pair of equations, one of which may be discarded without altering the system. Provided that we omit the proper lines, we may repeat this process until an independent set of equations remains. Thus, when we obtain a system in which each of the remaining eigenvalues $\lambda_1, \dots, \lambda_M$ are nonzero, then a solution to this reduced system can be found. In the following subsection, we examine a technique for identifying those terms in (4.5) that must be eliminated when an independent set of equations cannot be generated from the entire quadratic expansion.

b. Complete-data sets

For each data type, solutions to the parameterized models will be computed numerically for four test cases. These cases provide examples in which the stabilities and the configurations of the steady solutions vary in complexity, allowing a systematic examination of the skills of the parameterized models. The fixed values of the dimensionless parameters in each test case are listed in Table 2. For the parameterized models, the values of \bar{h}_1 and σ_1 used with the normal distribution, and the intervals $[h_{1a}, h_{1b}]$ used with the uniform distribution, are given in Table 3. The cross-sections of the solutions for the test cases appear in Figs. 1-4, and we begin examining the results of the parameterized models using the complete sets of solutions, which correspond to data types C_U and C_N .

1) The subset {1,2,5}

If we consider the three-equation subset (3.17) and parameterize a_3 and a_4 according to (4.3), then we obtain

$$\begin{aligned} a'_n = & F_{n0} + F_{n1} a_1 + F_{n2} a_2 + F_{n5} a_5 + F_{n11} a_1^2 + F_{n12} a_1 a_2 + F_{n15} a_1 a_5 \\ & + F_{n22} a_2^2 + F_{n25} a_2 a_5 + F_{n55} a_5^2, \quad n = 3, 4. \end{aligned} \quad (4.6)$$

Now with (4.6) as the foundation of two sets of linear inhomogeneous equations of the form of (4.4), we compute the moments using the solutions in Figs. 1-4 as data. For example, we consider test case 1 and use type C_U data. Because we are interested in testing the ability of the parameterization to preserve the nonlinear behavior of the steady states, we include forcing values which produce multiple steady solutions in the data. Based on the symmetry of the solutions in Fig. 1, we consider values of h_1 in the interval $[-0.05, 0.05]$ and compute the moments according to the specifications for the type C_U data

Table 2.

Fixed parameter values for the four test cases in Figures 1 - 4.

	Case 1	Case 2	Case 3	Case 4
h_2	0.300	-0.300	2.000	-0.670
h_3	0	-0.400	3.000	-1.005
h_4	0	0.100	1.000	0.335
h_5	0	0	1.000	0
k	1	1	1	1
v	0.040	0.040	0.040	0.040
β	0	0	0.500	0.500

Table 3.

The values for each test case of the mean zonal heating rate h_1 and the standard deviation σ_1 used with the normal distribution, and the interval $[h_{1a}, h_{1b}]$ used with the uniform distribution.

	Case 1	Case 2	Case 3	Case 4
\bar{h}_1	0	0	0	-0.26
σ_1	0.01	0.03	5.00	0.03
$[h_{1a}, h_{1b}]$	$[-0.05, 0.05]$	$[-0.50, 0.50]$	$[-3.00, 3.00]$	$[-0.40, -0.10]$

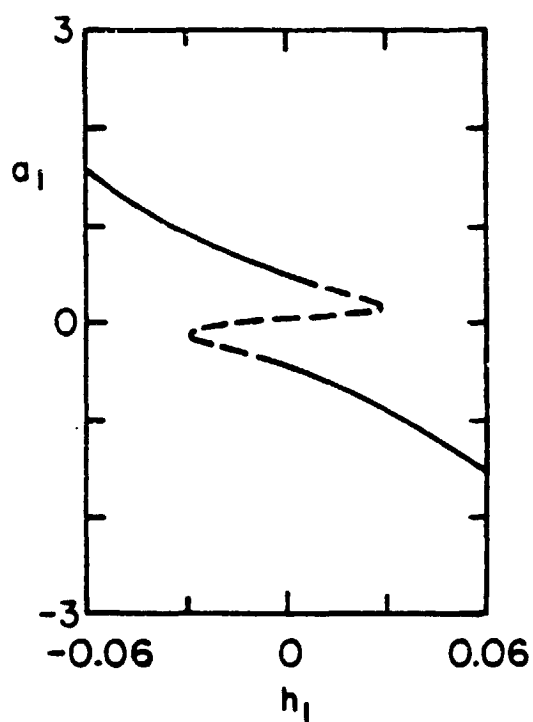


Figure 1 Cross-section of the steady solutions to the five-component model for case 1. Stable solutions are denoted by solid lines, and unstable solutions by dashed lines. Hopf bifurcations occur on the upper and lower branches near $h_1 = \pm 0.01$.

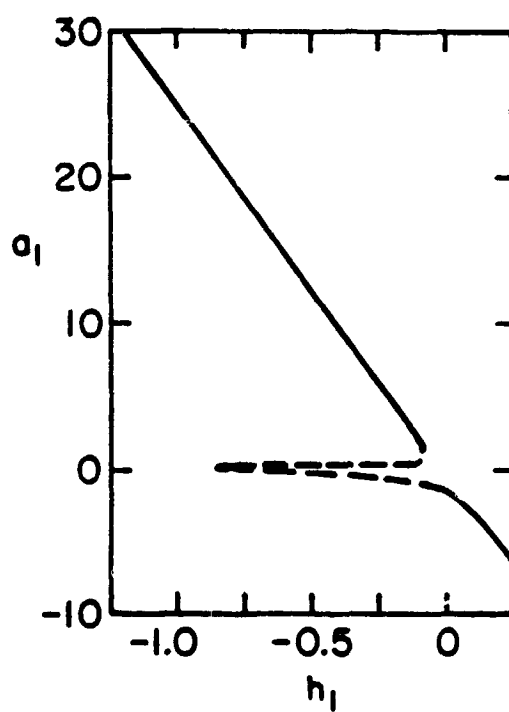


Figure 2 As in Fig. 1 for case 2. A Hopf bifurcation occurs on the lower branch near $h_1 = -0.1$.

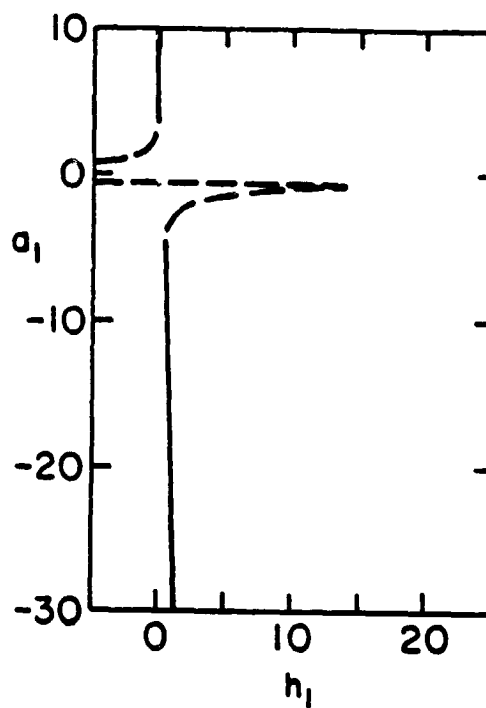


Figure 3 As in Fig. 1 for case 3. A Hopf bifurcation occurs on the middle branch (underside of spike) near $h_1 = 5.0$ so that there are three positive eigenvalues as the tip of the fold, or spike, is encountered. At this point, one eigenvalue vanishes and the upper branch is unstable with two positive, but unequal, eigenvalues.

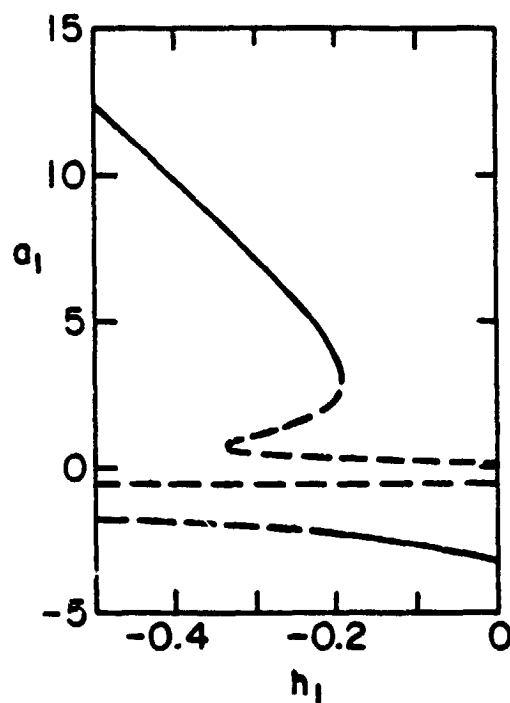


Figure 4 As in Fig. 1 for case 4. Hopf bifurcations appear on the middle branch of the configuration near the fold point at approximately $h_1 = -0.33$, and on the lower branch near $h_1 = -0.23$.

in Table 1. In this case, the right sides of the linear systems generated from (4.6) contain only nonzero eigenvalues so that $M = 10$ equations can be solved to obtain the parameterized expansion for each spectral component. This is true for both components in all four test cases in Figs. 1-4. In each case, the interval $[h_{1a}, h_{1b}]$ includes data in regions of multiple solutions. The values of F_{α} for all four cases using type C_U data are presented in Table 4.

From Table 4, we see that several terms in F_{α} consistently obtain negligible values when compared with the remaining ones. Those terms that are negligible in all four cases are F_{n1} , F_{n11} , F_{n22} , F_{n25} and F_{n55} , $n = 3, 4$. Several other terms sometimes obtain negligible values but these cannot be neglected generally. If we omit the five terms mentioned above, then (4.6) can be written

$$a'_n = F_{n0} + F_{n22} a_2 + F_{n55} a_5 + F_{n1212} a_1 a_2 + F_{n1515} a_1 a_5, \quad n = 3, 4. \quad (4.7)$$

Significantly, the quadratic terms in (4.7) are linear functions of the disturbance components a_2 and a_5 , and this permits the use of simple linear techniques to obtain a steady polynomial for the parameterized model. Moreover, it is pleasing to note that, with the exception of an additional linear term in (4.7), the forms of the expansions for a'_n using the $m = 5$ significant terms in the solutions F_{α} correspond to those in the analytical expressions (4.1) and (4.2). However, as shown in Table 4, this additional linear term is negligible in cases when $\beta = 0$. Thus, to some extent, each term in (4.7) appears to play the same role as its counterpart in the analytical expressions. For example, we observe in Table 2 that cases 3 and 4 differ only in the values of their forcing rates h . In (4.1) and (4.2) the forcing appears only in the inhomogeneous terms h_n/V_n , $n = 2, 4$. Analogously, we see

Table 4.

Values of the parameterization functions F_{α} for
the subset {1,2,5} using type C_U data.

	Case 1 [-0.05,0.05]	Case 2 [-0.5,0.5]	Case 3 [-3.0,3.0]	Case 4 [-0.4,-0.1]
F ₃₀	8.03x10 ⁻³	5.00	-22.70	11.59
F ₃₁	7.15x10 ⁻¹⁴	4.91x10 ⁻¹⁴	-4.78x10 ⁻¹³	2.26x10 ⁻¹⁰
F ₃₂	1.39x10 ⁻¹²	6.91x10 ⁻⁸	-3.06	-3.06
F ₃₅	6.48	6.48	6.45	6.45
F ₃₁₁	7.23x10 ⁻¹³	9.73x10 ⁻¹⁵	9.45x10 ⁻¹⁵	-1.07x10 ⁻¹¹
F ₃₁₂	-5.03	-5.03	-4.93	-4.93
F ₃₁₅	1.57x10 ⁻¹⁰	-2.11x10 ⁻⁶	1.11	1.11
F ₃₂₂	3.10x10 ⁻¹³	8.44x10 ⁻¹²	1.15x10 ⁻¹¹	7.06x10 ⁻⁹
F ₃₂₅	7.14x10 ⁻¹³	4.77x10 ⁻¹⁰	2.18x10 ⁻⁹	-1.07x10 ⁻⁷
F ₃₅₅	3.64x10 ⁻⁹	-5.49x10 ⁻¹⁰	-2.12x10 ⁻⁹	9.69x10 ⁻⁸
F ₄₀	0.03	-0.28	-1.73	-1.19
F ₄₁	1.09x10 ⁻¹⁵	-1.23x10 ⁻¹⁴	7.11x10 ⁻¹⁵	2.19x10 ⁻¹⁴
F ₄₂	8.00x10 ⁻³	8.00x10 ⁻³	0.08	0.08
F ₄₅	1.36x10 ⁻¹³	5.30x10 ⁻⁷	-0.04	-0.04
F ₄₁₁	7.80x10 ⁻¹⁴	-2.19x10 ⁻¹⁵	7.99x10 ⁻¹⁷	8.91x10 ⁻¹⁵
F ₄₁₂	-7.32x10 ⁻¹⁷	1.11x10 ⁻⁷	0.12	0.12
F ₄₁₅	1.40	1.40	1.37	1.37
F ₄₂₂	3.53x10 ⁻¹⁴	-1.65x10 ⁻¹²	1.49x10 ⁻¹³	6.15x10 ⁻¹³
F ₄₂₅	4.33x10 ⁻¹⁴	-1.08x10 ⁻¹⁰	3.07x10 ⁻¹¹	-4.00x10 ⁻¹¹
F ₄₅₅	4.27x10 ⁻¹⁰	-1.30x10 ⁻¹⁰	-3.08x10 ⁻¹¹	9.89x10 ⁻¹¹

in Table 4 that only the values of the inhomogeneous terms F_{n0} in (4.7) differ between cases 3 and 4 for each parameterized component.

If we substitute (4.7) into (3.17) and apply the same linear techniques as those used in Section 2, then the first equation in (3.17) becomes

$$\begin{aligned}
 & -D_1 \left[F_{30} + \frac{1}{\delta_{25}} (F_{32}s_2 + F_{35}s_5 + F_{312}a_1s_2 + F_{315}a_1s_5) \right] \\
 & \times \left[F_{40} + \frac{1}{\delta_{25}} (F_{42}s_2 + F_{45}s_5 + F_{412}a_1s_2 + F_{415}a_1s_5) \right] \\
 & + \frac{D_1 s_2 s_5}{\delta_{25}^2} - V_1 a_1 - h_1 = 0 \quad , \quad (4.8)
 \end{aligned}$$

in which

$$a_l = \frac{s_l}{\delta_{25}} = \frac{c_{l3}a_1^3 + c_{l2}a_1^2 + c_{l1}a_1 + c_{l0}}{d_4a_1^4 + d_3a_1^3 + d_2a_1^2 + d_1a_1 + d_0} \quad , \quad l = 2, 5 \quad . \quad (4.9)$$

The polynomial coefficients in (4.9) are lengthy and are given in Gelaro (1983). However, it can be shown that the coefficient d_0 of δ_{25} can never vanish, implying that the solutions a_l exist for all parameter values except the physically inadmissible case $V_l = 0$. Because δ_{25} is quartic in a_1 and the viscous term $-V_1 a_1$ is linear in a_1 , (4.8) becomes a ninth-degree polynomial in a_1 when the denominator has been cleared and multiplied by δ_{25}^2 . The real roots of (4.8) are the steady solutions to the parameterized subset {1,2,5}. The fact that (4.8) is of odd-degree, similar to the steady polynomial for the five-component model, is essential for preserving the structure of the original steady solutions.

Figs. 5-8 depict the numerical calculations of the steady solutions to the parameterized subset {1,2,5} using the values of F_n given in Table 4.

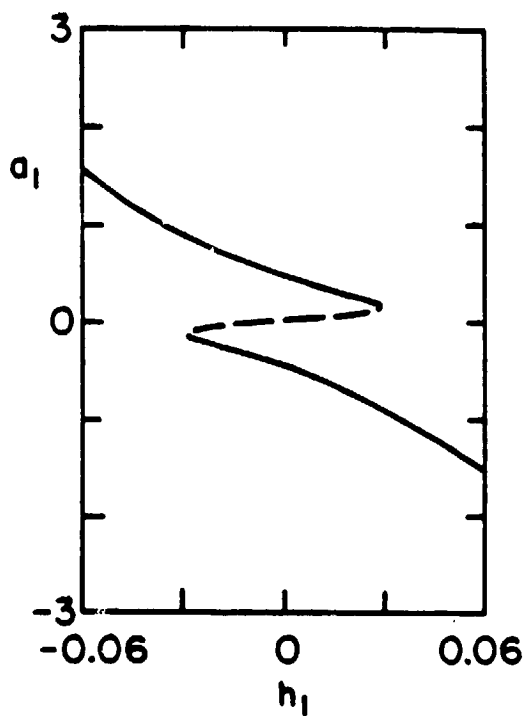


Figure 5 Cross-section of the steady solutions to the parameterized subset $\{1,2,5\}$ for case 1 using the values of F in Table 4. Note that the Hopf bifurcations on the upper and lower branches in Fig. 1 do not appear here so that these branches remain stable up to each fold point.

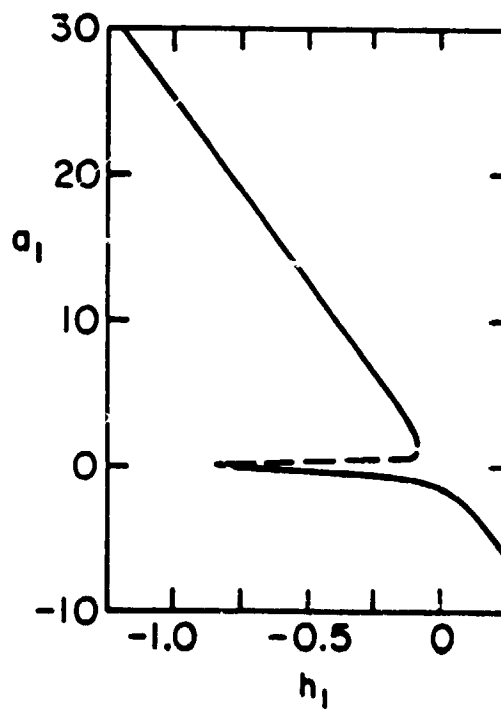


Figure 6 As in Fig. 5 for case 2. The Hopf bifurcation that occurs on the lower branch in Fig. 2 near $h_1 = -0.1$ has been shifted to approximately $h_1 = -0.8$.

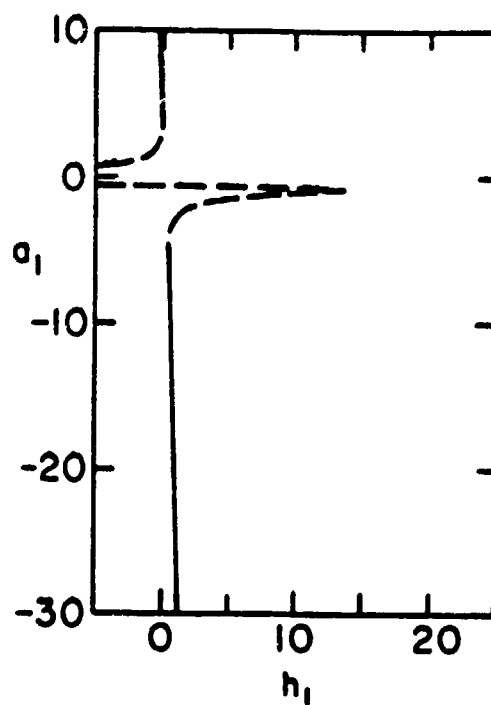


Figure 7 As in Fig. 5 for case 3. Although the stabilities of the solutions appear similar to those in Fig. 3, the Hopf bifurcation that appears on the middle branch in the original cross-section has been shifted to the upper branch in the parameterized model. Thus, the numbers of positive and negative eigenvalues differ for the corresponding solutions in each model.

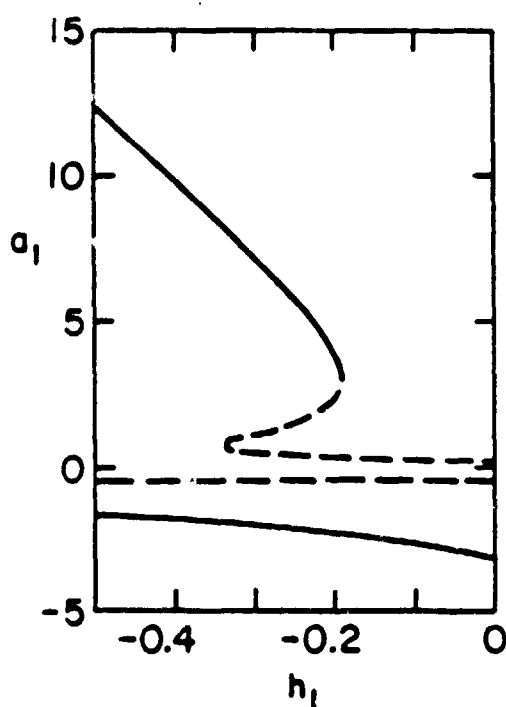


Figure 8 As in Fig. 5 for case 4. The Hopf bifurcation that appears on the lower branch in Fig. 4 does not appear in the solutions to the parameterized model.

Clearly, the parameterization has reproduced the configurations of the steady states quite accurately in all four cases, implying that the steady bifurcation points are well preserved. Even in case 3 (Figs. 3 and 7) involving five nonzero rates of forcing and rotation, the magnitudes of the solutions to the original and to the parameterized models agree to several decimal places. However, the stabilities of the solutions to each model differ owing to the lack of information in the parameterized model concerning the original temporal solutions. For example, the upper and lower solutions of the cusp surface in Fig. 5 of the parameterized model lose stability upon meeting the middle solution at each fold point. However, Hopf bifurcations on the upper and lower solutions in Fig. 1 result in a loss of stability before the fold points. In this case, the Hopf bifurcation points on the solutions to the original model do not appear on those to the parameterized model. In some cases, Hopf bifurcations appear on the solutions to the parameterized models, but their locations are not preserved well. This is demonstrated in Figs. 2 and 6. Here the lower solution in each figure loses stability at a point other than fold point, but the locations of these points differ in each model. Similar behavior can be seen in the two remaining cases (Figs. 1, 4, 5 and 8).

Analogous to the above testing conducted with the type C_U data, values of the parameterization functions F_{α} for the subset $\{1,2,5\}$ were computed for the four test cases using the type C_N data described in Table 1. The values of \bar{h}_1 and σ_1 for each case are selected so that the regions of interest in Figs. 1-4 are bounded by values of h_1 that are no more than approximately $\pm 3\sigma_1$ from the mean. The resulting values of F_{α} are nearly identical to those obtained with the type C_U data (and thus, not shown here), further confirming that the $m = 5$ significant terms in (4.7) are those required for an optimum

parameterization of the components a_3 and a_4 . Moreover, the fact that the same values of v and θ yield similar values of F_2 for the homogeneous terms in each case in Table 4 indicates that these coefficients have functional forms similar to those obtained in (4.1) and (4.2) for the special case. It may be noted that values of F_2 were computed in a similar way for the special subsets $\{1,2,4\}$ and $\{1,3,5\}$. The resulting values of the significant terms in the solution F_2 were the same as those of the analytical coefficients obtained for the parameterized components in each subset. For example, in (4.1) it can be shown that $-D_2/V_2 = F_{213} = 5.305$. Unfortunately, such direct comparisons are possible only for the special cases, but they do demonstrate the validity of the numerical scheme.

2) The subset $\{1,2,3\}$

To apply the parameterization technique to the subset $\{1,2,3\}$, we begin with expressions for a_4 and a_5 that are analogous to (4.6). Again, we consider type C_U data and use the same intervals $[h_{1a}, h_{1b}]$ as before. However, in contrast to the preceding results, it is impossible to generate $M = 10$ linearly independent equations from the original expansions in any of the test cases. In each case, the right side of the complete system contains one vanishing eigenvalue, indicating two linearly dependent equations. Here, it is difficult to suspect insufficient data coverage as being the primary cause of this dependence, owing to the fact that the same intervals of h_1 were used as for the subset $\{1,2,5\}$. Also, the test cases are dissimilar enough to make it unlikely that, in every case, insufficient data coverage results in exactly one vanishing eigenvalue. Rather, this behavior may be either a result of the truncation itself, or the way in which the ten equations are generated.

Following the procedure discussed in the previous section, we eliminate a column and corresponding row from the system until we obtain a set of

equations which yields nine nonzero eigenvalues. In all of the test cases, the elimination of either the lines corresponding to the term $F_{n22}a_2^2$ or to the term $F_{n33}a_3^2$ yields a set of nine equations for which all eigenvalues $\lambda_M \neq 0$. It may be noted that both of these terms are among those neglected in the parameterized expansions for the subset $\{1,2,5\}$. Moreover, if we solve the nine-equation systems which result when either of these terms is eliminated from the expansions, then the resulting m significant terms of F_{α} correspond precisely to those obtained for the subset $\{1,2,5\}$. From these results it is clear that the most general form for the parameterized components is analogous to that of (4.7).

Because the parameterized components a_4 and a_5 are of the proper form, a steady polynomial is obtained easily for the parameterized subset $\{1,2,3\}$. Figs. 9-12 depict the numerical calculations of the steady solutions for the four test cases using the values of F_{α} in Table 5. Again, the cross-sections reveal that the steady bifurcation points are preserved in the parameterized model so that the configurations of the solutions agree well with the original solutions in Figs. 1-4. As before, differences in stability may be attributed to Hopf bifurcations.

Although the truncation type does not affect the optimum form of the parameterized expansions, it may indeed be a factor in determining the termination point M of the series (3.3). We note that the dependent equations in the linear system described above arise from the two terms in the expansion containing the squares of the disturbance components a_2 and a_3 . Unlike the disturbance components a_2 and a_3 in the subset $\{1,2,5\}$, these components represent different phases of the same wave number $n = 1$. As a consequence, it may be difficult to generate independent statistics corresponding to the terms a_2^2 and a_3^2 . Hence, one of these terms must be eliminated from the

Table 5.

Values of the parameterization functions F_{α} for
the subset {1,2,3} using type C_U data.

	Case 1 [-0.05,0.05]	Case 2 [-0.5,0.5]	Case 3 [-3.0,3.0]	Case 4 [-0.4,-0.1]
F ₄₀	0.58	-0.83	1.74	-2.34
F ₄₁	-1.68×10^{-13}	-4.69×10^{-16}	-1.89×10^{-13}	4.44×10^{-12}
F ₄₂	0.15	0.15	0.21	0.21
F ₄₃	-1.91×10^{-12}	-1.18×10^{-8}	-0.46	-0.46
F ₄₁₁	-1.28×10^{-12}	1.45×10^{-15}	-1.44×10^{-14}	-5.08×10^{-13}
F ₄₁₂	-9.65×10^{-12}	3.99×10^{-8}	9.55×10^{-2}	9.55×10^{-2}
F ₄₁₃	-0.78	-0.78	-0.76	-0.76
F ₄₂₂	-3.5×10^{-14}	-3.20×10^{-13}	4.28×10^{-12}	4.16×10^{-12}
F ₄₂₃	3.35×10^{-13}	1.60×10^{-13}	-3.35×10^{-11}	-9.60×10^{-12}
F ₅₀	-1.22×10^{-11}	-0.77	3.07	-1.65
F ₅₁	-7.30×10^{-13}	-9.02×10^{-15}	2.84×10^{-14}	1.33×10^{-12}
F ₅₂	-3.24×10^{-12}	2.33×10^{-8}	0.46	0.46
F ₅₃	0.15	0.15	0.21	0.21
F ₅₁₁	-2.69×10^{-13}	5.42×10^{-16}	2.33×10^{-15}	-1.19×10^{-13}
F ₅₁₂	0.78	0.78	0.76	0.76
F ₅₁₃	1.71×10^{-11}	-1.80×10^{-7}	9.55×10^{-2}	9.55×10^{-2}
F ₅₂₂	-1.96×10^{-13}	2.08×10^{-13}	-5.36×10^{-13}	1.07×10^{-12}
F ₅₂₃	3.83×10^{-14}	3.52×10^{-13}	4.39×10^{-12}	-3.81×10^{-12}

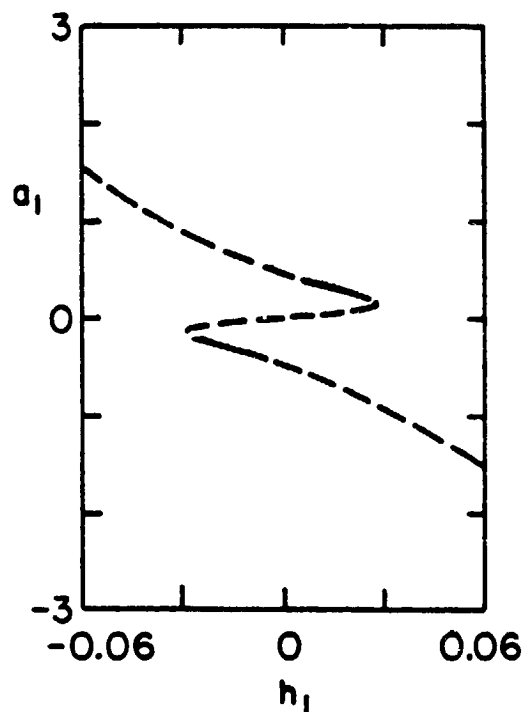


Figure 9 Cross-section of the steady solutions to the parameterized subset $\{1,2,3\}$ for case 1 using the values of F_{α} in Table 5. The Hopf bifurcations that appear on the upper and lower solutions near $h_1 = \pm 0.01$ in the original model have been shifted slightly to approximately $h_1 = \pm 0.005$. However, the sense of the stabilities of the upper and lower branches is reversed compared with the solutions in Fig. 1.

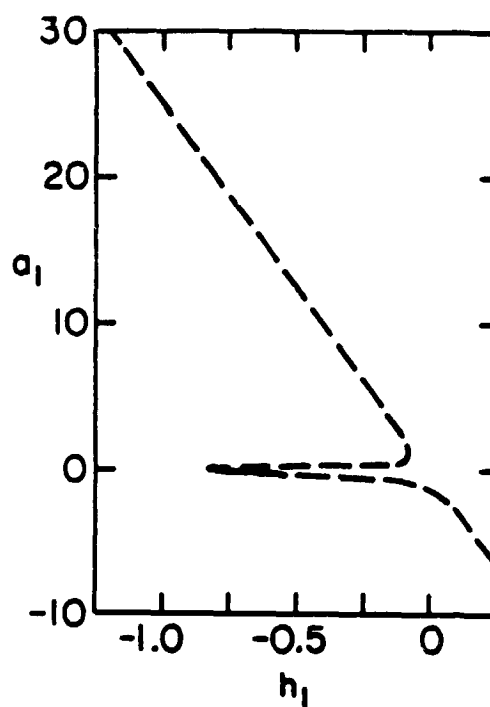


Figure 10 As in Fig. 9 for case 2. Here the upper branch is unstable via a Hopf bifurcation. The Hopf bifurcation that appears on the lower branch in the original solutions near $h_1 = -0.1$ has been shifted to approximately $h_1 = -0.58$ and the sense of the stability of this branch is reversed.

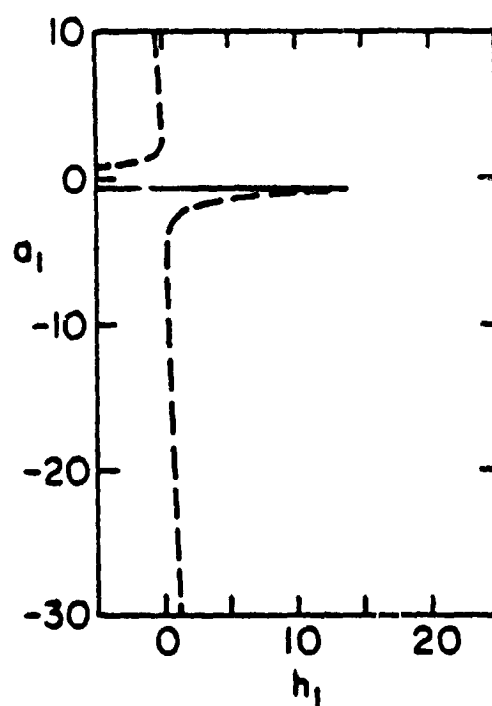


Figure 11 As in Fig. 9 for case 3. In contrast to both Figs. 3 and 7, the lower branch, which tends toward strongly negative values of a_1 , is found to be unstable via a Hopf bifurcation. Note also that the upper solution is stable here.

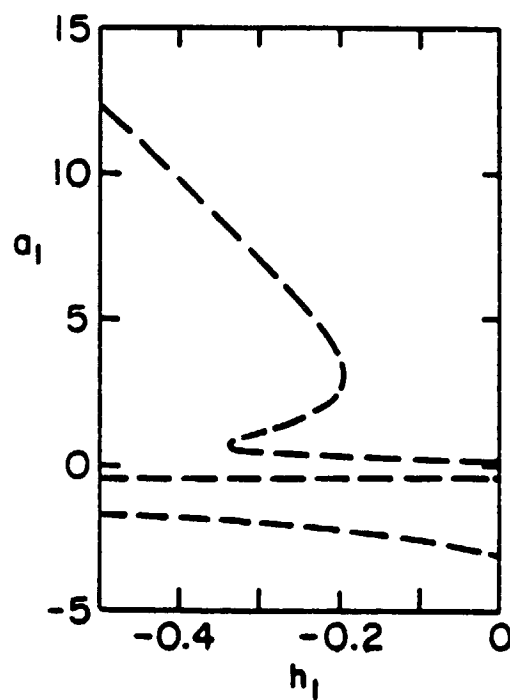


Figure 12 As in Fig. 9 for case 4. Here the upper branch is unstable via a Hopf bifurcation. Although a Hopf bifurcation occurs near $h_1 = -0.2$ on the lower branch of the configuration, it is unnoticeable in the figure because this branch is unstable for all values of h_1 in the cross-section.

parameterized expansions in order to produce a linearly independent system. Similar results occur when the subset $\{1,4,5\}$ is considered. In this case, the disturbance components both represent wave number $n = 3$. Consequently, the elimination from the parameterized expansions of one of the terms containing the squares a_4^2 or a_5^2 is necessary to produce a linearly independent system of equations. In general, we may conclude that the physical differences between the class I and class II truncations have little effect on their abilities to reproduce the steady behavior of a larger system provided that the data coverage is sufficient. However, in cases where data is sparse, the use of a class II truncation, in which a representative of each wave number is retained, may be more likely to produce a sufficiently independent set of correlations in the data.

c. Observable-data sets

The feasibility of using this parameterization scheme operationally depends on its success when unstable solutions are excluded from the data. However, the maximum value of M for which a linearly independent system of equations can be generated may be reduced significantly when the data used to compute the moments includes only stable, or observable, solutions. This corresponds to data types O_U and O_N in Table 1. It can be seen from Figs. 1-4 that a significant loss of information may result concerning the nonlinear characteristics of the cross-sections when the unstable solutions are excluded. It will be shown that, in some cases, this loss of information makes difficult the successful use of the Hermite approximation of the moments, owing to the relatively severe limitation that \bar{h}_1 and σ_1 place on the data coverage. For brevity, we limit the discussion in this section to the subset $\{1,2,5\}$. However, we have verified that all remarks may be generalized to apply to both classes of truncations.

As in the complete-data experiments, $M = 10$ linearly independent equations can be generated to obtain the values of F_{α} for case 1 (Fig. 1), using either data type O_U or O_N . The resulting m significant values of F_{α} are the same as those obtained for the complete-data experiments shown in Table 4. Here, little information concerning the nonlinearity of the cross-section is lost when the unstable solutions are excluded because the stable portions of the upper and lower solutions overlap considerably. Thus, a sufficiently large region of multiple solutions remains to necessitate at least a cubic solution to the cross-section.

We obtain similar results for case 2 shown in Fig. 2. Again, $M = 10$ linearly independent equations can be produced using the type O_U data with the interval $[-0.5, 0.5]$. Using the type O_N data, we obtain ten independent equations by slightly adjusting the value of σ_1 to include several values of h_1 which yield multiple stable solutions within a range of $\pm \sigma_1$ from the mean \bar{h}_1 .

However, the maximum permissible value of M is less than ten for both test cases 3 and 4. For example, if we consider test case 3 and use type O_U data over the interval $[-3.0, 3.0]$, then we obtain three vanishing eigenvalues on the right sides of the linear systems used to compute the values of F_{α} . Thus, we expect that a maximum value of $M = 7$ linearly independent equations can be generated from this data set. Using the expansion (4.7) from the complete-data experiments as a guide, in addition to the analytical results (4.1) and (4.2), we find that a linearly independent system of equations remains when the lines corresponding to the terms F_{n22} , F_{n25} and F_{n55} are eliminated from the system. When this is done, the remaining $M = 7$ equations yield the same m significant values of F_{α} found in Table 4 so that the parameterized expansions are of the form (4.7).

These results are remarkable because it can be seen by locating the stable solutions in Fig. 3 that a significant amount of information is lost when the unstable solutions are excluded. In contrast to case 1, the loss of information makes it impossible to generate $M = 10$ equations. But even this drastic loss of information affects only the termination point M of (3.3), and not the optimum forms of the parameterized spectral components. Thus, we see evidence again that the functional forms of the coefficients in the parameterized expansions are very similar to those of the analytical expressions (4.1) and (4.2), which depend only on the values of the parameters D_n , B_n , V_n and h_n . It may be noted that for case 4, $M = 9$ linearly independent equations can be generated using the type O_N data over the interval $[-0.4, -0.1]$. In this case, the elimination from the system of any of the lines pertaining to the three terms F_{n22} , F_{n25} or F_{n55} yields a solvable system of equations whose solution is analogous to the one shown in Table 4.

The maximum permissible values of M for cases 3 and 4 are reduced further when type O_N data is employed. By slightly adjusting the values of \bar{h}_1 and σ_1 , we obtain $M = 5$ and $M = 7$ linearly independent equations for cases 3 and 4 respectively. For case 3, it is necessary to exclude all but the m significant terms from the original expansion. For case 4, the three terms F_{n22} , F_{n25} and F_{n55} must be eliminated. The resulting optimum expansions have the same forms as before, but the values of the parameterization functions may differ in the first or second decimal places, especially in case 3. As in the complete-data experiments, tests were conducted in which the moments were computed using two hundred normally distributed values of \bar{h}_1 instead of the Hermite approximation. This was done to determine whether the difficulties of the type O_N data experiments were a result of the small number of data values used in the Hermite approximation. However, the results of these

experiments were no more successful, and in some cases, were less successful than those obtained with the Hermite approximation. Thus, with observable data, data coverage requirements appear more readily satisfied by the use of uniformly distributed forcing values. Moreover, the use of normally distributed values of h_1 requires precise choices for the values of \bar{h}_1 and σ_1 when the amount of available data is limited. In contrast, with the random selection of uniformly distributed forcing values, the range of the interval $[h_{1a}, h_{1b}]$ appears to be less critical for satisfying data coverage requirements.

5. Conclusion

A parameterization technique has been developed for general nonlinear hydrodynamical systems via the objective use of data sets that are derived from the solutions to a larger model. The goal of this work is to facilitate an improvement in the efficiency of truncated models of hydrodynamical flows by parameterizing nonlinear interactions involving components outside the truncated set. Toward this end, we have shown that the intricate branching behavior exhibited by the steady solutions to a severely truncated nonlinear spectral model can be represented successfully in a parameterized subset of this system provided we incorporate a knowledge of the general structure of the solution surfaces. The general implication of this result is that the loss of information due to truncation in all hydrodynamical models is to some extent recoverable. Typically, this information concerns the nonlinear interactions between different scales of motion in a flow, and represents the effects of physical processes that may be essential in predicting its long-term behavior.

The general relevance of the results of this study derive from the fact that the basic mathematical structure of the forced, dissipative quasi-geostrophic equation is representative of that in most hydrodynamical systems. Moreover, the recurrence of this structure in the expansions for the parameterized spectral components appears to be fundamental to the preservation of the complete forms of the steady states. Not surprisingly, we found that the optimum form for the parameterized spectral components is that of a truncated power series containing terms analogous to those in the spectral equations themselves. In addition, by examining analytically certain special cases in the original five-component spectral model, we determined that physical effects such as rotation and forcing were controlled by

analogous linear and inhomogeneous terms in both the parameterized expansions and their analytically obtained counterparts. Owing to the tractability of such special cases, it is likely that their exploitation will be a necessary step in understanding many physical and mathematical aspects of future hydrodynamical models, such as the selection of appropriate truncations.

The presence of specific nonlinear terms in the optimum form of the parameterized spectral components appears to be a robust result that is unaffected by the characteristics of a particular data set. The results of this study indicate that both the data distribution and the truncation type may affect the available number of degrees of freedom in computing the values of the coefficients in the parameterized expansions. In the most difficult cases examined here, the maximum amount of freedom is afforded by using uniformly distributed data with a truncation that retains a representative component of each wave number in the original model. However, it should be noted that all possible classes of truncations examined in this study demonstrated approximately equal skill in preserving the steady solutions to the original model. Also, additional tests are required to determine how the values of the coefficients in the expansions for the parameterized components will be affected by the use of data sets that are less well behaved than the ones considered in this work.

The results of this study suggest some important topics for future research. An obvious example is the application of this parameterization technique to significantly larger hydrodynamical models containing many components. Research in this area might be useful in determining the extent to which we can parameterize the nonlinear processes in a model without significantly altering the behavior of the system in its original form. This information could be used as a guideline in attempts to represent the behavior

of a large complicated model via a smaller parameterized subset of the original system.

Another topic of future research is the preservation in the parameterized models of the stabilities of the original steady solutions by accounting for the appearance of Hopf bifurcation points. These are points at which a steady solution loses stability to a temporally periodic one. Procedures must be developed to incorporate information into the parameterization scheme concerning these temporally periodic solutions. Work on this issue has begun in Chapter 6 of Shirer and Wells (1983) concerning the unfolding of spectral models. This work may provide some insight into the development of parameterization techniques in which the parameters necessary to portray temporally periodic behavior may be identified.

Finally, because all hydrodynamical models consist of finite stems of ordinary differential equations, we believe that advances in numerical modeling techniques derived from studies of low-order spectral models will be applicable in a general sense.

Appendix A

Interaction Coefficients of the Fourier Transformation (2.3)

The quantities D_p and C_q represent interaction coefficients for the Jacobian and rotational terms respectively in (2.3), and are defined as

$$D_p = \int_{\underline{x}} \frac{\lambda_n \bar{\psi}_n}{\lambda_n} J(\psi_k, \psi_m) d\underline{x} \quad , \quad \begin{aligned} n &= 1, \dots, N \\ p &= k, m, n \end{aligned}$$

$$C_q = \int_{\underline{x}} \frac{\bar{\psi}_n}{\lambda_n} \frac{\partial \psi_l}{\partial x} d\underline{x} \quad . \quad \begin{aligned} q &= r, m \end{aligned}$$

Appendix B

Definitions of Parameters in the Truncated Steady Spectral Model (2.5)

The parameters of D_n , V_n , B_n and h_n in (2.5) are coefficients that represent the effects of nonlinear interactions, viscosity, rotation and forcing respectively, and are defined as

I. Interaction coefficients: $D_1 = \left[\frac{\lambda_3 - \lambda_4}{\lambda_1} \right] \frac{4k}{15\pi}$,

$$D_2 = \left[\frac{\lambda_1 - \lambda_3}{\lambda_2} \right] \frac{8k}{3\pi} ,$$

$$D_3 = \left[\frac{\lambda_1 - \lambda_5}{\lambda_2} \right] \frac{8k}{15\pi} ,$$

$$D_4 = \left[\frac{\lambda_1 - \lambda_3}{\lambda_4} \right] \frac{8k}{15\pi} ,$$

$$D_5 = \left[\frac{\lambda_1 - \lambda_5}{\lambda_4} \right] \frac{72k}{35\pi} ,$$

II. Viscous terms: $V_n = \nu \lambda_n$, $n = 1, \dots, 5$

III. Rotation terms: $B_n = \frac{gk}{\lambda_n}$, $n = 2, \dots, 5$

IV. Forcing terms: $h_1 = \frac{H_1}{\lambda_1 \pi}$,

$$h_n = \frac{2H_n}{\lambda_n \pi} , \quad n = 2, \dots, 5$$

Acknowledgments

We gratefully acknowledge the contributions of Professor John A. Dutton who suggested the basic techniques from which this work has evolved. We are also indebted to him for his guidance throughout this study. The research reported here was partially funded by the National Science Foundation through Grants ATM79-08354, ATM81-13223 and ATM83-07213, and by the National Aeronautics and Space Administration through Grant NAS8-33794.

References

- Abramowitz, M. and I.A. Stegun, 1964: Handbook of Mathematical Functions with Formulas, Graphs, and Mathematical Tables, National Bureau of Standards Applied Mathematics Series 55, U.S. Dept. of Commerce, 1046 pp.
- Charney, J.G. and J.G. DeVore, 1979: Multiple flow equilibria in the atmosphere and blocking. J. Atmos. Sci., 36, 1205-1216.
- Dutton, J.A., 1976a: The Ceaseless Wind: An Introduction to the Theory of Atmospheric Motion. McGraw-Hill, 579 pp.
- _____, 1976b: The nonlinear quasi-geostrophic equation. Part II: Predictability, recurrence and limit properties of thermally-forced and unforced flows. J. Atmos. Sci., 33, 1431-1453.
- _____, 1982: Fundamental theorems of climate theory-some proved some conjectured. S.I.A.M. Review, 24, 1-33.
- _____, and R. Wells, 1984: Topological Issues in Hydrodynamic Predictability. In Predictability of Fluid Motions, pp. 11-43, AIP Conference Proceedings, No. 106, American Institute of Physics, New York.
- Egger, J., 1978: Dynamics of blocking highs. J. Atmos. Sci., 35, 1788-1801.
- _____, 1979: Stability of blocking in barotropic channel flow. Contrib. Atmos. Phys., 52, 27-43.
- Gelaro, R. 1983: Some topological aspects of parameterization in nonlinear spectral models of quasi-geostrophic flows. M.S. Thesis, The Pennsylvania State University, 228 pp.
- Lorenz, E.N., 1960: Maximum simplification of the dynamic equations. Tellus, 12, 243-254.
- _____, 1963: Deterministic nonperiodic flow. J. Atmos. Sci., 20, 130-141.
- _____, 1980: Attractor sets and quasi-geostrophic equilibrium. J. Atmos. Sci., 37, 1685-1699.
- Marsden, J.E. and M. McCracken, 1976: The Hopf Bifurcation and Its Applications. Applied Mathematical Sciences, 19. Springer-Verlag, 408 pp.
- Minorsky, N., 1962: Nonlinear Oscillations. Van Nostrand, 714 pp.
- Mitchell, K.E. and J.A. Dutton, 1981: Bifurcations from stationary to periodic solutions in a low-order model of forced, dissipative barotropic flow. J. Atmos. Sci., 38, 690-716.

- Phillips, N.A., 1954: Energy transformations and meridional circulations associated with simple baroclinic waves in a two-level, quasi-geostrophic model. Tellus, 6, 273-286.
- Shirer, H.N., 1980: Bifurcation and stability in a model of moist convection in a shearing environment. J. Atmos. Sci., 37, 1586-1602.
- _____, and J.A. Dutton, 1979: The branching hierarchy of multiple solutions in a model of moist convection. J. Atmos. Sci., 36, 1705-1721.
- _____, and R. Wells, 1982: Improving spectral models by unfolding their singularities. J. Atmos. Sci., 39, 610-621.
- _____, and R. Wells, 1983: Mathematical Structure of the Singularities at the Transitions between Steady States in Hydrodynamic Systems. Lecture Notes in Physics, 185, Springer-Verlag, 276 pp.
- Vicroy, J.G. and J.A. Dutton, 1979: Bifurcation and catastrophe in a simple, forced, dissipative quasi-geostrophic flow. J. Atmos. Sci., 36, 42-52.
- Wiin-Nielsen, A., 1979: Steady states and stability properties of a low-order barotropic system with forcing and dissipation. Tellus, 31, 375-386.

N86-11753

CHAPTER 5

A Numerical Study of Global Axisymmetric States and
Their Stability to Quasi-Geostrophic Disturbances

by

Harry W. Henderson
and
John A. Dutton

Department of Meteorology
The Pennsylvania State University
University Park, PA 16802

PRECEDING PAGE BLANK NOT FILMED

1. Introduction

Recently, Miller and Gall (1983a) presented the results of a numerical investigation of the axisymmetric states for an incompressible fluid in a spherical shell. The work represented an extension of the work by Williams (1967) for the cylindrical annulus. In part, the work reported by Miller and Gall was motivated by a desire to model the base states that may be observed in the NASA Spacelab experiment AGCE (Atmospheric General Circulation Experiment). This experiment will study the response of an incompressible fluid, confined to a hemispherical shell, to imposed external temperature differences. The fluid will have a dielectric property such that an electric field across the shell will simulate the effect of gravity. More information on this experiment may be found in Miller and Gall (1983a), Fowles and Fichtl (1977), and the NASA Contractor Report NAS8-3198 (Hart 1984).

From the report by Hart (1984), it appears that the experiment may not be suitable for a study of fluid response to baroclinic effects. However, the studies of deep, buoyant convection remain appropriate for the experiment.

The numerical results of Miller and Gall (1983a) and Hart (1984) give some indication of the potential problems that may arise when the parameters of the experiment are chosen to be representative of large-scale flows. The velocities in the meridional plane are mostly restricted to boundary layers near the walls of the shell. The zonal flow reaches the largest values at high latitudes, and shows a rather complicated structure. These results raise some questions as to the usefulness of the AGCE experiment as a model of atmospheric flows. It is also difficult to point to the specific deficiencies that lead to the results.

In addition, Hart examined the axisymmetric states for stability to quasi-geostrophic disturbances. He concluded that the geometry of the cell

was not adequate to model flows characterized by sufficiently small Ekman number for baroclinic instability studies.

While these studies seem to preclude the use of the GFFC (Geophysical Fluid Flow Cell) for large-scale baroclinic studies, they at least do suggest something of the nature of the axisymmetric flow of the atmosphere. There are some striking similarities between these results and the results that were obtained in the dissertation study I completed (Henderson 1982 - designated by H). The numerical method used in H was that of a spectral approach, and the fluid was taken to be compressible. The forcing was chosen to be internal heating, and was based upon observational studies of large-scale, atmospheric heating patterns. In spite of these differences, the flow in the meridional plane was very similar to the results of Miller and Gall (1983a). Furthermore, when the axisymmetric flow was tested for stability to quasi-geostrophic disturbances, the transition from lower symmetric Hadley to Rossby regimes was found, but no upper symmetric regime could be found. This result is consistent with the speculation presented near the end of the Miller and Gall (1983a) paper. Since the findings of this study are in agreement with and extend the results of these other studies (although the modeling techniques and physical properties of the fluid are different) a description of the results in H will be of interest to those investigators studying large-scale axisymmetric flows.

Lorenz (1953) was apparently the first to point out that a heated, rotating fluid possesses an axisymmetric solution which is capable of achieving the necessary fluxes of heat and momentum between the appropriate sources and sinks. For certain ranges of heating and rotation rates, the axisymmetric solution is unstable to asymmetric disturbances. A circulation pattern characterized by horizontal waves appears, and the axisymmetric

solution is never observed in laboratory experiments. In order to determine the values of the heating and rotation parameters that will show the wave regime for the AGCE experiment, it is thus necessary to calculate the base states first, and to then test them for stability to asymmetric disturbances. Miller and Gall (1983b) do perform such a stability test, but for the cylindrical annulus. A paper describing the results for a sphere has been promised, but has not been published as of June 1984.

The direction of this study will also be two-fold. In the next section, a mathematical model of compressible, axisymmetric flow will be presented. The physical basis of the model and some of the assumptions made will be explained. The last part of the section will show the results for a few selected cases of steady, axisymmetric flow. The third section will use the results of the axisymmetric calculations for a stability study. The axisymmetric base states will be tested for stability to quasi-geostrophic disturbances. The stability tests are by no means exhaustive - they were made (at the time) in order to show the practicality of doing both base state and stability calculations by a spectral approach. Perhaps more suitable parameters could have been chosen here, but the results demonstrate that the transition curve to Rossby flows may be found numerically. The final section is a discussion of the results and some of the limitations that were encountered.

2. Axisymmetric Model

The system of equations developed in this section will model the steady solutions to the atmospheric global convection problem. The model was presented by Dutton (1982) in order to establish mathematical existence and uniqueness of the Hadley response of the atmosphere to axisymmetric heating fields and viscosity. The equations will be presented here because of the different coordinate system used in this study.

The last half of this section is a discussion of the numerical results from the model. Figures from two cases are shown, and other cases are compared qualitatively to the presented cases. These results are also compared to those of other investigators.

a. Axisymmetric Model Equations

The meteorological equations are most naturally set in spherical coordinates, but the spherical framework contains terms that are not essential to a mathematical model of global convection. Consequently, it was decided that a rotating cylindrical system would be simpler and would retain the necessary terms for a suitable model. Figure 1 shows a thin disk rotating about a vertical axis. As the disk rotates, it sweeps out the volume of a sphere. The axisymmetric motion over a rotating sphere and the motion over the rotating disk would be similar except for the horizontal convergence due to the converging meridians in the spherical case. The terms that account for horizontal convergence are generally several orders of magnitude smaller than the most important terms. Thus a geometry that does not contain such terms should be able to model the problem of interest here.

Since the problem to be studied is essentially one of convection, it is also possible to linearize the pressure gradient (Boussinesq approximation) by neglecting small density changes from a known reference state. It is also

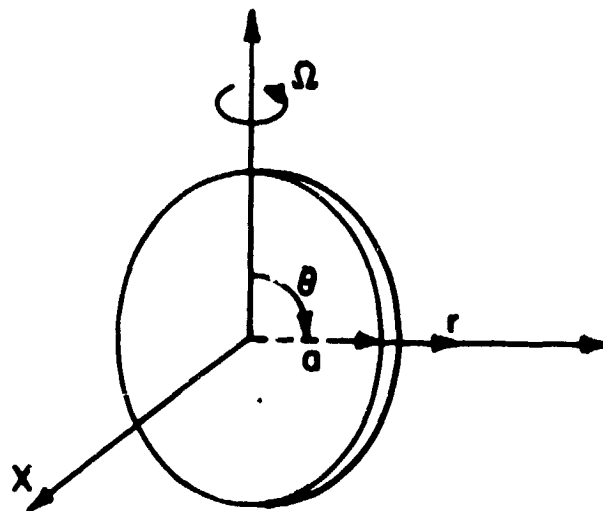


Figure 1. Model geometry and orientation of axes. The axes are rotating with the thin disk.

appropriate to neglect such small departures in the continuity equation (deep convection approximation). In order to maintain energetic consistency, the first law of thermodynamics is replaced by one governing the evolution of potential temperature perturbations. The result is a model adequate for the study of deep, global convection. The five, steady equations are

$$\frac{v}{a} \frac{\partial u}{\partial \theta} + w \frac{\partial u}{\partial z} + 2\Omega \cos \theta v = F_x(u) \quad (2.1)$$

$$\frac{v}{a} \frac{\partial v}{\partial \theta} + w \frac{\partial v}{\partial z} - 2\Omega \cos \theta u = -\frac{1}{a} \frac{\partial \eta}{\partial \theta} + F_x(v) \quad (2.2)$$

$$\frac{v}{a} \frac{\partial w}{\partial \theta} + w \frac{\partial w}{\partial z} = -\frac{\partial \eta}{\partial z} + g\tau K + F_x(w) \quad (2.3)$$

$$\frac{v}{a} \frac{\partial \tau}{\partial \theta} + w \frac{\partial \tau}{\partial z} + \frac{w}{H_0 K} = \frac{Q}{c_p \rho_0 T_0 K} + \frac{F_x(\tau)}{Pr} \quad (2.4)$$

$$\frac{1}{a} \frac{\partial}{\partial \theta} (\rho_0 v) + \frac{\partial}{\partial z} (\rho_0 w) = 0 \quad (2.5)$$

where θ is co-latitude and v is positive southward, u is the zonal velocity, w the vertical velocity, a the radius of the earth, Ω the angular rotation of the earth, η the product of the Exner function perturbation and the reference state potential temperature, $F_x(\)$ is an unspecified form of friction, g is gravity, Pr the Prandtl number ($Pr = \nu/k$), c_p the specific heat of air at constant pressure, T is temperature, ρ is density, H_0 a scale height of potential temperature ($1/H_0 = 1/\theta \partial \theta / \partial z$), z the vertical direction, and τ a scaled potential temperature perturbation ($\tau = \theta' / K \theta_0$ where $1/K = (gH_0/Pr)^{1/2}$).

These five equations may be simplified further, because the two-dimensional continuity equation permits the definition of a meridional stream-function. It may be verified by substitution that $w = -1/a \partial \psi / \partial \theta$ and

$v = 1/\rho_0 \partial(\rho_0 \psi)/\partial z$ satisfy the continuity equation. The vorticity is, approximately, $\zeta = \partial v/\partial z - 1/a \partial w/\partial \theta$. In terms of the streamfunction, the vorticity becomes $\zeta = \nabla^2 \psi - 1/H \partial \psi/\partial z$ where H is the scale height for density. The Laplacian is

$$\nabla^2(\) = \frac{1}{a^2} \frac{\partial^2(\)}{\partial \theta^2} + \frac{\partial^2(\)}{\partial w^2} \quad (2.6)$$

A meridional vorticity equation may now be formed by differentiating the meridional momentum equation with respect to z and subtracting it from the vertical momentum equation differentiated with respect to co-latitude. The original five equations are reduced to just three, along with the definitions of v and w in terms of the streamfunction. These three equations are

$$\frac{v}{a} \frac{\partial u}{\partial \theta} + w \frac{\partial u}{\partial z} + 2\Omega \cos \theta \ v = v \alpha_0 \nabla \cdot \rho_0 \nabla u \quad (2.7)$$

$$\frac{v}{a} \frac{\partial \zeta}{\partial \theta} + w \frac{\partial \zeta}{\partial z} + \frac{\zeta w}{H} - 2\Omega \cos \theta \ \frac{\partial u}{\partial z} = - \left(g \frac{Pr}{H_\theta}\right)^{1/2} \frac{1}{a} \frac{\partial \tau}{\partial \theta} + v \alpha_0 \nabla \cdot \rho_0 \nabla \zeta \quad (2.8)$$

$$\left(\frac{v}{a} \frac{\partial \tau}{\partial \theta} + w \frac{\partial \tau}{\partial z}\right) Pr + \left(g \frac{Pr}{H_\theta}\right)^{1/2} w = \left(g Pr H_\theta\right)^{1/2} \frac{Q}{c_p \rho_0 T_0} + v \alpha_0 \nabla \cdot \rho_0 \nabla \tau \quad (2.9)$$

The form of friction has been specified here.

These equations still contain more information than is needed to model the axisymmetric flow. The usual method used to determine the important terms of the model is scale analysis. In order to supply estimates of the various terms, some knowledge of the answer is needed. This approach has been successful in dealing with quasi-geostrophic flow (and other types), but has been less successful with axisymmetric flows. In light of these problems, this study first employed the full set of three equations 2.7 - 2.9. The set

was solved at a truncation level that was quite severe. These results allowed a comparison of the various terms in the three equations. It was found that the three nonlinear terms in the vorticity equation were several orders of magnitude smaller than the remaining terms. This meant that the zonal flow was nearly in geostrophic balance, except for the effects of dissipation at the upper and lower boundaries. The results also showed that the meridional transport of temperature in the first law was smaller than the vertical transports, in keeping with Hart's (1984) estimates. In addition, the meridional transport of zonal momentum in the first momentum equation was generally smaller (by about an order of magnitude than any of the other terms). However, these two meridional transport terms were retained in this study, as their importance near the boundaries could be greater. The final set of equations becomes

$$\frac{v}{a} \frac{\partial u}{\partial \theta} + w \frac{\partial u}{\partial z} + 2\Omega \cos \theta v = \nu_0 \nabla^2 u + \rho_0 \nabla u \quad (2.10)$$

$$\left(\frac{v}{a} \frac{\partial \tau}{\partial \theta} + w \frac{\partial \tau}{\partial z} \right) + (gPr/H_0)^{1/2} w = q + \nu_0 \nabla^2 \tau + \rho_0 \nabla \tau \quad (2.11)$$

$$(gPr/H_0)^{1/2} \frac{1}{a} \frac{\partial \tau}{\partial \theta} - 2\Omega \cos \theta \frac{\partial u}{\partial z} = \nu_0 \nabla^2 \zeta + \rho_0 \nabla \zeta \quad (2.12)$$

It may be of interest that the reduced set of equations formed by deleting the meridional transport terms and the dissipation of vorticity permits the formulation of a single equation in terms of the potential temperature perturbation. This can be done, provided that the static stability meets certain requirements. Perhaps the resulting equation could be of use in certain analytic studies of axisymmetric flow.

The distribution of the atmospheric variables over a sphere corresponds to that of even modes. Specifically, variables such as the zonal wind,

temperatures, and isobaric heights are nearly symmetric about the equator. The meridional wind component is approximately antisymmetric. In terms of the variables used in this study, consistency is achieved if the zonal wind, temperature perturbation, and heating function are latitudinally symmetric while the streamfunction is latitudinally antisymmetric. With these relationships in mind, an inspection of the three equations of the axisymmetric model shows that the terms in the zonal wind equation and the first law of thermodynamics possess even symmetry about the equator, while the meridional vorticity equation has antisymmetry about the equator. The total number of modes is about half that of the general case.

The symmetry conditions for the three variables is as follows

$$u \sim \sum_{n \text{ odd}}^{N+1} \bar{u}_n(z) \sin(n\theta) \quad (2.13)$$

$$\psi \sim \sum_{n \text{ even}}^N \bar{\psi}_n(z) \sin(n\theta) \quad (2.14)$$

$$\tau \sim \sum_{n \text{ even}}^N \bar{\tau}_n(z) \cos(n\theta) \quad (2.15)$$

It should be noted that the expansions for u and τ (both symmetric about the equator) differ from each other. This is due to the additional imposed boundary conditions at the pole - u must vanish at the poles, while τ generally does not. ψ must also vanish at the poles - this means that ψ vanishes at all the boundaries along with the first derivative at the upper and lower boundaries.

The variables were expanded in a series of orthogonal functions that were most suitable to reduce the complexity of the dissipation terms. For example, the zonal wind is expanded in terms of the functions that are the solution to the problem

$$\alpha_0 \nabla \cdot \rho_0 \nabla u = -\lambda u \quad (2.16)$$

The boundary condition was taken to be the no-slip condition, that is $u = 0$ at $z = 0, z_T$. This effectively places a lid at the upper surface. The lid allows an expansion of discrete functions for all three variables, but apparently results in some unrealistic solutions for some parameter values. Some of the consequences of the lid are discussed later.

As a result of solving the eigenvalue problem for u , the following expansion is obtained

$$u = \sum_{n \text{ odd}}^{N+1} \sum_{m=1}^M u_n^m \sin(n\theta) \sin\left(\frac{\pi m z}{z_T}\right) e^{z/z_T} \quad (2.17)$$

The vertical modes are simply a sine expansion on a half interval, with the size of the function increasing upward due to the exponential weighting.

The potential temperature perturbation is expanded in terms of a similar equation

$$\alpha_0 \nabla \cdot \rho_0 \nabla \tau = -\lambda \tau \quad (2.18)$$

But the boundary conditions at the lower and upper surfaces are different from the zonal wind case. For the temperatures, the first derivative is taken to be zero at these surfaces - in effect, an assumption that the boundaries are insulated. The resulting expansion contains two parts - one of which possesses no vertical variation. The expansion is

$$\tau = \sum_{n \text{ even}}^N \tau_n^0 \cos(n\theta) + \sum_{n \text{ even}}^N \sum_{m=1}^M \tau_n^m \cos(n\theta) \left\{ \sin\left(\frac{\pi m z}{z_T}\right) - \pi m \cos\left(\frac{\pi m z}{z_T}\right) \right\} e^{z/z_T} \quad (2.19)$$

The vertical eigenfunctions are trigonometric, have the first derivative zero

at the upper and lower boundaries, and increase upward in size because of the exponential weighting.

The streamfunction is expanded in terms of the solution to the equation

$$\alpha_0 \nabla \cdot \rho_0 \nabla (\alpha_0 \nabla \cdot \rho_0 \nabla \psi) = \lambda^2 \psi \quad (2.20)$$

This equation differs from the defining equations for u and τ in that it is fourth order, and the right hand side contains λ^2 instead of $-\lambda$. The latter condition is simply taken for convenience.

A fourth order problem requires two additional boundary conditions beyond the previous second order problems. However, these additional conditions follow quite naturally from the no-slip condition used previously. The velocity components are related to the stream function by the equations $v = \partial \psi / \partial z = \psi / H$ and $w = -1/a \partial \psi / \partial \theta$. The condition of no-slip requires that $v = w = 0$ at the upper and lower surfaces. It is seen by inspection that the conditions $\partial \psi / \partial z = 0$ and $\psi = 0$ fulfill these requirements.

The solution to this type of eigenvalue problem has been presented by Harris and Reid (1958). The present treatment differs from their problem in that there is a vertical weighting by density here, and a resulting shift in the position of the eigenvalues. Hence, the eigenvalues were calculated numerically and stored.

The solution to the problem (called Chandra functions in the engineering literature) behave like trigonometric functions in that they may be separated into even and odd parts. These parts will be designed by

$$C_n^m = \frac{\cosh(a_n^{*m} z^*)}{\cosh(a_n^{*m}/2)} - \frac{\cos(b_n^{*m} z^*)}{\cos(b_n^{*m}/2)} \quad (2.21)$$

and

$$S_n^m = \frac{\sinh(\hat{a}_n^m z^*)}{\sinh(\hat{a}_n^m/2)} - \frac{\sin(\hat{b}_n^m z^*)}{\sin(\hat{b}_n^m/2)} \quad (2.22)$$

where

$$z^* = \frac{z}{Z_T} - \frac{1}{2} \quad (-1/2 \leq z^* \leq 1/2) \quad (2.23)$$

and the scaling factors are

$$a_n^{*m} = (\lambda_n^{*m} Z_T^2 + n^2 Z_T^2 / a^2 + 1)^{1/2} \quad (2.24)$$

$$b_n^{*m} = (\lambda_n^{*m} Z_T^2 - n^2 Z_T^2 / a^2 - 1)^{1/2} \quad (2.25)$$

$$\hat{a}_n^m = (\hat{\lambda}_n^m Z_T^2 + n^2 Z_T^2 / a^2 + 1)^{1/2} \quad (2.26)$$

$$\hat{b}_n^m = (\hat{\lambda}_n^m Z_T^2 - n^2 Z_T^2 / a^2 - 1)^{1/2} \quad (2.27)$$

The eigenvalues are denoted by the λ 's. These results allow the stream-function to be expanded according to

$$\psi = \sum_{n \text{ even}}^N \sum_{m=1}^M \sin(n\theta) \{ \psi_n^{*m} C_n^m + \hat{\psi}_n^m S_n^m \} e^{z/Z_T} \quad (2.28)$$

where the even and odd coefficients have been taken to be ψ_n^{*m} and $\hat{\psi}_n^m$ respectively.

Because these functions are not routinely found in the meteorological literature, graphs showing their behavior against z are presented in

Figures 2a and 2b. Once again the size of the eigenfunctions increases with height due to the effects of stratification.

The spectral equations are obtained by substituting the expansions for each variable into the three equations 2.10 - 2.12. Each equation is multiplied by a particular eigenfunction of the dissipation term, and the result is integrated over the meridional domain. The details of the procedure are excessive, and will be omitted here. The resulting equations are also quite lengthy, and therefore have been placed in the Appendix.

The treatment of the heating term is based upon work of Johnson and Dutton - a figure of which may be found on page 407 of Dutton (1976). It was found that the heating field may be adequately expanded in terms of the potential temperature eigenfunctions. Higher levels of truncation reproduce the original picture quite closely, but it is the highly truncated ones that were of interest in this study. Figure 3 shows the field that is obtained from a truncation point of $m = 1$ and $n = 2$. The heating is found at low levels in the tropics, while the cooling is generally distributed throughout the polar regions. It is this picture of idealized heating that was used in the numerical studies that follow.

b. Axisymmetric Results

Because of the nonlinear nature of the axisymmetric model, the task of finding steady solutions to the model was attacked numerically. Several algorithms were tested, but most were unable to determine a solution unless good initial guesses were supplied. An algorithm that was less sensitive to the initial guess was found in the International Mathematical and Statistical Library of Subprograms (IMSL). The routine, called ZXSSQ, used the Marquardt-Levenberg technique to minimize the sum of squares for the more general case of a nonlinear least squares problem. The routine would also seek the

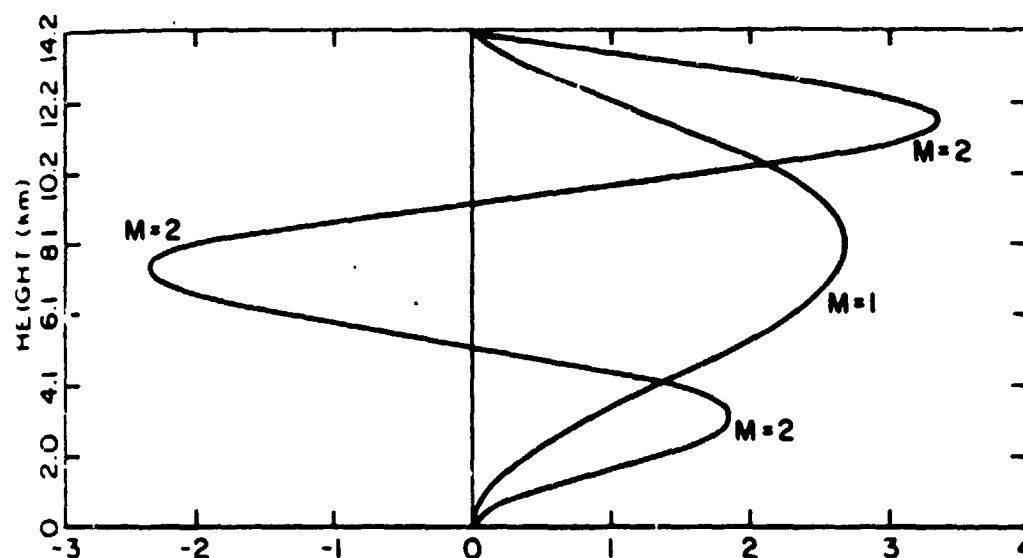


Figure 2a. Plots of the first two even modes of the vertical part of the streamfunction expansion. The modes are unnormalized.

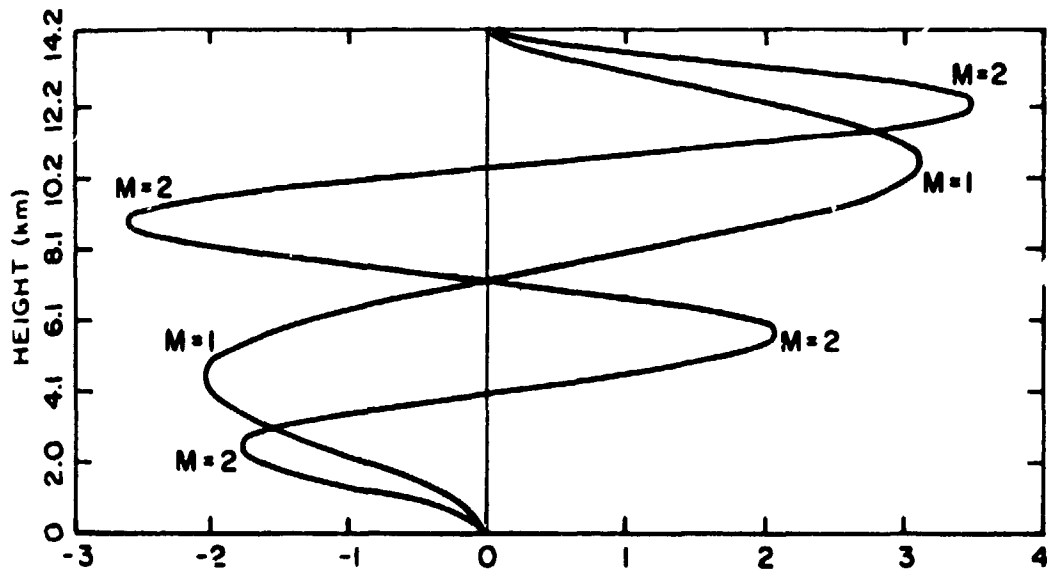


Figure 2b. Plots of the first two odd modes of the vertical part of the streamfunction expansion. The modes are unnormalized.

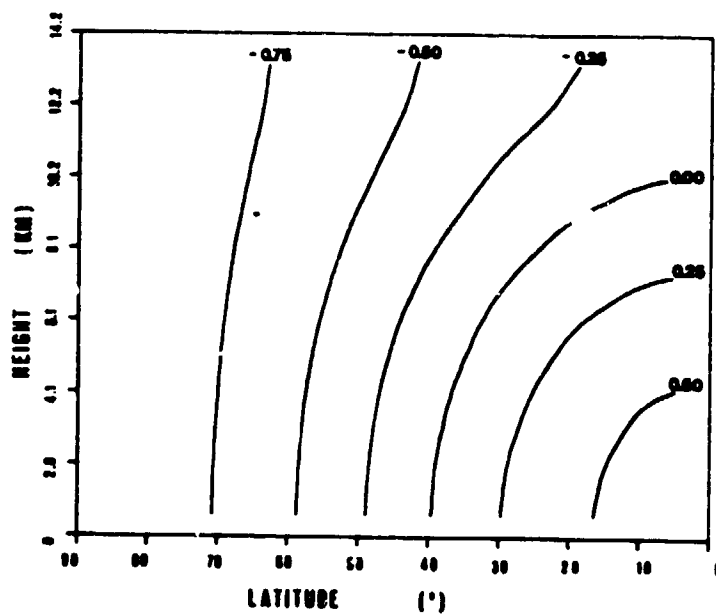


Figure 3. The spectral expansion of the net heating field at a truncation point of $m=1$, $n=2$. The units are $^{\circ}\text{C day}^{-1}$.

solution of an exactly specified nonlinear system if the tolerance of the residual sum of squares were set to a very small number. The routine proved to be quite satisfactory in practice. Solutions were always found as long as the parameters of the model were within a factor of five of values normally associated with the atmosphere. For parameter values outside this range, the routine would usually not be able to arrive at a solution within a reasonable amount of time. It was not determined if more time were needed, or an improved initial guess were required. Since the model was scaled for conditions not unlike those observed for the atmosphere, the model solutions associated with extreme parameter values may be of little value. The reader is referred to the IMSL documentation for further information and references regarding the Marquardt-Levenberg technique.

In order to demonstrate the nature of the solutions that were found, figures from two of the cases were selected for discussion. All of the cases of this study used the idealized heating pattern mentioned earlier, and contained 23 coefficients at a truncation point of wavenumber 2 in the vertical and wavenumber 5 in the horizontal. Also, the Prandtl number was set at a value of 4.

The first case used the unscaled heating values from the idealized pattern. This meant that the differential heating between pole and equator was about 1.4°K . The viscosity was taken to be $37 \text{ m}^2\text{sec}^{-1}$, which may be a little low for the scales under consideration, but is difficult to specify more exactly in any case.

The zonal wind speed is found to be about 12 m sec^{-1} at 50°N and 8 km (Figure 4). There is no indication of any strong boundary layer effects at any boundary. This is due in part to the restricted resolution of the model, although tests with a truncation point that included one more wave in both the

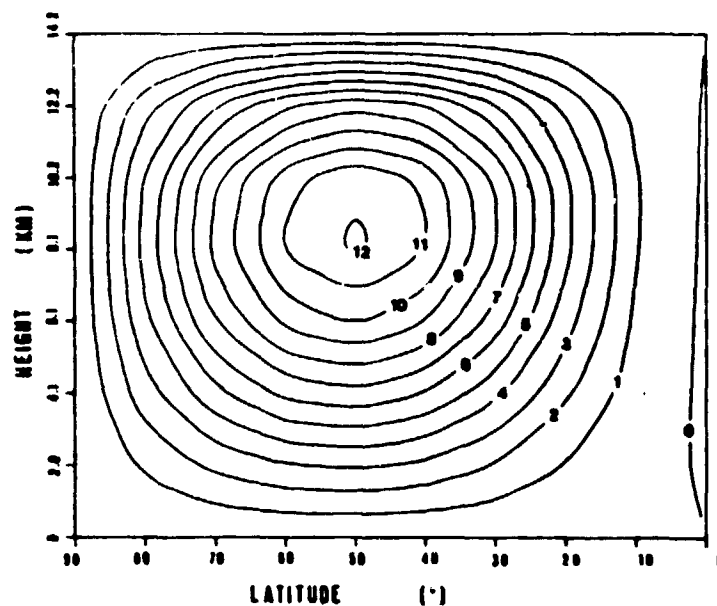


Figure 4. Case 2. The zonal wind field from a model with 23 coefficients and parameter values of $Pr=4$, $Q=H$, and $\nu=37 \text{ m}^2 \text{ sec}^{-1}$. The contour interval is 1.0 sec^{-1} .

vertical and the horizontal showed no significant differences from these pictures. The temperature field, shown in Figure 5, shows the correct slope for approximate geostrophic balance. There is a reversal of the gradient above 10 km. A check of the static stability showed values that were much higher than in the observed atmosphere. This may be inferred by inspection, since the isentropes are rather evenly spaced throughout the domain. In the atmosphere, the isentropes are spaced further apart in the troposphere and packed more closely in the stratosphere.

The picture of the meridional streamfunction, shown in Figure 6, is most interesting. The pattern is one of a two-cell structure, with the position of the upper cell being a little closer to the pole. The basic cell is a thermally direct one, but there is some "leakage" of the return flow at middle levels. The northward flow (Figure 7) reaches a maximum at two levels, with the flow in the top level moving at 2.5 m sec^{-1} and in the lower level at 1.5 m sec^{-1} . The return flow also occurred at two levels, with the stronger flow near the surface. Here the flow reaches 1.5 m sec^{-1} , while in the upper cell the maximum speed was 1.0 m sec^{-1} . The vertical motion field, shown in Figure 8, also reflected the two-cell structure. The maximum vertical velocities were about 0.15 cm sec^{-1} .

A number of experiments were run with different values of the parameters. It was found that the most important parameter in determining the meridional cell structure was the eddy viscosity. The two-cell structure appeared for values of ν below $100 \text{ m}^2\text{sec}^{-1}$. For larger values, the meridional flow was in the form of a single, direct Hadley cell. An example of the streamfunction at the same parameter values for the preceding example, except that the value of ν is taken to be $148 \text{ m}^2\text{sec}^{-1}$, is shown in Figure 9. It is seen that the circulation is one of a direct cell, centered at 40°N and 6 km. It was also

OF POOR

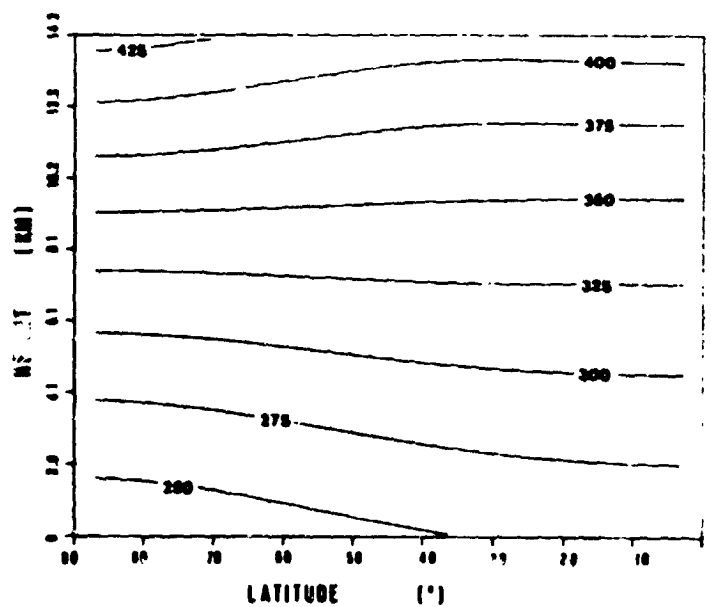


Figure 5. Case 2. The potential temperature field from a model with 23 coefficients and parameter values of $Pr=4$, $\chi=H$, and $\nu=37 \text{ m}^2 \text{ sec}^{-1}$. The contour interval is 25°K .

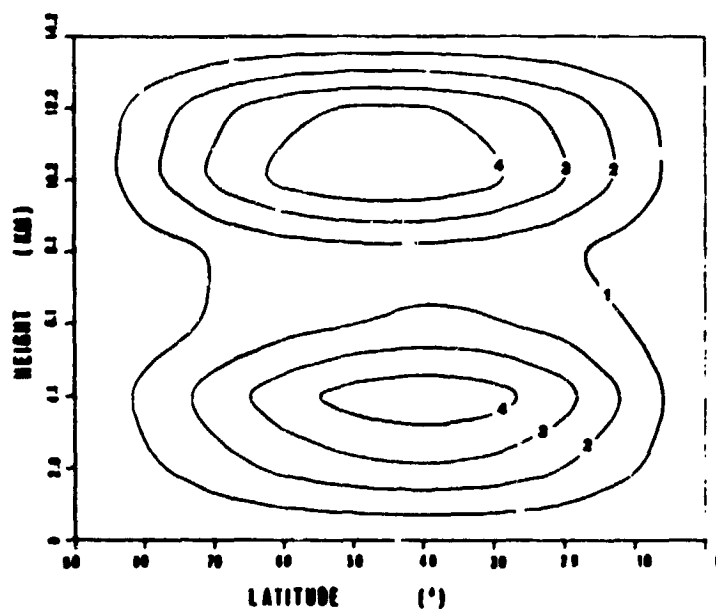


Figure 6. Case 2. The meridional streamfunction field from a model with 23 coefficients and parameter values of $Pr=4$, $Q=H$, and $\nu=37 \text{ m}^2 \text{ sec}^{-1}$. The contour interval is $1000 \text{ m}^2 \text{ sec}^{-1}$.

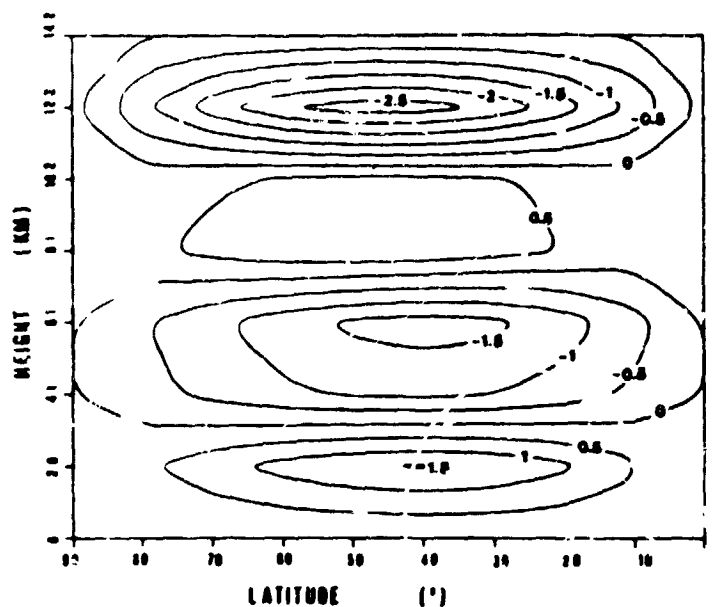


Figure 7. Case 2. The meridional wind field from a model with 23 coefficients and parameter values of $Pr=4$, σ_H , and $\nu=37 \text{ m}^2 \text{ sec}^{-1}$. The contour interval is 0.5 m sec^{-1} .

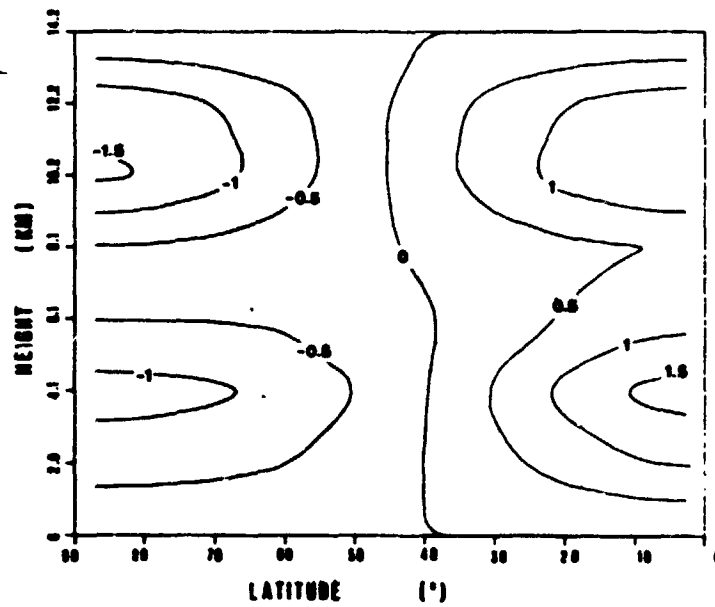


Figure 8. Case 2. The vertical motion field from a model with 23 coefficients and parameter values of $Pr=4$, $Q=H$, and $\nu=37 \text{ m}^2 \text{ sec}^{-1}$. The contour interval is 0.5 mm sec^{-1} .

C-3

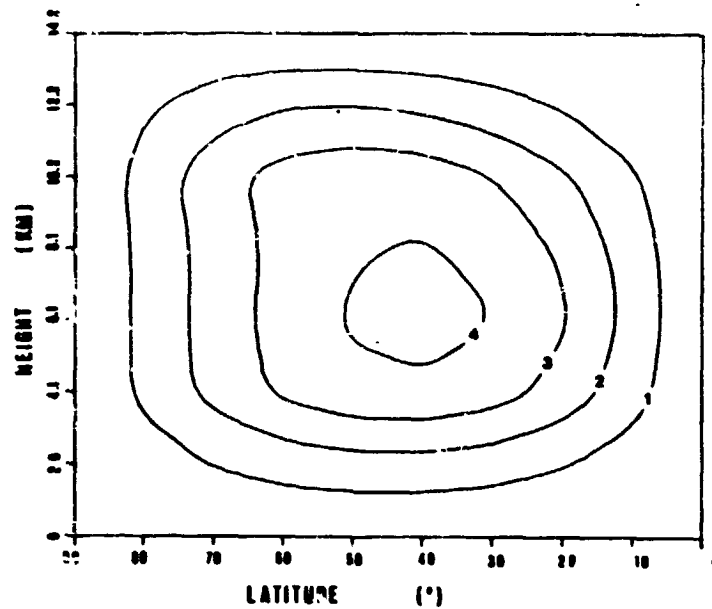


Figure 9. Case 1. The meridional streamfunction field from a model with 23 coefficients and parameter values of $Pr=4$, $Q=H$, and $\nu=148 \text{ m}^2 \text{ sec}^{-1}$. The contour interval is $1000 \text{ m}^2 \text{ sec}^{-1}$.

found that a reduction in the rotation rate would also favor a single cell. For a viscosity value of $100 \text{ m}^2\text{sec}^{-1}$, it was necessary to lower the rotation rate to 50 percent (and less) of the rotation rate of the earth in order to produce the single cell.

It might be assumed that the meridional circulation was splitting to a multi-celled structure as the flow became more energetic. While this study could not absolutely deny the possibility that an even greater number of cells might appear, the results of other cases with even lower values of viscosity suggested that there was actually a simple shift of the center of the Hadley cell to lower levels of the domain. There was little evidence to suggest that the flow would proceed to an even higher number of cells as the viscosity was decreased further.

There were several runs made with different values of the heating field. All of the runs used the same idealized pattern, but the entire field was multiplied by a scaling factor to achieve different heating gradients. The results were quite consistent in that the response of the flow was nearly linear to the heating field. That is, if the heating field were scaled larger by a factor of two, the zonal wind maximum and the maximum streamfunction value also increased by a factor of two. Raising or lowering the heating values did not result in important changes in the overall patterns of the dependent variables.

There were also two experiments made with different choices of resolution. Neither experiment suggested that there would be strong flow in very narrow boundary layers as the resolution was increased, but then again, the addition of only 1 or 2 wavenumbers in either the vertical or horizontal direction may have been inadequate to answer this question. A check of the energy by wavenumber showed that the spectrum dropped sharply with increasing

wavenumber - but it was only possible to check this out to wavenumber 8 in the horizontal. Perhaps a more detailed heating pattern would force a more complicated fluid response.

Also shown is a case where the various parameters in the model have been set to what is believed to be most nearly the proper atmospheric values. The resolution has been increased by one additional wavenumber in each direction (for a total of 46 coefficients) and the differential heating has been increased by a factor of 2 (for a pole to equator difference of 2.8°K). The rotation rate is that of the earth. This picture, Figure 10, shows that the two-cell structure is dominant, with the upper cell displaced toward the pole. The picture is quite similar to the results of Miller and Gall (1983a) as shown in their Figure 5(A). This similarity has occurred in spite of different numerical procedures, large differences in model resolution, different heating configurations, and fluid compressibility - to name the more important differences. However, in contrast to the results of Miller and Gall (1983a), the zonal wind pattern was found to be quite smooth - it is not shown because it differs little from the pattern in Figure 4. The maximum value is 15 m sec^{-1} and is found at 45°N rather than at 50°N as in Figure 4.

The axisymmetric flow described so far is interesting in its own right. But the logical next step is to seek some answers as to the stability of the flow. Specifically, at what parameter values will small asymmetric disturbances begin to grow?

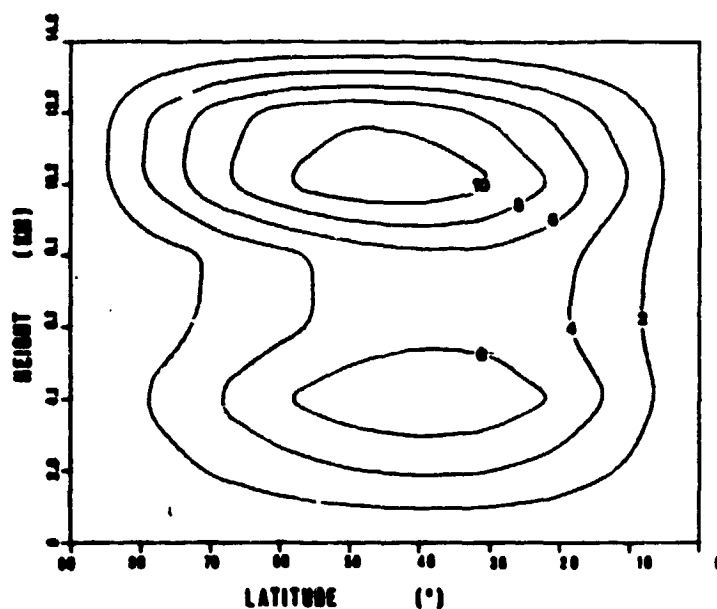


Figure 10. Case 7. The meridional streamfunction field from a model with 46 coefficients and parameter values of $Pr=4$, $Q=2H$, and $\nu=100 \text{ m}^2 \text{ sec}^{-1}$. The rotation rate has been increased to that of the earth. The contour interval is $2000 \text{ m}^2 \text{ sec}^{-1}$.

3. Asymmetric, Quasi-Geostrophic Model

The axisymmetric equations cannot be easily extended to three dimensions for a stability study. In order to do so, it would be necessary to include the pressure perturbation that was eliminated in the axisymmetric formulation. Also, the simplifications obtained by using a meridional streamfunction in the axisymmetric model cannot be extended to the three dimensional case. So, instead of studying the full three-dimensional problem, it was decided to study the stability of the axisymmetric flow to quasi-geostrophic disturbances. There is just one equation governing the evolution of quasi-geostrophic disturbances, and these disturbances are the most apparent of the transient synoptic features.

a. Quasi-Geostrophic Model Equations

A quasi-geostrophic model may be developed from the original global model that was presented in Section 2a. Of course, the time derivative terms must be retained here. The quasi-geostrophic scaling assumptions (Dutton 1976a) which are used here are: 1) a vertical scale height of about 8 km, 2) horizontal scales of about 1000 km (quarter wavelength), 3) time scale of one day (quarter period), 4) Rossby number of about $1/10$, and 5) a Richardson number of about 30. It will be noted here that the friction term will be retained in the model, in spite of the fact that the scaling results would indicate that its magnitude is small and should be omitted. The term is kept because it is desired to study the forced disturbances and the friction term is the dissipation mechanism. If the horizontal velocities are assumed to be representable through the streamfunction ψ , then the velocities and vorticity may be written $u = 1/a \partial\psi/\partial\theta$, $v = -\partial\psi/\partial x$ and $\zeta = (1/a \partial^2 u/\partial\theta^2 - \partial^2 v/\partial x^2) = \nabla_H^2 \psi$. The quasi-geostrophic equation may be expressed

$$\frac{\delta}{\delta t} \left\{ \nabla_H^2 \psi + \frac{1}{\rho_0} \frac{\partial}{\partial z^*} \left(\rho_0 \frac{\partial \psi}{\partial z^*} \right) \right\} + \frac{2\Omega \sin \theta}{a} \frac{\partial \psi}{\partial x} =$$

(3.1)

$$\frac{1}{\rho_0} \frac{\partial}{\partial z^*} \left(\frac{\rho}{\sqrt{Pr}} q \right) + F_* \left\{ \nabla_H^2 \psi + \frac{1}{Pr \rho_0} \frac{\partial}{\partial z^*} \left(\rho_0 \frac{\partial \psi}{\partial z^*} \right) \right\}$$

where $z^* = \{g/f_0^2 H_0\}^{1/2} z$ and the material derivative is defined as

$$\begin{aligned} \frac{\delta}{\delta t} \{ \} &= \frac{\partial}{\partial t} \{ \} + u \frac{\partial}{\partial x} \{ \} + \frac{v}{a} \frac{\partial}{\partial \theta} \{ \} \\ &= \frac{\partial}{\partial t} \{ \} + J(\psi, \{ \}) \end{aligned}$$

(3.2)

The perturbation equation may be gained by following the usual procedure, where the streamfunction is assumed to be composed of a basic state plus a disturbance $\psi = \hat{\psi} + \psi'$ where the circumflex denotes the base state and a prime indicates the disturbance. If this decomposition of ψ is substituted into the expression for the quasi-geostrophic potential vorticity, there results

$$\begin{aligned} &= \left\{ \frac{1}{a} \frac{\partial \hat{u}}{\partial \theta} + \frac{1}{\rho_0} \frac{\partial}{\partial z^*} \left(\rho_0 \sqrt{Pr} \hat{\tau} \right) \right\} + \left\{ \nabla_H^2 \psi' + \frac{1}{\rho_0} \frac{\partial}{\partial z^*} \left(\rho_0 \frac{\partial \psi'}{\partial z^*} \right) \right\} \\ &= \hat{\zeta} + \zeta' \end{aligned} \quad (3.3)$$

The hydrostatic equation has been used to relate the vertical derivative of $\hat{\psi}$ to the reference potential temperature. Finally, the quasi-geostrophic equation may be separated into one equation governing the growth of the disturbances

$$\begin{aligned}
& \frac{\partial \zeta'}{\partial t} + \hat{u} \frac{\partial \zeta'}{\partial x} + \frac{\hat{v}}{a} \frac{\partial \zeta'}{\partial \theta} - \frac{\partial \psi'}{\partial x} \frac{1}{a} \frac{\partial \zeta'}{\partial \theta} + \frac{2\Omega \sin \theta}{a} \frac{\partial \psi'}{\partial x} \\
& = \frac{1}{\rho_0} \frac{\partial}{\partial z^*} \left(\frac{\rho_0}{\sqrt{Pr}} q' \right) + F_x \{ \nabla_H^2 \psi' + \frac{1}{Pr} \rho_0 \frac{\partial}{\partial z^*} (\rho_0 \frac{\partial \psi'}{\partial z^*}) \}
\end{aligned} \tag{3.4}$$

and another equation for the quasi-geostrophic base state

$$\begin{aligned}
& \frac{\hat{v}}{a} \frac{\partial \zeta}{\partial \theta} - \frac{2\Omega \sin \theta}{a} \hat{v} = \frac{1}{\rho_0} \frac{\partial}{\partial z^*} \left(\frac{\rho_0}{\sqrt{Pr}} \hat{q} \right) \\
& + F_x \left\{ \frac{1}{a} \frac{\partial \hat{u}}{\partial \theta} + \frac{1}{\sqrt{Pr}} \rho_0 \frac{\partial}{\partial z^*} (\rho_0 \hat{\tau}) \right\}
\end{aligned} \tag{3.5}$$

This last equation is not used to supply the base state in this study; instead, the results of the axisymmetric experiments of the previous section are substituted. It may be seen in this last equation just what the important difference in form is between the axisymmetric model and the quasi-geostrophic axisymmetric model. In the case of the former, it is the vertical advection terms which are most important, with the horizontal advection terms playing a less important role. The situation is just the opposite with the quasi-geostrophic features.

In order to transform the equation to the spectral form, it is necessary to first specify the form of the eigenfunctions of the streamfunction. This is gained by solving an eigenvalue problem - in this case the most natural one is to require the quasi-geostrophic potential vorticity to satisfy

$$\nabla_H^2 \psi' + \frac{1}{\rho_0} \frac{\partial}{\partial z^*} (\rho_0 \frac{\partial \psi'}{\partial z^*}) = -\lambda \psi' \tag{3.6}$$

The horizontal boundary conditions are taken to be cyclic in the longitudinal direction, and the condition $\partial\psi'/\partial x = 0$ at the latitudinal boundaries $0, \pi/2$. This last condition does not permit any flow by the perturbations through the lateral boundaries. Thus the domain may be viewed as a channel with lateral boundaries at 0 and $\pi/2$ with the flow patterns repeating every 2π in the longitudinal direction.

The specification of the vertical boundary condition is more difficult. It would be best if the no-slip condition could be specified at the upper and lower boundaries, along with the condition of no heat flux. However, the posed eigenvalue problem is of second order, so it is not generally feasible to fulfill all three conditions simultaneously. It seemed that the choice $\psi' = 0$ at the two surfaces satisfies at least two of the three conditions. The perturbation velocities and the vorticity will be zero, but the condition of no heat flux is not satisfied. As a consequence of the heat flux at the boundaries, a vertical velocity may occur there, although there is no horizontal motion. It may be found from the first law of thermodynamics, in the absence of friction and heating, that the vertical velocity at the upper and lower boundaries may be related to the local time derivative of the temperature perturbation by

$$\frac{\partial \tau'}{\partial t} + \left(\frac{g}{PrH_0}\right)^{1/2} w = 0 \quad (3.7)$$

As discussed in Dutton (1976b), the upper and lower surfaces are not true lids but may be viewed as surfaces to adjacent boundary layers.

The eigenvalue problem may be solved by standard methods, and the expansion is found to be

$$\psi' = \sum_{l=0}^L \sum_{n=0}^N \sum_{m=0}^M \{ \psi_{mnl}^* \cos(\frac{2\pi mx}{L}) + \hat{\psi}_{mnl} \sin(\frac{2\pi mx}{L}) \}$$

$$\sin(2n\theta) \sin(\frac{l\pi z^*}{Z_T^*}) e^{z^*/Z_T^*} e^{\omega t}$$

Note that the expansion in the vertical and latitudinal directions is just that of a sine expansion, while the longitudinal expansion is a general trigonometric one.

The expansion for ψ' may be differentiated as needed and substituted back into the quasi-geostrophic equation. The base state variables are differentiated from their spectral forms given in section 2.1 and also substituted into the equation. The equation is now multiplied by a particular function of the perturbation streamfunction, and integrated over the domain. The resulting spectral equations are again quite lengthy, and may be found in the Appendix.

b. Stability Results

It was found by experimentation that the stability of the basic state was strongly dependent upon the magnitude of the eddy viscosity coefficient. The magnitude of the viscosity coefficient used to obtain the axisymmetric results was in the range $10 - 150 \text{ m}^2 \text{sec}^{-1}$. When a coefficient in this range was used in the linearized model to test for stability, it was found that the basic state was stable to all but the most strongly heated cases. Further thought suggested the reason for this result. In the axisymmetric case the eddy viscosity formulation was being used to parameterize the effects of sub-grid processes. Richardson's work (1926) appears to supply reasonable estimates of the eddy viscosity coefficient in this case. But the linearized model demands not a sub-grid parameterization, but an estimate of the actual dissipation

mechanisms effecting the perturbations. The size of the coefficient must be reduced considerably in order to model just the dissipation mechanism.

The size of ν_e may be estimated in the manner of Dutton (1982). For standard atmospheric values of the known variables, the range of ν_e is found to be $0.4 - 1.2 \text{ m}^2\text{sec}^{-1}$. Accordingly, with this uncertainty of ν_e , the value of $1.0 \text{ m}^2\text{sec}^{-1}$ was selected to be the representative value.

The position of the transition curve between the Hadley and Rossby regimes has been reported from laboratory experiments (Fultz et al., 1959), deduced from a low order model (Lorenz, 1965), and calculated numerically (Miller and Gall, 1983) for the annulus. Apparently there have been no similar calculations for the atmosphere although the position of the curve has been estimated by Geisler and Fowles (1979) and Dutton (1982). The estimate from Dutton (1982) shows that the curve is considerably to the left of the results from the annulus experiments, although there is some uncertainty due to the high orders of some of the parameters involved. For example, the abscissa of the figures shown by Dutton are proportional to h^4 . An error of two in the estimate here will shift the curve left or right by a factor of 16. In spite of the uncertainties, there is approximate agreement as to the position of the curve from the calculations performed here and the estimates.

About 20 base states were calculated from an axisymmetric model with a value of the eddy viscosity set to about $15 \text{ m}^2\text{sec}^{-1}$ and $\text{Pr} = 4$. The heating rates were varied from $Q = 0.5H$ to $Q = 10H$ (H represents the unscaled heating field values), and the rotation rates are varied from 0.25Ω to 1.5Ω . These states were then tested for stability to asymmetric, quasi-geostrophic disturbances. The results for rotation rates smaller than 0.25Ω and heating rates larger than $10H$ are probably out of range of the original scaling of the axisymmetric model. For this reason, the stability results of Figure 11 do

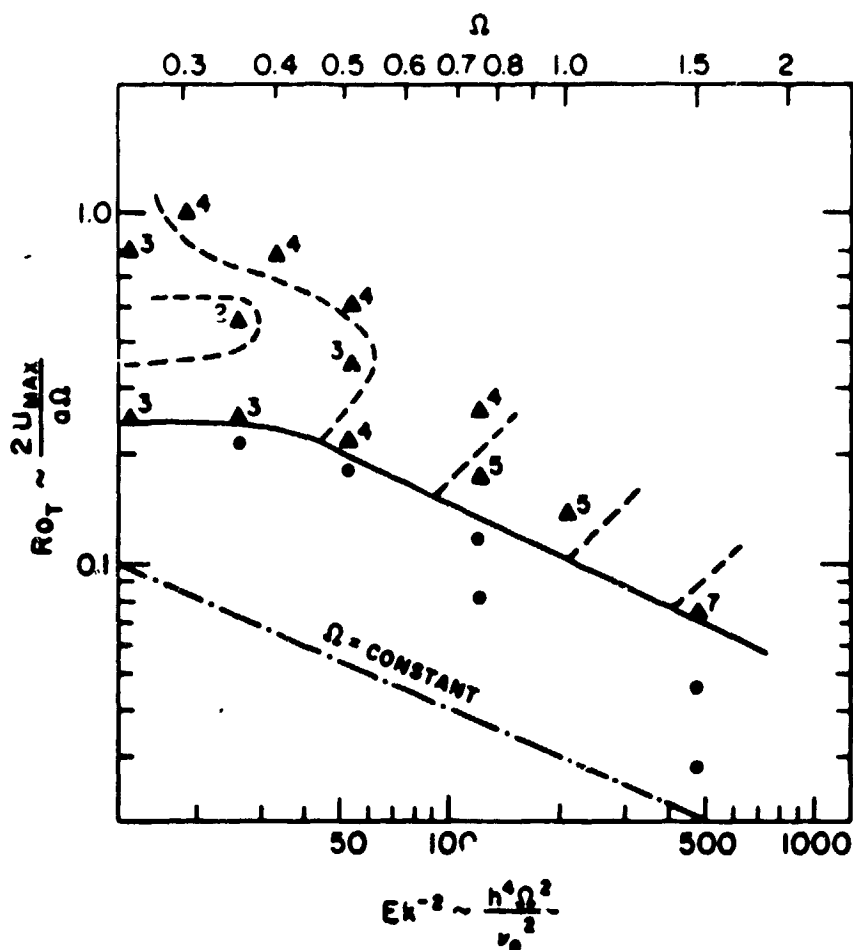


Figure 11. Flow regimes for quasi-geostrophic disturbances growing at the expense of a calculated axisymmetric flow. The calculated flow was from a model with 23 coefficients, $\nu=15 \text{ m}^2 \text{ sec}^{-1}$, and $Pr=4$. The stable Hadley regime is found below the heavy curve, while the Rossby regime is found above it. The initially dominant longitudinal wavenumbers are indicated by numbers next to the sampled points. Points represented by open circles were stable. The abscissa is the inverse square of the Ekman number (proportional to Ω^2) while the ordinate is the thermal Rossby number (a measure of the horizontal temperature gradient).

not show data points beyond these values. In the Figure, the open circles are stable points, while the numbers next to the triangles indicate the longitudinal wavenumber of the most rapidly growing asymmetric disturbance. The dashed lines indicate, approximately, the regions dominated by a particular mode. The Ekman number is given by $Ek = \frac{v}{2\Omega h^2}$.

There are three points to be mentioned concerning these results. First, the agreement between Dutton's estimates and the present calculations is good provided that the scaled value of d is 450 m. This number seems reasonable as is the quarter-wavelength of the eddies in the free atmosphere which seem to be most important in the dissipation of energy. Second, the transition curve appears at a value of the vertical wind shear of $2 \text{ m sec}^{-1} \text{ km}^{-1}$ — in agreement with the results of baroclinic instability studies. Third, the dominant wavenumber decreases with decreasing values of Ek^{-2} , in agreement with the results of Geisler and Fowles.

The transition curve represented a true instability boundary from a steady regime to a wave-like regime. The eigenvalues of the frequency occurred in complex pairs. The real part was negative for the stable cases, indicating that the disturbances were being damped. But as the heating was increased, the real part approached zero and finally changed sign — indicating an amplification of the disturbances. Since the imaginary part was nonzero, the amplifying disturbances were also periodic (wave-like). This behavior of the eigenvalues signals a Hopf bifurcation. For a point that is barely unstable — at a value of $Ek^{-2} = 220$ in Figure 11 — the e-folding time was about 1800 days and had a phase speed of 3 m sec^{-1} . The most unstable point at the same value of Ek^{-2} had an e-folding time of 8 days and a phase speed of 7 m sec^{-1} .

Further study was made of the growth rates with a different set of axisymmetric model parameters. The goal here was to seek the axisymmetric state which would yield growth rates similar to results published in other studies.

Giesle and Garcia (1977) illustrate the initial growth rates for disturbances growing in a baroclinically unstable, horizontally uniform zonal flow. The conditions are assumed to be inviscid. Both the Green modes and Charney modes are present. The calculations were performed for several combinations of three wind profiles and two temperature profiles. The results included a description of the amplitudes and phases of the unstable modes, but it is the growth rates that will be discussed here.

It was found that Charney modes had an initial e-folding time of 2.5 days and the green modes about 8 days for profiles of wind and temperature that are characteristic of the mid-latitudes in winter. The calculations were repeated with the same wind profile and an isothermal temperature distribution in order to assess the effects of increasing static stability. The results indicated a generally slower rate of growth for all waves. The Charney modes had an e-folding time of 3 days, and the Green modes about 11 days.

In order to compare the results of Geisler and Garcia with those of this study, it was decided to calculate axisymmetric base states for increasing heating rates and to test them for stability to quasi-geostrophic disturbances. A model of 46 coefficients was selected ($\nu = 86 \text{ m}^2\text{sec}^{-1}$) along with a heating pattern that was more representative of the observed pattern. The Prandtl number was set to 4, and the viscosity parameter in the quasi-geostrophic equation was set to zero.

It was found by experiment that the base state had to be very energetic in order to achieve growth rates of 2.5 days for the Charney modes. For the

selected value of $\nu = 86 \text{ m}^2\text{sec}^{-1}$ the heating rates had to approach 10°K/day in the tropics and polar regions — of course, lower heating rates would be sufficient if the viscosity coefficient were taken to be smaller.

The axisymmetric flow that corresponds to the large heating rate is a very energetic one. The zonal wind has a maximum value of 70 m sec^{-1} at 50°N and 10 km. The Hadley circulation contains a single cell centered at 30°N and 10 km. The meridional velocities peak at 26 m sec^{-1} in the upper levels and reach 13 m sec^{-1} in the return flow at lower levels. The maximum vertical velocity is 3 cm sec^{-1} at the equator.

Profiles of zonal wind and potential temperature from the model at 50°N are shown in Figure 12 and 13. For comparison, observed profiles for the winter period are shown as dashed lines. The model solution is seen to be much stronger, with vertical wind shears being 3-4 times larger. The potential temperature profile is more stable than the observed one. The model profile deviates relatively little about the isothermal state up to 8 km. The only region of low static stability is from 8-10 km, and the value of the stability in this region is about equal to that observed throughout most of the troposphere.

From the results of quasi-geostrophic theory, it is known that the growth rates are dependent on both the static stability and the wind shears. The dominant term here involves the square of the vertical wind shear divided by the static stability ($\sim \frac{f_0^2 H_\theta}{g} (\frac{\partial u}{\partial z})^2$). In the case of the observed profile the low static stability and smaller wind shear yield the calculated growth rate of ~ 3 days. For the model results, rather high static stabilities need correspondingly large vertical wind shears to give the same growth rates.

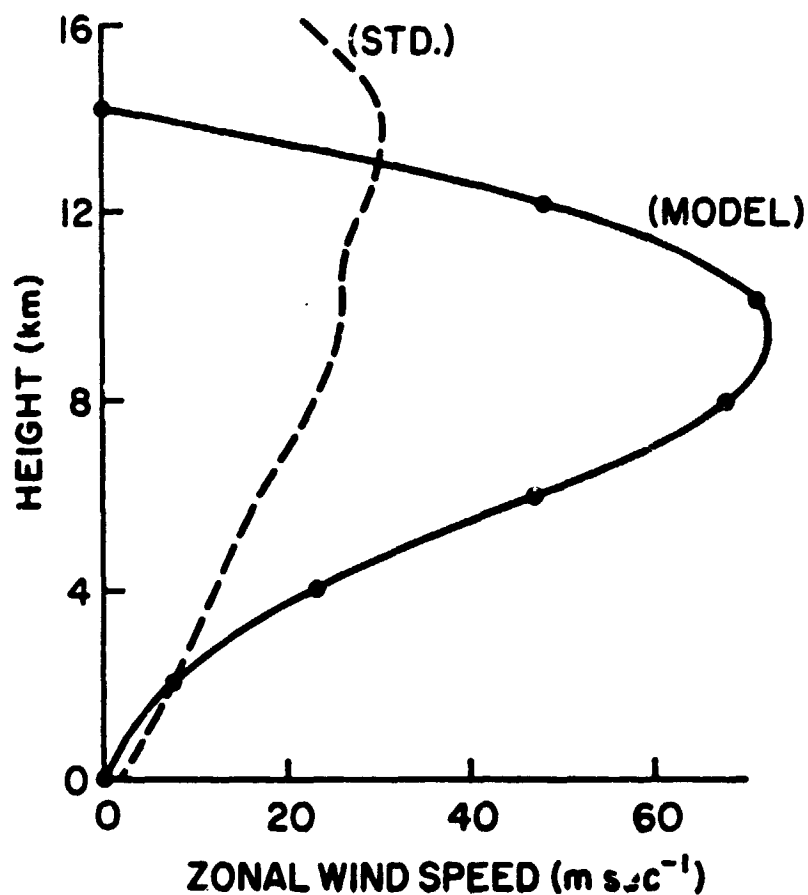


Figure 12. Zonal wind speed profiles. Solid line - for a calculated axisymmetric base state at 50°N and a maximum heating rate of 10°K day⁻¹. Dashed line - an observed, averaged profile at 40°N in the winter (December - February).

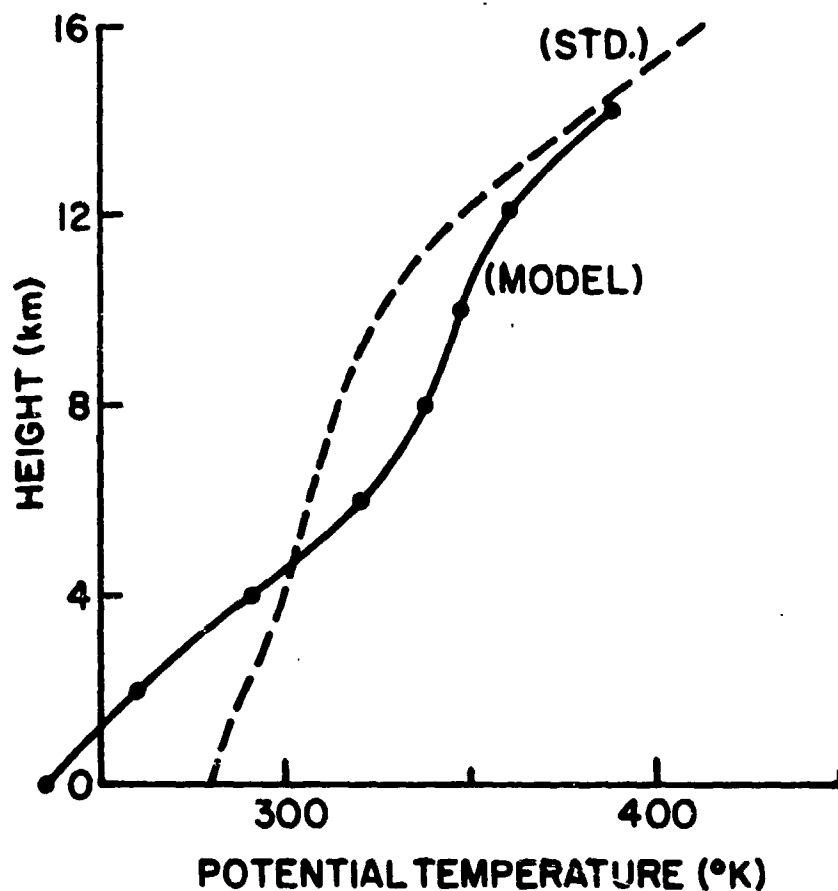


Figure 13. Potential temperature profiles. Solid line - for a calculated axisymmetric base state at 50°N and a maximum heating rate of 10°K day⁻¹. Dashed line - an observed, averaged profile at 40°N in the winter (December - February).

4. Discussion

The results of this study showed the practicality of calculating steady, axisymmetric base states and of testing these states for stability to quasi-geostrophic disturbances by spectral methods. The base states were either one or two-celled in structure, not the three-celled structure of observed axisymmetric flow. Similar base states were calculated by Miller and Gall (1983a) for a spherical annulus, although the numerical procedures and forcing characteristics were quite different. As suggested by them and found in this study, the upper lid appears to have a profound effect on the nature of the flows. This lid seems to be responsible for the splitting of the single Hadley cell into two cells at sufficiently low viscosity and/or strong forcing.

The nature of the heating may also play a critical role in determining the nature of the steady flows. In the annulus experiments (and models) the forcing is accomplished by maintaining the boundaries at specified temperatures. The fluid response is to establish narrow, boundary layer jets adjacent to the boundaries. The forcing used in this study was of a smoothly varying field over the interior of the fluid. There was little reason to expect narrow boundary layer jets to form, and this was basically the case. The possible exception was near the lid, where a relatively narrow layer of poleward moving fluid could form if the system were heated strongly enough. There is additional evidence that the nature of the steady solutions differ rather fundamentally between internally forced and externally forced flows. Higgins (1984) has found from a low order spectral approach that externally forced flows have more regions of multiple solutions than do those that are internally forced. The complexity of the equations of this study, although numbering only 23, was more than sufficient to prevent the search for regions of multiple solutions.

The presence of the lid also appears to be the cause of the high static stabilities in the upper levels. This is achieved by trapping the warm, rising fluid under the lid. The result of this is to form a profile that is statically stable at the top and bottom, but has low stability in the interior. In fact, as the heating was strengthened, it was found that this interior layer became less and less stable, while the fluid at the top and bottom remained stable.

The axisymmetric flow was tested for stability to quasi-geostrophic disturbances. The domain for the disturbances differs from that of the axisymmetric flow in that the disturbances are not contained by a true lid. This difficulty arises because of the problem of matching the boundary conditions between the axisymmetric flow and that of the quasi-geostrophic disturbances. The use of boundary conditions, chosen to be both similar and convenient, results in horizontal surfaces that are no-slip with respect to the horizontal velocity components, but permit vertical velocities. It is difficult to assess the effects of this condition on the growing disturbances. There should, for example, be some reflection of waves from the upper and lower surfaces, but it would take additional study to determine the relative size of the effects and their importance on the incipient disturbances.

Because this study was devoted to demonstrating a particular technique in support of the stability studies, there was no study of many interesting aspects of the stability calculations. For example, no studies of the structure of the amplifying waves were done such as in Miller and Gall (1983b), nor was the stability curve of Figure 11 calculated for base states with different parameters other than the chosen set. More complicated heating patterns could have been used, along with somewhat more generous truncation limits to the axisymmetric model.

The study re-affirmed the fact that the axisymmetric solutions are not quasi-geostrophic in nature. Further, the stability results will differ from other studies because the disturbances are growing at the expense of a Hadley cell that is statically more stable over most of its domain than the observed axisymmetric flow. The observed flow is presumably the end result of the growing disturbances and presents a less stable environment for the local growth of later baroclinic disturbances. Thus the physical interpretation of the present study differs from those based upon observed profiles for the base state.

APPENDIX

The spectral equations of the axisymmetric model and the quasi-geostrophic disturbances are given below. More detail as to their derivation may be found in Henderson (1982). First we consider the axisymmetric model. The three partial differential equations (zonal momentum, meridional vorticity, and thermodynamic equations) become five spectral equations. This is because the even and odd modes of the meridional vorticity equation are most conveniently written separately, and the thermodynamic equation may be written as two equations governing the modes possessing vertical variation and the barotropic modes. The zonal momentum equation is

$$\sum_{m=1}^M \sum_{r \text{ odd}}^{R+1} \sum_{s=1}^S \{ u_r^s \hat{\psi}_{u+r}^m (r\pi v NC1_{u+r}^{mvs} - u\pi s NC1_{u+r}^{msv} + (r-u) NC2_{u+r}^{mvs})$$

$$+ u_r^s \hat{\psi}_{u-r}^m (r\pi v NC1_{u-r}^{mvs} + u\pi s NC1_{u-r}^{msv} + (r+u) NC2_{u-r}^{mvs})$$

$$- u_r^s \hat{\psi}_{r-u}^m (r\pi v NC1_{r-u}^{mvs} + u\pi s NC1_{r-u}^{msv} + (r+u) NC2_{r-u}^{mvs})$$

$$+ u_r^s \hat{\psi}_{u+r}^m (r\pi v NS1_{u+r}^{mvs} - u\pi s NS1_{u+r}^{msv} + (r-u) NS2_{u+r}^{mvs})$$

$$+ u_r^s \hat{\psi}_{u-r}^m (r\pi v NS1_{u-r}^{mvs} + u\pi s NS1_{u-r}^{msv} + (r+u) NS2_{u-r}^{mvs})$$

$$- u_r^s \hat{\psi}_{r-u}^m (r\pi v NS1_{r-u}^{mvs} + u\pi s NS1_{r-u}^{msv} + (r+u) NS2_{r-u}^{mvs})$$

$$\begin{aligned}
& + \Omega a \sum_{m=1}^M \{ \psi_{u+1}^{*m} (I_{u+1}^{vm} + J_{u+1}^{vm}) + \hat{\psi}_{u+1}^m (K_{u+1}^{vm} + L_{u+1}^{vm}) \\
& + \psi_{u-1}^{*m} (I_{u-1}^{vm} + J_{u-1}^{vm}) + \hat{\psi}_{u-1}^m (K_{u-1}^{vm} + L_{u-1}^{vm}) \\
& - \psi_{1-u}^{*m} (I_{1-u}^{vm} + J_{1-u}^{vm}) - \hat{\psi}_{1-u}^m (K_{1-u}^{vm} + L_{1-u}^{vm}) \} \\
& - \nu a Z_T \left(\frac{u^2}{a^2} + \frac{\pi^2 v^2}{Z_T^2} + \frac{1}{Z_T^2} \right) u^v = 0
\end{aligned} \tag{A.1}$$

The two thermodynamic equations are

$$\begin{aligned}
& \text{Pr} \sum_{m=1}^M \sum_{r \text{ even}}^R \sum_{s=1}^S (1 + \pi^2 s^2) u \{ \tau_r^s \psi_{r-u}^{*m} J_{r-u}^{sm} + \tau_r^s \hat{\psi}_{r-u}^m L_{r-u}^{sm} \\
& - \tau_r^s \psi_{r+u}^{*m} J_{r+u}^{sm} - \tau_r^s \hat{\psi}_{r+u}^m L_{r+u}^{sm} \\
& - \tau_r^s \psi_{u-r}^{*m} J_{u-r}^{sm} - \tau_r^s \hat{\psi}_{u-r}^m L_{u-r}^{sm} \} \\
& - 2 \frac{\sqrt{gPr}}{\sqrt{H_0}} \sum_{m=1}^M u Z_T \{ \psi_u^{*m} M_u^m + \hat{\psi}_u^m N_u^m \} \\
& - a Z_T (1 - e^{-2}) (q_u^0 - \frac{u^2}{a^2} \tau_u^0) = 0
\end{aligned} \tag{A.2}$$

$$\begin{aligned}
& \Pr \sum_{m=1}^M \sum_{r \text{ even}}^R r(1+\pi^2 v^2) \{ \tau_r^{o^*m} J_{u+r}^{vm} + \tau_r^{o^*m} L_{u+r}^{vm} \\
& - \tau_r^{o^*m} J_{u-r}^{vm} - \tau_r^{o^*m} L_{u-r}^{vm} \\
& + \tau_r^{o^*m} J_{r-u}^{vm} + \tau_r^{o^*m} L_{r-u}^{vm} \} \\
& - \Pr \sum_{m=1}^M \sum_{r \text{ even}}^R \sum_{s=1}^S \{ \tau_r^{s^*m} (r\pi s(1+\pi^2 v^2) NC1_{u+r}^{msv} \\
& - u\pi v(1+\pi^2 s^2) NC1_{u+r}^{mvs} - (r(1+\pi^2 v^2) - u(1+\pi^2 s^2)) NC2_{u+r}^{mvs}) \\
& - \tau_r^{s^*m} (r\pi s(1+\pi^2 v^2) NC1_{u-r}^{msv} + u\pi v(1+\pi^2 s^2) NC1_{u-r}^{mvs} \\
& - (r(1+\pi^2 v^2) + u(1+\pi^2 s^2)) NC2_{u-r}^{mvs}) \\
& + \tau_r^{s^*m} (r\pi s(1+\pi^2 v^2) NC1_{r-u}^{msv} + u\pi v(1+\pi^2 s^2) NC1_{r-u}^{mvs} \\
& - (r(1+\pi^2 v^2) + u(1+\pi^2 s^2)) NC2_{r-u}^{mvs}) \\
& + \tau_r^{s^*m} (r\pi s(1+\pi^2 v^2) NS1_{u+r}^{msv} - u\pi v(1+\pi^2 s^2) NS1_{u+r}^{mvs}
\end{aligned}$$

$$\begin{aligned}
& - (r(1+\pi^2 v^2) - u(1+\pi^2 s^2)) NS2_{u+r}^{mvs}) \\
& - \tau_r^s \hat{\psi}_{u-r}^m (r\pi s(1+\pi^2 v^2) NS1_{u-r}^{msv} + u\pi v(1+\pi^2 s^2) NS1_{u-r}^{mvs} \\
& - (r(1+\pi^2 v^2) + u(1+\pi^2 s^2)) NS2_{u-r}^{mvs}) \\
& + \tau_r^s \hat{\psi}_{r-u}^m (r\pi s(1+\pi^2 v^2) NS1_{r-u}^{msv} + u\pi v(1+\pi^2 s^2) NS1_{r-u}^{mvs} \\
& - (r(1+\pi^2 v^2) + u(1+\pi^2 s^2)) NS2_{r-u}^{mvs}) \} \\
& - 2 \frac{\sqrt{gPr}}{\sqrt{H_\theta}} \sum_{m=1}^M u Z_T \{ \psi_u^m (J_u^{vm} - I_u^{vm}) + \hat{\psi}_u^m (L_u^{vm} - K_u^{vm}) \} \\
& - a Z_T (1+\pi^2 v^2) q_u^v + v a Z_T (1+\pi^2 v^2) \left(\frac{u^2}{a^2} + \frac{\pi^2 v^2}{Z_T^2} + \frac{1}{Z_T^2} \right) \tau_u^v = 0 \quad (A.3)
\end{aligned}$$

The two meridional vorticity equations are

$$\begin{aligned}
& - \Omega a \sum_{m=1}^M \{ u_{u+1}^m + u_{u-1}^m - u_{1-u}^m \} (J_u^{mv} + I_u^{mv}) \\
& - 2 \frac{\sqrt{gPr}}{\sqrt{H_\theta}} Z_T u \tau_u^0 M_u^v - \sum_{m=1}^M 2 \frac{\sqrt{gPr}}{\sqrt{H_\theta}} u Z_T \tau_u^m (J_u^{mv} - I_u^{mv}) \\
& - 2 v a \hat{\psi}_u^v \{ (\lambda_u^v)^2 N(C_u^v) \} = 0 \quad (A.4)
\end{aligned}$$

and

$$\begin{aligned}
& - \Omega a \sum_{m=1}^M \{u_{u+1}^m + u_{u-1}^m - u_{1-u}^m\} (L_u^{mv} + K_u^{mv}) \\
& - 2 \frac{\sqrt{gPr}}{\sqrt{H_0}} Z_T u \tau_u^0 N_u^v - \sum_{m=1}^M 2 \frac{\sqrt{gPr}}{\sqrt{H_0}} u Z_T \tau_u^m (L_u^{mv} - K_u^{mv}) \\
& - 2 v a \hat{\psi}_u^v \{(\hat{\lambda}_u^v)^2 N(S_u^v)\} = 0
\end{aligned}
\tag{A.5}$$

The perturbation form of the quasi-geostrophic equations may also be split into even and odd modes. The equation governing the even modes is

$$\begin{aligned}
& (-\omega - v \frac{\lambda_{uvw} \bar{\lambda}_{uvw}}{\lambda_{uvw}})^* \hat{\psi}_{uvw} + \sum_{n=0}^N 8 \frac{\Omega \Gamma_{1vn}}{a L_x \lambda_{uvw}} \hat{\psi}_{unw} \\
& - \sum_{r \text{ odd}}^{R+1} \sum_{s=1}^S \sum_{n=0}^N \sum_{l=0}^L \frac{16u}{L_x Z_T \lambda_{uvw}} \{\lambda_{unl}^* \\
& - \frac{r^2}{a^2} \Gamma_{rvn}^{NV1} l_{ws} (\hat{u}_r^s)_0 \hat{\psi}_{unl} \\
& + \sum_{r \text{ even}}^R \sum_{s=0}^S \sum_{n=0}^N \sum_{l=0}^L \frac{16n \lambda_{unl}^* \Delta_{rvn} \hat{\psi}_{unl}}{a Z_T \lambda_{uvw}} ((\hat{\psi}_r^s)_0 l_{rNC1}^{slw}
\end{aligned}$$

$$+ w_{\pi} N C 1_r^{swl} + 2 N C 2_r^{slw} + (\hat{\psi}_r^s)_0 (l_{\pi} N S 1_r^{slw} + w_{\pi} N S 1_r^{swl} + 2 N S 2_r^{slw}) \}$$

$$- \sum_{r \text{ even}}^R \sum_{s=1}^S \sum_{n=0}^N \sum_{l=0}^L \frac{16 r u \sqrt{Pr}}{a L_x Z_T \lambda_{uvw}} \left\{ \frac{2}{Z_T^*} - Z_T^* \left(\frac{r^2 s^2}{Z_T^{*2}} \right. \right.$$

$$+ \left. \frac{1}{Z_T^{*2}} \right\} \Gamma_{rvn}^{NV1} l_{ws} (\hat{\tau}_r^s)_0 \hat{\psi}_{unl}$$

$$- \sum_{r \text{ even}}^R \sum_{n=0}^N \frac{16 r u \sqrt{Pr}}{a L_x Z_T \lambda_{uvw}} \Gamma_{rvn} (\hat{\tau}_r^0)_0 \hat{\psi}_{unw}$$

$$+ \sum_{r \text{ even}}^R \sum_{s=0}^S \sum_{n=0}^N \sum_{l=0}^L \frac{32 \pi u s \sqrt{Pr}}{a L_x Z_T Z_T^* \lambda_{uvw}} \Gamma_{rvn}^{NV2} l_{ws} (\hat{\tau}_r^s)_0 \hat{\psi}_{unl}$$

$$= \frac{8 e^{-u t}}{\pi Z_T \sqrt{Pr} \lambda_{uvw}} \int_0^{2\pi} \int_0^{\pi/2} \int_0^{Z_T} \frac{\rho_0}{\rho(0)} \cos(ux^*) \sin(2v\theta)$$

$$\sin\left(\frac{w y z}{Z_T}\right) e^{z/Z_T} \frac{1}{\rho_0} \frac{\partial}{\partial z^*} (\rho_0 q') dz d\theta dx^* \quad (A.6)$$

while that of the odd modes is

$$(-\omega - v \frac{\lambda_{uvw} \tilde{\lambda}_{uvw}}{\lambda_{uvw}}) \hat{\psi}_{uvw} - \sum_{n=0}^N 8 \frac{\Omega u}{a L_x \lambda_{uvw}} \Gamma_{lvn} \psi_{uav}^*$$

$$+ \sum_{r \text{ odd}}^{R+1} \sum_{s=0}^S \sum_{n=1}^N \sum_{l=0}^L \frac{16u}{L_x Z_T \lambda_{uvw}} \{\lambda_{unl}^*$$

$$- \frac{r^2}{a} \} \Gamma_{rvn} NV1_{lws} (\hat{u}_r^s) \psi_{unl}^*$$

$$+ \sum_{r \text{ even}}^R \sum_{s=0}^S \sum_{n=0}^N \sum_{l=0}^L \frac{16n}{\pi a Z_T \lambda_{uvw}} \frac{\lambda_{unl}^* \Delta_{rvn} \hat{\psi}_{unl}}{\lambda_{uvw}} \{ (\hat{\psi}_r^s)_0 (l \pi NC1_r^{slw}$$

$$+ w_r NC1_r^{swl} + 2NC2_r^{slw}) + (\hat{\psi}_r^s)_0 [l \pi NS1_v^{slw} + w_r NS1_r^{swl} + 2NS2_r^{slw}) \}$$

$$+ \sum_{r \text{ even}}^R \sum_{s=1}^S \sum_{n=0}^N \sum_{l=0}^L \frac{16ru/\overline{Pr}}{a L_x Z_T \lambda_{uvw}} \cdot \{ \frac{2}{Z_T} - Z_T^* (\frac{r^2}{Z_T^*})^2$$

$$+ \frac{1}{Z_T^* 2} \} \Gamma_{rvn} NV1_{lws} (\hat{\tau}_r^s) \psi_{unl}^*$$

$$+ \sum_{r \text{ even}}^R \sum_{n=0}^N \frac{16ru/\overline{Pr}}{a L_x Z_T^* \lambda_{uvw}} \Gamma_{rvn} (\hat{\tau}_r^0) \psi_{ulw}^*$$

$$= \sum_{r \text{ even}}^R \sum_{s=0}^S \sum_{n=0}^N \sum_{l=0}^L \frac{32\pi r u s \sqrt{Pr}}{a L_x Z_T Z_T^* \lambda_{uvw}} \Gamma_{rvn} NV2_{lws} (\hat{r}_r^s)^* \psi_{unl}$$

$$= \frac{8e^{-\omega t}}{\pi^2 Z_T \sqrt{Pr} \lambda_{uvw}} \int_0^{2\pi} \int_0^{\pi/2} \int_0^{Z_T} \frac{\rho_0}{\rho(0)} \sin(ux^*) \sin(2v\theta)$$

$$\sin\left(\frac{w\pi z}{Z_T}\right) e^{z/Z_T} \frac{1}{\rho_0} \frac{\partial}{\partial z^*} (\rho_0 q') dz d\theta dx^* \quad (A.7)$$

There are several factors which arise from the integrations. These are given below in their integral form; most can be expressed in a closed form which may be found in Henderson (1982).

$$I_n^{vm} = \frac{\pi v}{Z_T} \int_0^{Z_T} \rho_0 \cos\left(\frac{\pi v z}{Z_T}\right) C_n^m e^{2z/Z_T} dz \quad (A.8)$$

$$J_n^{vm} = \frac{1}{Z_T} \int_0^{Z_T} \rho_0 \sin\left(\frac{\pi v z}{Z_T}\right) C_n^m e^{2z/Z_T} dz \quad (A.9)$$

$$K_n^{vm} = \frac{\pi v}{Z_T} \int_0^{Z_T} \rho_0 \cos\left(\frac{\pi v z}{Z_T}\right) S_n^m e^{2z/Z_T} dz \quad (A.10)$$

$$L_n^{vm} = \frac{1}{Z_T} \int_0^{Z_T} \rho_0 \sin\left(\frac{\pi v z}{Z_T}\right) S_n^m e^{2z/Z_T} dz \quad (A.11)$$

$$M_n^m = \frac{1}{Z_T} \int_0^{Z_T} \rho_0 C_n^m e^{z/Z_T} dz \quad (A.12)$$

$$N_n^m = \frac{1}{Z_T} \int_0^{Z_T} \rho_0 S_n^m e^{z/Z_T} dz \quad (A.13)$$

$$T_n^{mv} = \int_0^{Z_T} \frac{\partial C_n^m}{\partial z} \frac{\partial C_n^v}{\partial z} dz \quad (A.14)$$

$$W_n^{mv} = \int_0^{Z_T} \frac{\partial S_n^m}{\partial z} \frac{\partial S_n^v}{\partial z} dz \quad (A.15)$$

$$NC1_n^{mvs} = \frac{1}{Z_T} \int_0^{Z_T} e^{z/Z_T} C_n^m \cos\left(\frac{\pi v z}{Z_T}\right) \sin\left(\frac{\pi s z}{Z_T}\right) dz \quad (A.16)$$

$$NC2_n^{mvs} = \frac{1}{Z_T} \int_0^{Z_T} e^{z/Z_T} C_n^m \sin\left(\frac{\pi v z}{Z_T}\right) \sin\left(\frac{\pi s z}{Z_T}\right) dz \quad (A.17)$$

$$NS1_n^{mvs} = \frac{1}{Z_T} \int_0^{Z_T} e^{z/Z_T} S_n^m \cos\left(\frac{\pi v z}{Z_T}\right) \sin\left(\frac{\pi s z}{Z_T}\right) dz \quad (A.18)$$

$$NS2_n^{mvs} = \frac{1}{Z_T} \int_0^{Z_T} e^{z/Z_T} S_n^m \sin\left(\frac{\pi v z}{Z_T}\right) \sin\left(\frac{\pi s z}{Z_T}\right) dz \quad (A.19)$$

$$\Delta_{rvn} = \int_0^{\pi/2} \sin(r\theta) \sin(2v\theta) \cos(2n\theta) d\theta \quad (A.20)$$

$$\Gamma_{rvn} = \int_0^{\pi/2} \sin(r\theta) \sin(2v\theta) \sin(2n\theta) d\theta \quad (A.21)$$

$$NV1_{lws} = \int_0^{Z_T} e^{z/Z_T} \sin\left(\frac{l\pi z}{Z_T}\right) \sin\left(\frac{w\pi z}{Z_T}\right) \sin\left(\frac{s\pi z}{Z_T}\right) dz \quad (A.22)$$

$$NV2_{lws} = \int_0^{Z_T} e^{z/Z_T} \sin\left(\frac{l\pi z}{Z_T}\right) \sin\left(\frac{w\pi z}{Z_T}\right) \cos\left(\frac{s\pi z}{Z_T}\right) dz \quad (A.23)$$

$$N(C_n^m) = \int_0^{Z_T} \rho_0 C_n^m C_n^m e^{2z/Z_T} dz$$

$$N(S_n^m) = \int_0^{Z_T} \rho_0 S_n^m S_n^m e^{2z/Z_T} dz$$

ACKNOWLEDGMENTS

Professor John H. E. Clark provided valuable guidance during the course of this research. His careful approach to the study helped to guide me away from some of the more serious pitfalls that I might have encountered.

The computer program used to solve the set of simultaneous, nonlinear equations in this study was shown to me by Dr. William H. Mach. Dr. Mach had gained experience in the use of various algorithms during the time he was a Ph.D. candidate at The Pennsylvania State University. He willingly shared his knowledge with me, which greatly eased the burden of writing the computer programs used in this study.

While a graduate student, I was supported by a National Defense Education Act Title IV Fellowship, and grants from the National Aeronautics and Space Administration (Grant #NAS-33794) and the National Science Foundation (Grant #ATM79-08354).

REFERENCES

- Antar, B.N. and W.W. Fowlis, 1981: Baroclinic instability of a rotating Hadley cell. J. Atmos. Sci., 38, 2130-2141.
- and ----, 1982: Symmetric baroclinic instability of a Hadley cell. J. Atmos. Sci., 39, 1280-1289.
- Dutton, J.A. and D.R. Johnson, 1967: The theory of available potential energy and a variational approach to atmospheric energetics. Advances in Geophysics, 12, 333-436.
- , 1976a: The Ceaseless Wind: An Introduction to the Theory of Atmospheric Motion. McGraw-Hill, 579 pp.
- , 1976b: The nonlinear quasi-geostrophic equation. Part II: Predictability, recurrence, and limit properties of thermally forced and unforced flows. J. Atmos. Sci., 33, 1431-1453.
- , 1982: Fundamental theorems of climate theory - some proved, some conjectured. S.I.A.M. Review, 24, 1-33.
- and P.E. Kloeden, 1983: The existence of Hadley convective regimes of atmospheric motion. J. Austral. Math. Soc., 24, (Series B), 318-338.
- Fultz, D., et al., 1959: Studies of thermal convection on a rotating cylinder with some implications for large-scale atmospheric motions. Meteor. Monogr., 4, No. 21, 104 pp.
- Geisler, J.E. and R.R. Garcia, 1977: Baroclinic instability at long wavelengths on a beta-plane. J. Atmos. Sci., 34, 311-321.
- and W.W. Fowlis, 1979: Theoretical regime diagrams for thermally driven flows in a beta-plane channel. J. Atmos. Sci., 36, 1530-1541.
- Harris, D.L. and W.H. Reid, 1958: On orthogonal functions which satisfy four boundary conditions. I Tables for use in Fourier type expansions. Ap. J. Suppl., 3, 429-447.
- Henderson, H.W., 1982: A numerical study of the global axisymmetric circulation with varying heating and rotation rates. Ph.D. Thesis, The Pennsylvania State University, 256 pp.
- Higgins, R.W., H.N. Shirer and J.A. Dutton, 1985: On modeling axisymmetric flows in the annulus and the hemisphere. Submitted to J. Atmos. Sci.
- Lorenz, E.N., 1953: A proposed explanation for the existence of two regimes of flow in a rotating symmetrically-heated cylindrical vessel. Fluid Models in Geophysics. Proceedings of the 1st Symposium on the Use of Models in Geophysical Fluid Dynamics, Baltimore, 73-80.
- Miller, T.L. and R.L. Gall, 1983a: Thermally driven flow in a rotating spherical shell: Axisymmetric states. J. Atmos. Sci., 40, 856-868.

---- and ----, 1983b: A linear analysis of the transition curve for the baroclinic annulus. J. Atmos. Sci., 40, 2293-2303.

Richardson, L.F., 1926: Atmospheric diffusion shown on a distance-neighbour graph. Proc. Royal Soc., Ser. A, 110, 709-737.

Schneider, E.K. and R.S. Lindzen, 1977: Axially symmetric steady-state models of the basic state for instability and climate studies. Part I. Linearized calculations. J. Atmos. Sci., 34, 263-279.

----, 1977: Axially symmetric steady-state models of the basic state for instability and climate studies. Part II. Nonlinear calculations. J. Atmos. Sci., 34, 280-296.

N86-11754

CHAPTER 6

On Cloud Street Development in Three Dimensions:

Parallel and Rayleigh Instabilities

Hampton N. Shirer

Department of Meteorology
The Pennsylvania State University
University Park, PA 16802

1. Introduction

Cloud streets in the atmosphere generally are believed to occur as a result of a combination of two dynamic and one thermodynamic mechanisms (Kelly, 1977; Brown, 1980). The first dynamic mechanism is an irrotational one by which secondary circulations may grow via extraction of energy from the component of the large-scale wind perpendicular to the roll axis; because this can occur only when an inflection point exists in the wind profile, this instability is called the inflection point instability (Brown, 1972; Etling and Wippermann, 1975). The second dynamic mechanism is a combination of a rotational and a viscous one by which roll circulations may develop via extraction of energy from the component of the large-scale wind parallel to the roll axis, and so this instability is called the parallel instability (Lilly, 1966). Most investigators believe that this latter dynamic mechanism, which requires rotational and viscous terms of the same order of magnitude, is of secondary importance (Brown, 1980), although there are some who believe it may be significant (e.g. Etling, 1971; Gammelsrød, 1975). The thermal mechanism is manifested by convective perturbations extracting energy from the basic state thermal structure, and this instability is labelled the Rayleigh-Bénard instability (Asai, 1970; Kuettner, 1971). Latent heating effects can be incorporated into the thermal instability, resulting in a modified form for the governing dimensionless parameter, the Rayleigh number (Krishnamurti, 1975; Mitchell and Agee, 1977; Shirer and Dutton, 1979). In the absence of rotational effects, the wind shear perpendicular to the roll provides a stabilizing effect (Ogura and Yagihashi, 1969; Kuettner, 1971; Asai, 1972), and as a result of this, the convective rolls have alignments for which the influence of the perpendicular shear is minimized (Shirer, 1980).

Although three mechanisms for roll development have been identified, they do not lead necessarily to three independent roll solutions once the effects of wind and stratification are included in a single analysis. Indeed, in a preliminary study of moist, three-dimensional shallow convection, Shirer (1982) presented evidence that the parallel and Rayleigh-Bénard instabilities are actually special cases of a single instability mechanism. But his model was not sufficiently general, primarily because it could not support nonlinear roll solutions for the case of pure parallel instability, which is given physically by neutral stratification and mathematically by the vanishing of the modified Rayleigh number. In addition, the latent heating effects were not included correctly, and this led to incorrect branching results. In this article, we present a larger three-dimensional truncated spectral model of shallow convection in order to eliminate the above deficiencies. We will find that the results on expected roll geometry that are given in Shirer (1982) are correct; but they are incomplete because more roll modes than he found are possible in a weakly stably stratified atmosphere.

The present model is a generalized version of the one presented in Shirer (1980), in which only two-dimensional convection was discussed. In that study, an arbitrary background height-dependent horizontal wind was included, although no rotational effects were, and so the ambient wind shear was not an energy source for the secondary flow. Latent heating was assumed to occur everywhere in the upward branch of the circulation, and so all upward motion was assumed to be moist adiabatic, all downward motion, dry adiabatic. In addition, eddy dissipation terms were included to represent energy loss to smaller scales. Several improvements have been made in the formulation of the model discussed here. Three-dimensional convective flow is assumed and rotational effects are included; moreover, a cloud base at a prescribed level

z_1 in the middle of the domain is possible, in which case only the upward moving air above the level z_1 is assumed to be cooling moist adiabatically. As was found in the preliminary version (Shirer, 1982), the form of the nonlinear convective flow is two-dimensional when the Fourier coefficients of the wind shear profile are nonzero, so that roll solutions develop first. The model can represent the parallel instability mechanism, because branching solutions occur in the neutral limit of vanishing modified Rayleigh number when both the Coriolis parameter and the Fourier coefficient of the roll-parallel shear component are nonzero. Apparently the inflection point instability mechanism is filtered by the restriction to wave number 1 Fourier components of the background wind field; additional harmonics would be needed in order to capture the inflection point in the wind profile, and hence the instability mechanism. As in the preliminary model, latent heating does not affect either the roll geometry or the existence of convective instability, but serves primarily to reduce the necessary critical value of the environmental lapse rate. Physically, this reduction corresponds to that given by the slice method (Bjerknes, 1938), which is a modified version of the conditional convective instability criterion for parcel motion; moreover, this reduction is proportional to the cross-sectional area of the cloudy region in which latent heating is occurring.

Of primary concern in this article is a discussion of those results from the model that may be compared with observations such as those taken during the Fall 1981 convection and turbulence experiment KonTur (Brümmer and Grant, 1985). The simplest comparisons can be made between the modelled and observed alignments of the cloud bands, given here by the angle θ between the roll axis and east, and the horizontal wavelength L of the bands, given by the aspect ratio $A = 2z_T/L$ and by the domain, or circulation, height z_T . Expected

values of these parameters are obtained from an analysis of the linear stability of the conductive solution from which the nonlinear flow develops. In many studies (e.g. Lilly, 1966; Brown, 1970, 1972; Asai and Nakasuji, 1973), the linearized partial differential equations can be reduced either to a single high-order ordinary differential equation in the amplitude of one of the dependent variables, or to a system of ordinary differential equations in all of the amplitudes. The resulting system is solved numerically, often by using finite differences to represent vertical derivatives, and then the expected values of θ and L are those associated with perturbations having the fastest exponential growth rates. Thus, the temporal behavior in the vicinity of an unstable solution is assumed to provide information on the resulting stable nonlinear solution. A serious shortcoming of this approach, though, is that it is strictly valid only for slightly supercritical cases, but it is often applied to a wide range of supercritical parameter values. When the numerical results are interpreted, a standard assumption is that different ranges of θ and L are characteristic of solutions originating from different physical instability mechanisms; however, the possibility exists either that only one response might be allowed or that a wide variety of responses might be created by the combination of two or more instability mechanisms. To aid in determining which possibility occurs, a more direct method of analysis than that outlined above is needed.

Such a method is provided by an alternate approach to the problem that is equivalent in many respects to the above point of view. In this second approach the critical value R_c of an external parameter such as the Rayleigh number Ra or the Reynolds number Re is determined; at the critical value, the trivial, or conductive, solution is neutrally stable and nonlinear convective solutions emanate, or bifurcate, from the trivial solution at this critical

value (Iooss and Joseph, 1980). When the solution branches toward larger values of R , we find the following: For values of $R < R_c$, perturbations damp, and for values of $R > R_c$, perturbations grow toward the stable nonlinear convective solution. But the values of R_c depend on the magnitudes of such auxiliary parameters as θ and L , and so the preferred values of θ and L are those that produce the minimum values of R_c ; physically this corresponds to a release of the instability and a vertical transport of heat via a convective configuration that can most easily accomplish that task. Moreover, bifurcation theory ensures that each such minimum value of R_c is associated with a nonlinear branching solution and hence a possible roll mode. When truncated spectral models are used rather than infinite-dimensional partial differential equations, then the functional dependence of R_c on the other parameters of the problem can be determined via examination of either an explicit expression for R_c or from the real roots of an explicit polynomial governing R_c . In addition, the amplitudes of the nonlinear roll solutions can be given explicitly, and they usually correspond to cloud bands having the same spacing L that was given by the minimization procedure (Shirer, 1980). Thus, a more thorough knowledge of the dependence of the expected roll geometry on such additional parameters as the Coriolis parameter f or the Prandtl number P can be obtained from such an analytical analysis than that possible from a purely numerical one.

A major drawback of the low-order spectral approach is the severe truncation to a very few horizontal and vertical wavenumbers. In the model presented here, only a portion of the background wind shear is considered in the dynamic forcing—that portion having the same vertical wavenumber as that of the convective cell. But this can be a serious disadvantage in some cases. For example, at least two vertical wavenumbers would be needed in order to

capture even some of the information concerning the existence or location of an inflection point in the wind profile. As a consequence, the nonlinear response to the inflection point instability cannot be studied, although such a filter has the advantage of allowing a direct study of only the parallel modes. Thus the present analysis is only one step in a series of studies in which more information is added gradually until eventually the essential information in the large-scale forcing can be separated from the inessential.

In the problem examined here, a crucial observation is that the critical parameter values of R_c are nonlinear functions of the other parameters. By interpreting physically the minimum value of R_c to be the acceptable one, we must perform an extremum analysis on this nonlinear function. This type of analysis leads to consideration of a nonlinear polynomial in the auxiliary parameters, and as a consequence the linear problem becomes a nonlinear one. Surprisingly, because it is one involving such qualitative information as the number of real roots to the polynomial describing the minima of R_c , we are led naturally to ask the same type of topological questions concerning the form of the expected critical value of the bifurcation point that were discussed in Shirer and Wells (1983) about the form of the branching nonlinear solution itself. In the present analysis, if multiple solutions to the minimizing polynomial are possible, then we must ask whether all classes of transitions from one preferred mode to another are able to occur. If some transitions are not allowed, then in some sense the model is too restricted and some crucial degrees of freedom are missing. With the technique developed in Shirer and Wells (1983), the necessary degrees of freedom could be added and the resulting parameters associated with crucial physical effects. Results of this type are not possible from numerical analyses of the governing linearized

partial differential equations because explicit polynomials controlling the branching behavior are not determined.

In the present model, we find that only one minimum value for R_c exists when the atmosphere is stratified neutrally or unstably. For an Ekman profile in a neutral atmosphere, the preferred orientations and aspect ratios depend strongly on the Ekman depth, which we can consider explicitly here because we do not use it as a scaling parameter. For Ekman depth $D = z_T/(2\pi)$, we find an orientation angle $\theta \sim -18^\circ$ with respect to the geostrophic wind vector and a dimensionless wavelength $L/D \sim 18$. These values agree fairly well with those reported by Lilly (1966), Faller and Kaylor (1966), and others for the parallel mode. A depth of $z_T/(1.3\pi)$ produces $\theta \sim 4^\circ$ and $L/D \sim 13$ in excellent agreement with Faller and Kaylor (1967). Moreover, when $D = z_T/\pi$, we find that $\theta \sim 18^\circ$ and $L/D \sim 11$, which are values normally attributed to the inflection point mode (Brown, 1972; Asai and Nakasugi, 1973). These dependencies on the Ekman depth do not seem to be addressed in the literature and indicate that the usual convention of using D as a scaling parameter might mask some interesting behavior. In both of the above cases, the horizontal wavelengths L are of the order of 4.5 km when the circulation depth z_T is 1 km; ratios L/z_T of this magnitude are larger than those often cited for the inflection point and thermal modes (Brown, 1980), but have been observed to characterize some cloud streets by Walter (1980), Walter and Overland (1984), and Kelly (1982, 1984).

The above results apply to parallel modes that extract energy from a cosine mode of the background wind profile, and the values of θ and L seem to agree with previous ones when $D/z_T \sim 1/3 - 1/5$. But Ekman depths for actual cloud streets can be in the range $z_T/2 - z_T$ (Brümmer and Grant, 1985) for which the cosine parallel modes have unrealistic orientations. Here we

briefly consider the parallel modes originating from a sine mode of the background wind and we find that these roll circulations are oriented in the range $\pm 20^\circ$ when $D \sim z_T/2$ or larger. These calculations are intriguing and suggest that the cosine parallel modes characterize boundary layers having small Ekman depths, while the sine parallel modes characterize boundary layers having larger Ekman depths. Further work is needed to substantiate these conclusions.

When the stratification is stable as many as five local minima for R_c exist and the branching rolls derive their energy from the shear in the mean wind. The resulting roll geometries divide into two types. The first type is characterized by aspect ratios that are much less than 1 (or $L \gg 2z_T$), corresponding to rolls that are relatively widely spaced, and by orientation angles for which the Fourier coefficient of the roll-perpendicular shear is nearly zero; this roll derives significant energy from the roll-parallel wind shear. Sommeria and LeMone (1978) and Walter and Overland (1984) present evidence of such widely spaced rolls, which have width to height ratios of 15-30. The second type involves aspect ratios of order 1 (or $L \sim 2z_T$), corresponding to rolls that are about half as deep as they are wide, and by orientation angles for which both Fourier coefficients of the shear are non-zero; this roll derives significant energy from both components of wind shear. Two orientations are possible for these second modes, and they are 30° - 50° on either side of the orientation for a roll developing in a neutrally stratified atmosphere. Of note is that when the Ekman depth $D = z_T/(2\pi)$, then these second modes would have orientations near $\pm 15^\circ$ and dimensionless wavelengths L/D near 12. These are the orientations normally associated with inflection point instability and so there is the possibility that these second modes are related to the inflection point modes. Of course, for this

hypothesis to be verified, we would need to examine a model containing enough additional wavenumbers to represent explicitly the inflection point modes themselves. An alternative possibility is that these modes are the ones found by Kaylor and Faller (1972) in a stable rotating Ekman layer. They associated these modes with propagating internal gravity waves; moreover, they found that these modes extracted energy from the background wind field via the same mechanism as that responsible for the parallel instability modes.

Thus, we find that for a wide range of Reynolds numbers, or wind speeds at the top of the domain, the aspect ratios of both classes are within those typically reported when that particular class is associated with the global minimum value of R_c (see LeMone, 1973, and Kelly, 1984 for recent summaries). Although the above variations in orientation angles are large, some investigators have reported observed alignments in the range $\pm 25^\circ$ from the mean wind direction (Plank, 1966; Weston, 1980). With increasing wind speed at the top of the domain, different local minima become the global minimum, leading to discontinuous jumps in the preferred orientations and aspect ratios of the rolls. This may be interpreted as a change of mode within the parallel/thermal instability regime; more complicated behavior might be expected when enough degrees of freedom are included to allow modeling of the inflection point instability. In addition, we find that rolls may develop for all ranges of lapse rates owing to the combined parallel/thermal instability mechanism. But this is not a contradiction of the results of previous investigators (e.g. Brown, 1972; Wippermann et al., 1978) who showed that rolls could not develop in a sufficiently stable atmosphere. The values of both the Rayleigh number and the Reynolds number must exceed their respective critical values for rolls to develop, and this is equivalent to requiring that the value

of a Richardson number must not be too large. In this sense, then, rolls may exist only in either a weakly stable or an unstable thermal stratification.

We conclude that the problem of expected roll geometry is a surprisingly complicated nonlinear one that must be studied carefully. Because analyses of truncated spectral models lead to specific polynomials controlling the critical values of the external parameters and their extrema, these models are the natural ones to use for identification of all possible observable modes. Moreover, with recently developed techniques from nonlinear mathematics (Shirer and Wells, 1983), we can identify the crucial physical effects governing transitions from one class of modes to another. In this article, we present an analysis of a low-order model able to represent secondary circulations arising from a combination of the parallel and thermal instability mechanisms; we illustrate the results with an Ekman profile, and show how they depend on the Ekman depth. Application of the results to three cases from KonTur is presented in Shirer et al. (1985).

2. Development of the model

We study here three-dimensional moist shallow Boussinesq convection arising in a rotating fluid that is forced both thermally and dynamically. Consequently, we consider the secondary flow to be a perturbation superimposed on a hydrostatic, stratified, moving reference state given by

$$\underline{V}_H(z) = U(z) \underline{i} + V(z) \underline{j} \quad (2.1)$$

$$T_0(z) = T_{00} - \gamma_e z \quad (2.2)$$

$$p_0(z) = p_{00} - \rho_{00} g z \quad (2.3)$$

$$\rho_0(z) = \rho_{00} \quad (2.4)$$

in which the unit vectors are directed eastward and northward and T_{00} , P_{00} , ρ_{00} , and the environmental lapse rate γ_e are constants. The basic current $V_H(z)$ is of larger temporal and spatial scales than the convective flow and so is not constrained to be a solution to the Boussinesq equations. Moreover, we assume that the basic state is time-independent and so investigate only the means by which mean wind shear and thermal stratification affect the initial development of the convective motion.

The domain is illustrated in Fig. 2.1 in which the cloudy areas are indicated by hatching. The domain is 2π -periodic in the x - and y -directions, but is bounded in the vertical by the ground and the inversion height z_T ; for simplicity we assume these to be free upper and lower boundaries on which the vertical motion and temperature perturbations vanish. The cloudy areas are modeled by assuming that only the upward moving component of the flow above cloud base z_1 is moist adiabatic, with all other parts of the flow being dry adiabatic. In this way, the effects of water and its phase changes are represented implicitly. This is a refinement of the assumption used previously in Shirer and Dutton (1979) and Shirer (1980), in which all upward motion was moist adiabatic. The present approximation corresponds to the slice method stability criterion introduced by Bjerknes (1938).

Upon writing the dependent variables as

$$v(x, y, z, t) = V_H(z) + v'(x, y, z, t) \quad (2.5)$$

$$T(x, y, z, t) = T_0(z) + T'(x, y, z, t) \quad (2.6)$$

$$p(x, y, z, t) = p_0(z) + p'(x, y, z, t) \quad (2.7)$$

$$\rho(x, y, z, t) = \rho_0(z) + \rho'(x, y, z, t) \quad (2.8)$$

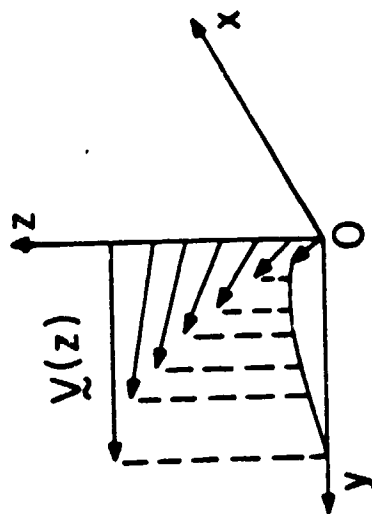
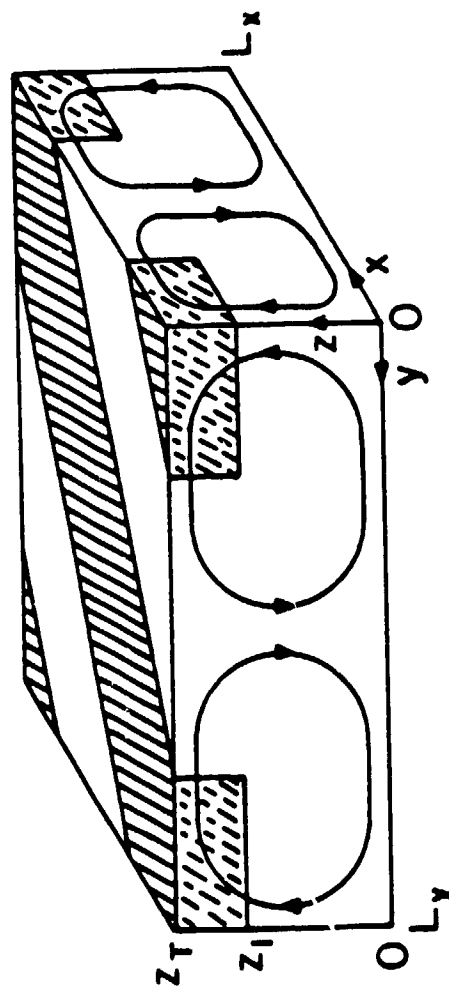


Figure 2.1 The model domain in which roll circulations are shown schematically. The hatched areas above cloud base z_1 denote cloud, regions of moist adiabatic flow.

we may write the shallow Boussinesq system as

$$\begin{aligned} \frac{\partial \mathbf{y}'}{\partial t} + \mathbf{y}' \cdot \nabla \mathbf{y}' + \mathbf{v}_H \cdot \nabla \mathbf{y}' + w' \frac{\partial \mathbf{y}_H}{\partial z} + 2\bar{\Omega} \times \mathbf{y}' + \rho_{oo}^{-1} \nabla p' \\ - g T' T_{oo}^{-1} \mathbf{k} - \nu \nabla^2 \mathbf{y}' = 0 \end{aligned} \quad (2.9)$$

$$\frac{\partial T'}{\partial t} + \mathbf{y}' \cdot \nabla T' + \mathbf{v}_H \cdot \nabla T' + w'(\gamma_d - \gamma_e) + w'_+(\gamma_m - \gamma_d)\delta - \kappa \nabla^2 T' = 0 \quad (2.10)$$

$$\nabla \cdot \mathbf{y}' = 0 \quad (2.11)$$

in which κ is the (constant) eddy thermometric conductivity, ν is the (constant) eddy viscosity, γ_e is the (constant) environmental lapse rate, γ_d is the dry adiabatic lapse rate, γ_m is the (constant) moist adiabatic lapse rate, and $\bar{\Omega}$ is the angular velocity of the earth. For the latent heating term $w'_+(\gamma_m - \gamma_d)\delta$, we define

$$w_+ = \begin{cases} w & \text{if } w > 0 \\ 0 & \text{if } w \leq 0 \end{cases} \quad (2.12)$$

$$\delta = \begin{cases} 1 & \text{if } z_1 \leq z \leq z_T \\ 0 & \text{if } 0 \leq z < z_1 \end{cases} \quad (2.13)$$

in which z_1 is cloud base. We note that because the horizontal and vertical velocity components are of the same order, we have included both the horizontal and vertical components $e = 2\bar{\Omega}\cos\phi$ and $f = 2\bar{\Omega}\sin\phi$ of the Coriolis force in (2.9). Also, we note that a solution to (2.9)-(2.11) is one for which all perturbations vanish, and this solution will be referred to as the

conductive, or trivial, one. Nonvanishing perturbations will correspond to the roll solution.

2.1. Dimensionless forms

For convenience we cast the system (2.9)-(2.11) in dimensionless form. The horizontal wavelengths of the periodic flow are L_x and L_y respectively, and they provide the appropriate horizontal length scales. The inversion height z_T is used to define the vertical scale, but this corresponds to only a half wavelength (Fig. 2.1). Consequently we define

$$x = x^* L_x / (2\pi) \quad (2.14)$$

$$y = y^* L_y / (2\pi) \quad (2.15)$$

$$z = z^* z_T / \pi \quad (2.16)$$

We did not use an Ekman depth D in (2.14)-(2.16) because we are developing a model having more applications than to only an Ekman profile. We show in Section 3.2.1 that variations in D can produce some large changes in the preferred orientations and wavelengths of the rolls.

In order for the systems to have as limits the two-dimensional cases $L_x \rightarrow \infty$ and $L_y \rightarrow \infty$, we use the horizontal wavelength

$$L_H = (L_x^{-2} + L_y^{-2})^{-1/2} \quad (2.17)$$

in the following definitions

$$t = t^* z_T L_H / (2\pi^2 \kappa) \quad (2.18)$$

$$u' = u^* \kappa \pi / z_T \quad (2.19)$$

$$v' = v^* \kappa \pi / z_T \quad (2.20)$$

$$w' = w^* 2\pi\kappa/L_H \quad (2.21)$$

$$U = U^* \kappa\pi/z_T \quad (2.22)$$

$$V = V^* \kappa\pi/z_T \quad (2.23)$$

$$T' = T^* \nu\kappa T_{00} \pi^3/(g z_T^3) \quad (2.24)$$

$$p' = p^* \rho_{00} \kappa^2 \pi^2/z_T^2 \quad (2.25)$$

We have chosen the length scales in (2.19)-(2.23) merely for convenience. The dimensionless systems will have a simpler form with the above choice than it would if u and v had been scaled by L_H and w by z_T .

With the additional definitions of the aspect ratios

$$a = 2 z_T/L_x \quad (2.26)$$

$$b = L_x/L_y \quad (2.27)$$

$$A = 2 z_T/L_H = a (1 + b)^{2/3} \quad (2.28)$$

the Rayleigh number

$$R = g z_T^4 (\gamma_e - \gamma_d)/(\nu\kappa T_{00}\pi^4) \quad (2.29)$$

the latent heating parameter

$$H = g z_T^4 (\gamma_d - \gamma_m)/(\nu\kappa T_{00}\pi^4) \quad (2.30)$$

the rotating Reynolds numbers, or dimensionless Coriolis terms,

$$e^* = e z_T^2/(\nu\pi^2) \quad (2.31)$$

$$f^* = f z_T^2/(\nu\pi^2) \quad (2.32)$$

the Prandtl number

$$P = \nu/\kappa \quad (2.33)$$

and the gradient and Laplacian operators

$$\tilde{\nabla} = j (1 + b^2)^{-1/2} \frac{\partial}{\partial x^*} + j b (1 + b^2)^{-1/2} \frac{\partial}{\partial y^*} + k \frac{\partial}{\partial z^*} \quad (2.34)$$

$$\tilde{\nabla}^2 = a^2 \frac{\partial^2}{\partial x^{*2}} + a^2 b^2 \frac{\partial^2}{\partial y^{*2}} + \frac{\partial^2}{\partial z^{*2}} \quad (2.35)$$

we may rewrite (2.9)-(2.11) in the dimensionless forms

$$\frac{\partial u^*}{\partial t^*} + y^* \cdot \tilde{\nabla} u^* + y_H^* \cdot \tilde{\nabla} u^* + w^* \frac{\partial u^*}{\partial z^*} - f^* P A^{-1} v^* + e^* P w^* \quad (2.36)$$

$$+ (1+b^2)^{-1/2} \frac{\partial p^*}{\partial x^*} - P A^{-1} \tilde{\nabla}^2 u^* = 0$$

$$\frac{\partial v^*}{\partial t^*} + y^* \cdot \tilde{\nabla} v^* + y_H^* \cdot \tilde{\nabla} v^* + w^* \frac{\partial v^*}{\partial z^*} + f^* P A^{-1} u^* \quad (2.37)$$

$$+ b(1+b^2)^{-1/2} \frac{\partial p^*}{\partial y^*} - P A^{-1} \tilde{\nabla}^2 v^* = 0$$

$$\frac{\partial w^*}{\partial t^*} + y^* \cdot \tilde{\nabla} w^* + y_H^* \cdot \tilde{\nabla} w^* - e^* P A^{-2} u^* + A^{-2} \frac{\partial p^*}{\partial z^*} \quad (2.38)$$

$$- P A^{-2} T^* - P A^{-1} \tilde{\nabla}^2 w^* = 0$$

$$\frac{\partial T^*}{\partial t^*} + y^* \cdot \tilde{\nabla} T^* + y_H^* \cdot \tilde{\nabla} T^* - R w^* - H w^* \delta - A^{-1} \tilde{\nabla}^2 T^* = 0 \quad (2.39)$$

$$\tilde{\nabla} \cdot y^* = 0 \quad (2.40)$$

That (2.36)-(2.40) is a suitable generalization of a two-dimensional system can be verified easily by noting that $b \neq 0$, or $L_H \neq L_x$, produces a system with no variation in the y^* -direction, and $b = \infty$, or $L_H \neq L_y$ produces one with no variations in the x^* -direction.

2.2. Spectral model

The smallest spectral model of rotating convection was studied by Veronis (1966), and it is the appropriate one on which to base the present model; in the irrotational case, the Veronis model reduces to the one discussed by Lorenz (1963). In the Veronis system, one wavenumber is used for representing the vertical velocity field, two for the horizontal velocity field, and two for the thermal perturbation. Here we use the same distribution of harmonics as in the Veronis model, but because we are studying three-dimensional flows in the presence of an arbitrary horizontal basic current $V_H(z)$, we must use all four possible combinations of the trigonometric functions in order to represent all possible phase relationships created by the linear terms in (2.36)-(2.40).

Consequently, an appropriate form for the spectral expansion is

$$\begin{aligned} q^* = & [q_1 \sin(x^* - y^*) + q_2 \cos(x^* - y^*) + q_3 \sin(x^* + y^*) \\ & + q_4 \cos(x^* + y^*)] \cos(z^*) + q_5 \sin[2(x^* - y^*)] \\ & + q_6 \cos[2(x^* - y^*)] + q_7 \sin[2(x^* + y^*)] \\ & + q_8 \cos[2(x^* + y^*)] \end{aligned} \quad (2.41)$$

$$\begin{aligned} w^* = & [w_1 \cos(x^* - y^*) + w_2 \sin(x^* - y^*) + w_3 \cos(x^* + y^*) \\ & + w_4 \sin(x^* + y^*)] \sin(z^*) \end{aligned} \quad (2.42)$$

$$T^* = [T_1 \cos(x^* - y^*) + T_2 \sin(x^* - y^*) + T_3 \cos(x^* + y^*) + T_4 \sin(x^* + y^*)] \sin(z^*) + T_5 \sin(2z^*) \quad (2.43)$$

in which q^* represents the form for the u^* , v^* , and p^* expansions. These expansions provide representations of every linear term in (2.36)-(2.40), except for the horizontal component e^* of the rotating Reynolds number. Either more wavenumbers in the vertical or a mixture of $\sin z^*$ and $\cos z^*$ terms would be needed in the expansions in order for e^* terms to remain in the spectral system; we consider the latter case briefly in Section 3.3. We note that the filtering of the e^* effects by the above truncation does not seem to cause serious problems in view of the results of Etling (1971), who notes that the orientation angles of the rolls are controlled by the vertical component f^* of the Coriolis force.

2.2.1 The roll form. The 33-coefficient spectral model obtained by substitution of (2.41)-(2.43) into (2.36)-(2.40) can be reduced to a 17-component one by using the spectral version of $\tilde{\nabla} \cdot \mathbf{v}^* = 0$ first to produce diagnostic equations relating the pressure coefficients p_1 to the other coefficients u_1 , v_1 , w_1 , and T_1 , and second to express the v_1 components as functions of u_1 , w_1 , and T_1 . This is the standard approach for three-dimensional incompressible systems (e.g. Dutton, 1976) and accomplishes the same task as that of the formation of vorticity equations in two-dimensional systems. Upon inspection of the resulting 17-component model, we find that the complete spectral system is composed of two 9-component subsystems:

$$R_1 = (u_1, u_2, u_5, u_6, w_1, w_2, T_1, T_2, T_5)$$

$$R_2 = (u_3, u_4, u_7, u_8, w_3, w_4, T_3, T_4, T_5)$$

If all the components of one subsystem are zero initially, then they always

will remain so; as in earlier models (Shirer and Dutton, 1979; Shirer, 1980), this behavior is typical of the primary convective solution that branches from the conductive, or trivial, one at the critical modified Rayleigh number. Nonlinear solutions in which all 17 components are nonzero would be secondary branches in this model, but we do not consider them here. Because the equations contain Fourier coefficients of the background wind field, the R_1 and R_2 subsystems cannot be reduced further. Upon inspection of the expansions (2.41)-(2.43) for the dependent variables, we see that R_1 is associated physically with two-dimensional rolls having axes parallel to the line $x^* = y^*$, while R_2 is associated with rolls having axes parallel to the line $x^* = -y^*$. Thus, R_1 and R_2 represent roll solutions that are perpendicular to one another in the dimensionless coordinate system, but are actually separated by the angle

$$\beta = 2 \tan^{-1}(1/b) = 2 \tan^{-1}(L_y/L_x) \quad (2.44)$$

We conclude then that a fundamental role of the basic wind field is to organize the convective solution into bands, a result consistent with the typical observation that rolls develop during windy, statically unstable conditions (Kuettnner, 1971). The same type of organization also will occur during windy, stable conditions, however, when the secondary circulations can derive energy from the mean wind.

In order to determine the expected roll geometry, we assume that the preferred orientation angles and aspect ratios are those that yield the smallest values for the critical modified Rayleigh number R_{mc} , or equivalently the smallest values for the critical Reynolds number Re_c . For some values of the external parameters, we will find in Section 3 that two or more orientation angles may produce minimum values for R_{mc} ; these angles rarely differ by as much as 90° , and when they do, the values of R_{mc} are not identical. Without loss of

generality, then, we may assume that one branch, say R_1 , will be associated with the roll that develops first at the absolute minimum value of R_{mc} . In order to simplify greatly the analysis, we rotate the (x^*, y^*) coordinate system in the horizontal plane to (\hat{x}, \hat{y}) , in which the \hat{x} and \hat{y} axes are respectively parallel to and perpendicular to the roll axis (Fig. 2.2). The orientation angle θ is then the angle between east and the roll axis, with angles north of east being positive and those south of east being negative.

The appropriate rotations for the eight u_i and v_i components in the (x^*, y^*) systems to the \tilde{u}_i and \tilde{v}_i components in the (\hat{x}, \hat{y}) system are

$$\tilde{u}_i = (bu_i + v_i)(1+b^2)^{-1/2} \quad i = 1, \dots, 8 \quad (2.45)$$

$$\tilde{v}_i = (-u_i + bv_i)(1+b^2)^{-1/2} \quad i = 1, \dots, 8 \quad (2.46)$$

If we denote temporal derivatives by an overdot, then the resulting spectral system is

$$\dot{\tilde{u}}_1 = -w_1 \tilde{u}_5 + w_2 \tilde{u}_6 - [P(A^2+1)/A] \tilde{u}_1 - \tilde{\Lambda}_2 \tilde{u}_2 + (f^*P/A) w_1 - \tilde{\Gamma}_1 w_2 \quad (2.47)$$

$$\dot{\tilde{u}}_2 = -w_1 \tilde{u}_6 - w_2 \tilde{u}_5 + \tilde{\Lambda}_2 \tilde{u}_1 - [P(A^2+1)/A] \tilde{u}_2 - \tilde{\Gamma}_1 w_1 - (f^*P/A) w_2 \quad (2.48)$$

$$\dot{\tilde{u}}_5 = \frac{1}{2} \tilde{u}_1 w_1 + \frac{1}{2} \tilde{u}_2 w_2 - 4PA \tilde{u}_5 - (\tilde{\Lambda}_2 + \tilde{\Lambda}_4) \tilde{u}_6 \quad (2.49)$$

$$\dot{\tilde{u}}_6 = -\frac{1}{2} \tilde{u}_1 w_2 + \frac{1}{2} \tilde{u}_2 w_1 + (\tilde{\Lambda}_2 + \tilde{\Lambda}_4) \tilde{u}_5 - 4AP \tilde{u}_6 \quad (2.50)$$

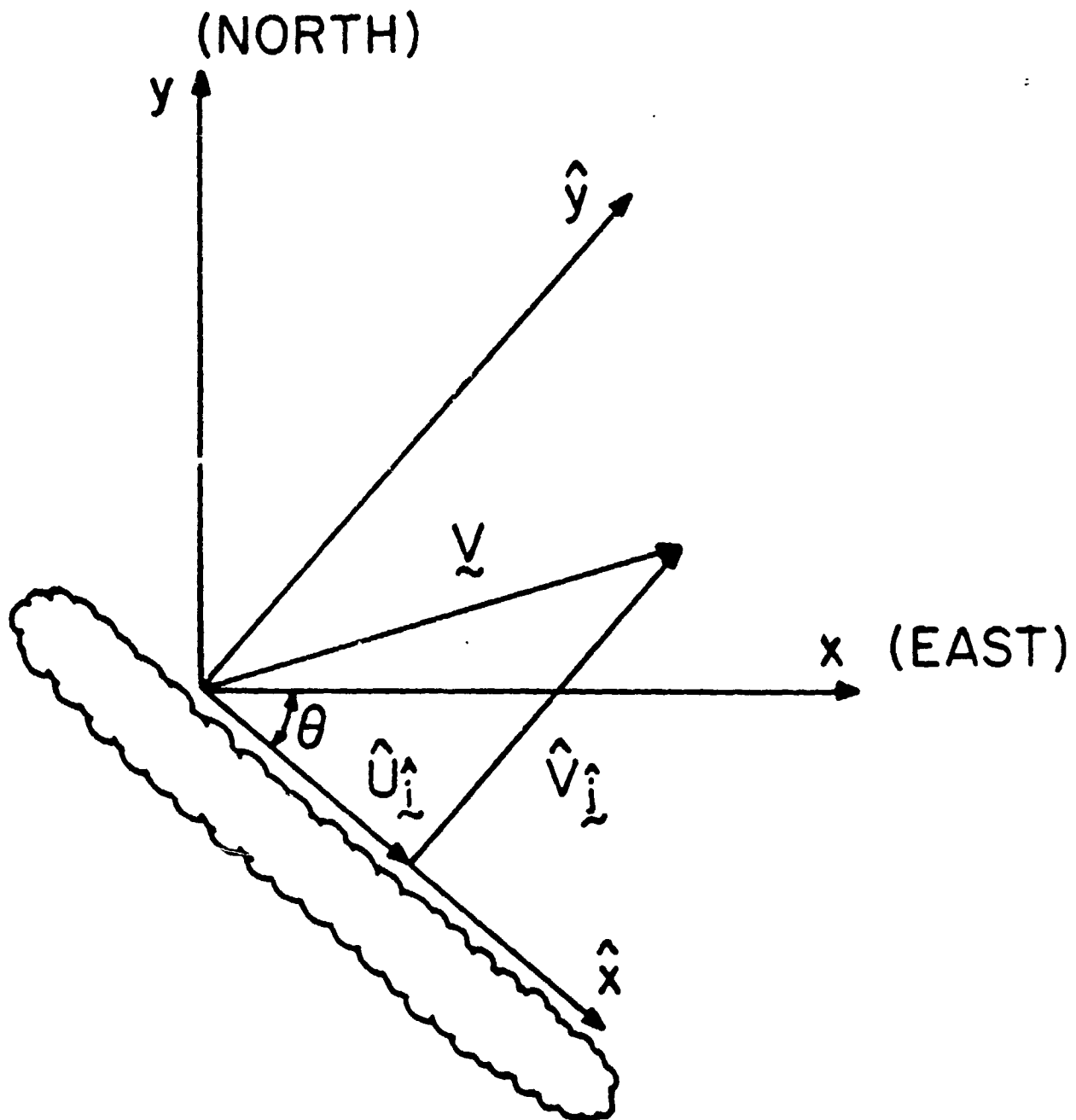


Figure 2.2 Relationship between the natural coordinate system (x^* , y^*) and the roll coordinate system (\hat{x} , \hat{y}). The orientation angle between east and the roll axis is denoted by θ ; orientations north of east are given by positive values of θ , south of east by negative values of θ .

$$\begin{aligned}\dot{w}_1 = & -\{f^*P/[A(A^2+1)]\}\bar{u}_1 - [P(A^2+1)/A]w_1 \\ & + \{[2\bar{\Lambda}_2+(A^2-1)\bar{\Lambda}_4]/(A^2+1)\}w_2 + [P/(A^2+1)]T_1\end{aligned}\quad (2.51)$$

$$\begin{aligned}\dot{w}_2 = & \{f^*P/[A(A^2+1)]\}\bar{u}_2 - \{[2\bar{\Lambda}_2+(A^2-1)\bar{\Lambda}_4]/(A^2+1)\}w_1 \\ & - [P(A^2+1)/A]w_2 + [P/(A^2+1)]T_2\end{aligned}\quad (2.52)$$

$$\dot{T}_1 = w_1T_5 + (R + Hn_1)w_1 - [(A^2+1)/A]T_1 + \bar{\Lambda}_4T_2 \quad (2.53)$$

$$\dot{T}_2 = w_2T_5 + (R + Hn_1)w_2 - \bar{\Lambda}_4T_1 - [(A^2+1)/A]T_2 \quad (2.54)$$

$$\dot{T}_5 = -\frac{1}{2}(w_1T_1 + w_2T_2 + w_3T_3 + w_4T_4) - (4/A)T_5 \quad (2.55)$$

$$\begin{aligned}& + \frac{1}{2\pi} Hn_3 \int_0^{2\pi} [w_1^2 + w_2^2 + w_3^2 + w_4^2 \\ & + 2(w_1w_3 - w_2w_4)\cos(2x^*) \\ & + 2(w_1w_4 + w_2w_3)\sin(2x^*)]^{1/2} dx^*\end{aligned}$$

$$\dot{\tilde{v}}_3 = -w_3\tilde{v}_7 + w_4\tilde{v}_8 + F_1\tilde{v}_3 + S_1\tilde{v}_4 + F_2w_3 + S_2w_4 - B_1T_3 \quad (2.56)$$

$$\dot{\tilde{v}}_4 = -w_3\tilde{v}_8 - w_4\tilde{v}_7 - S_1\tilde{v}_3 + F_1\tilde{v}_4 + S_2w_3 - F_2w_4 + B_1T_4 \quad (2.57)$$

$$\dot{\tilde{v}}_7 = \frac{1}{2}\tilde{v}_3\tilde{w}_3 + \frac{1}{2}\tilde{v}_4\tilde{w}_4 + B_2(\tilde{w}_3^2 - \tilde{w}_4^2) - 4AP\tilde{v}_7 + S_3\tilde{v}_8 \quad (2.58)$$

$$\dot{\tilde{v}}_8 = \frac{1}{2}\tilde{v}_4\tilde{w}_3 - \frac{1}{2}\tilde{v}_3\tilde{w}_4 - 2B_2\tilde{w}_3\tilde{w}_4 - S_3\tilde{v}_7 - 4AP\tilde{v}_8 \quad (2.59)$$

$$\dot{\tilde{w}}_3 = -F_3\tilde{v}_3 - F_4\tilde{w}_3 - S_4\tilde{w}_4 + B_3T_3 \quad (2.60)$$

$$\dot{\tilde{w}}_4 = F_3\tilde{v}_4 + S_4\tilde{w}_3 - F_4\tilde{w}_4 + B_3T_4 \quad (2.61)$$

$$\dot{T}_3 = \tilde{w}_3T_5 + (R + Hn_1)\tilde{w}_3 - B_4T_3 - S_5T_4 \quad (2.62)$$

$$\dot{T}_4 = \tilde{w}_4T_5 + (R + Hn_1)\tilde{w}_4 + S_5T_3 - B_4T_4 \quad (2.63)$$

in which the definitions for B_i , F_i , and S_i are given in Appendix A.

2.2.2. Controlling parameters. From inspection of the above spectral system, we see that the appropriate vertical aspect ratio governing the stability will be $A = a(1 + b^2)^{1/2}$ in (2.28) which is given by the domain height z_T divided by half the horizontal wavelength L_H of the roll. For convenience, in the remainder of the article we will drop the subscript H when referring to the wavelength L of the roll. Also, we have used the following Fourier coefficients $\tilde{\Lambda}_1$ for the basic wind field and $\tilde{\Gamma}_1$ for the basic wind shear:

$$\tilde{\Lambda}_1 = 2\pi^{-1} \int_0^\pi \hat{U}^*(z^*) \cos^2 z^* dz^* \quad (2.64)$$

$$\tilde{\Lambda}_2 = 2\pi^{-1} \int_0^\pi \hat{V}^*(z^*) \cos^2 z^* dz^* \quad (2.65)$$

$$\tilde{\Lambda}_3 = 2\pi^{-1} \int_0^\pi \hat{U}^*(z^*) \sin^2 z^* dz^* \quad (2.66)$$

$$\tilde{\Lambda}_4 = 2\pi^{-1} \int_0^\pi \hat{V}^*(z^*) \sin^2 z^* dz^* \quad (2.67)$$

$$\tilde{\Gamma}_1 = \pi^{-1} \int_0^\pi \frac{\partial \hat{U}^*}{\partial z^*} \sin(2z^*) dz^* = \tilde{\Lambda}_3 - \tilde{\Lambda}_1 \quad (2.68)$$

$$\tilde{\Gamma}_2 = \pi^{-1} \int_0^\pi \frac{\partial \hat{V}^*}{\partial z^*} \sin(2z^*) dz^* = \tilde{\Lambda}_4 - \tilde{\Lambda}_2 \quad (2.69)$$

In which \hat{U}^* and \hat{V}^* denote the components of the background wind in the along-roll and the cross-roll directions, respectively (Fig. 2.2).

The Fourier coefficients for the latent heating terms are

$$n_1 = (1 - z_1^*/\pi)/2 + (4\pi)^{-1} \sin(2z_1^*) \quad (2.70)$$

$$n_3 = -4(3\pi^2)^{-1} \sin^3 z_1^* \quad (2.71)$$

In which z_1^* is the dimensionless cloud base height. We note that the Fourier coefficients (2.64)-(2.69) represent the portion of the ambient wind field felt directly by the roll, and as we show in Section 3, provide energy to the roll solutions via the parallel instability.

Latent heating effects enter the system (2.47)-(2.63) in two qualitatively different ways. First, they lead to definition of a modified Rayleigh number

$$R_m = R + Hn_1 \quad (2.72)$$

for which $R_m > 0$ occurs when the environmental lapse rate γ_e exceeds a weighted average of the dry and moist adiabatic lapse rates; this inequality may be written as

$$\gamma_e > (1 - n_1) \gamma_d + n_1 \gamma_m \quad (2.73)$$

Because n_1 can be interpreted as the cross-sectional area of the cloudy region, (2.73) is equivalent to the slice method instability criterion of Bjerknes (1938). The modification (2.72) of the Rayleigh number is the only manner by which the latent heating effects will enter the characteristic equation and the stability determination in Section 3.

However, when cloud base is between the bottom and the top of the domain, a second latent heating term n_3 is produced in the equation (2.55) for the coefficient T_5 of (2.43) that represents the convective alteration of the vertical temperature profile. The term n_3 was not in the models of Shirer and Dutton (1979) or Shirer (1980) because they assumed that the cloud base z_1^* was at the bottom of the domain; from (2.71), we see that $n_3 = 0$ in their case of $z_1^* = 0$. In (2.55) we correct an error in Shirer (1982) who did not calculate this latent heating term correctly and who consequently produced a qualitatively incorrect branching diagram in his Fig. 3.

The need for n_3 in (2.55) arises from the assumption that latent heating occurs only in regions of upward motion in the upper portions of the domain. Consequently, the convective solution alters the background temperature profile differently above and below cloud base z_1^* and n_3 represents some of this effect. From (2.71) we see that this asymmetric heating is most pronounced and n_3 reaches its largest value when $z_1^* = \pi/2$ corresponding to a cloud base in the middle of the domain; as z_1^* approaches either 0 or π , the asymmetry in heating vanishes and so does n_3 . As noted above, this affects only the nonlinear

convective solution through the magnitude of T_5 and does not alter the critical value of R_m .

The coefficient of the n_3 term in (2.55) is an elliptic integral involving the Fourier coefficients of the vertical velocity and so its value depends on the magnitude of the solution itself; moreover, it provides an energy source in the equation for the only term that links the magnitudes of the R_1 and R_2 rolls. The possibility exists that a secondary branch connecting the two roll solutions is present and significantly affected by the magnitude of the n_3 term. However, the details of this secondary branch would be modified greatly in all likelihood in a spectral model containing more degrees of freedom. Also, the occurrence of an elliptic integral makes analytic study of these branching solutions quite difficult. Thus, we do not investigate the secondary branching properties of (2.47)-(2.63). Fortunately, however, the elliptic integral can be calculated for the two-dimensional R_1 and R_2 branches; in these cases, (2.55) simplifies either to

$$\dot{T}_5 = -\frac{1}{2}w_1T_1 - \frac{1}{2}w_2T_2 - (4/A)T_5 + Hn_3 (w_1^2 + w_2^2)^{1/2} \quad (2.74)$$

or to

$$\dot{T}_5 = -\frac{1}{2}w_3T_3 - \frac{1}{2}w_4T_4 - (4/A)T_5 + Hn_3 (w_3^2 + w_4^2)^{1/2} \quad (2.75)$$

The forms (2.74)-(2.75) eliminate the transcritical bifurcation shown in Fig. 3 of Shirer (1982) and thereby lead to qualitatively correct Hopf bifurcations (see Iooss and Joseph, 1980). In addition, the corrected system contains temporally periodic roll solutions that are sinusoidal functions of time and whose amplitudes can be calculated analytically, as found by Shirer (1980) in the case of $z_1^* = 0$.

From inspection of (2.47)-(2.63) and (A.1)-(A.13) we see that the R_1 roll does not depend on the horizontal aspect ratio b , and so this roll does not feel the presence of the R_2 roll at all. When $b=1$ and the two rolls are perpendicular to one another, we find that the equations governing the R_2 roll have the same form as those for the R_1 roll. But when $b \neq 1$, the R_2 roll depends strongly on b , and therefore via (2.44) on the angle β separating the two. Because there is no nonlinear coupling of the two roll forms, there is no way in this model to determine a preferred value of b or β . A larger model would be needed containing a secondary solution linking the two rolls (cf. Chang and Shirer, 1984), and minimizing with respect to b the corresponding secondary bifurcation point on the R_1 branch would likely lead to the expected separation angle β . Thus, in the remainder of the article, we consider only the development of the R_1 roll.

2.2.3. Energetics. In order to elucidate the energy sources for the R_1 roll, we form an energy equation from (2.47)-(2.54) and (2.74). Upon defining the energy E as

$$E = \frac{1}{2} \tilde{u}_1^2 + \frac{1}{2} \tilde{u}_2^2 + \tilde{u}_5^2 + \tilde{u}_6^2 + \frac{1}{2}(A^2+1)(w_1^2 + w_2^2) + \frac{1}{2} PT_1^2 + \frac{1}{2} PT_2^2 + PT_5^2 \quad (2.76)$$

we find that

$$\begin{aligned} \dot{E} = & (R + Hn_1 + 1)P(w_1 T_1 + w_2 T_2) + 2Hn_3 P(w_1^2 + w_2^2)^{1/2} T_5 \\ & - \tilde{f}_1 (\tilde{u}_1 w_2 + \tilde{u}_2 w_1) \\ & - [P(A^2 + 1)/A] [\tilde{u}_1^2 + \tilde{u}_2^2 + (A^2 + 1)(w_1^2 + w_2^2) + T_1^2 + T_2^2] \\ & - 8PA(\tilde{u}_5^2 + \tilde{u}_6^2) - (8P/A)T_5^2 \end{aligned} \quad (2.77)$$

The first two terms on the right side of (2.77) are heat flux terms, the first of which representing the source for the convective instability. The third term is the usual Reynolds stress term (Dutton, 1976); because it depends on the shear component $\bar{\tau}_1$ parallel to the roll, it represents the source of the parallel instability. Not revealed by the energy equation is the need for the Coriolis term f^* in order for this instability to exist, but the linear analysis in Section 3 will demonstrate that f^* is indeed necessary. We note that the perpendicular shear component $\bar{\tau}_2$ does not appear in (2.77); thus, because this component is the energy source for the inflection point modes, we should not expect to find them as solutions to the model. The last terms are the dissipation terms; instability and roll development occur when the energy source terms are larger in magnitude than the dissipation terms. If there were no eddy viscous or conductivity effects included, then there would be no dissipation and therefore no energetically steady solutions possible, only amplifying or decaying ones. Although the appropriateness of using eddy viscosities in atmospheric models is in dispute, they are necessary here in order to create an energetically consistent system.

3. Expected roll geometry

The simplest results for observable roll characteristics are those given by a linear analysis of the stability of the trivial solution to (2.47)-(2.63). This analysis will provide both the preferred alignment and the expected ratio of the height to the width of the rolls, and these parameters are natural ones to be compared with observations such as those from KonTur (Shirer et al., 1985). In this section, we will find that a variety of roll configurations are possible, particularly when the thermal stratification is stable.

The (linear) stability of the conductive solution to (2.47)-(2.63) is governed by a seventeenth-degree polynomial that factors into a linear equation and two eighth-degree polynomials. The coefficients of one eighth-degree polynomial depend only on the Fourier coefficients (2.64)-(2.69) of the rotated wind field and so from this polynomial we may determine the value of the critical modified Rayleigh number R_{mc} (or critical Reynolds number Re_c --see (3.5) below) for the R_1 roll. The second eighth-degree polynomial governs the values of R_{mc} for the R_2 roll; as mentioned in the previous section, these values will be greater than those for the R_1 roll, and so are not considered in the analysis.

Each eighth-degree polynomial factors further into a product of quadratic and sixth-degree polynomials. Neutral (linear) stability, bifurcation and nonlinear roll solutions are signalled by the vanishing of the real part of one of the roots of the characteristic equation, and it is easy to show that this cannot happen for the roots of the quadratic. Consequently, the sixth-degree polynomial governs the development of the rolls, and this polynomial can be factored as follows

$$\begin{aligned}
 & \{(A^2 + 1) (A\lambda)^3 - (a_1 + ib_1) (A\lambda)^2 - (c_0 R_m + c_1 + id) (A\lambda) \\
 & - [e_0 R_m + e_1 + i(f_0 R_m + f_1)]\} \times \{(A^2 + 1) (A\lambda)^3 \\
 & - (a_1 - ib_1) (A\lambda)^2 - (c_0 R_m + c_1 - id) (A\lambda) \\
 & - [e_0 R_m + e_1 - i(f_0 R_m + f_1)]\} = 0
 \end{aligned} \tag{3.1}$$

in which the coefficients are given in Appendix B. Hopf bifurcation to a temporally periodic nonlinear solution, which has limiting frequency $\text{Im}(\lambda)$, is given by $\text{Re}(A\lambda) = 0$, or by $A\lambda = \pm i\alpha$. When this form is substituted into (3.1), we obtain the coupled system in the critical Rayleigh number R_{mc} and α :

$$a_1 \alpha^2 + d\alpha - (e_0 R_{mc} + e_1) = 0 \quad (3.2)$$

$$(A^2 + 1)\alpha^3 - b_1 \alpha^2 + (c_0 R_{mc} + c_1)\alpha + f_0 R_{mc} + f_1 = 0 \quad (3.3)$$

Only real values for α are admissible solutions to (3.2)-(3.3). The common roots of (3.2)-(3.3) can be found by dividing the quadratic (3.2) into the cubic (3.3) and then requiring that the remainder vanishes. This leads to a cubic equation in R_{mc}

$$l_3 R_{mc}^3 + l_2 R_{mc}^2 + l_1 R_{mc} + l_0 = 0 \quad (3.4)$$

the coefficients of which are given in Appendix B. It is easy to show that real roots of (3.4) occur if and only if real roots of (3.2)-(3.3) occur and so all real roots of (3.4) are acceptable.

Significantly, the coefficients l_i do not depend on the wind coefficients $\bar{\Lambda}_1 - \bar{\Lambda}_4$, but on the shear coefficients $\bar{\Gamma}_1$ and $\bar{\Gamma}_2$; so the stability of the conductive solution, and hence the value of R_{mc} , can be altered only when secondary circulations develop in the presence of mean wind shear. This result is consistent with that obtained by Kuettner (1971) and Shirer (1980). The magnitudes of $\bar{\Gamma}_1$ and $\bar{\Gamma}_2$ vary as the roll alignment varies, and so the magnitude of R_{mc} depends on the orientation angle θ . Finding the minimum values R_g of R_{mc} will yield expected orientation angles by producing preferred values for $\bar{\Gamma}_1$ and $\bar{\Gamma}_2$. As we will see below, the fact that R_{mc} is governed by a cubic equation that may have either 1 or 3 real roots complicates the analysis considerably.

We can separate the orientation angle from $\bar{\Gamma}_1$ and $\bar{\Gamma}_2$ by noting that we may normalize the wind profile by the wind speed $|V(z_T)|$ at the inversion height z_T and define a Reynolds number Re by

$$Re = |V(z_T)| z_T/\nu = |V^*(\pi)| \pi/P \quad (3.5)$$

With the fact that both the wind shear coefficients \tilde{r}_1 and \tilde{r}_2 are given by differences between two coefficients for the wind components themselves (cf. (2.68)-(2.69)), we may express \tilde{r}_1 and \tilde{r}_2 as

$$\tilde{r}_1 = Re P [a_5 \cos(\theta) + a_6 \sin(\theta)] \quad (3.6)$$

$$\tilde{r}_2 = Re P [a_6 \cos(\theta) - a_5 \sin(\theta)] \quad (3.7)$$

in which

$$a_5 = -2[|V^*(\pi)|\pi^2]^{-1} \int_0^\pi U^*(z^*) \cos(2z^*) dz^* \quad (3.8)$$

$$= -2[\pi|V(z_T)|z_T]^{-1} \int_0^{z_T} U(z) \cos(2\pi z/z_T) dz$$

$$a_6 = -2[|V^*(\pi)|\pi^2]^{-1} \int_0^\pi V^*(z^*) \cos(2z^*) dz^* \quad (3.9)$$

$$= -2[\pi|V(z_T)|z_T]^{-1} \int_0^{z_T} V(z) \cos(2\pi z/z_T) dz$$

and U and V are the background wind components in the natural east/north coordinate system. Here θ is the angle between east and the roll axis, with positive values for angles north of east. Thus, we see from (3.6)-(3.7) that \tilde{r}_1 and \tilde{r}_2 are equivalent to Re and θ ; in addition, we have separated the wind shear components into easily measurable quantities a_5 and a_6 that depend exclusively on the ambient wind profile and the dimensionless parameters Re and P that depend on the less accessible values of eddy viscosity ν and conductivity κ . With KonTur data in Shirer et al. (1985), we determine a_5 and a_6

from aircraft observations of $\bar{v}(z)$ and z_T and then we ask whether reasonable values of ν and κ will produce consistent values for θ , A^2 , $R_g = \min(R_{mc})$, and $\min(Re_c)$.

With (3.6)-(3.7) we find that (3.4) may be written in the form

$$\begin{aligned} R_{mc}^3 + (k_1 + k_2 Re_c^2) R_{mc}^2 + (k_3 + k_4 Re_c^2 + k_5 Re_c^4) R_{mc} \\ + (k_6 + k_7 Re_c^2 + k_8 Re_c^4 + k_9 Re_c^6) = 0 \end{aligned} \quad (3.10)$$

We note that if we should view Re_c^2 as the critical parameter, then (3.10) is a cubic polynomial in Re_c^2 . In the analysis presented in Section 3.2, we will view the problem as simultaneously one in R_{mc} and Re_c^2 and admit only those modes corresponding to minima with respect to both critical values. The results then will not depend on the prejudices of the investigator. Also, we note that for very large values of Re_c^2 , (3.10) becomes a cubic equation in the (moist) critical Richardson number (Asai and Nakasuj1, 1973)

$$Ri_c = - R_{mc} (Re_c^2 P)^{-1} \quad (3.11)$$

Requiring that R_m and Re both exceed their respective critical values then is equivalent to requiring that $Ri < Ri_c$.

3.1 Special cases

There are three cases in which the cubic equation (3.4) for R_{mc} or Re_c^2 can be factored easily. As a prelude to the general situation presented below in Section 3.2, we briefly discuss these cases here.

3.1.1 $f^* = 0$. The irrotational case was considered previously in the two-dimensional model of Shirer (1980). Here the roots of the cubic (3.4) are given by

$$R_{mc} = (A^2 + 1)^3/A^2 + 4\tilde{\Gamma}_2^2 [(A^2 + 1)(P + 1)^2]^{-1} \quad (3.12)$$

and

$$R_{mc} = 2(P + 1) (A^2 + 1)^3/A^2 - (A^2 - 1)\tilde{\Gamma}_2^2/P \\ \pm i 2(A^2 + 1) \tilde{\Gamma}_2 [A^4 (P - 1) + 3P + 1] (AP)^{-1} \quad (3.13)$$

The first root is the same as that found in Shirer (1980) and shows that the effect of the perpendicular shear is to suppress convection; the minimum value R_s of R_{mc} is given by the vanishing of $\tilde{\Gamma}_2$ in order that the roll does not feel directly the perpendicular shear. From (3.7) we see that $\tilde{\Gamma}_2 = 0$ is given by the value θ_0 of θ for which

$$\tan(\theta_0) = a_6/a_5 \quad (3.14)$$

This angle is the same as α_2 in Shirer (1980). In addition, the preferred value $A^2 = 1/2$ for the squared aspect ratio is the same as that found in Rayleigh-Bénard convection.

The second root is complex, except in the singular case $P = (A^4 - 1)/(A^4 + 3)$. This can occur only when $A^2 > 1$ and $P < 1$. When P and A^2 are related in this way, we obtain from (3.13) a value for R_{mc} that is reduced by the magnitude of the perpendicular shear component $\tilde{\Gamma}_2$. This is a signature of the inflection point instability, by which rolls would be able to extract energy from the shear component $\tilde{\Gamma}_2$. But because of the singular nature of this second solution, we cannot conclude that inflection point modes exist in the model. However, we can conclude that modes in which $A^2 > 1$ and $\tilde{\Gamma}_2$ is nonzero might be possible in the rotational case, and in Section 3.2, we will demonstrate that indeed they do exist.

3.1.2 $\bar{\Gamma}_2 = 0$ and $F = 1$. Because the expected orientation angle is given

by $\bar{\Gamma}_2 = 0$ when $f^* = 0$, it is natural to investigate the rotational solutions in this case. The cubic (3.4) yields only one root for R_{mc} and it is given by

$$R_{mc} = [(A^2 + 1)^3 + f^{*2}] A^{-2} - f^{*2} \bar{\Gamma}_1^2 [4(A^2 + 1)^3]^{-1} \quad (3.15)$$

When $f^* \sim 0.1$, Shirer (1982) showed that (3.15) gives a good approximation to R_{mc} when $\bar{\Gamma}_2 \neq 0$; values of $f^* \sim 1$ can occur commonly, however.

The first term in (3.15) is the usual critical Rayleigh number for convection in a rotating fluid (Chandrasekhar, 1961; Veronis, 1966), and the second represents a destabilizing term arising in the presence of rotation from the wind shear component parallel to the roll axis. This is a manifestation of the parallel instability mechanism of Lilly (1966), which would be given here by the case $R_{mc} = 0$. We note that f^* is essential to the existence of this mechanism, in agreement with Lilly (1966) who found that the parallel modes disappeared in the irrotational (Orr-Sommerfeld) case. Inspection of (2.47)-(2.48) reveals that the Coriolis and viscous terms are of the same order of magnitude when $f^* \sim 1$ and this also agrees with an observation Lilly (1966) made concerning a necessary condition for the existence of this mode. The form of (3.15) suggests that in the present model, there is one instability mechanism having as special cases the two mechanisms of thermal and parallel instability. Apparently, then, it might not be correct to view them as separate mechanisms leading to convective solutions having different characteristic geometries (Etling, 1971; Asai and Nakasugi, 1973). The model discussed here effectively links the two mechanisms, although we will find in Section 3.2 that three branching nonlinear solutions are possible in some cases and that for some values of Re , one root yields the minimum value R_g of R_{mc} , while for different values of Re , the other two roots produce R_g .

3.1.3 $R_{mc} = 0$. Parallel instability is usually discussed in the absence of thermal effects, which corresponds here to a (moist) neutral stratification. The constant term l_0 in (3.4) can be factored, but when $R_{mc} = 0$ only one root exists for which Re_c^2 is both real and positive. This root is given by

$$\begin{aligned} & [(A^2 + 1)^3 + f^{*2}] A^{-2} - f^{*2} \tilde{\Gamma}_1^2 [4P^2 (A^2 + 1)^3]^{-1} \\ & + (A^2 - 1)^2 \tilde{\Gamma}_2^2 [4P^2 (A^2 + 1)]^{-1} = 0 \end{aligned} \quad (3.16)$$

When we use (3.6)-(3.7) to express (3.16) in terms of Re_c^2 and θ , we find that the minimum value of Re_c^2 occurs when $\tan(\theta) = a_6/a_5$. This is the same orientation angle that we found in (3.14) for the general irrotational case; of interest here is that θ_0 gives the maximum value for the along-roll shear component $\tilde{\Gamma}_1$, a fact consistent with the occurrence of parallel modes. For this orientation angle θ_0 , the critical value Re_c^2 of Re^2 is given by

$$Re_c^2 = 4(A^2 + 1)^3 [(A^2 + 1)^3 + f^{*2}] [A^2 f^{*2} (a_5^2 + a_6^2)]^{-1} \quad (3.17)$$

which is independent of the Prandtl number P . For the expected aspect ratio A , we find from $\partial Re_c^2 / \partial A^2 = 0$ that A^2 and f^* must be related by

$$(A^2 + 1)^3 (5A^2 - 1) + f^{*2} (2A^2 - 1) = 0 \quad (3.18)$$

showing that $1/5 < A^2 < 1/2$, which corresponds to broader cells than provided by Rayleigh-Bénard instability. When $f^* \sim 0.1$ and Re_c^2 is large in magnitude, we have $A^2 \sim 0.201$; but when $f^* \sim 1.0$, we have $A^2 \sim 0.25$. For a domain height of 1 km, we find that $A^2 \sim 0.2$ corresponds to roll wavelengths $L \sim 4500$ m, while $A^2 \sim 0.25$ corresponds to $L \sim 4000$ m. Observational evidence for such large ratios of L/z_T have been given recently by Walter (1980) and Kelly (1984).

We will find that the minimum value of R_{mc} can be given in the general case by $R_{mc} = 0$, and in this case Re_c^2 , θ , A^2 , and f^* satisfy (3.14), (3.17), and (3.18). We note that the truncated model presented here, unlike the one discussed in Shirer (1982), has a nontrivial nonlinear solution when $R_{mc} = 0$; this occurs because, unlike in the Lorenz (1963) form on which the Shirer (1982) model was based, the rotating convection truncation of Veronis (1966) produces nonlinear terms in the equations of motion (2.47)-(2.50).

3.2 The general case

We have found in the previous subsection that the single branching mode occurring when $f^* = 0$ or $R_{mc} = 0$ has an orientation given by $\tilde{r}_2 = 0$ or $\tan(\theta) = a_6/a_5$; for this mode we discovered that the preferred value of A^2 decreased from $1/2$ as the value of Re_c^2 was increased. Thus, as discussed in Shirer (1982), we might expect in the general case to find preferred orientations near $\theta_0 = \tan^{-1}(a_6/a_5)$ and squared aspect ratios satisfying $A^2 \ll 1$. But R_{mc} is governed by a cubic polynomial and so two other real roots having correspondingly different geometries might be possible. As hinted by the complex roots in the irrotational case (Section 3.1.1), we will find here that other modes near $A^2 \sim 1.0$ are indeed possible when the value of Re_c^2 is large enough.

In order to develop a coherent picture of the expected branching behavior, we first determine for fixed Re_c the minimum values of R_{mc} with respect to the orientation angle θ and for fixed R_{mc} the minimum values of Re_c^2 : both are given by (3.10). As mentioned previously, this is consistent with the view that the value of Ri must be smaller than an appropriate one Ri_c . Upon implicitly differentiating (3.10) with respect to θ and using the fact that both $\partial R_{mc}/\partial \theta = 0$ and $\partial Re_c^2/\partial \theta = 0$ at a minimum, we obtain

$$k_{10}R_{mc}^2 + (k_{11} + k_{12}Re_c^2) R_{mc} + k_{13} + k_{14}Re_c^2 + k_{15}Re_c^4 = 0 \quad (3.19)$$

We may combine (3.10) and (3.19) via polynomial division to produce a single polynomial in Re_c^2 governing the extrema of R_{mc} (or of Re_c):

$$r_6Re_c^{12} + r_5Re_c^{10} + r_4Re_c^8 + r_3Re_c^6 + r_2Re_c^4 + r_1Re_c^2 + r_0 = 0 \quad (3.20)$$

Once Re_c^2 is obtained from (3.20), we obtain R_{mc} from (3.19). The above analysis introduces spurious roots into (3.20), which can be identified from the division calculation. Moreover, the roots of (3.20) provide both maxima and minima of R_{mc} and Re_c^2 , but these can be identified from the signs of $\partial^2 R_{mc} / \partial \theta^2$ and $\partial^2 Re_c^2 / \partial \theta^2$. Only extrema that are minima of both R_{mc} and Re_c are accepted, and so the problem yields the same results whether we view the critical parameter to be R_m or to be Re .

As an example, we use the Ekman profile

$$U^*(z^*) = |v_g^*| [1 - \exp(-z^*/D^*) \cos(z^*/D^*)] \quad (3.21)$$

$$V^*(z^*) = |v_g^*| \exp(-z^*/D^*) \sin(z^*/D^*) \quad (3.22)$$

Here $D^* = D\pi/z_T$ is a dimensionless Ekman depth, which in some cases will be related to f^* via $D^* = (2/f^*)^{1/2}$; but because we have not constrained U^* and V^* to solve the governing system (2.36)-(2.40), we will not always link D^* and f^* . Here an orientation angle of 0° corresponds to a roll aligned parallel to the (westerly) geostrophic wind. We note that in Shirer et al. (1985), we show for the KonTur cases that the preferred wavelengths of the rolls are not particularly sensitive to the form of the wind profile, although the orientation angles are.

3.2.1 Parallel modes. In Table 1 we show how the Fourier coefficients a_5 and a_6 vary as functions of Ekman depth D when the domain height is 1 km and the latitude is 45°N ; for convenience we have assumed that $|V(z_T)| = |V_g|$ in (3.8)-(3.9). We also give the preferred orientation angles θ_0 , dimensionless wavelengths L/D and critical Reynolds numbers Re (3.17) and

$$Re_D = |V_g|D/\nu \quad (3.23)$$

We consider both the cases in which f^* is tied to D^* via $f^* = 2/D^{*2}$ (denoted by T) and the case in which f^* is untied to D^* (denoted by U); when f^* is untied we instead link it to Re_c so that $|V_g| = 10$ m/sec. In all cases f^* and A^2 are related by (3.18), and we may calculate corresponding values of $|V_g|$ and ν .

An inspection of Table 1 reveals that, whether f^* is tied to D^* or not, the orientation angles and dimensionless wavelengths depend strongly on D . From depictions of roll circulations obtained in previous studies (e.g. Faller and Kaylor, 1966) we find that the roll circulations are in the range $5D-6D$; moreover, they are oriented at -15° to -20° when they have dimensionless wavelengths of 20-24 but they are oriented at $2^\circ-6^\circ$ when they have wavelengths of 13-17 (Lilly, 1966; Faller and Kaylor, 1966, 1967). For the tied case usually considered in the literature, the reported values agree with those in Table 1: when $D = 159$ m we find that $\theta = -18^\circ$ and $L/D = 18$ and when $D = 245$ m we have $\theta = 4^\circ$ and $L/D = 13$. The values of Re_D are smaller than those normally cited (e.g. Lilly, 1966). But we have used free rather than rigid boundary conditions in formulating the model, and Faller and Kaylor (1967) noted that the critical Reynolds number is smaller in the free case. Thus, we conclude that we are representing correctly the parallel instability mode. But we discover from Table 1 that for small values of D , only in the untied case do the values of ν and $|V_g|$ correspond to atmospheric ones, and

Table 1.

Preferred geometries for pure parallel modes at latitude 45°N (U-untied, T-tied).

D(m)	D*	a5	a6	f*	$\theta(\text{deg})$	L/D	Re	ReD	$v(\text{m}^2/\text{s})$	$ v_g (\text{m/s})$
159.	0.50	0.06068	-0.02022	{ 0.36U 8.0T	-18.4 -18.4	27.5 18.3	346. 83.	55.1 13.2	29. 1.3	10. 0.11
245.	0.77	0.07168	0.00503	{ 0.34U 3.4T	4.4 4.4	17.9 13.1	326. 81.	79.8 19.9	31. 3.1	10. 0.25
318.	1.0	0.06342	0.02114	{ 0.35U 2.0T	18.4 18.4	13.8 11.1	338. 101.	108. 32.0	30. 5.2	10. 0.53
440.	1.4	0.04410	0.03042	{ 0.40U 1.0T	34.6 34.6	9.9 9.1	380. 179.	167. 78.9	26. 10.	10. 1.9
623.	2.0	0.02454	0.02806	{ 0.48U 0.52T	48.8 48.8	6.9 6.9	460. 428.	286. 267.	22. 20.	10. 8.6
763.	2.4	0.01624	0.02377	{ 0.55U 0.35T	55.7 55.7	5.6 5.8	528. 797.	402. 608.	19. 30.	10. 24.

so, although the wavelengths are larger in this case, we generally prefer to view f^* and D^* as independent parameters.

As the value of D increases, the orientation changes markedly to one having positive values, the dimensionless wavelength decreases and the magnitude of Re increases dramatically. Remarkably, when $D^* = 1$, which is the value used in Shirer (1980, 1982), the values of θ and L/D agree with those usually cited for the inflection point modes. It is difficult to discern from previous studies whether the height of the circulation shrinks in half from $6D$ to $3D$ as the orientation switches from -20° to 20° , and so it is unclear whether the above calculations might provide an explanation for these other reported modes. In any case, because the results are sensitive to the value of D , it appears to be unwise to use the Ekman depth D to scale the variables in the equations.

3.2.2. Parallel/thermal modes. For the case $D^* = 1$, in Fig. 3.1 we show for 4 values of A^2 the magnitudes of Re_c as functions of θ for which simultaneous extrema in R_{mc} and Re_c^2 occur. In this example, we have chosen $z_T = 1000$ m, $P = 1$, and $\nu = 14 \text{ m}^2 \text{ sec}^{-1}$, which yield $f^* = 0.5 \neq 2/D^{*2}$. These values for ν and P are consistent with those typically cited (e.g. Krishnamurti, 1975). On the right side of Fig. 3.1 we show the dimensional values of $|V_g|$ corresponding to those on the left side for Re_c . In the figure, local minimum values of both R_{mc} and Re_c^2 are denoted by the solid lines, and local maximum values of both by dashed lines; the angle $\theta_0 = \tan^{-1}(a_6/a_5)$ and the values Re_0 of Re_c yielding $R_{mc} = 0$ are also denoted.

From Fig. 3.1 we obtain a picture remarkably similar to that often obtained in an entirely different context (Shirer and Wells, 1983). Diagrams having forms similar to those in Fig. 3.1 can be produced by cross-sections through surfaces whose altitudes represent the magnitudes of nonlinear

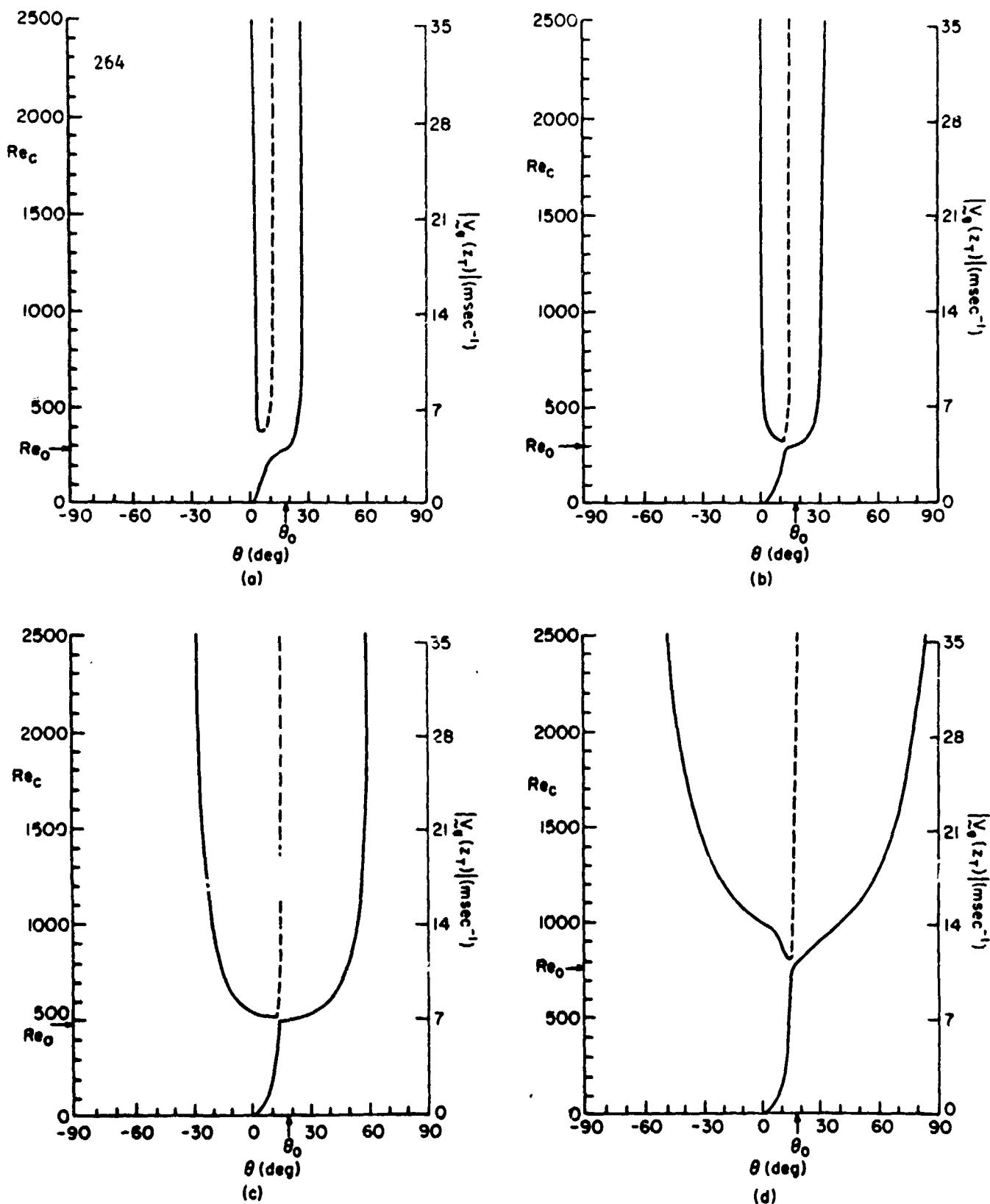


Figure 3.1 The magnitude of Re_c for which both R_{mc} and Re_c^2 are minima (solid lines) or maxima (dashed lines) with respect to θ . Here the mean wind is given by an Ekman profile (3.21)-(3.22), $z_T = 1000$ m, $D = 318$ m, $P = 1$, $v = 14$ m²sec⁻¹, $f^* = 0.5$ and $A^2 = 0.1$ (a), 0.5 (b), 1.0 (c) and 1.5 (d).

solutions to truncated spectral models. Here, however, we obtain a cross-section through a surface describing the relationship between two auxiliary parameters that is required to produce extreme values for the bifurcation point R_{mc} or Re_c^2 from which nonlinear solutions branch. Both types of surfaces are governed by polynomials and so it is not really surprising that qualitatively similar diagrams would be obtained in the two analyses.

From Fig. 3.1c we note that the mode having orientation angles near $\theta = \theta_0$ is a minimum when $Re_c < 490$ and $R_{mc} \leq 0$. But when two other minima appear, this mode becomes a maximum. Here, then, the vanishing of $\partial^2 R_{mc} / \partial \theta^2$ signalling a coalescence of a maximum and a minimum is analogous to the vanishing of a characteristic eigenvalue signalling a coalescence of two steady states (Iooss and Joseph, 1980). Interestingly, the transition from one extremum to three extrema occurs at values of Re_c corresponding to $R_{mc} < 0$, or to stable stratification. However, the three modes never meet; the closest the double point gets to the neutral case $R_{mc} = 0$ is $R_{mc} = -0.0698$ when $\theta = 13.45^\circ$ and $A^2 = 1.04$. As hinted by the irrotational special case (Section 3.1.1), the two new modes are born near $A^2 = 1$, at values of R_{mc} near $R_{mc} = 0$, and at orientation angles for which $\tilde{t}_2 \neq 0$.

As the values of A^2 are increased or decreased from $A^2 = 1$, however, the nose point moves gradually away from the other mode (Fig. 3.1b, d). As noted above, the form of these figures is that given by cross-sections through a cusp surface, with the one in Fig. 3.1c most nearly resembling the trident obtained by a cross-section through the cusp point. But typical cross-sections through cusp surfaces would show the isolated pairs of solutions switching places from the left to the right side of the other curve as the value of a second crucial parameter is varied. This switch does not occur in this example when $P = 1$, but it almost does near $A^2 = 1$ and $R_{mc} = 0$. Thus, the

fact that the neutral case produces only one acceptable root appears to signal that the present model might be missing a qualitatively crucial parameter. This parameter might be related to the Fourier coefficients of the wind profile having larger wavenumbers than the roll itself; these parameters would be necessary, for example, in order to describe enough characteristics of the wind profile that the inflection point instability mechanism could become active. Currently, we are investigating this possibility.

From the results presented here, we expect that as the wind speed increases, an orientation near that given by $\theta = \theta_0$ would be observed if the stratification were unstable, but that a rapid variation in orientation angle from $\theta = \theta_0$ to one far from $\theta = \theta_0$ would occur as the necessary stratification given by the values of R_{mc} , changes from unstable to stable. Large deviations of θ from θ_0 would be expected when the values of Re_c are large and the stratification is stable. We note that when the expected orientation angle problem is viewed as a problem in the branching behavior of a governing polynomial, then the existence of a range of Re_c for which θ varies rapidly can be predicted in advance if multiple solutions are possible because this behavior is typical of cross-sections through canonical surfaces like cusp surfaces. What is important physically is that the rapid variation in θ occurs near $R_{mc} = 0$ for which the boundary layer stratification is neutral, and so the alignment angle would be very sensitive to the sign of the value of R_{mc} .

When the requirement for minimum values of R_{mc} and Re_c^2 with respect to A^2 is added to the one discussed above, then the curves shown in Fig. 3.1 disconnect. Five curves for the local minima R_s of R_{mc} (and Re_c^2) occur when $P = 1$ and $f^* = 0.5$, as shown in Fig. 3.2 together with some selected corresponding values of A^2 . The solid curves denote the lines for which R_s is

a global minimum and so would provide the expected values of the parameters and consequently the observed geometry of the rolls. Although the global minimum occurs on the outer right curve when $Re_C \geq 750$, we note that the values for R_g associated with the outer left curve are very nearly the same as those for the outer right one and hence might provide global minima in a slightly more general model. We note that the left curve will produce a global minimum when the magnitude of P is of the order of 0.1.

Although we see that five local minima are possible in this case, we find that they divide into two classes. When the stratification necessary for roll development is unstable, which here is given by $Re_C = 230$ or very light winds, one mode exists near $\theta = \theta_0$. The aspect ratio for this mode decreases to $A^2 \sim 0.2$ or $L \sim 4.5$ km when $R_{mc} = 0$ and decreases further to extremely small values of $A^2 \sim 0.002$ or $L \sim 45$ km when $Re_C \sim 2400$. Thus, the first class is characterized by rolls having very small aspect ratios or very large horizontal wavelengths. Two other modes, one near $\theta = 0^\circ$ and the other near $\theta = 30^\circ$ are also in this first class, but they come into existence near $Re_C = 400$. The squared aspect ratios for these modes are larger than the ones for the middle mode, but the values of A^2 still decrease markedly as the value of Re_C is increased. The last two modes are in the second class, and they are born near $Re_C = 600$; these modes exist at very large angles (30° - 50°) relative to θ_0 , and they have squared aspect ratios $A^2 \sim 1$ that increase, or wavelengths $L \sim 2$ km that decrease, as the value of Re_C increases. Rolls in the second class, then, are characterized by aspect ratios of order one or horizontal wavelengths within a factor of 2 of the depth of the boundary layer. Importantly, these wavelengths are within the range often observed.

Upon considering the global minima for R_{mc} and Re_C^2 , from Fig. 3.2, we see that both the expected orientation angle θ and the squared aspect ratio A^2

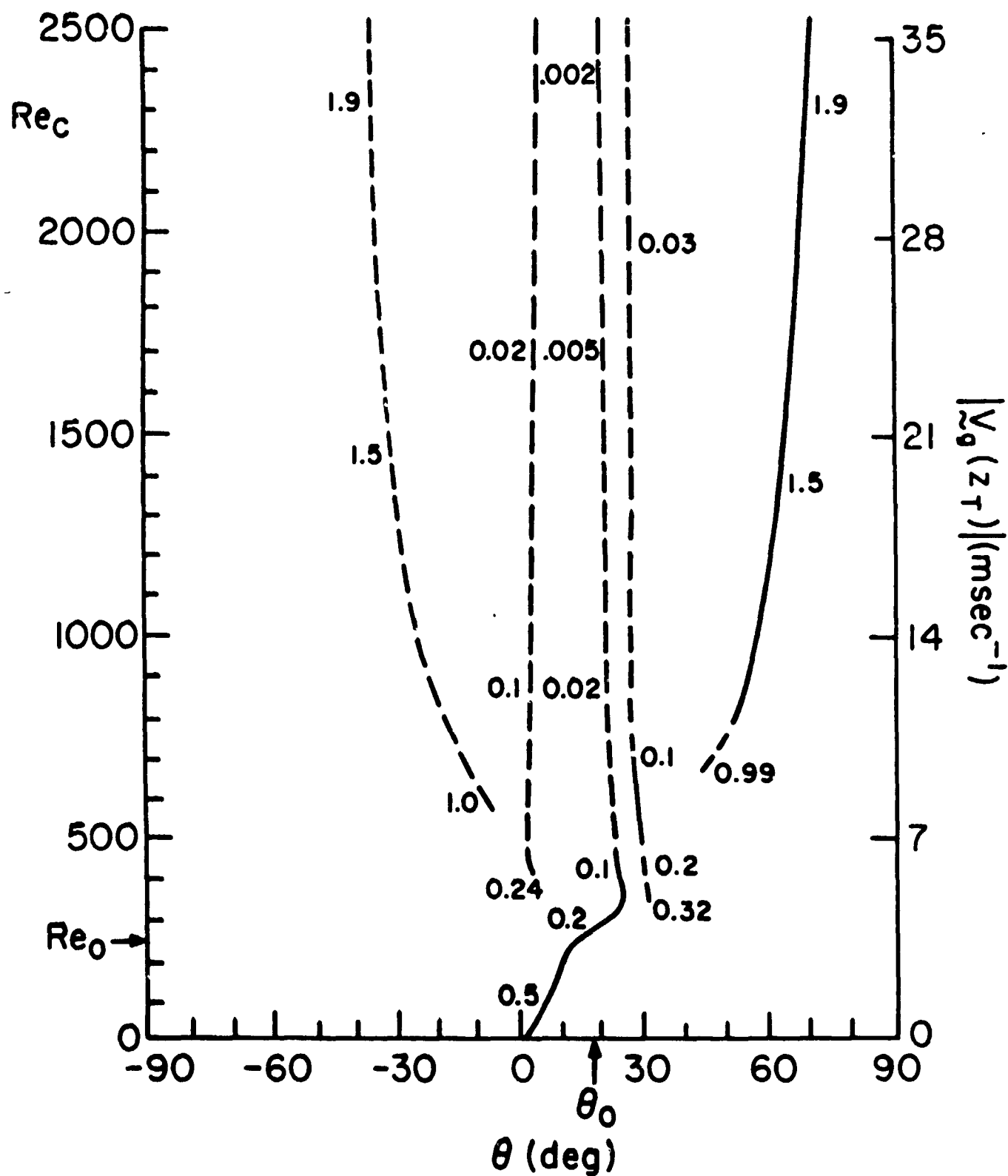


Figure 3.2 Global minima (solid lines) and other local minima (dashed lines) with respect to A^2 and θ of both Re_c and Re_c^2 for the case given in Fig. 3.1. A few values of A^2 are given next to each curve.

make two discontinuous jumps as the magnitude of the Reynolds number Re_c is increased from zero. First the value of A^2 decreases from 0.5 to 0.09 as the value of θ increases from 0° to 24° ; but then at $Re_c \approx 450$, there is a sudden increase in the magnitude of A^2 from 0.09 to 0.18 and of θ from 24° to 31° . The first jump is between two rolls in the first class. At $Re_c \approx 750$, though, there is a more significant jump in the expected value of A^2 from $A^2 = 0.08$ to $A^2 = 1.11$ and in the expected value of θ from $\theta = 29^\circ$ to $\theta = 52^\circ$. This second discontinuous change is between class one and class two rolls and corresponds to a dramatic alteration in the preferred geometry of the cloud band. As the magnitude of Re_c is increased further, we find that the values of A^2 increase gradually from 1.11 and that the angles θ increase slowly from 52° to as much as 70° .

To clarify further the content of Fig. 3.2, we show in Fig. 3.3 seven constant- Re_c cross-sections on which projections of the minimum values of R_{mc} with respect to A^2 are given as functions of θ in order to illustrate their relative magnitudes and the means by which the discontinuous jumps in the preferred values occurs. The values of A^2 for each local minimum R_s of R_{mc} are given as well. The lines on Fig. 3.2 trace the variation in the location of the valleys shown in Fig. 3.3.

For the case $Re_c = 200$ (Fig. 3.3a), we obtain the usual parabolic shape for R_{mc} , in which only one minimum occurs at $\theta = 12^\circ$ and $A^2 = 0.29$. However, we note that the bottom of the parabola is flattened a bit, and from Fig. 3.3b we find that at $Re_c = 300$ a dimple has developed at $\theta = 25^\circ$ and $A^2 = 0.19$. A saddle point is apparent in Fig. 3.3b near the previous value of $\theta = 12^\circ$. The occurrence of this dimple is a manifestation of the rapid variation in the value of θ near $R_{mc} = 0$ that was created by the introduction of two additional modes (Fig. 3.1). When $Re_c = 400$ (Fig. 3.3c), we observe that two

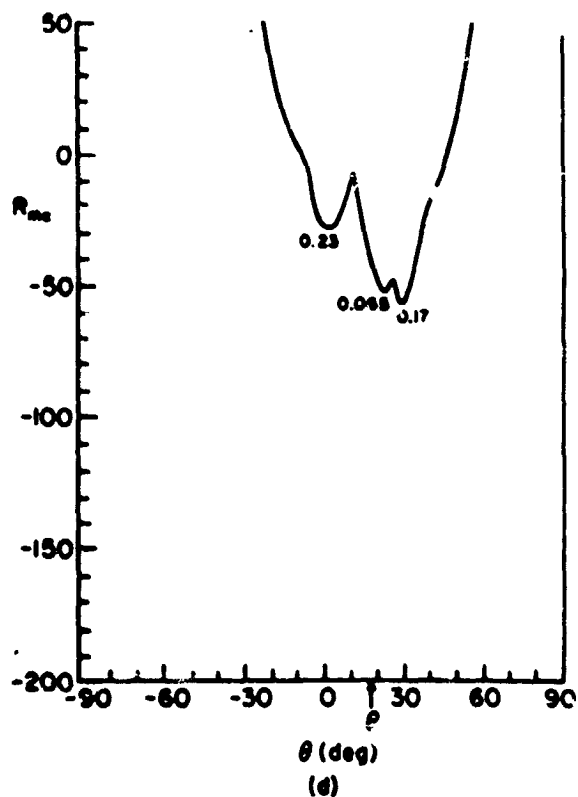
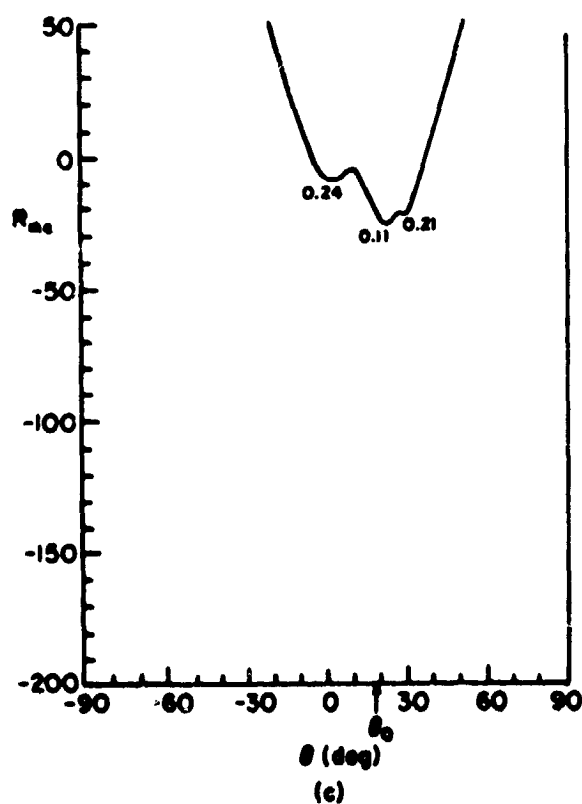
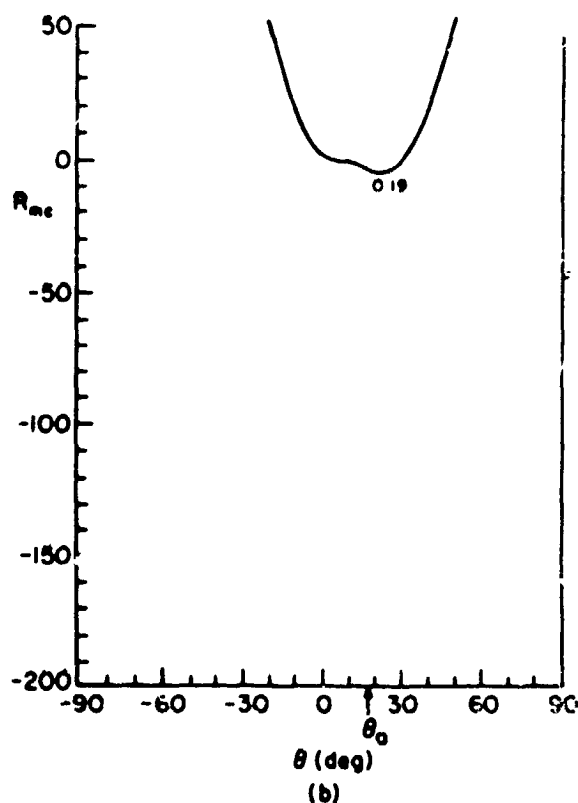
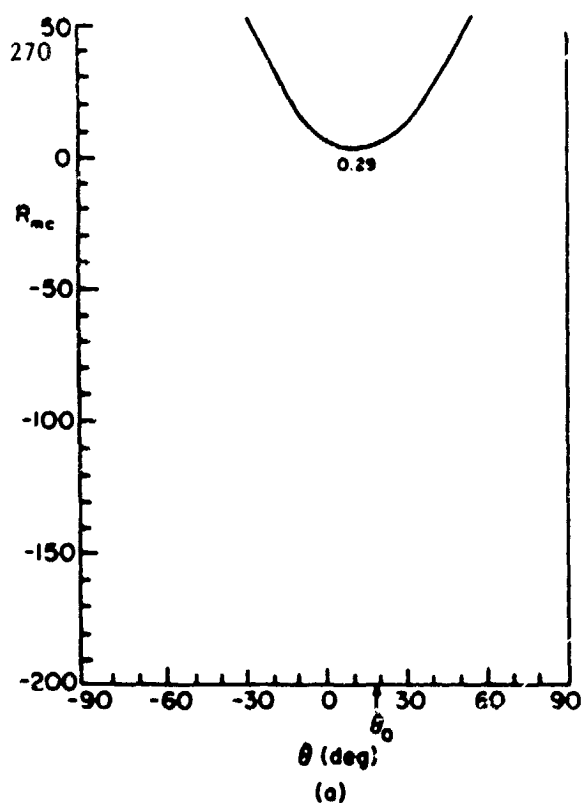


Figure 3.3 Minimum values of R_{mc} with respect to Λ^2 for seven values of Re_c for the case given in Fig. 3.1. Here $Re_c = 200$ (a), 300 (b), 400 (c), 500 (d), 600 (e), 700 (f), and 800 (g). Values of Λ^2 at the local minima of R_{mc} with respect to θ are shown.

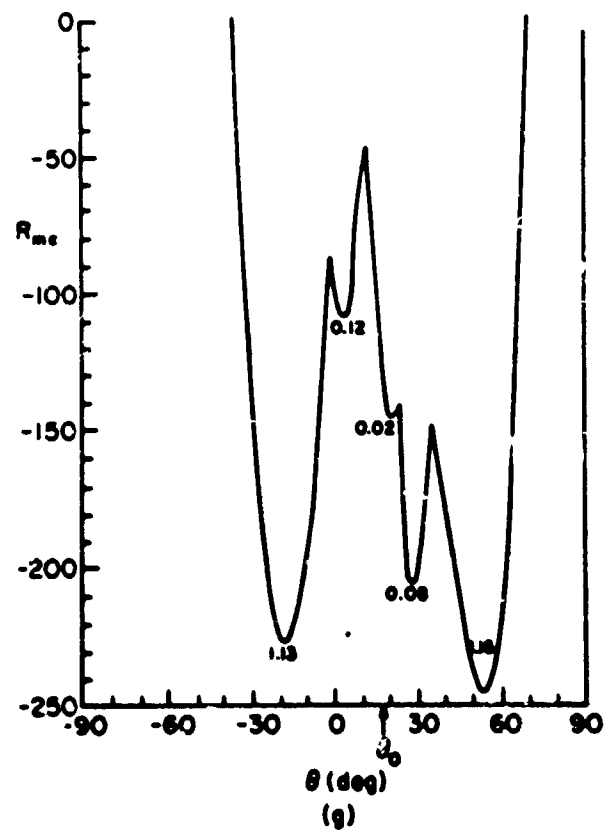
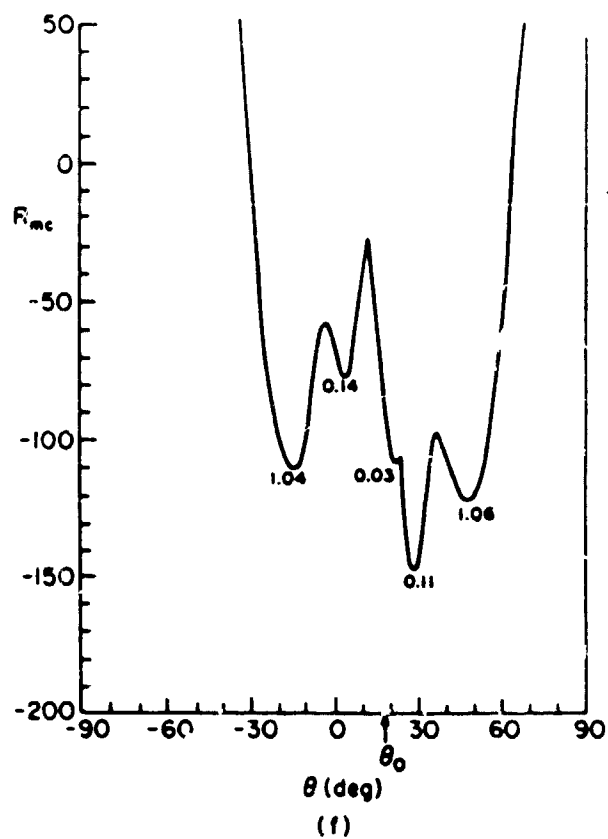
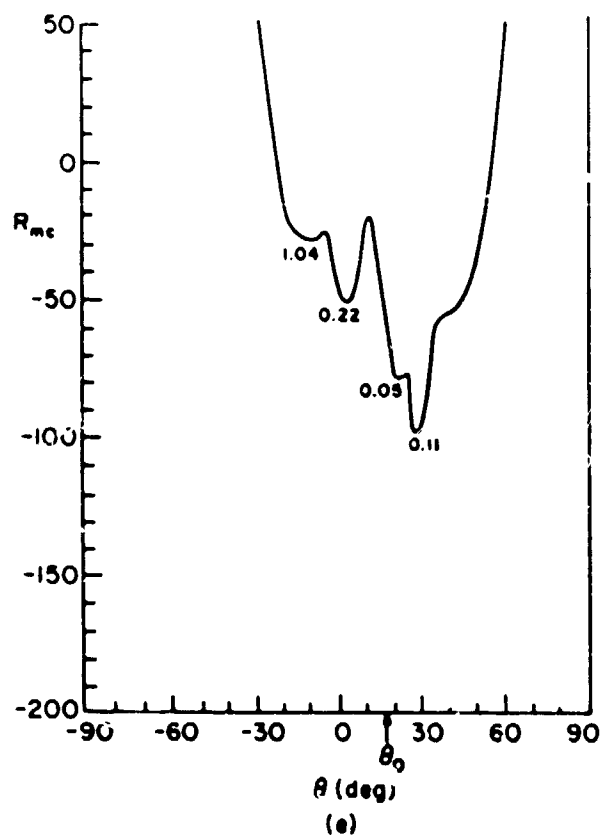


Figure 3.3 (con't.)

local minima have joined the original one, and that the new minima have A^2 values that are approximately double the one for the global minimum. At $Re_C = 500$ (Fig. 3.3d), we discover that the original inner mode is no longer the global minimum because the one at $\theta = 30^\circ$ has overtaken it. We note that saddle points are beginning to appear near $\theta = -5^\circ$ and $\theta = 45^\circ$. As can be seen from Fig. 3.3e when $Re_C = 600$, the saddle point for $\theta < 0$ has developed into a local minimum at $\theta = -10^\circ$ and has a characteristic value of $A^2 \sim 1$. The mode near $\theta = 30^\circ$ is still the global minimum, however. At $Re_C = 700$ (Fig. 3.3f), the right outer mode now exists and has expected values of A^2 and R_g that are very nearly equal to those for the outer left mode. Finally, when $Re_C = 800$ (Fig. 3.3g), the outer modes have the two smallest values for R_g and $A^2 \sim 1.15$ for both of them. With subsequent increases in the magnitudes of Re_C , the two outer modes have increasingly smaller values of R_g , and no other local minima were found. The values of R_g for the outer modes are always within a few percent of one another, even though the right mode is the global minimum; thus, it seems plausible that either outer mode would be observable. As mentioned above, this depends on the value of P , with the right mode occurring for $P > 0.4$ and the left mode for $P < 0.4$.

A misleading aspect of the manner in which the above results have been depicted is the conclusion that rolls can develop in any stably stratified atmosphere. But for any given stratification, given by R_{mc} , the wind speed at z_T must exceed a certain value given by Re_C . This amounts to requiring that the value of a Richardson number Ri (3.11) be sufficiently small or negative. This conclusion agrees with that of others (e.g. Brown, 1972; Wippermann et al., 1978) who showed that rolls can exist only in stable atmospheres having small characteristic values of Ri . To see this in the present context, in Fig. 3.4 we show as functions of R_{mc} and Re_C the curves

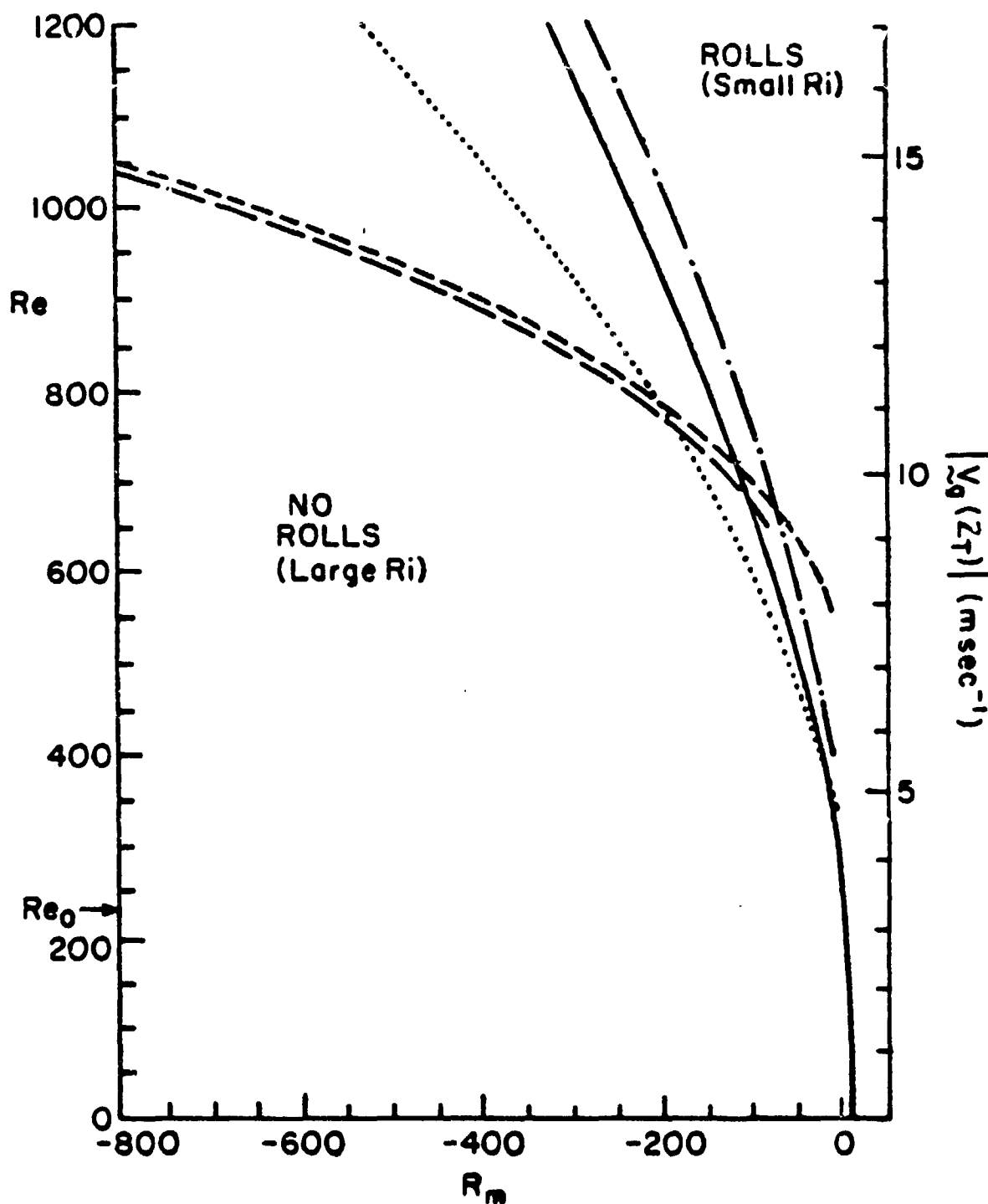


Figure 3.4 The critical values of Re_c and R_{mc} for the five local minima given in Fig. 3.2. The inner mode near 18° is denoted by a solid line, the mode near 30° by a dotted line, the mode near 60° by a long dashed line, the mode near 0° by a dash/dotted line and the mode near -30° by a short dashed line. Rolls may develop in regions in the Re - R_a plane to the right and above the critical lines.

for the five local minima discussed above. Roll modes are possible only when both the values of R_m and Re exceed their critical ones, that is when R_m and Re have values that are above and to the right of the curves. The leftmost curve is the one associated with the expected mode and the transitions between the three modes are clearly seen as portions of three of the curves are the leftmost. Of note is that for large values of Re , the outer modes denoted by the long and short dashes in Fig. 3.4 occur for larger values of Ri than do the other inner modes. The occurrence of a second class of modes at larger values of Ri in a rotating Ekman layer was noted by Kaylor and Faller (1972), who associated these second modes with internal gravity waves.

The pattern depicted in Fig. 3.2 is very robust: its form does not vary much with f^* or P . As the value of f^* is increased, the value of Re_0 (3.17) is decreased and the outer modes can exist for smaller values of Re . The outer modes always occur in the range of 30° - 50° from the orientation angle θ_0 that depends only on the Fourier coefficients a_5 and a_6 of the background wind shear. These outer modes then are well approximated by the orientations given by $\tilde{\Gamma}_1 = \tilde{\Gamma}_2$ or $\tilde{\Gamma}_1 = -\tilde{\Gamma}_2$, the formulas for which are given respectively by

$$\theta_3 = \tan^{-1} [(a_6 - a_5)/(a_5 + a_6)] \quad (3.24)$$

$$\theta_4 = \tan^{-1} [(a_6 + a_5)/(a_5 - a_6)] \quad (3.25)$$

Although a solid physical explanation for these outer modes remains elusive, the fact that the Fourier coefficients for the along-roll $\tilde{\Gamma}_1$ and the cross-roll $\tilde{\Gamma}_2$ wind shear coefficients are nearly equal suggests that the modes are related to some combination of the parallel and inflection point modes that derive energy from the $\tilde{\Gamma}_1$ and $\tilde{\Gamma}_2$ components, respectively.

Although the inflection point instability is not represented here in the neutral case, its singular presence was indicated in Sec. 3.1.1 when $f^* = 0$. If we hypothesize that the outer modes given by $A^2 \sim 1$ would extend to the neutral case given by Re_0 , then we could see whether their existence is suggested by previous studies. Because the location of all the orientation curves are tied to θ_0 via a_5 and a_6 , we may infer from Table 1 that when $D^* = 1/2$ and $\theta_0 = -18^\circ$, which correspond most closely with the previously reported situations, then the right outer mode would first occur 30° - 40° to the right of θ_0 , or in the range 12° - 22° . Moreover, $A^2 \sim 1$ corresponds to $L/D \sim 12$ in this case, and because the inner mode is the global minimum when $Re = Re_0$, the outer mode would exist for larger values of Re . These values of θ , L/D , and Re are in the range reported for the inflection point instability. Thus, there is the possibility that the outer modes are extensions of these inflection point modes, but a larger model containing more degrees of freedom would be needed to test this hypothesis.

3.3 Alternate parallel modes

The discussion presented so far has concerned rolls developing from a cosine mode of the background wind profile (cf (3.8)-(3.9)). However, a Fourier analysis of the Ekman profile (3.21)-(3.22) reveals that there is significant energy in the sine modes as well. In addition, Shirer (1980) noted that three orientation angles corresponding to three roll responses to the cosine and sine modes might be possible (see his equations (3.16)-(3.18) for the angles $\alpha_1, \alpha_2, \alpha_3$), and Kelly (1984) notes that all three angles correspond well with the alignment observed during a case of cloud streets. Moreover, theoretical studies of rolls developing in a stratified shearing atmosphere (e.g. Faller and Kaylor, 1969) reveal that the rolls tilt significantly with height, suggesting that both $\sin(z)$ and $\cos(z)$ modes might

be important in modeling the nonlinear response with a perturbation stream function ψ . Although use of $\cos(z)$ modes in the expansion for ψ is not compatible with direct application to the atmospheric boundary layer, their use will allow a preliminary investigation of the roll modes developing from a sine mode of the background wind. More suitable vertical eigenfunctions are given by Chandrasekhar (1961). Because the analysis is much more algebraically difficult in this case, we present here only a brief summary of the results for these alternate parallel instability modes.

To create the alternate model we must replace the vertical eigenfunctions of the even-numbered terms of (2.41)-(2.43) with ones that are 90° out of phase. For example, for the R_1 roll, (2.42) becomes

$$w^* = w_1 \cos(x^* - y^*) \sin(z^*) + w_2 \sin(x^* - y^*) \cos(z^*) \quad (3.26)$$

For the parallel modes given by $R_m = 0$, this new expansion leads to a spectral system in which e^* (2.31) remains and for which the branching behavior depends on the four Fourier coefficients (cf. (3.8)-(3.9))

$$b_1 = 2[\pi^2 |V(z_T)|]^{-1} [U(z_T) - U(0)] \quad (3.27)$$

$$b_2 = 2[\pi^2 |V(z_T)|]^{-1} [V(z_T) - V(0)] \quad (3.28)$$

$$b_3 = -2[\pi |V(z_T)| z_T]^{-1} \int_0^{z_T} U(z) \sin(2\pi z/z_T) dz \quad (3.29)$$

$$b_4 = -2[\pi |V(z_T)| z_T]^{-1} \int_0^{z_T} V(z) \sin(2\pi z/z_T) dz \quad (3.30)$$

The polynomial governing a Hopf bifurcation to a periodic roll solution is either a quartic or a sixth-degree polynomial in Re_C , depending on whether

e^* and f^* are tied or untied to the Ekman depth D^* (see Sec. 3.2.1.). The present case simplifies to that for the cosine modes only when $e^* = 0$, $b_1 = 0$, and $b_2 = 0$, for which Re_c , f^* and α_3 are given by (3.14), (3.17), and (3.18) once the coefficients a_5 and a_6 have been replaced by b_3 and b_4 respectively. We also note that α_3 in Shirer (1980) corresponds to $\tan\theta = [(b_2 - 2b_4)/(b_1 - 2b_3)]$, but this is not the preferred orientation in the rotational case discussed here.

For the Ekman profile (3.21)-(3.22), in Table 2 we show the results associated with these alternate parallel modes when $e^* = 0$ and in Table 3 those when $e^* = f^*$. As in Table 1, when e^* and f^* are independent of D^* , we tie them to Re_c so that $|V_g| = 10$ m/sec. From Tables 2 and 3, and in agreement with Etling (1971), we see that e^* only has a small effect on the preferred orientation angles or the dimensionless wavelengths, although it does alter somewhat the critical value of Re . Orientation angles that are in the range $\pm 20^\circ$ occur when the Ekman depth $D \geq 440$ m in the untied case and $D \geq 173$ m in the tied one; this is in contrast to the results in Table 1 for the cosine modes, in which we found orientation angles in the range $\pm 20^\circ$ only when $D < 440$ m. These results suggest that for very small Ekman depths, the cosine modes might be appropriate ones, while for larger depths, the sine modes might be relevant ones. In Shirer et al. (1985) we present evidence that the sine parallel modes provide better predictions than do the cosine parallel modes for the orientations and wavelengths of the cloud streets observed during KonTur, for which the Ekman depth divided by the circulation depth was in the range 0.5-1.0. We caution that the above results for the sine modes are preliminary because they depend on use of marginally appropriate vertical basis functions in the spectral expansions.

Table 2.

Preferred geometries for alternate parallel modes at latitude 45°N when $e^* = 0$ (U-untied, T-tied).

D(m)	D*	b ₁	b ₂	b ₃	b ₄	f*	$\theta(\text{deg})$	L/D	ReD	$v(\text{m}^2/\text{s})$	$ v_g (\text{m/s})$
159.	0.50	0.20226	0.	0.02023	-0.04046	{ 0.15U 8.0T	-71. 59.	28.9 20.7	23.4 8.6	68. 1.3	10. 0.07
245.	0.77	0.20464	-0.00216	0.05899	-0.05125	{ 0.15U 3.4T	-48. 75.	19.8 14.4	34.8 13.4	70. 3.1	10. 0.17
318.	1.0	0.21140	0	0.08456	-0.04228	{ 0.16U 2.0T	-33. -58.	13.1 12.6	50.0 23.9	64. 5.2	10. 0.39
440.	1.4	0.21612	0.01001	0.11312	-0.01892	{ 0.21U 1.0T	-16. -30.	9.3 9.7	89.8 53.4	49. 10.	10. 1.2
623.	2.0	0.20405	0.04067	0.10293	0.00689	{ 0.31U 0.52T	-3. -7.	7.0 7.0	184.5 145.7	34. 20.	10. 4.7
763.	2.4	0.18860	0.05280	0.09587	0.01805	{ 0.37U 0.35T	3. 3.	5.7 5.9	270.1 279.0	28. 30.	10. 11.
881.	2.8	0.17517	0.05904	0.08913	0.02370	{ 0.40U 0.26T	5. 9.	5.5 5.2	341.2 451.9	26. 40.	10. 21.
985.	3.1	0.16393	0.06238	0.08337	0.02683	{ 0.43U 0.21T	7. 13.	4.9 4.7	403.4 664.2	24. 50.	10. 34.

Table 3.

Preferred geometries for alternate parallel modes at latitude 45°N when $e^* = f^*$ (U-untied, T-tied).

D(m)	D*	$e^* = f^*$	$\theta(\text{deg})$	L/D	Rep	$v(\text{m}^2/\text{s})$	$ v_g (\text{m}/\text{sec})$
159.	0.50	{ 0.16U 8.0T	-71. 90.	26.8 22.2	24.5 9.2	65. 1.3	10. 0.08
245.	0.77	{ 0.16U 3.4T	-48. 77.	19.8 14.7	38.2 13.6	64. 3.1	10 0.17
318.	1.0	{ 0.18U 2.0T	-33. -61.	15.3 12.8	56.2 24.4	57. 5.2	10. 0.40
440.	1.4	{ 0.24U 1.0T	-17. -35.	10.7 10.2	99.5 51.1	44. 10.	10. 1.2
623.	2.0	{ 0.31U 0.52T	-4. -10.	7.4 7.4	186.4 136.9	33. 20.	10. 4.4
763.	2.4	{ 0.35U 0.35T	1. 1.	6.2 6.2	258.4 261.0	30. 30.	10. 10.
881.	2.8	{ 0.38U 0.26T	3. 8.	5.7 5.2	319.5 424.2	28. 40.	10. 19.
985.	3.1	{ 0.40U 0.21T	5. 12.	5.1 4.8	373.5 619.5	26. 50.	10. 31.

4. Concluding remarks

In this article, we have presented significant physical and theoretical results on boundary layer rolls from a study of a truncated spectral model of shallow Boussinesq convection. Physically, we have shown that the hypothesized developmental mechanisms of the parallel and thermal instabilities are, in fact, special cases of one instability mechanism, because in many cases boundary layer stratification and mean wind shear combine to allow one secondary flow to develop. Theoretically, we have demonstrated that the apparently linear problem of finding preferred orientation angles and aspect ratios for the branching solutions is actually an intricate nonlinear one that can be understood completely with the aid of the recently emerging perspective of (contact) catastrophe theory.

The necessity of performing a nonlinear analysis arises from the assumption that the preferred geometry of the rolls is given by the values of the spatial parameters that minimize the values of the bifurcation points that can be determined from a linear stability analysis of the conductive solution. In this problem, expressions for the critical values are nonlinear functions of the orientation angle and aspect ratio. As a consequence, study of the function controlling these critical values leads to a polynomial relating the auxiliary parameters and to questions concerning whether unique or multiple admissible solutions, and therefore roll modes, exist. Thus, the province of contact catastrophe theory has been entered (Shirer and Wells, 1983), and a new set of topological questions can be posed concerning the necessary generality of the model under study.

Although we find that the present spectral model might not be able to describe all possible interchanges among preferred modes, we do obtain several significant results. In addition to linking the parallel and thermal

instability mechanisms, we discovered that the external wind field organizes the secondary circulation into two-dimensional rolls by introducing certain linear terms into the spectral model. When the thermal stratification is either unstable or neutral, only one minimum value for the critical Rayleigh number or the critical Reynolds number exists and hence only one roll mode is preferred; this mode has horizontal wavelengths that broaden significantly with increasing values of the Reynolds number Re , which is proportional to the wind speed at the top of the domain. Once the stratification becomes stable, there is an upper limit to the spacing of the cloud streets because other minima become possible. When the value of Re is sufficiently large, the preferred roll spacing becomes discontinuously much smaller, to one within a factor of 2 of the boundary layer depth. Generally, the orientation angles of the broadly separated rolls are near those for which the Fourier coefficient of the wind shear parallel to the roll is much larger than that of the component perpendicular to the roll; but for the narrowly separated rolls, both shear components are large and nearly equal in magnitude. Although several orientation angles and aspect ratios are associated with local minima in the value of the critical Rayleigh number, the particular one that provides the global minimum depends on the magnitude of the Prandtl number P .

The results presented here are applied in Shirer *et al.* (1985) to three cloud street cases observed during the 1981 convection and turbulence experiment KonTur. Qualitatively, they are the same as those discussed here for an Ekman wind profile.

Acknowledgments

The results presented in this article are from a model whose initial form I developed during my one-year visit of the Department of atmospheric Processes of the Max-Planck-Institut für Meteorologie, Hamburg, West Germany, at the invitation of Professor Dr. H. Hinzpeter. I gratefully acknowledge his help in making my visit possible through the granting to me of a Max-Planck postdoctoral fellowship for foreigners during the 1980-81 academic year, and I thank the members of his group for the many stimulating discussions that we had concerning the model formulation.

I also thank two anonymous reviewers for giving me very careful and thorough critiques of an earlier version of this manuscript; in addressing the points raised I was able to improve greatly on the presentation of my results.

This research was completed at The Pennsylvania State University with the partial support of the National Science Foundation through Grants ATM 78-02699, ATM 79-08354, ATM 81-13223, and ATM 83-07213, and of the National Aeronautics and Space Administration through Grants NAS 8-33794 and NAS 8-36150. I am indebted to Professors Dutton, Wells, and Clark for their interest and suggestions concerning interpretation and presentation of the results.

Appendix A

Coefficients in Spectral Model (2.47)-(2.63)

The definitions of the B_i coefficients are

$$B_1 = (b^2 - 1)P / [(b^2 + 1)(A^2 + 1)] \quad (A.1)$$

$$B_2 = (b^2 - 1) / [2(b^2 + 1)] \quad (A.2)$$

$$B_3 = P / (A^2 + 1) \quad (A.3)$$

$$B_4 = (A^2 + 1) / A \quad (A.4)$$

The F_i coefficients involve f^* and they are given by

$$F_1 = f^*P(b^2 - 1) / [2bA(A^2 + 1)] - P(A^2 + 1) / A \quad (A.5)$$

$$F_2 = f^*P[(b^2 - 1)^2 + 4b^2(A^2 + 1)] / [2b(b^2 + 1)A(A^2 + 1)] \quad (A.6)$$

$$F_3 = f^*P(b^2 + 1) / [2Ab(A^2 + 1)] \quad (A.7)$$

$$F_4 = f^*P(b^2 - 1) / [2bA(A^2 + 1)] + P(A^2 + 1) / A \quad (A.8)$$

The S_i coefficients involve the Fourier coefficients $\bar{\Lambda}_i$ and $\bar{\Gamma}_i$ of the wind and wind shear; these are defined in (2.64)-(2.66) and the $\bar{\Lambda}_i$ are

$$S_1 = [2b\bar{\Lambda}_1 + (b^2 - 1)\bar{\Lambda}_2] / (b^2 + 1) \quad (A.9)$$

$$S_2 = \{\bar{\Gamma}_1 4A^2 b(b^2 - 1) + \bar{\Gamma}_2 [A^2(b^4 - 6b^2 + 1) - (b^2 + 1)^2]\} / [(b^2 + 1)^2(A^2 + 1)] \quad (A.10)$$

$$S_3 = [2b(\bar{\Lambda}_1 + \bar{\Lambda}_3) + (b^2 - 1)(\bar{\Lambda}_2 + \bar{\Lambda}_4)] / (b^2 + 1) \quad (A.11)$$

$$\begin{aligned}
 s_4 = & [4b\tilde{\Lambda}_1 + 2(b^2 - 1)\tilde{\Lambda}_2 + (A^2 - 1)2b\tilde{\Lambda}_3 \\
 & + (A^2 - 1)(b^2 - 1)\tilde{\Lambda}_4] / [(b^2 + 1)(A^2 + 1)]
 \end{aligned}
 \tag{A.12}$$

$$s_5 = [2b\tilde{\Lambda}_3 + (b^2 - 1)\tilde{\Lambda}_4] / (b^2 + 1)
 \tag{A.13}$$

Appendix B

Coefficients in polynomial for the critical modified Rayleigh number R_{mc}

The coefficients in the factored characteristic equation (3.1) are

$$a_1 = -(A^2 + 1)^2 (2P + 1) \quad (B.1)$$

$$b_1 = A[(A^2 + 3)\bar{\Lambda}_2 + 2A^2\bar{\Lambda}_4] \quad (B.2)$$

$$c_0 = -A^2 \quad (B.3)$$

$$c_1 = P(P+2)(A^2+1)^3 + A^2[2\bar{\Lambda}_2^2 + (A^2-1)\bar{\Lambda}_4^2 + 2(A^2+1)\bar{\Lambda}_2\bar{\Lambda}_4] \\ - f^{*2} P^2 \quad (B.4)$$

$$d = A(A^2 + 1) \{ (A^2 + 3)(P+1)\bar{\Lambda}_2 + [A^2 - 1 + P(3A^2 + 1)]\bar{\Lambda}_4 \} \\ + A f^{*2} \bar{\Gamma}_1 P \quad (B.5)$$

$$e_0 = P^2 A^2 (A^2 + 1) \quad (B.6)$$

$$e_1 = -P^2(A^2 + 1)^4 + A^2(A^2 + 1) \{ 2\bar{\Lambda}_2^2 + (A^2 - 1)\bar{\Lambda}_4^2 P \\ + \bar{\Lambda}_2 \bar{\Lambda}_4 [A^2 - 1 + (A^2 + 3)P] \} - f^{*2} P^2 (A^2 + 1) \quad (B.7)$$

$$+ \bar{\Lambda}_4 \bar{\Gamma}_1 f^{*2} P A^2$$

$$f_0 = -\bar{\Lambda}_2 P A^3 \quad (B.8)$$

$$\begin{aligned}
f_1 = & -A^3 \bar{\Lambda}_2 \bar{\Lambda}_4 \{2\bar{\Lambda}_2 + (\Lambda^2 - 1)\bar{\Lambda}_4\} + \bar{\Lambda}_4 f^{*2} P^2 A \\
& + A P (\Lambda^2 + 1)^2 \{\bar{\Lambda}_2 (\Lambda^2 + 3) + \bar{\Lambda}_4 [P(\Lambda^2 + 1) + \Lambda^2 - 1]\} \quad (B.9) \\
& + f^* \bar{\Gamma}_1 A P (\Lambda^2 + 1)
\end{aligned}$$

The coefficients in the cubic polynomial (3.4) governing R_{mc} are

$$k_0 = a_1^2 + d g_1 h_1 - h_1^2 e_1 \quad (B.10)$$

$$k_1 = 2 g_0 g_1 a_1 + d g_0 h_1 + d g_1 h_0 - h_1^2 e_0 - 2 h_0 h_1 e_1 \quad (B.11)$$

$$k_2 = a_1 g_0^2 + d g_0 h_0 - h_0^2 e_1 - 2 h_0 h_1 e_0 \quad (B.12)$$

$$k_3 = - h_0^2 e_0 \quad (B.13)$$

in which

$$g_0 = a_1 b_1 e_0 + d e_0 (\Lambda^2 + 1) - f_0 a_1^2 \quad (B.14)$$

$$g_1 = b_1 a_1 e_1 + d e_1 (\Lambda^2 + 1) - f_1 a_1^2 \quad (B.15)$$

$$h_0 = c_0 a_1^2 + e_0 a_1 (\Lambda^2 + 1) \quad (B.16)$$

$$h_1 = c_1 a_1^2 + e_1 a_1 (\Lambda^2 + 1) + d b_1 a_1 + d^2 (\Lambda^2 + 1) \quad (B.17)$$

References

- Asai, T., 1970: Stability of a plane parallel flow with variable vertical shear and unstable stratification. J. Meteor. Soc. Japan, 48, 129-139.
- Asai, T., 1972: Thermal instability of a shear flow turning the direction with height. J. Meteor. Soc. Japan, 50, 525-532.
- Asai, T. and I. Nakasujii, 1973: On the stability of Ekman boundary layer flow with thermally unstable stratification. J. Meteor. Soc. Japan, 51, 29-42.
- Bjerknes, J., 1938: Saturated-adiabatic ascent of air through dry-adiabatically descending environment. Quart. J. Roy. Meteor. Soc., 64, 325-330.
- Brown, R.A., 1970: A secondary flow model for the planetary boundary layer. J. Atmos. Sci., 27, 742-757.
- Brown, R.A., 1972: On the inflection point instability of a stratified Ekman boundary layer. J. Atmos. Sci., 29, 850-859.
- Brown, R.A., 1980: Longitudinal instabilities and secondary flows in the planetary boundary layer. A review. Rev. Geophys. Space Phys, 18, 683-697.
- Brümmer, B. and A. Grant, 1985: Structure and dynamics of PBL rolls from KonTur aircraft observations. Submitted to Beitr. Phys. Atmos. for review.
- Chandrasekhar, S., 1961: Hydrodynamic and Hydromagnetic Stability. Clarendon Press, 652 pp.
- Chang, H.-R. and H.N. Shirer, 1984: Transitions in shallow convection: An explanation for lateral cell expansion. J. Atmos. Sci., 41, 2334-2346.
- Dutton, J.A., 1976: The Ceaseless Wind: An Introduction to the Theory of Atmospheric Motion. McGraw-Hill, 579 pp.

- Etling, D., 1971: The stability of Ekman boundary layer flow as influenced by the thermal stratification. Beitr. Phys. Atmos., 44, 168-186.
- Etling, D. and F. Wippermann, 1975: On the instability of a planetary boundary layer with Rossby-number similarity. Boundary Layer Meteor., 9, 341-360.
- Faller, A.J. and R.E. Kaylor, 1966: A numerical study of the instability of the laminar Ekman boundary layer. J. Atmos. Sci., 23, 466-480.
- Faller, A.J. and R.E. Kaylor, 1967: Instability of the Ekman spiral with applications to the planetary boundary layers. Phys. Fluids Suppl., IUGG-IUTAM Symposium, 19-24 September, Kyoto, Japan, S212-S219.
- Faller, A.J. and R.E. Kaylor, 1969: Instability of the thermal wind. Clear Air Turbulence and its Detection, Y.H. Pao and A. Goldburg (eds.), Plenum Press, 63-72.
- Gammelsrød, T., 1975: Instability of Couette flow in a rotating fluid and origin of Langmuir circulations. J. Geophys. Res., 80, 5069-5075.
- Iooss, G. and D.D. Joseph, 1980: Elementary Stability and Bifurcation Theory. Springer-Verlag, 286 pp.
- Kaylor, R. and A.J. Faller, 1972: Instability of the stratified Ekman boundary layer and the generation of internal waves. J. Atmos. Sci., 29, 497-509.
- Kelly, R.D., 1982: A single Doppler radar study of horizontal-roll convection in a lake-effect snowstorm. J. Atmos. Sci., 39, 1521-1531.
- Kelly, R.D., 1984: Horizontal roll and boundary-layer relationships observed over Lake Michigan. J. Atmos. Sci., 41, 1816-1826.
- Kelly, R.E., 1977: The onset and development of Rayleigh-Bénard convection in shear flows: A review. Physicochemical Hydrodynamics, D. B. Spalding (ed.) Advance Publications Limited, 65-79.
- Krishnamurti, R., 1975: On cellular cloud patterns. Part 3: Applicability of the mathematical and laboratory models. J. Atmos. Sci., 32, 1373-1383.

- Kuettner, J.P., 1971: Cloud bands in the earth's atmosphere: Observations and theory. Tellus, 23, 404-425.
- LeMone, M.A., 1973: The structure and dynamics of horizontal roll vortices in the planetary boundary layer. J. Atmos. Sci., 30, 1077-1091.
- Lilly, D.K., 1966: On the stability of Ekman boundary flow. J. Atmos. Sci., 23, 481-494.
- Lorenz, E.N., 1963: Deterministic nonperiodic flow. J. Atmos. Sci., 20, 130-141.
- Mitchell, D. and E.M. Agee, 1977: A theoretical investigation of atmospheric convective modes as a function of Rayleigh number, Prandtl number and eddy anisotropy. J. Meteor. Soc. Japan, 55, 341-363.
- Ogura, Y. and A. Yagihashi, 1969: A numerical study of convective rolls with a flow between horizontal parallel plates. J. Meteor. Soc. Japan, 47, 205-217.
- Plank, V.G., 1966: Wind conditions in situations of patternform and nonpatternform cumulus convection. Tellus, 18, 1-12.
- Shirer, H.N., 1980: Bifurcation and stability in a model of moist convection in a shearing environment. J. Atmos. Sci., 37, 1586-1602.
- Shirer, H.N., 1982: Toward a unified theory of atmospheric convective instability. Cloud Dynamics, E.M. Agee and T. Asai (eds.), D. Reidel Publishing Co., 163-177.
- Shirer, H.N., B. Brümmer, and A. Grant, 1985: Cloud streets during KonTur: A comparison of theory and observations. Submitted to Beitr. Phys. Atmos. for review.
- Shirer, H.N. and J.A. Dutton, 1979: The branching hierarchy of multiple solutions in a model of moist convection. J. Atmos. Sci., 36, 1705-1721.

- Shirer, H.N. and R. Wells, 1983: Mathematical Structure of the Singularities at the Transitions between Steady States in Hydrodynamic Systems. Lecture Notes in Physics, 185, Springer-Verlag, 276 pp.
- Sommeria, G. and M. LeMone, 1978: Direct testing of a three-dimensional model of the planetary boundary layer against experimental data. J. Atmos. Sci., 35, 25-39.
- Veronis, G., 1966: Motions at subcritical values of the Rayleigh number in a rotating fluid. J. Fluid Mech., 24, 545-554.
- Walter, B.A., 1980: Wintertime observations of roll clouds over the Bering Sea. Mon. Wea. Rev., 108, 2024-2031.
- Walter, B.A. and J.E. Overland, 1984: Observations of longitudinal rolls in a near neutral atmosphere. Mon. Wea. Rev., 112, 200-208.
- Weston, K.J., 1980: Observational study of convective cloud streets. Tellus, 32, 433-438.
- Wippermann, F., D. Etling, and H.J. Kirstein, 1978: On the instability of a planetary boundary layer with Rossby number similarity. Part II: The combined effect of inflection point instability and convective instability. Boundary Layer Meteor., 15, 301-321.

N86-11755

CHAPTER 7

Cloud Streets During KonTur:
A Comparison of Parallel/Thermal
Instability Modes with Observations

Hampton N. Shirer

Department of Meteorology
The Pennsylvania State University
University Park, PA 16802 USA

Burghard Brümmer

Sonderforschungsbereich 94 - Meeresforschung
Max-Planck Institut für Meteorologie
Hamburg, Germany

Alan Grant

British Meteorological Office
Bracknell, UK

1. Introduction

The purpose of this article is to compare the geometries and dimensionless parameter values that were characteristic of cloud streets observed during the 1981 convection and turbulence experiment KonTur with those values obtained from a model of parallel/thermal instability modes discussed by Shirer (1985). Previous comparisons of this type have been difficult because most models have been developed for study of an Ekman layer (e.g., Lilly, 1966; Faller and Kaylor, 1966; Brown, 1970; Asai and Nakasugi, 1973), whose wind profile only crudely approximates that found in the atmospheric boundary layer. An advantage of the model of Shirer (1985) is that it uses the Fourier coefficients of an arbitrary mean wind profile to estimate the preferred geometries of the cloud bands, and so direct comparisons between theory and observations are much easier.

That this approach might be a successful one was demonstrated recently by Kelly (1984) who compared observations of the alignment of some wintertime cloud streets over Lake Michigan with the orientations produced by a model of Rayleigh instability of Shirer (1980), and Kelly found good agreement between theory and observation. But his results might have been fortuitous because he had to use radiosonde data to calculate the Fourier coefficients of the wind profile, and generally these observations are too widely spaced (~ 300 m) for a sufficiently accurate computation of the Fourier coefficients. A more rigorous test of the approach can be obtained from the wind profiles measured by aircraft during KonTur; because this set has much greater vertical resolution (~ 10 m), this data set is better suited for an accurate computation of the necessary Fourier coefficients.

In the following section we briefly review the KonTur experiment and describe the relevant observations. In Section 3 we summarize the model of

Shirer (1985) and pay particular attention to those parameters that are amenable to comparison with observations. Finally in Section 4 we show which of the roll modes found by Shirer (1985) appear to describe the observed cloud streets.

2. Observations

The KonTur experiment was conducted above the German Bight of the North Sea during September and October, 1981. The goal of the experiment was to collect a data set of basic state and secondary flow variables characterizing several different classes of convection, ranging in scale from boundary layer rolls to open cells. On three days, 18, 20 and 26 September 1981, cloud streets were observed and the data subsequently analyzed in detail; a complete summary of these results is given in Brümmner and Grant (1985). On both 18 and 26 September, the rolls were observed ahead of an approaching warm front, and on 20 September behind a weak cold front.

Two instrumented airplanes, a German FALCON 20 and a British HERCULES C-130 were operated together during the experiment. At the beginning and the end of each flight mission, the aircraft measured the vertical profiles of the wind, temperature and water vapor mixing ratio down to 100 m above the ocean. In these profile runs, the horizontal wind components were measured to accuracies of ± 1 m/s and the temperatures to ± 0.05 K. These measurements form the data base for the present study, and the specific profiles are given in Brümmner and Grant (1985). During the main part of a flight mission, the aircraft flew coordinated "L"-shaped patterns having 25 nm long legs nearly perpendicular to and parallel to the streets.

Some of the measurements relevant to the present study are summarized in Table I. The alignments of the cloud streets could only be determined

Table I. Observations

Date	Time (GMT)	Cloud Base z_1 (m)	Inversion Height z_2 (m)	Cloud/Roll Top H(m)	Roll Orientation (deg)	Mean Wind Direction (deg)	Cloud/Roll Spacing L(m) Mean Range	Ekman Depth D(m)	Eddy Viscosity ν (m ² /s)
18/09/81	0855	270	390	530 \pm 50	160°	160°	2000 1200 3300	500	15
20/09/81	1206	700	1300	1300 \pm 100	240°	225°	3450 1500 6000	765	35
26/09/81	1120	-	440	500 \pm 50	135°	135°	1675 800 2700	540	17

visually by the scientists on board the aircraft to within $\pm 15^\circ$ of the actual orientations; on 18 and 26 September, the mean boundary layer wind direction was used but on 20 September, 15° to the right of the mean direction was used. Visual estimates and the time series that were measured during the cross-roll flight legs were used to determine the magnitudes of the cloud spacings L ; in the case without clouds (26 September) the mixing ratio data were used, while in the cases with clouds (18 and 20 September), the radiational flux data were used. Cloud base z_1 and cloud top were determined visually by the scientists in the aircraft; for the cases on 18 and 20 September, the highest cloud tops were used for the roll depth H , while on 26 September the highest levels at which significant turbulence was present were used. The inversion base z_1 was determined from the temperature profiles to be the level at which a sharp increase in potential temperature occurred. The eddy viscosity ν was calculated from the usual flux-gradient relationship; the appropriate momentum flux was found from the cross-roll momentum spectra by integrating over the portion of the spectrum to the right of the roll-scale frequency band. The uncertainties in the values of ν are large, and its actual values may vary between one-half and twice the reported ones. In any case, the given magnitudes of ν were used together with $f = 1.2 \times 10^{-4} \text{ s}^{-1}$ to calculate the values for the Ekman depth $D = (2\nu/f)^{1/2}$. From Table I we see that these values of D are in the range $(1/2)H$ to H , and these are larger than those normally found in studies of Ekman layers (e.g., Faller and Kaylor, 1966) for which $D \sim H/5$. Other relevant parameter values depend on the height of the model domain being considered, and they are presented in the next section.

3. Cloud Street Model

Shirer (1985) developed a nonlinear low-order spectral model of convection occurring in a three-dimensional, rotating environment containing thermal stratification and an arbitrary height-dependent horizontal wind. The model simulates two-dimensional planforms that originate from a combination of the thermal and parallel instability mechanisms proposed by others as candidates to explain cloud street development (Brown, 1980). Although the model is a nonlinear one, the critical values of the control parameters representing the forcings that drive the rolls are determined by obtaining the neutrally stable modes from a linear analysis of the basic state. The expected values of the response parameters representing the preferred roll geometry are those producing the smallest values of all the control parameters. The values of these response parameters are most easily compared with the observations; if good results are obtained, then the nonlinear model upon which the linear analysis is based likely has sufficient degrees of freedom for representing the nonlinear secondary circulations themselves. For a neutrally stratified boundary layer, Shirer (1985) considered rolls that extract energy from one of two sources: 1) the lowest order sine terms of a Fourier expansion of the mean wind shear profile, which are equivalent to the lowest order cosine terms of the mean wind profile, or 2) the average shear and lowest order cosine terms of the mean wind shear, which are equivalent to the sine terms of the wind profile. Here the principal results of the model are reviewed.

3.1 Governing parameters

The modeled rolls are able to derive their energy from an unstable thermal stratification, given by a modified Rayleigh number

$$R_m = gT^4[\gamma_0 - (1-n_1)\gamma_d - n_1\gamma_m]/[\nu\kappa T(0)\tau^4] \quad (3.1)$$

or from the shearing mean wind field whose intensity can be measured in part by a Reynolds number

$$Re = |V(z_T)| z_T / \nu \quad (3.2)$$

These are the two control parameters of the problem. In the definitions (3.1) and (3.2), z_T is the model domain top and the height of the roll circulation, γ_e is the constant environmental lapse rate, γ_m is the constant moist adiabatic lapse rate, γ_d is the dry adiabatic lapse rate, $T(0)$ is the air temperature at the bottom of the domain, n_1 is a Fourier coefficient defined in (3.4) that is related to the cross-sectional area of the cloudy region in which latent heating is assumed to occur, $|V(z_T)|$ is the wind speed at the domain top, ν is the constant eddy viscosity, and κ is the constant eddy thermometric conductivity. In addition, the Prandtl number $P = \nu/\kappa$ provides a measure of the relative importance of the dissipation of momentum to that of heat.

Because of the uncertainties in the observed roll heights, we consider several values for z_T that cover the reported ranges of cloud or roll tops H and inversion heights z_1 (see Table I). From (3.1) and (3.2) we see that R_m and Re can vary markedly with z_T , and in Table II we give their values together with those for the squared aspect ratio A^2 , which is defined here by

$$A^2 = (2z_T/L)^2 \quad (3.3)$$

To calculate values of R_m , we make several assumptions. For κ the value of $P=1$ is used. The values of γ_e are estimated from $[T(0) - T(z_T)]/z_T$, and as a result, they vary markedly with z_T . The ranges of γ_e in Table II are determined by using for the temperature $T(0)$ the following three estimates:

Table II. Observed Parameters That Depend on Model Domain Height

Case	Date	Time (GMT)	Model Domain Height z_T (m)	Squared Aspect Ratio A_z^2 Mean	Range	Lapse Rate γ_e (K/km)	Moist Rayleigh Number R_m	Wind Speed at Domain Height $ \underline{V}(z_T) $ (m/s)	Reynolds Number Re
A	18/09/81	0855	400	0.16	0.06 0.44	11.2 ± 1.2	70 ± 50	18.3	488
B	18/09/81	0855	450	0.20	0.07 0.56	8.9 ± 1.1	$- 10 \pm 70$	18.1	543
C	18/09/81	0855	500	0.25	0.09 0.69	6.0 ± 1.0	$- 270 \pm 100$	17.5	583
D	18/09/81	0855	550	0.30	0.11 0.84	3.6 ± 0.9	$- 710 \pm 130$	17.4	638
E	18/09/81	0855	600	0.36	0.13 1.00	4.1 ± 0.8	$- 870 \pm 160$	17.4	696
F	20/09/81	1206	1200	0.48	0.16 2.56	9.9 ± 0.4	540 ± 240	20.8	713
G	20/09/81	1206	1300	0.57	0.19 3.00	9.8 ± 0.4	820 ± 330	19.9	739
H	20/09/81	1206	1400	0.66	0.22 3.48	9.1 ± 0.3	540 ± 330	19.3	772
I	26/09/81	1120	450	0.29	0.11 1.27	5.1 ± 1.1	$- 230 \pm 50$	18.2	482
J	26/09/81	1120	500	0.36	0.14 1.56	5.0 ± 1.0	$- 360 \pm 70$	17.3	509
K	26/09/81	1120	550	0.43	0.17 1.89	4.9 ± 0.9	$- 540 \pm 100$	17.2	556

the first is obtained by extrapolation of the aircraft data down to the surface, and the other two are obtained by adding 0.5°C and 1.0°C to the first value (by these differences, the sea surface is warmer than the air). On the other hand, the same value (5 K/km) for the moist adiabatic lapse rate γ_m seems appropriate for all cases. Because the cloud top H and the domain height z_T do not coincide in some cases, we use the following definition for n_1 :

$$n_1 = (H - z_1)/(2z_T) - [\sin(2\pi H/z_T) - \sin(2\pi z_1/z_T)]/(4\pi) \quad (3.4)$$

For cases in which $H > z_T$, we set $H = z_T$ in (3.4). Equation (3.4) is a slightly more general form for n_1 than that given in Shirer (1985), in which $H = z_T$ is assumed. However, (3.4) is not completely general because the width l of the cloud is assumed to be half the horizontal wavelength L of the circulation; for cases F to H, (3.4) gives an overestimate for the cloudy area because $l < L/2$. From (3.1) we see that the necessary condition $R_m > 0$ for convection is equivalent to $\gamma_e > (1 - n_1)\gamma_d + n_1\gamma_m$, which is the slice method criterion for conditional parcel instability given by Bjerknes (1938).

As can be seen from the values of R_m in Table II, most cases on 18 September and all cases on 26 September correspond to statically stable conditions, and all cases on 20 September to statically unstable conditions. These are consistent with the observations on 18 and 26 September of rolls penetrating into an inversion associated with an approaching warm front and on 20 September of rolls occurring in the unstable air behind a weak cold front.

3.2 Possible cloud street modes

Shirer (1985) found that one cloud street mode is possible in statically unstable environments, but that three distinct ones are possible in statically

stable environments; all these modes derive their energy from combinations of thermal and dynamic forcing. The presence of a rotating environment is important because the Coriolis and the viscous terms in the equation of motion have the same order of magnitude. As noted by Lilly (1966), this is a signature of modes tapping energy from the wind shear component parallel to the roll, and he denoted these modes as the parallel instability ones. In the model of Shirer (1985), the sizes of the Coriolis terms are measured by the rotating Reynolds number f^* given by

$$f^* = f z_T^2 / (\nu \pi^2) \quad (3.5)$$

Of note here is that f^* is not independent of Re because both parameters contain ν in their definitions. The ratio of Re and f^* , given by the Rossby number

$$Ro = Re/f^* = |\underline{V}(z_T)|^2 / (z_T f) \quad (3.6)$$

is determined from the observations. In the discussion below we limit the use of the terms parallel instability and parallel modes to the neutrally stratified case when $R_m=0$.

3.2.1 Cosine parallel modes. The parallel instability modes found by Shirer (1985) to have preferred orientations and wavelengths that most closely agreed with those reported for Ekman layers by Lilly (1966), Fallor and Kaylor (1966, 1967) and others are those developing from the lowest order sine terms of the mean wind shear profile, or equivalently via integration by parts from the lowest order cosine terms of the ambient wind profile. These latter formulations are easier to calculate from observed wind data and are given by

$$a_5 = -2 [\pi |V(z_T)| z_T]^{-1} \int_0^{z_T} U(z) \cos(2\pi z/z_T) dz \quad (3.7)$$

$$a_6 = -2 [\pi |V(z_T)| z_T]^{-1} \int_0^{z_T} V(z) \cos(2\pi z/z_T) dz \quad (3.8)$$

in which $U(z)$ and $V(z)$ are the orthogonal wind components in a right-handed coordinate system. As a consequence of the form of the expressions (3.7)-(3.8), we refer to these modes as the cosine parallel instability modes.

The coordinate system used to define (3.7)-(3.8) is quite general and is chosen to be the one in which the data is presented; Shirer (1985) chose east to specify the x -axis only for convenience. In general, the orientation angle θ for the rolls will be the angle between the x -axis and the roll axis, with counterclockwise angles being positive. In the analysis in Section 4, the expected value of θ is 0° . The orientation angle θ and the aspect ratio A are the two response parameters of the problem, because the values of them that minimize the values of the control parameters R_m and R_e provide the expected geometry of the streets.

The wind shear coefficients $\bar{\Gamma}_1$ and $\bar{\Gamma}_2$ in the roll coordinate system are

$$\bar{\Gamma}_1 = \text{Re } P [a_5 \cos(\theta) + a_6 \sin(\theta)] \quad (3.9)$$

$$\bar{\Gamma}_2 = \text{Re } P [a_6 \cos(\theta) - a_5 \sin(\theta)] \quad (3.10)$$

in which $\bar{\Gamma}_1$ is the along-roll and $\bar{\Gamma}_2$ the cross-roll shear component. For these cosine parallel modes (or coincidentally for purely thermal modes developing in an irrotational environment), the cloud streets are found to choose an orientation that maximizes the along-roll shear (Shirer, 1980,

1985). From (3.9)-(3.10) we see that this orientation is given by

$$\theta_0 = \tan^{-1}(a_6/a_5) \quad (3.11)$$

and that it also causes the cross-roll shear to vanish. In his study, Kelly (1984) used (3.11) because it corresponds to the formula for α_2 in Shirer (1980).

Shirer (1985) found that the critical Reynolds number Re_0 in the neutral, parallel instability case, can be expressed as $R_m = 0$ and

$$Re_0^2 = 4(A_0^2 + 1)^3[(A_0^2 + 1)^3 + f_0^{*2}]/[A_0^2 f_0^{*2}(a_5^2 + a_6^2)] \quad (3.12)$$

whose minimum value with respect to both A^2 and θ occurs when

$$f_0^{*2} = (A_0^2 + 1)^3(1 - 5A_0^2)/(2A_0^2 - 1) \quad (3.13)$$

This result is independent of the Prandtl number P , but depends critically on inclusion of the Coriolis term f_0^* in the model. With the aid of (3.6), we may combine (3.12)-(3.13) to relate A_0^2 to the observed values of Re , a_5 and a_6 via

$$A_0^2 = \frac{5Re^2(a_5^2 + a_6^2) - 12 + 6[4 + 5Re^2(a_5^2 + a_6^2)]^{1/2}}{25 Re^2(a_5^2 + a_6^2)} \quad (3.14)$$

Once A_0 has been determined from (3.14), we may obtain a value for f_0^* from (3.13), for Re_0 from (3.12), and for v_0 from (3.2). These values together with θ_0 may then be checked against those reported in Tables I-II, and we do this in Section 4 (see Table III). Typical values for A_0^2 given by (3.14) are $A_0^2 \sim 1/5$, which corresponds to $L/z_T \sim 4.5$.

3.2.2 Cosine nonneutral modes. For a boundary layer characterized by $R_m > 0$ and $Re < Re_0$, (in which Re_0 is the critical value (3.12) in the neutral case), Shirer (1985) found that only one mode is possible. As the values of Re vary, the preferred orientation angles θ are approximately given by $\theta = \theta_0$, but the expected values of A^2 increase from $1/5$ to $1/2$ as the critical values of Re decrease and as those of R_m increase. For Rayleigh-Bénard convection in a calm environment, the aspect ratio obeys $A^2 = 1/2$ or $L/z_T = 2.8$.

For a boundary layer characterized by $R_m < 0$ and $Re > Re_0$, Shirer (1985) found a single mode having preferred alignments near θ_0 , but having wavelengths that broaden as the critical value of Re increases above that for Re_0 . However, in a boundary layer having a sufficiently stable stratification, a second mode occurs for which the along-roll and cross-roll shear coefficients $\bar{\Gamma}_1$ and $\bar{\Gamma}_2$ are nearly equal in magnitude. Kaylor and Fallor (1972) found modes similar to this second one, and they related them to propagating internal gravity waves. For these second modes to exist, Shirer discovered that the values of both Re and R_m have to exceed their respective critical values Re_3 and R_{m3} , and that this is consistent with the usual requirement that the value of a Richardson number $Ri = -R_m/(Re^2P)$ not be too large. These modes are consistently oriented 30° to 50° on either the right or the left of the alignment given by θ_0 and their angles are labeled θ_3 and θ_4 ; moreover the preferred values for A^2 are near 1, corresponding to $L/z_T \sim 2$.

For all the cosine modes, the expected values of A^2 fall in the ranges given in Table II. Thus, a critical test (in Section 4) is a comparison of observed and modeled orientation angles, for the two cosine modes are separated by 30° to 50° .

3.2.3 Sine parallel modes. As noted by Shirer (1985), not all the energy in the mean wind profile that is available for roll development is in the lowest order cosine terms a_5 and a_6 of a Fourier series. Indeed, as a_5 and a_6 decrease in magnitude, we see from (3.12) that Re_0 will increase in value; other modes having smaller critical Reynolds numbers might be possible and so become the expected ones. For example, there could be significant energy in the mean shear and lowest order sine terms of a Fourier expansion of the wind profile, and for an Ekman profile Shirer (1985) considered for the case $R_m=0$ the parallel instability modes that develop from these terms. These are referred to as the sine parallel modes and depend on the coefficients

$$b_1 = 2[\pi^2 |V(z_T)|]^{-1} [U(z_T) - U(0)] \quad (3.15)$$

$$b_2 = 2[\pi^2 |V(z_T)|]^{-1} [V(z_T) - V(0)] \quad (3.16)$$

$$b_3 = -2[\pi |V(z_T)| z_T]^{-1} \int_0^{z_T} U(z) \sin(2\pi z/z_T) dz \quad (3.17)$$

$$b_4 = -2[\pi |V(z_T)| z_T]^{-1} \int_0^{z_T} V(z) \sin(2\pi z/z_T) dz \quad (3.18)$$

In this case the wind shear coefficients in the roll coordinate system are (cf (3.9)-(3.10) for \tilde{f}_1 and \tilde{f}_2)

$$\tilde{f}_1 = Re P[(b_1 - b_3) \cos(\theta) + (b_2 - b_4) \sin(\theta)] \quad (3.19)$$

$$\tilde{f}_2 = Re P[(b_2 - b_4) \cos(\theta) - (b_1 - b_3) \sin(\theta)] \quad (3.20)$$

$$\bar{\epsilon}_3 = \text{Re } P[b_3 \cos(\theta) + b_4 \sin(\theta)] \quad (3.21)$$

$$\bar{\epsilon}_4 = \text{Re } P[b_4 \cos(\theta) - b_3 \sin(\theta)] \quad (3.22)$$

Unfortunately the fact that $\bar{\epsilon}_1 \neq \bar{\epsilon}_3$ and $\bar{\epsilon}_2 \neq \bar{\epsilon}_4$ greatly complicates the analysis, and eliminates the possibility for simple formulas comparable to those in (3.11)-(3.14) for the preferred parameter values. For example, the orientation angle for which the roll-perpendicular shear $\bar{\epsilon}_4$ vanishes is $\theta_p = \tan^{-1}(b_4/b_3)$. However, this angle does not lead to the vanishing of the other roll-perpendicular component $\bar{\epsilon}_2$, because in general $b_1 \neq 0$ and $b_2 \neq 0$. In addition, the alignment angle in Shirer (1980) analogous to that for the sine parallel modes is α_3 , given here by $\alpha_3 = \tan^{-1} [(b_2 - 2b_4)/(b_1 - 2b_3)]$. But this angle does not provide the preferred orientation of the rolls either.

Consequently, the preferred parameter values, which will be denoted by a subscript a , are determined numerically by solving a cubic equation in Re^2 ; as in the previous cosine parallel mode case, the appropriate values for A_a^2 , θ_a , f_a^* and v_a are those that produce the smallest critical value Re_a for Re . Generally, for both Ekman profiles and the Kontur profiles discussed in Section 4, the preferred angles θ_a are ones for which $|\bar{\epsilon}_3| \gg |\bar{\epsilon}_4|$. Thus, the rolls are aligned so that the magnitudes of the roll-parallel shear components greatly exceed those for the roll-perpendicular ones. The Coriolis parameter is necessary as well, so it is reasonable to refer to these modes as parallel modes. But $\bar{\epsilon}_2$ is often large in magnitude too, implying that there is a significant energy source from a perpendicular component of the wind. No such energy source exists for the cosine parallel modes.

Shirer (1985) found for Ekman profiles that the sine parallel modes are associated with orientations within $\pm 20^\circ$ of the geostrophic wind vector when D is in the range $z_T/2$ to z_T . This is the same range for D that characterizes the KonTur observations (see Table I). Unfortunately, Shirer (1985) did not consider the nonneutral sine modes and so did not determine whether modes could exist that are analogous to the nonneutral cosine ones for which $\bar{T}_1 = \bar{T}_2$. Of note is that because the spectral expansion for the stream function of the sine parallel modes contains both $\sin(z)$ and $\cos(z)$ terms, these rolls will be tilted in the vertical; the cosine parallel modes have only $\sin(z)$ terms in the stream function expansion and so these rolls cannot tilt.

4. Comparisons

In order to compare the observed and theoretical results, we assume that the observed values of Re and R_m are near their critical ones for instability. This will be an acceptable assumption if the roll-scale velocities and thermal perturbations are small in magnitude. From the observed cross-sections through the rolls on 18 and 20 September 1981 given in Brümmer and Grant (1985), we find that $|v'| \sim 0.2$ m/s and $|T'| \sim 0.1$ K, which are small values relative to those of the scaling variables $V \sim 10$ m/s and $T_0 \sim 290$ K used in the model.

From Table II, we see that the boundary layer is nearly neutrally stratified ($R_m \approx 0$) in cases A and B, and unstably stratified ($R_m > 0$) in cases F to H). From the results summarized in Section 3, we note that these are the cases most likely to have orientations near the angles associated with the parallel instability modes: in the neutral cases, we should find $Re \approx Re_0$.

for the cosine modes or $Re = Re_a$ for the sine modes, while in unstable cases we should have $Re < Re_0$ or $Re < Re_a$. The stably stratified cases ($R_m < 0$; cases C to E, I to K) might be well approximated by the cosine parallel mode, for which $\theta = \theta_0$ and $Re > Re_0$, the sine parallel mode for which $\theta = \theta_a$ and $Re > Re_a$, the cosine nonneutral mode for which $\theta = \theta_0 \pm 40^\circ$ and $Re > Re_3$ and $R_m > R_{m3}$, or the sine nonneutral mode which unfortunately was not considered by Shirer (1985).

4.1 Comparisons with cosine modes

In Table III we give the modeled and observed values of orientation angles θ , wavelengths L , Reynolds numbers Re and eddy viscosities ν for the 11 cases summarized in Table II. The observed wind profiles given in Brümmer and Grant (1985) are already in the roll coordinate system, and so the observed orientations are 0° .

Generally the results given in Table III show that the cosine parallel modes (subscript o) cannot explain the observed cloud streets: The orientations are too far from their observed values and the magnitudes of Re generally exceed those for Re_0 in both stably and unstably stratified situations, while $Re > Re_0$ is expected only for the stable cases. Generally the modeled values for L are within the reported ranges.

Expected orientation angles θ_0 that are much larger than the observed ones suggest that the second cosine modes, for which the Fourier coefficients of the along-roll, $\bar{\Gamma}_1$, and cross-roll, $\bar{\Gamma}_2$, wind shear components are nearly equal in magnitude, might explain the observations in the stably stratified cases. Table III also summarizes the expected values for these modes (subscripts 3 and 4). Again, the modeled orientations θ_3 and θ_4 rarely agree

Table III. Coarse Modes: Subscript o are neutral modes for parallel instability, subscripts 3 and 4 are nonneutral modes for which the along-roll and cross-roll shear coefficients are nearly equal in magnitude (P=0.4 used so moist Rayleigh numbers are nearly equal).

308

(1 - model domain height equal to inversion height, c - model domain height equal to cloud or roll top).

Case	Orientation (deg)		Wavelength (m)		Reynolds Number		Viscosity (m ² /s)		Moist								
	Observed	Modeled	Observed Range	Modeled	Observed	Modeled	Observed	Modeled	Observed	Modeled							
	θ_o	θ_3	θ_4	L_o	$L_3=L_4$	Re_o	$Re_3=Re_4$	ν_o	$\nu_3=\nu_4$	R_{mo}	$R_{m3}=R_{m4}$						
A(1)	0	-75	-42	71	1200-3300	1730	810	488	1690	3100	15	4	2	70	\pm 50	0	-36
B	0	69	-81	40	1200-3300	1970	920	543	1240	2150	15	7	4	-10	\pm 70	0	-28
C	0	75	-79	46	1200-3300	2200	1050	583	935	1550	15	9	6	-270	\pm 100	0	-22
D(c)	0	62	88	36	1200-3300	2420	1140	638	813	1350	15	12	7	-710	\pm 130	0	-23
E	0	67	-86	41	1200-3300	2650	1220	696	666	1100	15	16	10	-870	\pm 160	0	-24
F(c)	0	89	-55	51	1500-6000	5140	2420	713	770	1500	35	32	17	540	\pm 240	0	-44
G(1)	0	64	-81	28	1500-6000	5590	2610	739	650	1250	35	40	21	820	\pm 330	0	-42
H	0	49	85	16	1500-6000	6040	2790	772	549	1050	35	49	26	540	\pm 330	0	-43
I(1)	0	61	-89	32	800-2700	1970	920	482	1230	2150	17	7	4	-230	\pm 50	0	-30
J(c)	0	58	85	31	800-2700	2200	1030	509	869	1450	17	10	6	-360	\pm 70	0	-25
K	0	65	88	36	800-2700	2430	1160	556	742	1200	17	13	8	-540	\pm 100	0	-19

with the observed ones, the wavelengths L_j tend to be too small, and the values of the Reynolds numbers Re_j too large.

The poor agreement between the model results and the observations can be seen in Fig. 1, in which the observed ranges of R_m are shown as functions of the observed normalized values of Re . The dashed line gives the critical values of R_m and Re for those modes that correspond in the neutral case $R_m = 0$ to the cosine parallel modes, and the solid lines give in a few selected cases the critical values for the nonneutral cosine modes for which $|\tilde{r}_1| = |\tilde{r}_2|$. Rolls are expected when values of R_m and Re are to the right of the curves. No observed values of Re approach those associated with the nonneutral cosine modes, and they would not, even if the values of ν were adjusted by a factor of 2. Moreover, the locations of the critical curves for the nonneutral modes do not depend very much on the particular value of P ; the chosen value of P , $P = 0.4$, is the value for which both the right mode θ_3 and the left mode θ_4 have approximately the same critical values of R_m and Re .

From the above comparisons, we conclude that the cloud streets observed during KonTur did not derive their energy from the lowest order cosine terms in the Fourier expansion of the mean wind profile. The Ekman depths D observed during KonTur were quite large, when normalized by either the cloud top H or the domain height z_T (see Tables I and II). Shirer (1985) noted that the cosine parallel modes are more likely associated with secondary circulations developing in boundary layers having very small relative Ekman depths for which $D/z_T \sim 1/5$. He concluded that modes extracting energy from the average shear and sine terms b_1 to b_4 in the mean wind profile were more likely to explain the circulation patterns when D/z_T was in the range $1/2$ to 1 , as characterizes the KonTur cases. He also observed that these patterns would have appreciable tilts in the vertical; Brümmer and Grant (1985) noted

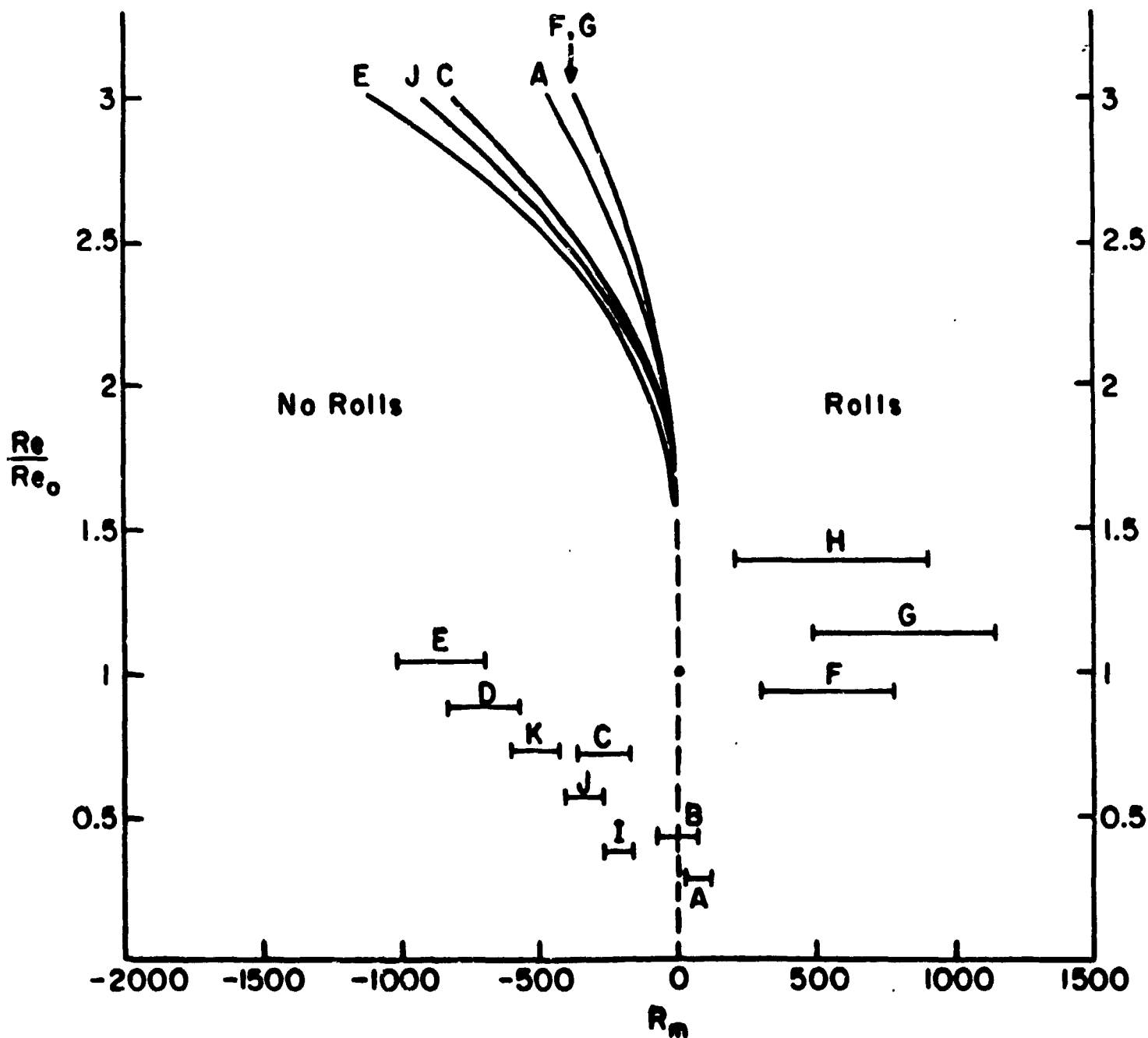


Figure 1. Critical values of R_m and normalized critical values of Re for the cosine modes when $P = 0.4$; for this value of P , the nonneutral modes have the same critical value of R_m . The dashed line gives the values for the modes that are associated with the parallel instability case; this case occurs at $R_m = 0$ and $Re = Re_0$ and it is labeled with a dot. The solid lines give in a few cases the modes for which the cross-roll and along-roll shear components are nearly equal in magnitude. Also shown are the observed values given in Table II.

that the cross sections through the rolls on 18 and 20 September showed appreciable tilt, particularly in the thermodynamic variables. The sine parallel modes, then, appear to be better candidates for explaining the KonTur observations.

4.2 Comparisons with sine parallel modes

Although Shirer (1985) did not consider the stratified problem, we may examine the neutrally stratified case here under the assumption that the actual orientations and wavelengths found in a stratified atmosphere would be near those applicable to the neutral case. We may test this hypothesis by checking whether the observed values of Re are greater than their theoretical values Re_g in the stable cases and whether $Re < Re_g$ in the unstable cases.

In Table IV we show the expected orientations θ_g and wavelengths L_g , as well as the values of Re_g and v_g , for the cloud streets associated with the sine parallel modes. In contrast to the cosine modes (Table III), we find that two or three alignments are possible in many cases; all are given, with the orientations associated with the smallest values of Re_g listed first. Many cases in Table IV give acceptable agreement in all displayed parameter values. Generally, the best agreement occurs when the inversion height z_i , rather than the cloud top H , is used as the model domain height z_T : in case A for 18 September, case G for 20 September and case I for 26 September, the orientations are within 10° of the observed values. Of note is that z_i is the altitude assumed by Shirer (1985) to correspond to the domain height; because he did not model circulations penetrating into the capping stable layer, it is not surprising that $z_T = z_i$ leads to better agreement than does $z_T = H$.

In addition, as depicted in Fig. 2, the relationship between Re and Re_g is generally as would be expected if the nonneutral sine modes are to explain

Table IV. Sine Parallel Instability Modes (i - model domain height equal to inversion height,
c - model domain height equal to cloud or roll top)

Case	Orientation (deg)		Wavelength (m)		Reynolds Number		Eddy Viscosity (m^2/s)	
	Observed	Modeled θ_a	Observed Range	Modeled L_a	Observed	Modeled Re_a	Observed	Modeled ν_a
A(1)	0	$\begin{Bmatrix} 10 \\ -14 \end{Bmatrix}$	1200-3300	$\begin{Bmatrix} 1630 \\ 2000 \end{Bmatrix}$	488	$\begin{Bmatrix} 508 \\ 733 \end{Bmatrix}$	15	$\begin{Bmatrix} 14 \\ 10 \end{Bmatrix}$
B	0	$\begin{Bmatrix} 23 \\ -23 \end{Bmatrix}$	1200-3300	$\begin{Bmatrix} 1800 \\ 2320 \end{Bmatrix}$	543	$\begin{Bmatrix} 387 \\ 692 \end{Bmatrix}$	15	$\begin{Bmatrix} 21 \\ 12 \end{Bmatrix}$
C	0	$\begin{Bmatrix} 33 \\ -44 \end{Bmatrix}$	1200-3300	$\begin{Bmatrix} 2430 \\ 2670 \end{Bmatrix}$	583	$\begin{Bmatrix} 375 \\ 745 \end{Bmatrix}$	15	$\begin{Bmatrix} 23 \\ 12 \end{Bmatrix}$
D(c)	0	$\begin{Bmatrix} 42 \\ -57 \end{Bmatrix}$	1200-3300	$\begin{Bmatrix} 2200 \\ 2940 \end{Bmatrix}$	638	$\begin{Bmatrix} 299 \\ 635 \end{Bmatrix}$	15	$\begin{Bmatrix} 32 \\ 15 \end{Bmatrix}$
E	0	$\begin{Bmatrix} 52 \\ -51 \end{Bmatrix}$	1200-3300	$\begin{Bmatrix} 2400 \\ 3330 \end{Bmatrix}$	696	$\begin{Bmatrix} 334 \\ 730 \end{Bmatrix}$	15	$\begin{Bmatrix} 31 \\ 14 \end{Bmatrix}$
F(c)	0	$\begin{Bmatrix} -9 \\ 68 \end{Bmatrix}$	1500-6000	$\begin{Bmatrix} 3890 \\ 6410 \end{Bmatrix}$	713	$\begin{Bmatrix} 1350 \\ 1370 \end{Bmatrix}$	35	$\begin{Bmatrix} 18 \\ 18 \end{Bmatrix}$
G(1)	0	$\begin{Bmatrix} -7 \\ 17 \\ -21 \end{Bmatrix}$	1500-6000	$\begin{Bmatrix} 5670 \\ 5540 \\ 4270 \end{Bmatrix}$	739	$\begin{Bmatrix} 834 \\ 870 \\ 931 \end{Bmatrix}$	35	$\begin{Bmatrix} 31 \\ 30 \\ 28 \end{Bmatrix}$
H	0	$\begin{Bmatrix} 31 \\ -34 \\ -8 \end{Bmatrix}$	1500-6000	$\begin{Bmatrix} 6790 \\ 4870 \\ 14000 \end{Bmatrix}$	772	$\begin{Bmatrix} 890 \\ 1010 \\ 1180 \end{Bmatrix}$	35	$\begin{Bmatrix} 30 \\ 27 \\ 25 \end{Bmatrix}$
I(1)	0	$\begin{Bmatrix} -10 \\ -21 \end{Bmatrix}$	800-2700	$\begin{Bmatrix} 1920 \\ 2010 \end{Bmatrix}$	482	$\begin{Bmatrix} 653 \\ 885 \end{Bmatrix}$	17	$\begin{Bmatrix} 13 \\ 9 \end{Bmatrix}$
J(c)	0	-28	800-2700	2180	509	790	17	11
K	0	$\begin{Bmatrix} 8 \\ -23 \end{Bmatrix}$	800-2700	$\begin{Bmatrix} 2350 \\ 2460 \end{Bmatrix}$	556	$\begin{Bmatrix} 427 \\ 591 \end{Bmatrix}$	17	$\begin{Bmatrix} 22 \\ 16 \end{Bmatrix}$

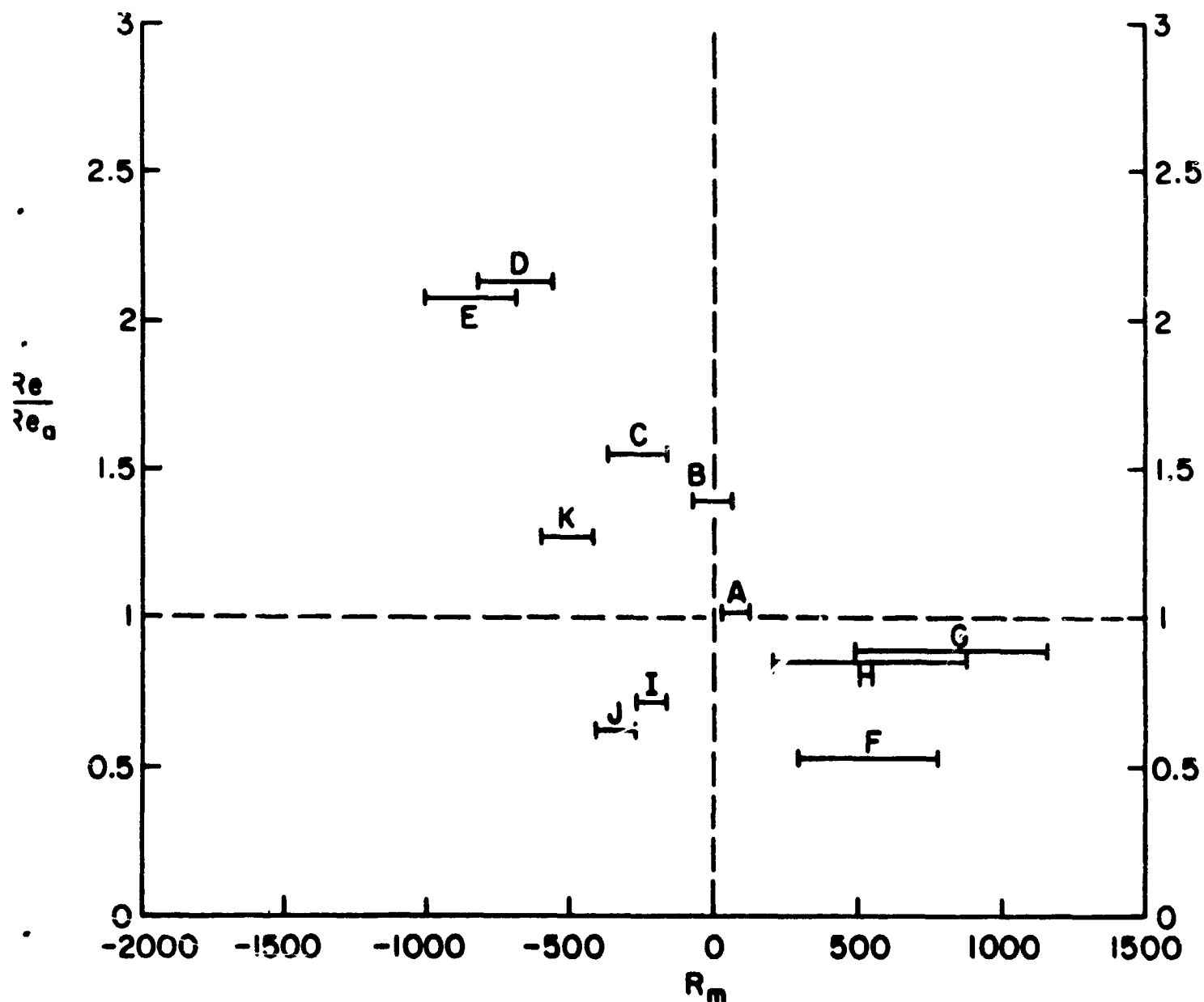


Figure 2. The observed values of R_m and Re normalized by the smallest values of Re_0 for the sine parallel modes for the 11 cases given in Table II. Under the assumption that the stratified cases follow curves as shown in Fig. 1, the unstable cases F, G, H should occur below and to the right of the dashed lines, the neutral cases A and B should occur near where the dashed lines cross, and the stable cases C, D, E, I, J, K should occur above and to the left of the dashed lines. Generally the data follow the expected trend.

the observations. We find that $Re/Re_a < 1$ for unstably stratified situations, and that $Re/Re_a > 1$ for stably stratified ones; this is in contrast to the cosine modes for which $Re/Re_0 < 1$ in the stable cases but $Re > Re_0$ in the unstable cases (Fig. 1). Moreover, in Fig. 2 the values appear to fall on a line when plotted as functions of Re_a , again in contrast to the previous case in Fig. 1. From Table IV, we find that the wavelengths L_a are well within the reported ranges in the cases A and B for streets developing in nearly neutral boundary layers. The wavelengths in the unstably stratified cases F to H are a bit too large, but as noted in Section 3, we expect that the values of L_a or L_0 will be smaller in the unstably stratified cases than in the neutral ones.

5. Concluding Remarks

In this article, we compared the orientations, wavelengths, and governing parameter values observed on three cloud street days during the 1981 KonTur experiment with the three parallel/thermal instability roll modes discussed by Shirer (1985) in a nonlinear model of shallow Boussinesq convection. Two of these modes derive energy from the lowest order cosine terms in the mean wind profile and the other mode from the average shear and lowest order sine terms. No evidence is found here that the observed cloud bands derive their energy from the cosine terms, which were noted by Shirer (1985) to be associated with small Ekman depths.

Instead, the roll modes deriving their energy from the sine terms of the wind profile appear to give agreement in all parameter values, even though only the neutrally stratified case could be considered in the model. The agreement is best when the inversion heights are assumed to represent the top of the roll circulations, even when there is appreciable penetration of the circulations into the stable layer; this is consistent with the assumption

used in the Shirer (1985) model that the environmental lapse rate is constant. The sine modes appear to characterize boundary layers having large Ekman depths, and the nonlinear solutions associated with these modes would have appreciable tilt with height. Both these features were found in the cloud street observations.

The results presented here do not contradict those presented in Brümmer and Grant (1985). They concluded that the rolls on 20 September were thermally driven and those on 18 and 26 September were dynamically driven, and this is consistent with the results given in Fig. 2. Moreover, Brümmer and Grant (1985) determined that the primary dynamic energy source for the rolls was that of the cross-roll wind component. As noted earlier, this would be incompatible with the cosine parallel instability modes for which the roll-perpendicular shear component vanishes, but it would be compatible with the sine parallel mode for which an appreciable roll-perpendicular wind component occurs. The sine modes can be called parallel modes because they are aligned so that the roll-parallel wind shear is much larger than the roll-perpendicular shear and because the Coriolis parameter must be included.

However, one deficiency of the Shirer (1985) model is that there is no representation of a primary dynamic mechanism — the inflection point instability — for extracting energy from the cross-roll mean shear. To study these inflection point modes, a crucial requirement is that more than one vertical harmonic must be included in the model. This observation, together with the results presented here, indicate that to represent completely all possible roll modes, a low-order model must include both the sine and cosine terms and at least two wavenumbers in the vertical. In this way sufficient

forcing by the ambient wind would be introduced into the model via inclusion of all of the first few terms of a Fourier expansion of the mean wind profile.

A second deficiency of the present model is that only the linear portion of the mean temperature structure is resolved. Since most roll circulations penetrate into inversions capping the boundary layer, the nonlinear portions of the mean temperature profile ought to be important to the development of the rolls. In spite of the deficiencies in the present model, the analysis in this article demonstrates a remarkable agreement between the observations and the theoretical modes deriving energy from only a limited part of the mean wind and temperature profiles.

Acknowledgments

The first author gratefully acknowledges the partial support given him by Professor Dr. H. Hinzpeter from the University of Hamburg so that he could attend the 1983 KonTur symposium in Hamburg during which the idea for performing the comparisons reported in this article was born. We also thank two anonymous reviewers for providing many useful criticisms of an earlier version of this manuscript.

This research was partially supported by the National Science Foundation through Grants ATM 79-08354, ATM 81-13223, ATM 83-07213 and by the National Aeronautics and Space Administration through Grants NAS 8-33794 and NAS 8-36130.

References

- Asai, T. and I. Nakasugi, 1973: On the stability of Ekman boundary layer flow with thermally unstable stratification. J. Meteor. Soc. Japan, 51, 29-42.
- Bjerknes, J., 1938: Saturated-adiabatic ascent of air through dry-adiabatically descending environment. Quart. J. Roy. Meteor. Soc., 64, 325-330.
- Brown, R.A., 1970: A secondary flow model for the planetary boundary layer. J. Atmos. Sci., 27, 742-757.
- Brown, R.A., 1980: Longitudinal instabilities and secondary flows in the planetary boundary layer. A review. Rev. Geophys. Space Phys., 18, 683-697.
- Brümmer, B. and A. Grant, 1985: Structure, dynamics, and energetics of boundary layer rolls from KonTur aircraft observations. Submitted to Beitr. Phys. Atmos. for review.
- Faller, A.J. and R.E. Kaylor, 1966: A numerical study of the instability of the laminar Ekman boundary layer. J. Atmos. Sci., 23, 466-480.
- Faller, A.J. and R.E. Kaylor, 1967: Instability of the Ekman spiral with applications to planetary boundary layers. Phys. Fluids Suppl., IUGG-IUTAM Symposium, 19-24 September, Kyoto, Japan, S212-S219.
- Kaylor, R.E. and A.J. Faller, 1972: Instability of the stratified Ekman boundary layer and the generation of internal waves. J. Atmos. Sci., 29, 497-509.
- Kelly, R.D., 1984: Horizontal roll and boundary-layer interrelationships observed over Lake Michigan. J. Atmos. Sci., 41, 1816-1826.
- Lilly, D.K., 1966: On the stability of Ekman boundary flow. J. Atmos. Sci., 23, 481-494.
- Shirer, H.N., 1980: Bifurcation and stability in a model of moist convection in a shearing environment. J. Atmos. Sci., 37, 1586-1602.
- Shirer, H.N., 1985: On cloud street development in three dimensions: Parallel and Rayleigh instabilities. Submitted to Beitr. Phys. Atmos. for review.

27
CHAPTER 8

N86-11756

On the Nonlinear Characteristics of the Axisymmetric Flow Regime:

Cylindrical and Spherical Systems

R. Wayne Higgins
John A. Dutton
and
Hampton N. Shirer

Department of Meteorology
The Pennsylvania State University
University Park, PA 16802

Abstract

The physical relationship between steady axisymmetric flows that might be observed in the atmosphere and in laboratory vessels is investigated theoretically. This is accomplished by comparing both the nonlinear structure and the thermal forcing mechanisms in two truncated spectral models of flow in the atmosphere and the rotating laboratory cylinder respectively. Under statically stable conditions, the response of the internally-forced spherical model (which is developed here from a set of new orthonormal basis functions) exhibits steady behavior different from that in the externally forced cylindrical model. Two regions of multiple steady solutions occur in the cylindrical model, under stable conditions, that are not found in the spherical one. The possible physical relevance of these multiple solutions is investigated by determining their location in parameter space with respect to the classical Hadley-Rossby transition curve. The results suggest that the wave flow regime, in an annulus, might develop catastrophically when an upper symmetric flow ceases to exist. Further examination of each model reveals that steady behavior is linked to the hydrostatic assumption and so to the aspect ratio and basis functions of each system. The results suggest that the manner by which regime transitions occur in externally forced vessels might differ from those for the internally (and externally) forced atmosphere. Significantly, internally forced laboratory vessels are found to have the greatest utility for studies of large-scale axisymmetric flow regimes in the atmosphere.

1. Introduction

Theories of the global structure and behavior of the atmosphere cannot be tested easily via direct experimentation. Thus, atmospheric scientists must develop suitable replicas, such as laboratory or mathematical models, to simulate thermally forced motion on rotating planets. If the objective is to produce an accurate prediction of large scale atmospheric flows, then a detailed replica that includes the effects of topography, radiation, cloudiness, etc., must be considered. However, the complexity of such a detailed model would obscure thorough understanding of the physical processes that produce the flow. Hence, to gain physical insight into the nature of atmospheric motions, it is often necessary to utilize simplified models in which only certain physical processes are emphasized.

Generally, a laboratory model is considered useful if it produces flows that resemble those of the atmosphere. A common assumption is that we can establish the relevance of certain experimental results to atmospheric flows by considering the degree of dynamic similarity between the two physical systems. Two systems are dynamically similar if we can determine, from the forces involved, an appropriate set of dimensionless parameters, similar values of which describe analogous motions in both systems (e.g., Panofsky and Dutton, 1983).

It is impossible to devise a complete, practical system that replicates the atmosphere exactly. Instead, we consider models having governing equations of motion that retain at least those few dimensionless ratios necessary for describing qualitatively important behavior in the atmosphere. Examples of qualitatively important behavior would include the number and type of transitions between flow regimes. Since Buckingham's Theorem guarantees that there are only a finite number of ratios from which to choose (Langhaar,

1951), we are assured that only a finite number will control such transitions.

In the laboratory, simple flows have been generated by subjecting a fluid within a rotating annulus to a series of externally imposed variations in horizontal temperature contrast and rotation rate (e.g. Fultz et al., 1959). The annular flows obtained at the critical values of the crucial parameters, which are usually taken to be the thermal Rossby number and the Taylor number, exhibit transitions between the symmetric Hadley regime and the wavy Rossby regime, as well as between flows within the Rossby regime. Apparently only two fundamental parameters are needed to specify these transitions qualitatively, although such geometric parameters as aspect ratio may affect them quantitatively.

Owing to both the variable orientation of the gravity vector relative to the axis of rotation and the spherical geometry of the earth, an efficacious laboratory model might be difficult to design. It is conceivable that neither of these physical aspects of the earth are crucial to the establishment of dynamic similarity between a laboratory model and the atmosphere. In fact, many investigators tacitly assume that these two aspects are not crucial when they consider cylindrical laboratory configurations, in which the gravity vector is oriented parallel to the axis of rotation. Intuitively, however, the rotating hemisphere seems preferable to the rotating cylinder for observational studies, because its geometry more closely matches that of the earth.

Space-based experimentation in micro-gravity environments offers the potential of using spherical vessels having the appropriate orientation for the body force. Recently, the Geophysical Fluid Flow Cell (GFFC), a hemispherical shell of dielectric fluid, has been proposed to take advantage of the zero gravity environment (Hart, 1984). So far, however, various design limitations

have restricted the projected overall usefulness of this particular instrument for studies of large scale planetary wave processes arising from the instability of axisymmetric flows.

In addition to design problems, there is no guarantee that the results obtained from such a spherical configuration would be qualitatively different from those obtained in a cylindrical one. Indeed, we might observe that similar parameters govern the same types of transitions (e.g., Hadley flows exchanging stability with Rossby flows, etc.) in both rotating vessels. In this situation, it is crucial to determine whether the characteristics of the transitions might change between the atmosphere and the laboratory vessels: in one system the transitions might be smooth, in another, sudden. This is crucial, because fundamental to the notion of dynamic similarity is the premise that transitions occur in the replica of interest for the same reasons that they occur in the atmosphere.

In this study, we present evidence that both the occurrences of and the characteristics of the transitions in a quasi-hydrostatic model, which is representative of the atmosphere, will not vary qualitatively with the types of thermal forcing. The term quasi-hydrostatic is used because the viscosity term is retained in the usual hydrostatic approximation. In contrast, we show that an appropriate non-hydrostatic model, which is based on the laboratory cylinder, exhibits different steady behavior and hence different branching behavior from that in the spherical case. These results are generalized to the corresponding physical systems to show that when modeling the atmosphere the type of thermal forcing is crucial in a cylindrical replica, but not in a spherical one. Hence, a laboratory cylinder must be forced suitably in order to model adequately the large-scale flow regime in the atmosphere.

In the analysis, we consider various combinations of two fundamental

types of thermal forcing mechanisms: external and internal. External forcing is applied at the boundaries of a laboratory model. For example, an externally imposed horizontal temperature difference is maintained in an annulus by heating the outer wall and cooling the inner one. Generally, this type of thermal forcing must be used also in spherical laboratory models. Internal forcing, on the other hand, must be applied directly to the working fluid inside a vessel. However, this mechanism is not easy to apply experimentally. If internal forcing is crucial to modeling transitions in the atmosphere, then it should be included in laboratory simulations.

To obtain the results mentioned above, we compare the solutions of two low-order spectral models that are truncated at the same level and that are based on spherical and cylindrical geometries, respectively. Obviously, this is a much more practical approach than comparing either the flows produced in two laboratory vessels or the solutions of two large mathematical models that describe the two physical systems. Indeed, the laboratory vessels, which require considerable resources to construct, might be difficult to use as Harv (1984) indicates for the rotating hemisphere. Moreover, large mathematical models are unwieldy and thereby impractical for this type of study in which we consider the transitions between steady state motions that in many cases are governed by only a small number of parameters (Shirer and Wells, 1983).

In this article, we begin by introducing suitable forms of the hydrodynamic equations. Utilizing the results of a recently developed method based on contact catastrophe theory (Shirer and Wells, 1982), and an application of Galerkin techniques, we obtain two five-component spectral models. The method based on contact catastrophe theory helps us to identify crucial parameters that define dynamic similarity and that govern the steady states of both physical systems. We choose spectral models because the

modeled flows are dominated by only a few spatial harmonics. Indeed, from observational studies using the rotating annulus (e.g., Fultz et al., 1959; Fowles and Hide, 1965), we know that the spectrum of flows is characterized by sudden transitions between observed states and hysteresis, which may be explained simply by low-order spectral models (e.g., Lorenz, 1962, 1963, 1984; Veronis, 1966; Vickroy and Dutton, 1979; and Yost and Shirer, 1982).

In Section 2, we discuss a new spherical model, which is developed here from a set of orthonormal basis functions recently proposed by Dutton (1982). These functions, which are derived by solving a linearized eigenvalue problem extracted from the original model equations, directly incorporate important aspects of the atmospheric dynamics. Initially, the model includes an internal thermal forcing mechanism that requires the heating field and temperature field to share identical eigenfunctions (Henderson, 1962). This mechanism is derived from atmospheric observations such as those in Dutton (1976). We find it necessary to add appropriate terms containing a Hadley number (Yost and Shirer, 1982) that is proportional to a horizontal temperature difference that might be imposed along the lower boundary, in order to compare the solutions of the spherical model with those of the cylindrical model.

The cylindrical model, which is discussed in Section 3, is a version of the five-component model of Veronis (1966), that has been modified suitably by Shirer and Wells (1983) to contain both a Hadley number and a Rayleigh number that measure the horizontal and vertical temperature differences respectively. The possible physical relevance of the multiple solution regions in this model, which occur in a statically stable rotating fluid, is investigated by determining the location of their boundaries in parameter space with respect to the observed symmetric flow-wave flow transition curve. The results from

this section suggest the possibility that the wave flow regime in an annulus might develop catastrophically when an upper symmetric flow ceases to exist rather than smoothly via a bifurcation, as one infers from the discussion in Lacher et al. (1977). This distinction is important, because it is essential to understand precisely how the transition from the Hadley to the Rossby regime is accomplished before we can model properly the transitions between flows within the Rossby regime itself. This philosophy is in accord with that of Chang and Shirer (1984) who suggest that, in many cases, all transitions within two-dimensional regimes must be modeled correctly before the transitions to the three-dimensional ones can be obtained correctly.

In Section 4, we compare the steady solution surfaces that arise in each low-order axisymmetric model and show that substantial differences occur. As mentioned above, we find that any combination of internal and external thermal forcing mechanisms in the spherical model, leads to unique real solutions in statically stable conditions. This result suggests that transitions between the Hadley and Rossby regimes in the atmosphere are likely to be smooth. If both models are forced externally, then we observe two cusps in the cylindrical model, in statically stable conditions, that are not found in the spherical replica. Consequently, in this case sudden transitions and hysteresis within the axisymmetric flow regime are possible in the cylindrical model, but not in the spherical one. The different behavior is linked to the hydrostatic assumption and so to the aspect ratio and basis functions of each system. Finally, if internal thermal forcing is used in both models, in the absence of externally imposed horizontal thermal forcing (i.e., a Hadley number), then unique real solutions are found in both models in statically stable conditions.

We conclude that an internally forced laboratory vessel would most

closely model the axisymmetric flow in the atmosphere. Thus, the results raise a number of questions concerning the utility of externally forced vessels for future studies of large-scale flow regimes in the atmosphere.

2. Axisymmetric flows in a rotating hemisphere

From a Boussinesq version of the Navier-Stokes equations and the first law of thermodynamics, we may derive an infinite set of nonlinear ordinary differential equations (o.d.e.'s). To accomplish this, we develop first a new set of orthonormal vector basis functions for the dependent variables from associated linear eigenvalue problems. In this investigation, the set of o.d.e.'s is truncated to yield a five-component axisymmetric model that is representative of the atmosphere. In the final part of this section, we obtain the steady solutions and construct the resulting steady solution surface, in anticipation of a comparison with the cylindrical model results.

a. The approximate equations for global axisymmetric flow

We choose to alter an approximate set of large-scale Boussinesq equations given in Dutton (1982), by imposing quasi-hydrostatic conditions and by assuming incompressibility. This system can be written as

$$\frac{\partial \underline{v}_H}{\partial t} + \underline{v} \cdot \nabla \underline{v}_H = -\nabla_H(\theta_0 \pi') - f \underline{k} \times \underline{v}_H + \nabla \cdot \nu \nabla \underline{v}_H, \quad (2.1)$$

$$\frac{\partial(\theta_0 \pi')}{\partial z} = g \frac{\theta'}{\theta_0} + \nabla \cdot \nu \nabla w, \quad (2.2)$$

$$\frac{\partial}{\partial t} \left(\frac{\theta'}{\theta_0} \right) + \underline{v}_H \cdot \nabla \left(\frac{\theta'}{\theta_0} \right) + w \frac{\partial}{\partial z} \left(\frac{\theta'}{\theta_0} \right) + \frac{w}{\theta_0} \frac{(\Delta_z \theta)}{Z_T} = \frac{Q}{\rho_0 c_p T_0} + \nabla \cdot \kappa \nabla \left(\frac{\theta'}{\theta_0} \right), \quad (2.3)$$

$$\nabla \cdot \underline{v}_H + \frac{\partial w}{\partial z} = 0, \quad (2.4)$$

in which the vector velocity is

$$\underline{v} = \underline{v}_H + w \underline{k} = u \underline{i} + v \underline{j} + w \underline{k}. \quad (2.5)$$

The Boussinesq approximation was applied by expanding all thermal variables θ , π and ρ in terms of perturbations superimposed on a reference state that was taken to be isentropic, isothermal, hydrostatic and isosteric; that is, we write $\phi = \phi_0 + \phi'$. Following the technique utilized in Yost and Shirer (1982), we write the perturbation potential temperature field as a sum of two terms: one depending on the time-independent imposed vertical temperature difference, which measures the static stability of the fluid, and the other on the thermal response θ' of the fluid to the imposed heating rate Q . Thus we may write

$$\theta = \theta_0 + \Delta_z \theta\left(\frac{z}{Z_T}\right) + \theta' \quad (2.6)$$

In (2.1) and (2.2), the pressure gradient term has been written in terms of potential temperature θ and Exner's function π . Dissipation in (2.1)-(2.3) is manifested via the eddy values of the coefficients of kinematic viscosity ν and thermometric conductivity κ . The thermodynamic equation (2.3) has been simplified by normalizing the perturbation potential temperature by θ_0 . The forcing Q represents a combination of radiant and latent heating rates.

Since we choose to represent (2.1)-(2.4) in spherical coordinates, the horizontal basis functions become the usual spherical harmonics. If ϕ is latitude, λ is longitude and z is radial distance, then the gradient operator ∇ and Laplacian operator ∇^2 are

$$\nabla = \frac{1}{a} \frac{1}{(1 - \mu^2)^{1/2}} \frac{\partial}{\partial \lambda} + j \frac{(1 - \mu^2)^{1/2}}{a} \frac{\partial}{\partial \mu} + k \frac{\partial}{\partial z} \quad (2.7)$$

and

$$\nabla^2 = \frac{1}{a^2 (1 - \mu^2)} \frac{\partial^2}{\partial \lambda^2} + \frac{\partial}{\partial \mu} \left(\frac{(1 - \mu^2)}{a^2} \frac{\partial}{\partial \mu} \right) + \frac{\partial^2}{\partial z^2} \quad (2.8)$$

where $\mu = \sin \phi$ and a is the mean radius of the earth.

We elect to switch from equations in terms of the pseudoscalars u and v , to equations in terms of true scalar variables that are independent of the coordinate system, namely the vorticity ζ and the divergence D . We shall see later that this presents no particular problem when determining expansion coefficients for u and v because they are determined from ζ and D via recurrence formulas and truncation relations.

With the Helmholtz Theorem, we write the horizontal velocity field as

$$\underline{v}_H = \underline{k} \times \nabla_H \psi + \nabla_H \chi, \quad (2.9)$$

in which ψ and χ are the usual stream function and velocity potential, respectively. If the vorticity and divergence are defined as $\zeta = \nabla_H^2 \psi$ and $D = \nabla_H^2 \chi$, then (2.1)-(2.4) become

$$\begin{aligned} \frac{\partial D}{\partial t} + \frac{1}{a} \frac{\partial}{\partial \mu} (U \zeta) + w \frac{\partial D}{\partial z} + \frac{1}{a} \frac{\partial w}{\partial \mu} \frac{\partial V}{\partial z} + \nabla_H^2 \left(\frac{U^2 + V^2}{2(1 - \mu^2)} \right) \\ = 2\Omega \left(\mu \zeta - \frac{U}{a} \right) - \nabla_H^2 \pi + v \nabla^2 D, \end{aligned} \quad (2.10)$$

$$\frac{\partial \pi}{\partial z} = g\tau + v \nabla^2 w, \quad (2.11)$$

$$D + \frac{\partial w}{\partial z} = 0, \quad (2.12)$$

$$\frac{\partial \zeta}{\partial t} + \frac{1}{a} \frac{\partial}{\partial \mu} (V \zeta) + w \frac{\partial \zeta}{\partial z} - \frac{1}{a} \frac{\partial w}{\partial \mu} \frac{\partial U}{\partial z} = -2\Omega \left(\mu D + \frac{V}{a} \right) + v \nabla^2 \zeta, \quad (2.13)$$

and

$$\frac{\partial \tau}{\partial t} + \frac{V}{a} \frac{\partial \tau}{\partial \mu} + w \frac{\partial \tau}{\partial z} = w R_s + q + \frac{v}{P} \nabla^2 \tau. \quad (2.14)$$

In (2.10)-(2.14), we have used the scaled u and v velocity components

$u = U/(1 - \mu^2)^{1/2}$ and $v = V/(1 - \mu^2)^{1/2}$ to avoid the singularities near the poles (Machenhauer, 1979), and we have invoked axisymmetric conditions by eliminating longitudinal derivatives. In addition, we simplified (2.10)-(2.14) by introducing a Prandtl number $P = \nu/\kappa$, a number proportional to a Rayleigh number

$$R_s = - \left(\frac{\Delta z \theta}{\theta_0} \right) Z_T, \quad (2.15)$$

and the definitions $\pi = \theta_0 \pi'$, $\tau = \theta'/\theta_0$ and $q = Q/(\rho_0 c_p T_0)$.

To complete the formulation of this problem, we employ boundary conditions over the spherical spatial domain

$$D_s = \{ \underline{x}: -1 \leq \mu \leq 1, 0 \leq z \leq Z_T \}, \quad (2.16)$$

of the axisymmetric model, where Z_T is the upper boundary. Appropriate boundary conditions are

$$w = 0 \quad \text{at} \quad z = 0 \quad \text{and} \quad z = Z_T, \quad (2.17)$$

$$\frac{\partial w}{\partial z} = 0 \quad \text{at} \quad z = 0 \quad \text{and} \quad z = Z_T, \quad (2.18)$$

$$\zeta = 0 \quad \text{at} \quad z = 0 \quad \text{and} \quad z = Z_T, \quad (2.19)$$

and

$$\frac{\partial \tau}{\partial z} = 0 \quad \text{at} \quad z = 0 \quad \text{and} \quad z = Z_T. \quad (2.20)$$

Hence, the boundary value problem for axisymmetric flow on a sphere consists of the equations (2.10)-(2.14) and the boundary conditions (2.17)-(2.20).

b. A five-component axisymmetric model

We aim to formulate a set of basis functions that couple the dependent

variables in (2.10)-(2.14) so that fewer expansion coefficients are needed to represent the flow. In general, this presents no mathematical difficulties when appropriate linear eigenvalue problems are extracted from the three-dimensional system (2.1)-(2.4). Indeed, Higgins (1983) showed that the velocity field \underline{v} and pressure field π could be coupled in this way and that the resulting spectral equations depended on only two sets of scalar coefficients. However, we ignore zonal variations in the axisymmetric model; this introduces some problems in coupling ζ and D in any chosen linear problem. In this situation, we are obliged to solve three separate linear problems. Three suitable problems, extracted from (2.10)-(2.14), are solved in detail in Appendix A.

The solutions to these problems produce spectral expansions that portray the spatial and temporal dependence of each variable in the axisymmetric model. When these Fourier expansions, given by (A.21)-(A.23), (A.29) and (A.32), are substituted into the model equations and Galerkin techniques are applied, then we obtain a coupled model having only three sets of spectral coefficients. This model is found in Higgins (1983).

In this investigation, an appropriate truncation of the complete spectral system must retain different terms that represent nonlinearities, rotation, and appropriate vertical and meridional thermal parameters. In addition, the truncation should retain the fewest number of components that are needed to maximize the information in the model. Finally, it must possess enough external control parameters to describe adequately the steady state solutions that are of interest here (Shirer and Wells, 1983).

Recognizing these facts, we impose a modified form of a triangular truncation on the spectral expansions (A.21)-(A.23), (A.29) and (A.32) for w , D , π , τ and ζ respectively, in which all components with $m > M$, $n > N$ and $m > n$

are set equal to zero, so that

$$\begin{bmatrix} w \\ D \\ \tau \end{bmatrix} = \sum_{n=0}^N \sum_{m=1}^M a_n^m P_n \begin{bmatrix} W_n^m \\ -\frac{\partial W_n^m}{\partial z} \\ \sigma_n^m \end{bmatrix}, \quad (2.21)$$

$$\tau = \sum_{n=0}^N b_n^0 P_n \phi_n^0 + \sum_{n=0}^N \sum_{m=1}^M b_n^m P_n \phi_n^m, \quad (2.22)$$

$$\zeta = \sum_{n=0}^N \sum_{m=1}^M c_n^m P_n \psi_n^m. \quad (2.23)$$

The expansions for the auxiliary variables are (e.g., Eliassen et al., 1970)

$$U = \sum_{n=0}^{N+1} \sum_{m=1}^M U_n^m P_n \psi_n^m, \quad (2.24)$$

and

$$V = - \sum_{n=0}^{N+1} \sum_{m=1}^M V_n^m P_n \frac{\partial W_n^m}{\partial z}. \quad (2.25)$$

The coefficients U_n^m and V_n^m are abbreviations for the recurrence relations

$$U_n^m = a \left(-\frac{1}{n} J_n c_{n-1}^m + \frac{1}{n+1} J_{n+1} c_{n+1}^m \right), \quad (2.26)$$

and

$$V_n^m = a \left(\frac{1}{n} J_n a_{n-1}^m - \frac{1}{n+1} J_{n+1} a_{n+1}^m \right), \quad (2.27)$$

where $J_n = [n^2/(4n^2 - 1)]^{1/2}$. Hence, if the expansion for either ζ or D is

given, then the series for U or V is easily computed. We note that the spectral expansions for U and V extend one degree higher in n than do the expansions for ζ and D . Thus, the number of U_n^m and V_n^m coefficients is larger than the number of c_n^m and a_n^m coefficients for any truncation; this leads to a closure problem for the cases $n = 0$ or $n = N$. Eliassen et al. (1970) showed that specific truncation relations resolved this problem. Later Orszag (1974) and Byrnak (1975) showed that these relations were equivalent to boundary conditions at the poles for the horizontal velocity field. Rather than present an extensive description of these relations, we give them when necessary following Eliassen et al. (1970).

By truncating the series (2.21)-(2.25), we limit the range of the basis functions to only those large scales at which energy contributions are significant. The smallest truncation available that maintains nonlinear interactions, Coriolis terms, and energy conversions contains five spectral components. Moreover, if we choose the truncation point at $M = 2$ and $N = 3$, then (2.21)-(2.23) reduce to

$$\begin{bmatrix} w \\ D \\ \tau \end{bmatrix} = a_2^1 P_2 \begin{bmatrix} w_2^1 \\ -\frac{\partial w_2^1}{\partial z} \\ \sigma_2^1 \end{bmatrix}, \quad (2.28)$$

$$\tau = b_0^1 P_0 \phi_0^1 + b_2^0 P_2 \phi_2^0, \quad (2.29)$$

and

$$\zeta = c_1^1 P_1 \psi_1^1 + c_1^2 P_1 \psi_1^2. \quad (2.30)$$

We note that even and odd modes have been selected from (2.21)-(2.25) in an appropriate way, in order to obtain (2.28)-(2.30). In general, zonal wind components, vertical velocities, temperature, and pressure exhibit even symmetry about the equator while meridional wind components possess odd symmetry. Thus, (2.28)-(2.30) constitute an adequate truncation because the vorticity expansion exhibits odd symmetry while all other expansions retain even symmetry with respect to the equator. Finally, the choice of vertical basis functions in this case was restricted because we used the hydrostatic approximation.

The auxiliary variables are given by

$$U = U_0^1 P_0 \psi_0^1 + U_2^1 P_2 \psi_2^1 + U_0^2 P_0 \psi_0^2 + U_2^2 P_2 \psi_2^2, \quad (2.31)$$

and

$$V = -v_1^1 P_1 \frac{\partial W_1^1}{\partial z} - v_3^1 P_3 \frac{\partial W_3^1}{\partial z}, \quad (2.32)$$

in which the coefficients U_n^m and V_n^m are given by (2.26) and (2.27). If U has an even latitudinal expansion, V has an odd latitudinal expansion, and the longitudinal wavenumber l equals zero, then the truncation relations

$$U_{N+1} = \frac{-1}{(2N+3)^{1/2}} \sum_{n=0}^{N-1} ((2n+1)^{1/2} U_n), \quad (2.33)$$

and

$$V_N = \frac{-1}{(2N+1)^{1/2}} \sum_{n=1}^{N-2} ((2n+1)^{1/2} V_n), \quad (2.34)$$

imply that

$$U_2^1 = -\frac{U_0^1}{(5)^{1/2}}; \quad U_2^2 = -\frac{U_0^2}{(5)^{1/2}}; \quad v_3^1 = -\left(\frac{3}{7}\right)^{1/2} v_1^1. \quad (2.35)$$

Hence, we observe that the model maintains two, rather than four, zonal velocity components and one, rather than two, meridional velocity components as well as two normalized potential temperature components.

Substituting the expansions (2.28)-(2.32) into the model equations (2.10)-(2.14), and utilizing the orthonormality property of the basis functions to eliminate the spatial dependence, we obtain the five component model

$$\dot{a}_2^1 = D_{112}^{121} c_1^1 c_1^2 + \Omega J_{12}^{21} c_1^2 - v E_{22}^{11} a_2^1 + g E_{22}^{01} b_2^0 - v \lambda_2^1 a_2^1, \quad (2.36)$$

$$\dot{b}_0^1 = F_{220}^{101} a_2^1 b_2^0 + q_0^1 - b_0^1 \Gamma_0^1 v/P, \quad (2.37)$$

$$\dot{b}_2^0 = -F_{202}^{110} a_2^1 b_0^1 + a_2^1 R + q_2^0 - b_2^0 \Gamma_2^0 v/P, \quad (2.38)$$

$$\dot{c}_1^2 = -B_{211}^{112} a_2^1 c_1^1 - \Omega J_{21}^{12} a_2^1 - v \Lambda_1^2 c_1^2, \quad (2.39)$$

$$\dot{c}_1^1 = B_{211}^{121} a_2^1 c_1^2 - v \Lambda_1^1 c_1^1, \quad (2.40)$$

in which the overdot denotes temporal differentiation.

It is important to note that the basis functions for τ are a suitable set of functions for representing the net heating field q (Henderson, 1982). Thus the thermal forcing field and temperature field are matched in (2.37) and (2.38); the heating coefficients q_2^0 and q_0^1 have the same indices as b_2^0 and b_0^1 respectively. In what follows, we refer to this type of thermal forcing mechanism as internal. If we define the horizontal (vertical) heating rate to be the component of heating that changes in the horizontal (vertical), then q_2^0 is a horizontal heating rate and q_0^1 is a vertical heating rate.

c. Steady states

To simplify analytical calculations of the steady solutions and to facilitate the model comparisons in Section 4, we rewrite the spectral components as

$$\begin{aligned} x_1 &= a_2^1 / Z_T, & x_2 &= b_2^0, & x_3 &= b_0^1, \\ x_4 &= c_1^2, & x_5 &= c_1^1. \end{aligned} \quad (2.41)$$

By rescaling the spectral component a_2^1 with the domain height, we modify the definitions of the interaction coefficients which appear in (2.36)-(2.40). For convenience, these definitions appear in Appendix B. They allow us to rewrite the spectral system as

$$\dot{x}_1 = D_1 x_4 x_5 + J_1 \Omega x_4 - \nu (E_1 + \lambda_1) x_1 + g E_2 x_2, \quad (2.42)$$

$$\dot{x}_2 = -F_1 x_1 x_3 + r_s x_1 + q_h - \nu P^{-1} x_2 \Gamma_1, \quad (2.43)$$

$$\dot{x}_3 = F_2 x_1 x_2 + q_v - \nu P^{-1} x_3 \Gamma_2, \quad (2.44)$$

$$\dot{x}_4 = -B_2 x_1 x_5 - \Omega J_2 x_1 - \nu x_4 \lambda_3, \quad (2.45)$$

$$\dot{x}_5 = B_1 x_1 x_4 - \nu x_5 \lambda_2, \quad (2.46)$$

in which

$$r_s = R_s Z_T, \quad (2.47)$$

and q_h and q_v are the horizontal and vertical heating rates, respectively. It is easy to show that the steady solutions to (2.42)-(2.47), hereafter referred

to as the S (or spherical) model, are governed by a seventh degree steady polynomial in x_1 , given by

$$d_7 x_1^7 + d_5 x_1^5 + d_4 x_1^4 + d_3 x_1^3 + d_2 x_1^2 + d_1 x_1 + d_0 = 0 \quad (2.48)$$

The expressions for d_i , $i = 0-7$, are found in Appendix B.

From Shirer and Wells (1983), we know that a certain number of independent external parameters are needed to describe completely all classes of transitions among the stationary solutions of (2.48). If these have been identified mathematically and interpreted physically, then the predictions of the model are insensitive to small errors, which are always present in observations, and are therefore experimentally applicable. In fact, Shirer and Wells (1983) show that in many cases the number of parameters required is given by the maximum possible multiplicity of the real roots. However, the simplest case of roots having multiplicity two produces the set of fold points, and this singularity set specifies fully the branching character of the nonlinear solutions. Thus, in order to find the values of the external parameters separating unique from multiple equilibria, it is logical to begin with a search for the fold point singularities.

When several parameters are present in the model, then the fold points form a curve in parameter space that delineates the transition regions as functions of the external parameters. In the S model, there are several ways to display the steady solution surface. As we shall see in Section 4, the qualitative behavior of the steady states in the S model, in accord with that of the solutions to the C (or cylindrical) model of Section 3, is independent of aspect ratio A , Prandtl number P , and rotation rate f . Therefore, any appropriate choice of A , P and f produces roughly the same solution surface.

Fig. 1 illustrates the relationship between the folded solution surface

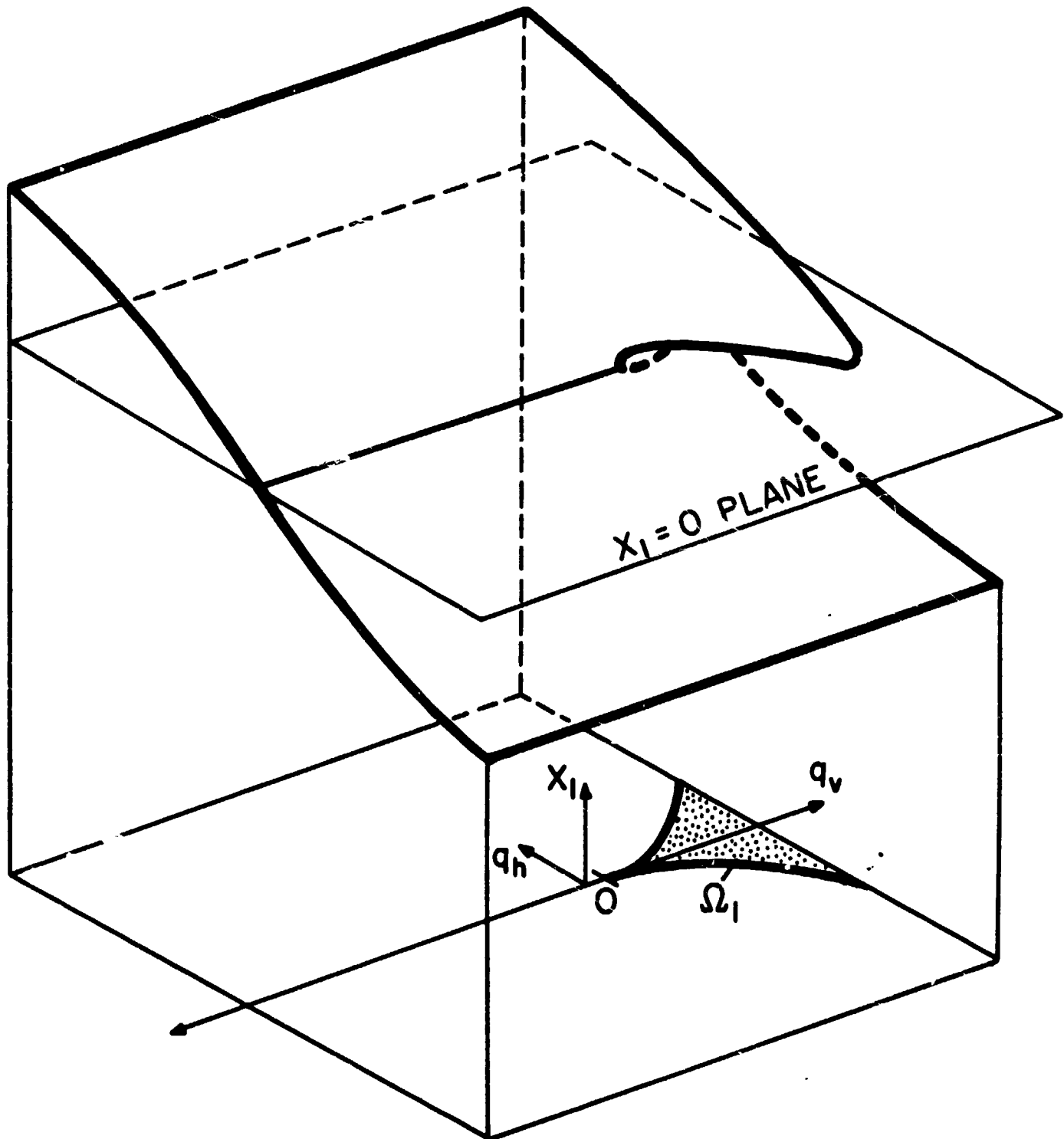


Fig. 1 A schematic diagram showing the relationship between the folded solution surface of the S model and the singularity set Ω_1 in the $q_v - q_h$ plane. For values of $q_v - q_h$ inside Ω_1 , three distinct real roots of the steady state polynomial exist, but for values of q_v and q_h outside Ω_1 , only one real root exists. In this case r_s was chosen so that the scale height is 8 km. It is important to note that qualitative steady behavior is independent of the aspect ratio A , Prandtl number P and rotation rate Ω (after Yost and Shirer, 1982).

of the S model and the singularity set Ω_1 , that divides the thermal parameter plane. This set consists of fold points and a cusp point, at which three solutions meet. Three real solutions occur for parameter values inside Ω_1 , and one real solution occurs for values outside it. As Fig. 1 shows, the steady states of the S model have the form of a cusp surface.

Four classes of axisymmetric flow occur in Fig. 1 depending on the sign of the vertical heating rate q_v . If $q_v > 0$, then the statically stable fluid given by $r_g < 0$ is being forced in the vertical and for sufficient heating we obtain a rotating Rayleigh-Bénard problem. If $q_v < 0$, then the static stability is being reinforced and the horizontal heating q_h leads to an atmospheric Hadley problem.

As is apparent from the figure, the steady states form a cusp surface for only positive values of q_v . This implies that multiple real solutions can occur in the S model only when the fluid is forced in the vertical. Moreover, these convective flows may be either direct or indirect, depending on the sign of the product $q_h x_1$. A thermally direct cell, in which warm fluid rises and cold fluid sinks, satisfies $q_h x_1 > 0$, whereas, a thermally indirect cell, in which warm fluid sinks and cold fluid rises, satisfies $q_h x_1 < 0$. As Shirer and Wells (1983) found, sudden transitions in this regime occur between direct and indirect circulations of equal intensities as the value of q_h is varied.

If $q_v < 0$, then unique real solutions occur for all values of the thermal parameters in this region, and there are no transitions among the steady states. Since the fluid is stably stratified, motion occurs primarily in response to q_h . In this situation, only thermally direct cells are possible since $q_h x_1 > 0$ everywhere.

Thus we conclude that for rotating axisymmetric flow the internally forced S model permits multiple real steady solutions only when forced

sufficiently in the vertical. This result is in contrast to the one obtained for the externally forced cylindrical model in the following section. We will explain the implications of this difference in Section 4.

3. Axisymmetric flows in an annulus

A simple mathematical model that is representative of a rotating cylindrical configuration can be developed from a version of the two-dimensional shallow Boussinesq equations used by Lorenz (1963). The version we consider is one that was originally studied by Veronis (1966), who added the Coriolis parameter and a meridional velocity component to the Lorenz system in order to study the rotating Rayleigh-Bénard problem. In addition, we utilize the results of Shirer and Wells (1983) who modified Veronis' system by adding appropriate terms that contained a parameter called the Hadley number (Yost and Shirer, 1982) that is proportional to an externally imposed horizontal temperature difference. As in the S model, the'r model includes a sufficient number of parameters to capture the crucial elements of simple steady axisymmetric flow and to unfold completely the physical system.

In this section, we discuss the five-component cylindrical spectral model and then illustrate the corresponding steady solution surface. These results are used in Section 4 when we compare the axisymmetric flow in both models.

In addition, we attempt to determine whether the multiple solution regions that occur on the statically stable side of the thermal parameter plane (i.e., $r < 0$) in this model are linked physically to laboratory flows. We investigate these solutions by determining their location with respect to the symmetric flow-wave flow transition curve that was obtained by Fultz et al. (1959) for a rotating annulus. The results are suggestive of a physical link between the boundary delineating regions of one and three solutions and the observed symmetric flow-wave flow transition curve. In addition, we deduce a possible explanation for a transition between upper and lower symmetric flows.

These results have a significant implication on the manner by which the

wave flow regime might replace the upper symmetric one: whether in effect by default when an upper symmetric flow ceases to exist or by a bifurcation originating from the loss of stability of an upper symmetric flow. In the latter case, the problem might become considerably more difficult if, for example, different solutions within the wave flow regime were to bifurcate from different possible upper symmetric flows. Thus it is crucial that we determine the physical significance of these results before attempting to model the transition sequence from the steady, axisymmetric Hadley regime to the temporally periodic Rossby regime.

a. Steady states of a five-component axisymmetric model

If the Coriolis parameter f , a meridional velocity component v , and appropriate terms containing the Hadley number h are added to the Lorenz (1963) system, then we obtain

$$\begin{aligned} \frac{\partial}{\partial t^*} \bar{v}^2 \psi^* = & -K(\psi^*, \bar{v}^2 \psi^*) - f^* \frac{\partial v^*}{\partial z^*} + P(1 + A^2)^{-1} \bar{v}^4 \psi^* \\ & + P(1 + A^2) \frac{\partial \theta^*}{\partial x^*} + P(1 + A^2)h \end{aligned} \quad (3.1)$$

$$\frac{\partial v^*}{\partial t^*} = -K(\psi^*, v^*) + f^* \frac{\partial \psi^*}{\partial z^*} + P(1 + A^2)^{-1} \bar{v}^2 v^* \quad (3.2)$$

$$\frac{\partial \theta^*}{\partial t^*} = -K(\psi^*, \theta^*) + r \frac{\partial \psi^*}{\partial x^*} + h \frac{\partial \psi^*}{\partial z^*} + (1 + A^2)^{-1} \bar{v}^2 \theta^* \quad (3.3)$$

The parameters in (3.1)-(3.3) are defined below. This system is considered in more detail in Shirer and Wells (1983). The dimensionless variables are denoted by asterisks or tildas; the velocity components satisfy $u^* = \partial \psi^* / \partial z^*$ and $w^* = -\partial \psi^* / \partial x^*$. From (3.1)-(3.3), we can develop an appropriate low order model that is based on the geometry of a rotating annulus or dishpan. The

steady solutions of this model can be compared with those in the S model of Section 2.

Yost and Shirer (1982) modeled irrotational axisymmetric flow in a rectangular domain by imposing external temperature differences $\Delta_z T$ and $\Delta_x T$ between the upper and lower surfaces and the lateral boundaries respectively. We follow their approach and choose the domain $0 \leq x^* \leq \pi$, $0 \leq z^* \leq \pi$. Hence the temperature field becomes

$$T = T_0 + \Delta_z T \left(\frac{z}{H} \right) + \Delta_x T \left(\frac{Ax}{H} \right) + \theta, \quad (3.4)$$

where T_0 is the value of T at $(x^*, z^*) = (0, 0)$ when $\theta = 0$, and θ is a perturbation that vanishes at the top and bottom. The Hadley number h is defined here by

$$h = -r \frac{\Delta_x T}{\Delta_z T}, \quad (3.5)$$

in which the normalized Rayleigh number $r = R/R_c$; the Rayleigh number R and critical Rayleigh number R_c are given by

$$R = -g \Delta_z T H^3 T_0^{-1} \nu^{-1} \kappa^{-1}, \quad (3.6)$$

and

$$R_c = (1 + A^2)^3 \pi^4 A^{-2}. \quad (3.7)$$

Other dimensionless parameters in (3.1)-(3.3) are the Prandtl number $P = \nu/\kappa$, the aspect ratio $A = H/L$ and the Coriolis parameter

$$f^* = f H^2 \pi^{-2} \kappa^{-1} (1 + A^2)^{-1}, \quad (3.8)$$

where H is the domain height, L is the domain width, ν is the coefficient of kinematic viscosity and κ is the coefficient of thermometric conductivity.

As in Section 2, we aim to deduce the smallest spectral system in which each variable ψ^* , v^* and θ^* occurs somewhere in a nonlinear term and in which rotation and appropriate meridional and vertical thermal parameters are preserved. A five-component model (after Veronis, 1966 and Shirer and Wells, 1983) that meets these criteria is specified by

$$\psi^* = \sqrt{2} y_1 \sin x^* \sin z^* \quad , \quad (3.9)$$

$$\theta^* = \sqrt{2} y_2 \cos x^* \sin z^* - y_3 \sin 2z^* \quad , \quad (3.10)$$

$$v^* = -\sqrt{2} y_4 \sin x^* \cos z^* + y_5 \sin 2x^* \quad . \quad (3.11)$$

After substitution of (3.9)-(3.11) into (3.1)-(3.3), multiplication by the proper basis functions, and integration over the domain, we obtain the five-component C model

$$\dot{y}_1 = -Py_1 + Py_2 + f^*(1 + A^2)^{-1} y_4 - 8\sqrt{2} Ph/\pi^2 \quad (3.12)$$

$$\dot{y}_2 = -y_1 y_3 + ry_1 - y_2 \quad , \quad (3.13)$$

$$\dot{y}_3 = y_1 y_2 - by_3 - 16\sqrt{2} h(3\pi^2)^{-1} y_1 \quad , \quad (3.14)$$

$$\dot{y}_4 = -y_1 y_5 - f^* y_1 - Py_4 \quad , \quad (3.15)$$

$$\dot{y}_5 = y_1 y_4 - Pb A^2 y_5 \quad , \quad (3.16)$$

in which $h = 4(1 + A^2)^{-1}$. It is important to note that the odd vertical mode was selected in (3.9) in order to ensure that an inhomogeneous term, representing the horizontal heating, occurs.

The steady solutions of the C model are found by the same method that was used for the S model. We obtain a fifth degree polynomial in y_1 , given by

$$y_1^5 + g_1 h y_1^4 + [g_2 + g_3 r + g_4 (f^*)^2] y_1^3 + g_5 h y_1^2 + [g_6 + g_7 r + g_8 (f^*)^2] y_1 + g_9 h = 0 \quad (3.17)$$

The expressions for $y_2 - y_5$ and $g_1 - g_9$ are found in Shirer and Wells (1983). As in Section 2 we determine the fold point singularities, at which two solutions meet, from (3.17) because we are mainly interested in comparing the basic nonlinear structures of the steady solution surfaces in the C and S models.

For a specific fluid in a given vessel, the control parameters in the C model are r , h and $(f^*)^2$. Moreover, we are willing to change the fluid or the vessel in any way that might be necessary to match the conditions in the spherical configuration. We solve (3.17) for r to obtain the steady solution surface given in Fig. 2. This surface has been constructed for a representative value of $(f^*)^2$ that might be used in laboratory studies, although qualitative steady behavior is independent of rotation rate. The relationship between the folded solution surface and the singularity set is the same as that in Fig. 1; it is a cusp separating regions of one and three steady solutions.

Both classes of axisymmetric flow also occur in Fig. 2, but here each class is defined by the sign of the external temperature difference in the vertical given by the normalized Rayleigh number r . In Fig. 2, the steady

C MODEL

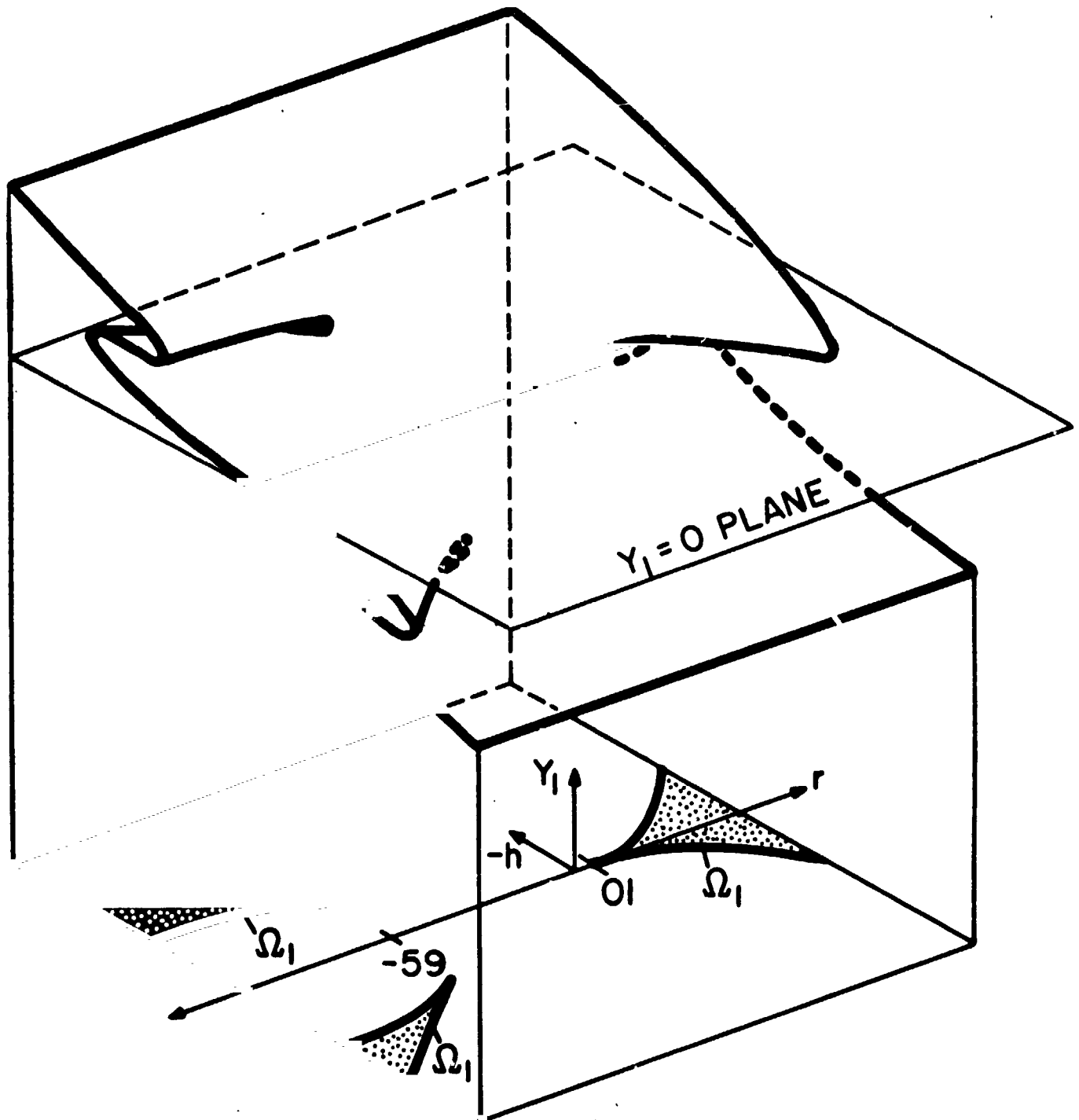


Fig. 2 A schematic diagram showing the relationship between the folded solution surface of the C model and the singularity set Ω_1 in the r - h plane. For values of r and h inside Ω_1 , three distinct real roots of the steady state polynomial exist, but for values of r and h outside Ω_1 , only one real root exists. Here we have chosen a rotation rate $\Omega = 0.05 \text{ s}^{-1}$, so the two cusps in stable stratification appear near $r = -59$. It is important to note that qualitative steady behavior is independent of the aspect ratio A , Prandtl number P and rotation rate Ω (after Yost and Shirer, 1982).

states form a cusp surface when the fluid is statically unstable and $r \geq 1$. If we compare the orientation of the axes in the $r - h$ thermal parameter plane of Fig. 2 with those in the $q_v - q_h$ thermal parameter plane of Fig. 1, then we observe that the parameter pairs (r, q_v) and $(-h, q_h)$ lead to qualitatively similar branching behavior in the respective models. This conclusion can be supported rigorously by applying a theorem of Mather as discussed in Shirer and Wells (1983). Thus, both the C model and the S model produce the same qualitative steady results for rotating Rayleigh-Bénard convection.

However, if the value of r is negative (i.e., for statically stable conditions), then two new cusps appear near $r = -59$ for this rotation rate. Moreover, as the value of $(f^*)^2$ increases, the magnitude of r , at which these cusps appear, increases. These results were obtained first by Yost and Shirer (1982) for the case $(f^*)^2 = y_4 = y_5 = 0$. They found that horizontal heating of sufficient magnitude, under statically stable conditions, leads to multiple real steady solutions in the C model. But in the corresponding region of the S model (Fig. 1) these cusps do not appear: there is only one steady state.

This is a significant qualitative difference that we investigate further. Since the fundamental physical cause of these different steady results cannot be ascertained from the topology of each steady solution surface, we must examine the C and S models directly and in more detail. In particular, we must determine whether the number of steady solutions under statically stable conditions is related to the thermal forcing, geometry, or some other aspect of the spectral model. In this way, we can outline also the possible consequences of using either configuration for studying the symmetric flow - wave flow transition in the atmosphere. Prior to this discussion, we examine qualitatively some of the links between the multiple solution regions

in the C model and the usual symmetric flow - wave flow transition curve obtained in observational studies.

b. Comparison with observational studies

The possible physical connection between the multiple solution regions that arise in the C model (for $r < 0$) and in laboratory flows has not been investigated previously. This new set of cusps, which first occurs in the irrotational convective situation at $r = -26$, is of physical interest because now multiple solutions in a stably stratified fluid are possible for sufficiently large horizontal heating rates. Here, we investigate whether the location of three multiple solution regions might play an important role in the transition sequence from the symmetric flow regime to the wave flow regime in an annulus.

To simplify a comparison of steady solutions in the C model with observations from laboratory studies, we redefine the $(f^*)^2$, P and h parameters as

$$(f^*)^2 = \frac{(1 + A^2)}{A^2} (F^*)^2, \quad (3.18)$$

$$P = \frac{P^*}{A}, \quad (3.19)$$

$$h = (b)^{1/2} Ha. \quad (3.20)$$

With (3.18)-(3.20), we can eliminate any apparent qualitative dependence of the multiple solution regions on the aspect ratio A and the Prandtl number P , and thereby produce more universal transition curves. If (3.18)-(3.20) are

substituted into the steady polynomial (3.17), then we have

$$y_1^5 + j_1 Ha y_1^4 + [j_2 + j_3 r + j_4 (F^*)^2] y_1^3 + j_5 Ha y_1^2 + [j_6 + j_7 r + j_8 (F^*)^2] y_1 + j_9 Ha = 0 \quad (3.21)$$

The definitions for j_i , $i = 1-9$, are provided in Appendix C.

For this comparison, we utilize Fig. 96 of Fultz et al. (1959). Their diagram provides the boundary between the symmetric flow and wave flow regimes and the boundaries separating the different wave forms in an annulus. The dimensionless parameters on the abscissa and ordinate of their diagram (see Fig. 4 for a simplified version) are a rotation parameter

$$(G^*)^{-1} = b \Omega^2 g^{-1} \quad (3.22)$$

and the thermal Rossby number

$$Ro_T^* = gcH \Delta_x T [2\Omega^2 b(b-a)]^{-1} \quad (3.23)$$

respectively. Here, ϵ is the coefficient of volume expansion, H is the depth of the fluid layer, b is the maximum radius at the top surface of the annulus and a is the inner radius of the annulus.

It is important to remember that both $(G^*)^{-1}$ and Ro_T^* depend on Ω^2 and $\Delta_x T$. To emphasize this fact, we rewrite (3.22) and (3.23) in the form

$$(G^*)^{-1} = M \Omega^2 \quad (3.24)$$

$$(Ro_T^*)^* = N \Delta_x T \Omega^{-2} \quad (3.25)$$

where $M = bg^{-1}$ and $N = gcH[2b(b-a)]^{-1}$.

A close examination of the regime diagram obtained by Fultz et al. (1959) reveals that the values of $\Delta_x T$ and $\Delta_z T$ are nearly constant along the lower portion of the transition curve, but the value of Ω^2 is not. Hence, from (3.5)-(3.7) we conclude that the values of the Hadley and Rayleigh numbers are constant along the same portion of the curve. This is a valuable observation that will simplify considerably the comparison which follows.

The control parameters $(F^*)^2$, Ha and r in the C model can be written as

$$(F^*)^2 = J\Omega^2 \quad (3.26)$$

$$Ha = K\Delta_x T \quad (3.27)$$

$$r = L\Delta_z T \quad (3.28)$$

in which

$$J = 4H^4 A^2 [(1 + A^2)^3 \pi^4 \kappa^2]^{-1}, \quad (3.29)$$

$$K = gH^3 A^2 [b^{1/2} T_0 \nu \kappa (1 + A^2)^3 \pi^4]^{-1}, \quad (3.30)$$

$$L = -gH^3 A^2 [T_0 \nu \kappa (1 + A^2)^3 \pi^4]^{-1}, \quad (3.31)$$

and $b = 4/(1 + A^2)$.

From (3.26)-(3.28) we observe that the problem is reduced to a comparison of the locations of the fold points in the $(\Delta_z T, \Delta_x T, \Omega^2)$ - space of the C model with the transition curve observed by Fultz et al. (1959). We note that the aspect ratio A and Prandtl number P^* from the C model, have been fixed at the values that were used to construct Fig. 96 in Fultz et al. (1959).

Although the location of each cusp in the C model is described by two fold point curves, at which transitions between flow regimes and hysteresis

are expected, its location is specified also by a cusp point (see Figs. 1 or 2). At such a point, two fold point curves meet tangentially and three real solutions coincide.

We know that a fold point curve can be specified by two parameters. In a three-parameter problem, as this one is, this curve becomes a surface. For the C model, this surface resembles a wedge, as Fig. 3 illustrates schematically. The wedge consists of two sheets of fold points that meet along a curve of cusp points. As we shall see, the cusp point curve is nearly independent of Ro_T^* in the C model.

In the C model, both the horizontal temperature difference $\Delta_x T$ and the vertical temperature difference $\Delta_z T$ are imposed externally. In the annulus a value of $\Delta_x T$ is imposed externally between the inner and outer walls, but the vertical temperature difference must be inferred by measuring the average value of $\Delta_z T$ via thermocouples placed in the working fluid. Hence, we might expect to find a difference between the observed and the calculated values of $\Delta_z T$ in the comparison which follows. If the calculated and observed values of both $\Delta_x T$ and Ω^2 match, however, then we are obliged to compare the calculated values of $\Delta_z T$ with the nearest measured value available. The measured values of $\Delta_z T$, that correspond to the points indicated by asterisks on Fig. 4, are given in Table 1. These values were obtained by using the definitions in Fultz et al. (1959).

Given a cusp point $(r, Ha)_c$, $(P^{*2})_c = \text{const.}$ from the C model (here the subscript c denotes a cusp point), we can determine the corresponding values of $(\Delta_z T, \Delta_x T)_c$ for $\Omega_c^2 = \text{const.}$ from (3.26)-(3.28). If we substitute the values of $(\Delta_x T)_c$ and Ω_c^2 into (3.24)-(3.25), then the corresponding point $((G^*)^{-1}, Ro_T^*)_c$ can be calculated. This point may be plotted directly on the regime diagram of Fultz et al. (1959).

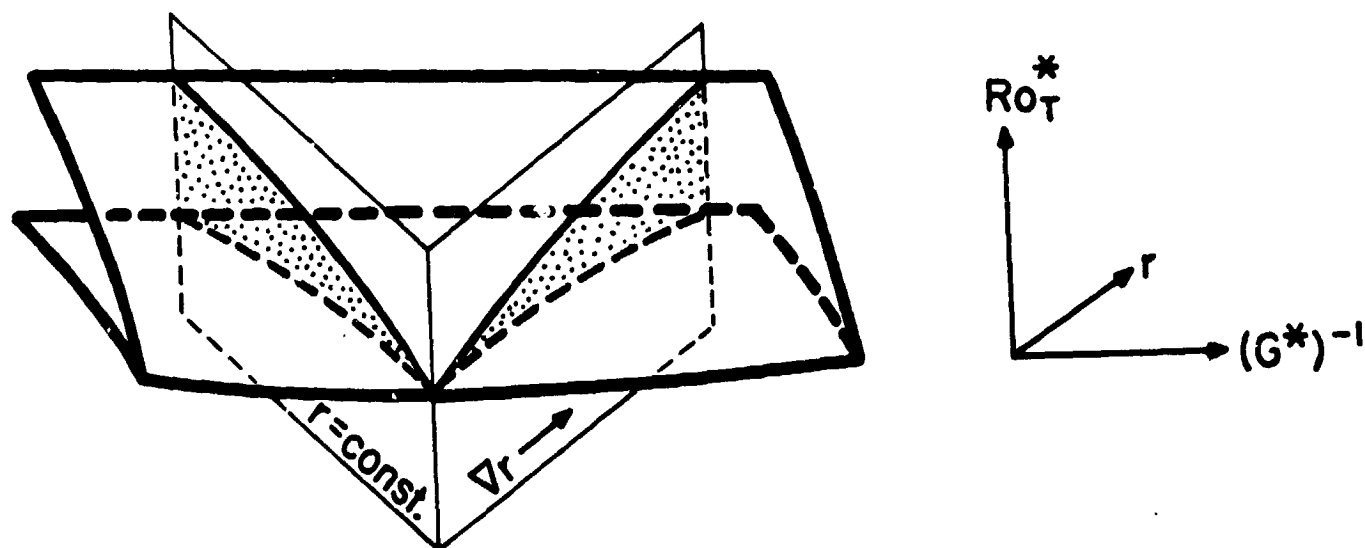


Fig. 3 A schematic of the singularity set surface for a statically stable stratification in the C model. Cross sections through this surface are given for $r = \text{const.}$ and along ∇r . The axes used here are the same as those in Fig. 4; note that the r -axis is skewed with respect to the other two axes, not perpendicular to them.

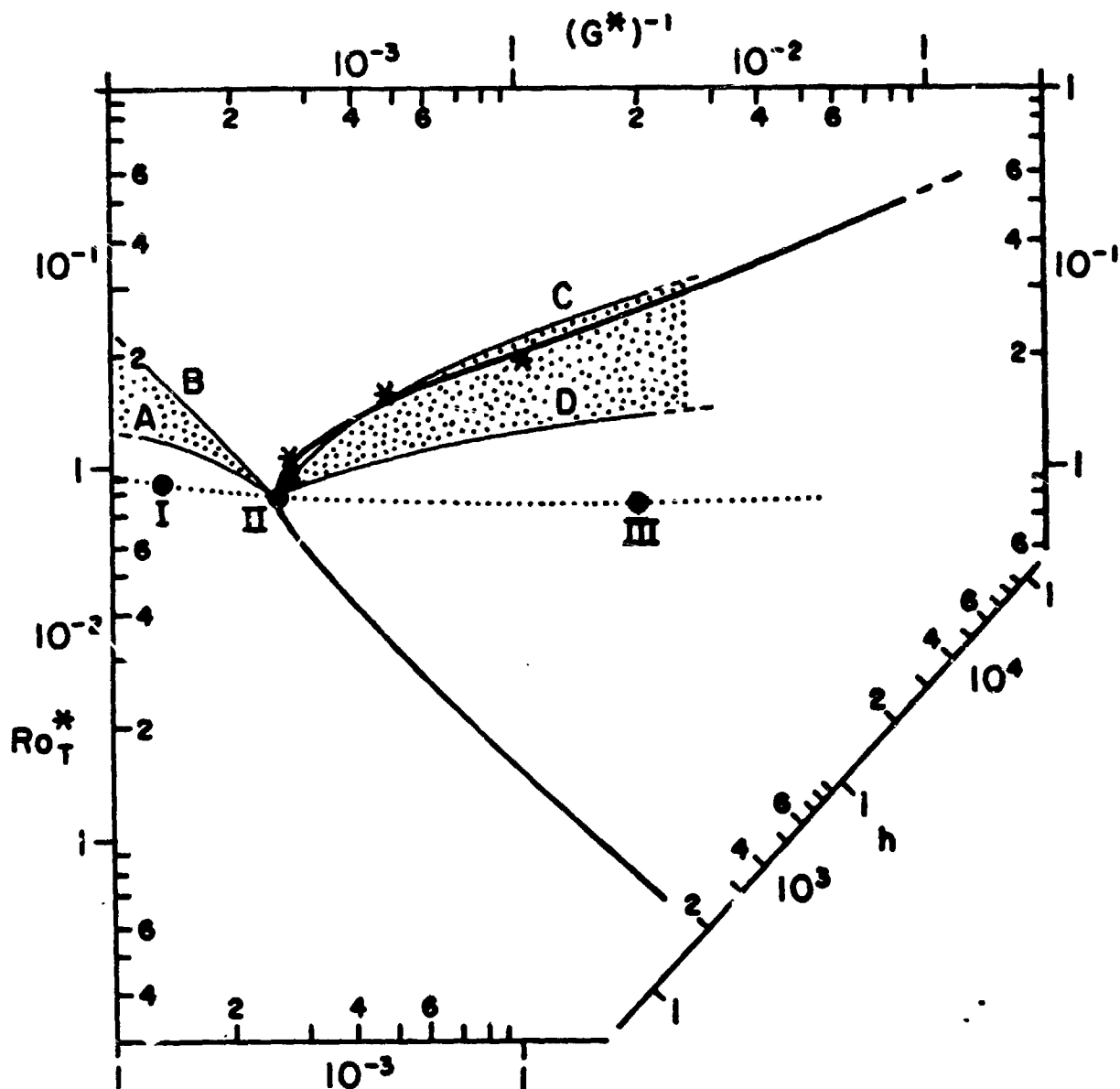


Fig. 4 An illustration of the location of the fold points (thin solid curves) for the C model with respect to the observed symmetric flow - wave flow transition (thick solid curve) from Fig. 96 of Fultz et al. (1959). Fold point curves are shown for cases in which $r = r_c$ (curves A, B) and in which r is varied to follow the trend in observed values along the upper portion of the transition curve (curves C, D). Cusp points from the C model are represented by a dotted line. Multiple solutions occur in the stippled regions. Asterisks denote locations along the transition curve where measurements of the vertical temperature difference ΔzT were available. The parameters, which have the same values as those in Fig. 96 of Fultz et al. (1959), typify conditions in a tall annulus: depth 13 cm, inner radius 2.5 cm, outer radius 4.95 cm, kinematic viscosity $9.6 \times 10^{-7} \text{ m}^2 \text{ s}^{-1}$, thermometric conductivity $1.4 \times 10^{-7} \text{ m}^2 \text{ s}^{-1}$, mean water temperature 21°C , coefficient of volume expansion $2.5 \times 10^{-4} \text{ }^\circ \text{C}^{-1}$.

Table 1. Observed parameter values at the four asterisks on Fig. 4
(starting from left).

Asterisk	$(G^*)^{-1}$	Ro_T^*	$\Delta_z T(K)$	r	h
1	2.7×10^{-3}	8.5×10^{-2}	0.55	-3.4×10^3	2.5×10^3
2	2.6×10^{-3}	1.05×10^{-1}	0.63	-3.9×10^3	3.2×10^3
3	4.9×10^{-3}	1.6×10^{-1}	1.51	-9.4×10^3	8.8×10^3
4	1.1×10^{-2}	2.0×10^{-1}	5.16	-3.2×10^4	2.4×10^4

We repeated the calculation described above for the entire range of rotation rates considered on Fig. 96. The curve of cusp points that results is depicted by a dotted, nearly straight line on Fig. 4. In Table 2, we give the values of each of the parameters for the three cusp points indicated on Fig. 4. In what follows, we will be interested primarily in cusp point II, which occurs where the cusp point curve and the transition curve intersect.

The fold points, associated with cusp point II, are obtained in a similar manner as that outlined above for the cusp points.

Because the vertical temperature difference $\Delta_z T$ is not included as a parameter on Fig. 4, we choose to calculate the fold points from the C model for two appropriate cases:

- (a) when the Rayleigh number is fixed at the value calculated at cusp point II, i.e., $r = r_c$.
- (b) when the Rayleigh number is varied appropriately to follow the trend in observed values along the upper portion of the transition curve.

Case (a) corresponds to the cross-section taken through the singularity set surface of Fig. 3 for $r = \text{const.}$ and (b) approximately to the cross-section in the direction ∇r .

The results for both cases are given on Fig. 4. In case (a), we obtain fold point curves A, B. In case (b), we obtain fold point curves C, D. Multiple solutions occur in the stippled regions of both cusps on Fig. 4. For a fixed value of r , the region of multiple solutions occurs entirely in the symmetric flow regime. When the magnitude of r is varied, the region of multiple solutions lies in the wave flow regime, with the boundary (curve C) along the transition curve. A comparison of the observed values of r along the transition curve with the corresponding calculated values on curve C nearby yields an average difference $\Delta_z T$ of roughly 1 K (Fig. 5).

Table 2. Calculated parameter values for the three cusp points indicated on Fig. 4.

	Cusp Point		
	I	II	III
r	-3.3×10^3	-6.9×10^3	-5.2×10^4
h	1.1×10^3	2.3×10^3	1.8×10^4
$(G^*)^{-1}$	1.3×10^{-3}	2.6×10^{-3}	2.0×10^{-2}
Ro_T^*	8.2×10^{-2}	8.0×10^{-2}	7.9×10^{-2}

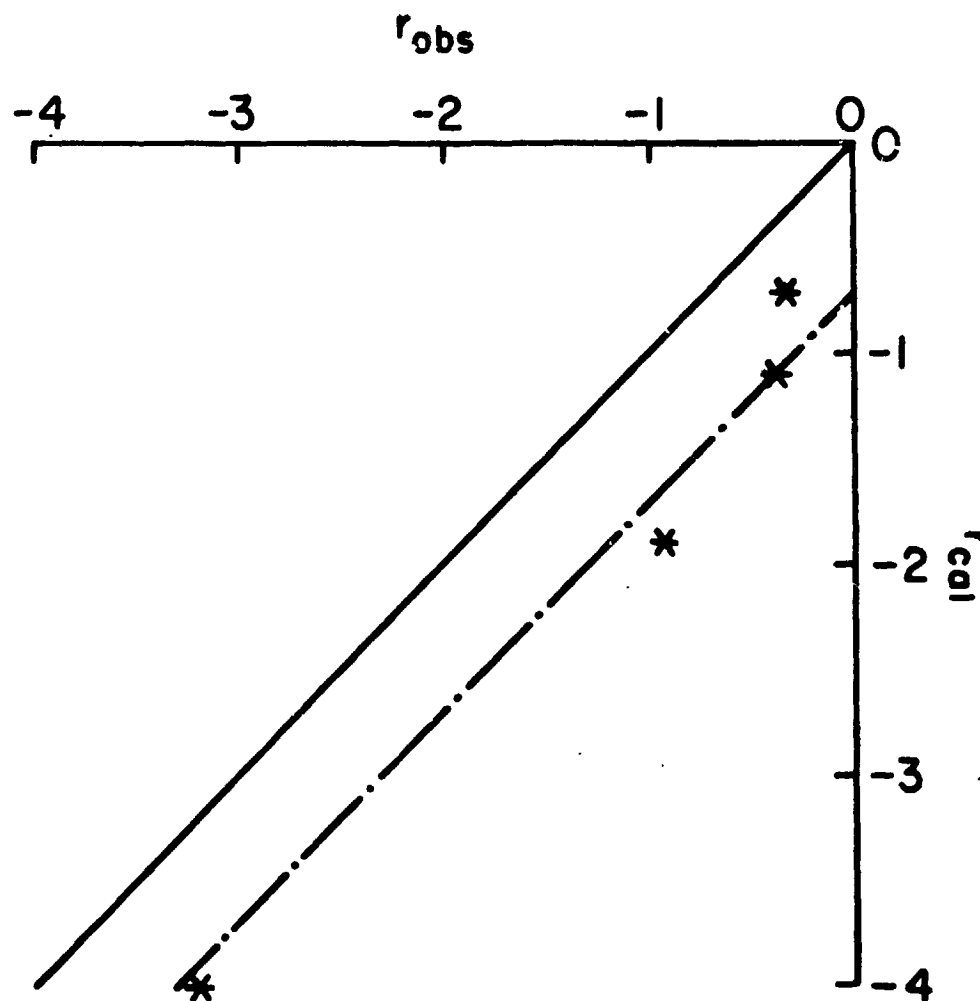


Fig. 5 The best uniform error fit (dot-dashed line) obtained when the observed values of r along the transition curve are compared with the corresponding calculated values on curve C, nearby. Along the solid line, there is no error. Asterisks correspond to the four locations on Fig. 4 at which observed values of r were available.

The results above are suggestive of two possible types of transitions. In case (a), Fig. 4 indicates that the upper symmetric flow regime, in an annulus, might develop catastrophically when a lower symmetric flow ceases to exist, and vice versa. Hysteresis occurs at both A and B. In case (b), Fig. 4 shows that the wave flow regime in an annulus might develop catastrophically when an upper symmetric flow ceases to exist, and vice versa. Hysteresis occurs at both C and D. The conclusion for case (b) is consistent with the evidence presented by Lacher et al. (1977) that the Rossby regime in an annulus might develop catastrophically when a Hadley flow ceases to exist, rather than smoothly via a bifurcation. Moreover, we believe that case (b) may provide the best indication of the actual location of the multiple solution regions with respect to the transition curve because the Rayleigh number has been varied in accordance with the observations.

Since multiple solutions do not occur when $q_v < 0$ in the S model, we conclude that the wave flow regime in the atmosphere might develop smoothly via a bifurcation from the symmetric flow regime.

Owing to observational errors, the precise location in parameter space of the symmetric flow-wave flow transition curve is not known. If the location of the curve is extremely sensitive to small changes in the observed parameter values, then we could imagine that a small increase (or decrease) in the magnitude of $\Delta_z T$, for example, might cause the curve to shift substantially. It may be possible to achieve these new values in the annulus if, for example, both horizontal and vertical external temperature differences are applied to the working fluid or if boundary layer temperature variations are included when measuring $\Delta_z T$. These types of investigations, as well as further sensitivity studies of the present result are needed.

4. Causes of different steady behavior of the C and S models.

In Sections 2 and 3 of this article, we determined the steady solutions to five-component spectral models based on the geometry of the atmosphere (S model) and of the laboratory cylinder (C model) respectively. Because the pairs $(q_v - q_h)$ and $(r - h)$ of thermal parameters control the nonlinear behavior in the S and C models, we were able to compare the steady solution surfaces for each geometry. We found that both models exhibited the same steady behavior under statically unstable conditions, but that under statically stable conditions, the C model possessed two cusps not found in the S model. Here, we investigate the possible reasons for this different steady behavior.

Both models were designed to simulate axisymmetric flows; atmospheric flows are represented in the S model and cylindrical laboratory flows are represented in the C model. It has been suggested that the laboratory flows that are simulated in the C model yield valuable information about atmospheric flows. But we have shown already that the topology of the steady solution surface in stable conditions is different for the C model than it is for the S model. Thus, we are at the very least raising some questions concerning the applicability of the flows produced in externally forced vessels such as the laboratory cylinder, to those found in the atmosphere.

In order to identify those factors in the parameter space that might be responsible for the existence of the regions of multiple equilibria, we examine the low order models further. In what follows, we show that several terms may be eliminated from each model without changing qualitatively the nature of the steady solutions. However, we do not intend to use the modified versions of each model to study the atmosphere per se, but rather to investigate the causes of unique versus multiple equilibria.

The C model (3.12)-(3.16) reduces to an unfolded version of the Lorenz model (Shirer and Wells, 1983) given by

$$\dot{y}_1 = -Py_1 + Py_2 - 8\sqrt{2} Ph/\pi^2 \quad , \quad (4.1)$$

$$\dot{y}_2 = -y_1y_3 + ry_1 - y_2 \quad , \quad (4.2)$$

$$\dot{y}_3 = y_1y_2 - by_3 - 16\sqrt{2} h(3\pi^2)^{-1}y_1 \quad , \quad (4.3)$$

when the latitudinal velocity components y_4, y_5 and rotation f^* are eliminated. The steady solution surface that we obtain from (4.1)-(4.3) is identical in form to the one produced by the complete C model (Fig. 2); the only change in the irrotational case is that the multiple solution regions for the stable conditions first appear near $(r, h) = (-26, \pm 27 \pi^2 \sqrt{b}/(8\sqrt{2}))$. This is in agreement with the results of Yost and Shirer (1982). We note that the scaled versions of the parameters P and h , which were used in Sec. 3b, are not the ones used in (4.1)-(4.3).

An analogous result is obtained for the S model. If we eliminate the longitudinal velocity components x_4, x_5 and rotation f , then the S model (2.42)-(2.46) becomes

$$\dot{x}_1 = -v\lambda_1 x_1 + gE_2 x_2 \quad , \quad (4.4)$$

$$\dot{x}_2 = -F_1 x_1 x_3 + r_s x_1 + q_h - vP^{-1} x_2 \Gamma_1 \quad , \quad (4.5)$$

$$\dot{x}_3 = F_2 x_1 x_2 + q_v - vP^{-1} x_3 \Gamma_2 \quad . \quad (4.6)$$

The steady polynomial obtained from (4.4)-(4.6) yields a single cusp in the thermal parameter plane in agreement with Fig. 1. Hence, we conclude that the modified versions of the C and S models yield the same steady behavior that we observed in the complete versions. Moreover, the velocity components and rotation terms that were eliminated in both models are not responsible for the

qualitative differences in steady behavior; they contribute only to locating the cusps in the parameter space.

A comparison of the modified C and S models reveals that their differential systems are nearly identical except for the location and type of thermal forcing. In fact, we recall that the S model has internal thermal forcing in which the heating field and temperature field share identical eigenfunctions. We believe that this type of forcing, which was derived from atmospheric observations such as those in Dutton (1976), is a reasonable choice for an atmospheric model. Alternatively, the C model possesses external thermal forcing that is manifested via imposed temperature differences between the boundaries of the domain.

It seems reasonable to expect that if the forcing in the S model is altered to match that in the C model, then the three-cusp behavior of the cylindrical model might be reproduced in the spherical one. Indeed, by the reverse argument we might eliminate the multiple solution regions on the statically stable side of the steady solution surface in the C model.

To test the first hypothesis we added inhomogeneous terms, like those that contain the Hadley number in the C model, to the modified S model so that

$$\dot{x}_1 = gE_2 x_2 - v\lambda_1 x_1 - K_1 h_s g \quad , \quad (4.7)$$

$$\dot{x}_2 = -F_1 x_1 x_3 + q_h + r_s x_1 - vP^{-1} x_2 \Gamma_1 \quad , \quad (4.8)$$

$$\dot{x}_3 = F_2 x_1 x_2 + q_v - vP^{-1} x_3 \Gamma_2 - K_2 h_s x_1 \quad . \quad (4.9)$$

The parameter h_s , which is proportional to a Hadley number, is given by

$$h_s = \frac{\Delta_\mu^2 \theta}{\theta_0} \quad , \quad (4.10)$$

in which θ_0 and $\Delta_\mu^2 \theta$ are defined in (4.11). The constants are $K_1 = \sqrt{2} Z_T / (\sqrt{5} (\alpha \pi)^2)$, $K_2 = 16/(9\sqrt{5})$ and $\mu = \sin(\phi)$. In addition, we eliminated the scaled versions of x_2 and x_3 given in (2.41). To obtain (4.7)-(4.9), we reexpressed the potential temperature field in the S model, following Yost and Shirer (1982), as

$$\theta = \theta_0 + \Delta_z \theta \left(\frac{z}{Z_T} \right) + \Delta_\mu \theta(\mu) + \Delta_\mu^2 \theta \frac{\mu^2}{2} + \theta' \quad . \quad (4.11)$$

The nonlinear term in this expansion must be included because the Fourier coefficients for the linear one vanish in the S model, but those for the nonlinear term do not.

When the temperature field (4.11) is written in this way, we know via Jeffrey's Theorem (Dutton, 1976) that motion must occur because there are horizontal temperature differences on level surfaces. The effects of an imposed horizontal temperature difference on the steady solutions to a highly truncated spectral model of Rayleigh-Bénard convection were examined by Yost and Shirer (1982).

In the present context, the S model contains terms that represent both internal and external forcing. Radiant and latent heating rates are represented via the internal heating coefficients q_h and q_v . The lateral lower boundary thermal forcing accounts for terms that contain the parameter h_s . Using (4.7)-(4.9), we derived the new steady polynomial from which the singularity set and the associated multiple solution regions are obtained. The results are provided on Fig. 6 for a case in which the internal heating

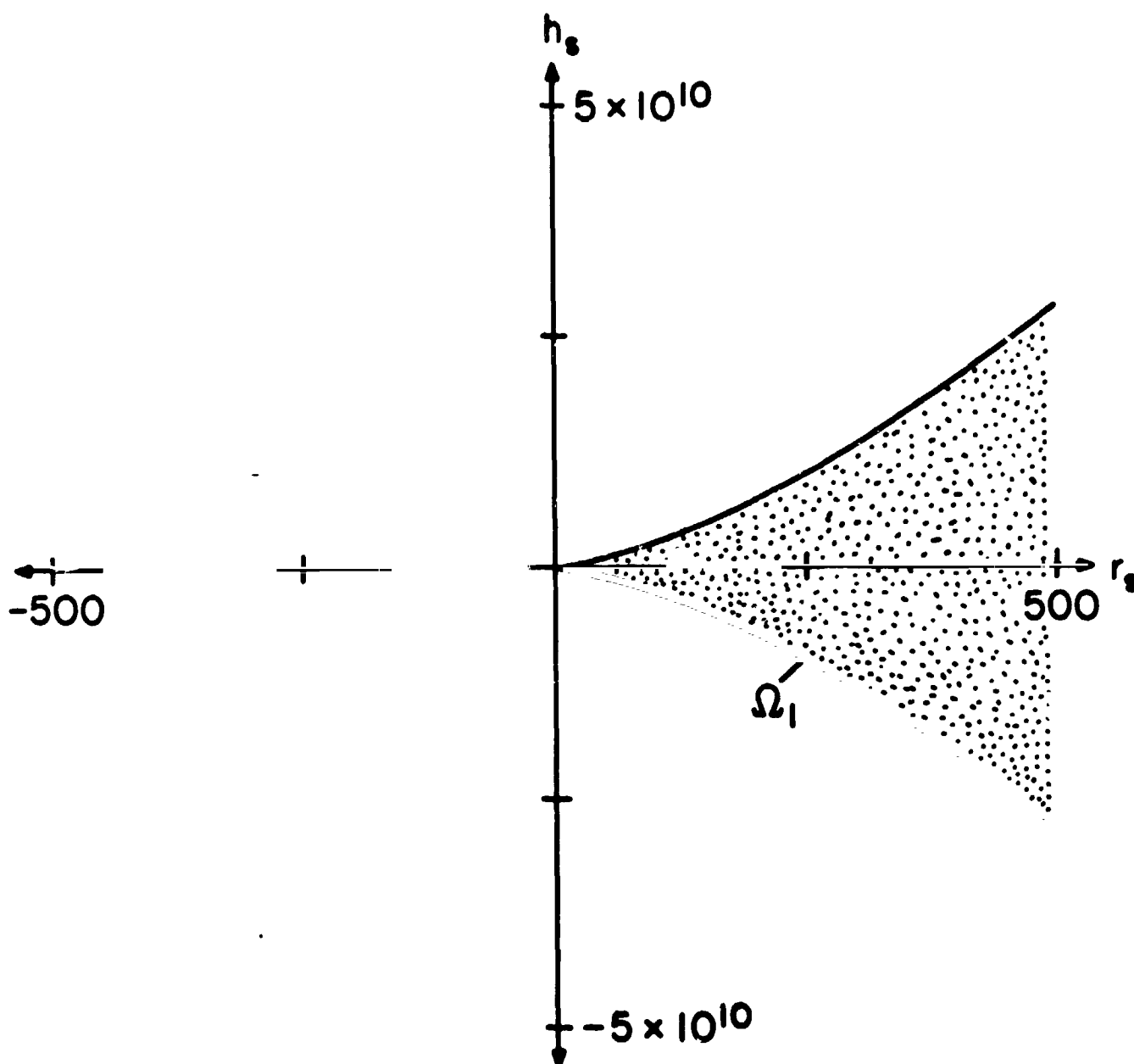


Fig. 6 Fold points in the thermal parameter plane of the modified S model, with both internal and external thermal forcing. For values of r_s and h_s inside Ω_1 (stipled region), three real roots of the steady state polynomial exist, but for values of r_s and h_s outside Ω_1 , only one real root exists. In this case, a set of parameters that typify the earth's atmosphere were chosen: depth 10^4 m, radius of the earth 6.37×10^6 m, eddy viscosity $100 \text{ m}^2 \text{ s}^{-1}$, eddy diffusivity $25 \text{ m}^2 \text{ s}^{-1}$. The horizontal and vertical internal heating coefficients were chosen to reproduce a net heating field of roughly $1^\circ \text{C day}^{-1}$.

coefficients q_h and q_v are constant and in which the fold points are given by the values of r_s and h_s . To construct this figure, we have chosen values for the parameters that typify the atmosphere. As the figure indicates, no qualitative change in the steady solution surface of the S model is obtained (compare the thermal plane in Fig. 1 with Fig. 6). We note that the behavior shown in Fig. 6 is independent of the values of the internal forcing parameters q_h and q_v . In fact, when $q_h = q_v = 0$, the same result is obtained; this latter case corresponds to an S model that is externally forced only, as is the C model.

Thus, the hypothesis that we suggested above was incorrect because the topological character of the steady solution surface in the S model is independent of the type of thermal forcing we choose. For all cases in the S model, including the externally forced one, we find unique solutions in the axisymmetric flow regime in stable conditions; this suggests that transitions, such as the one from the lower symmetric regime to the wave flow regime, will be smooth in the atmosphere. In contrast, two cusps appear in the externally forced C model in stable conditions implying that sudden transitions and hysteresis are likely within the axisymmetric flow regime for sufficient lateral lower boundary thermal forcing. This also implies that in stable stratification transitions would be smooth when externally imposed horizontal heating is too weak.

The externally forced differential systems (4.1)-(4.3) and (4.7)-(4.9) (with $q_h = q_v = 0$) are virtually identical except for quantitative differences in the linear and nonlinear coefficients of each system. With this in mind, we believe that a fundamental cause of the difference in steady behavior might be the hydrostatic approximation, which was used in the spherical system but not in the cylindrical one. Indeed, this approximation is linked directly to

the aspect ratio A and the basis functions of each system, and so to the values of the constants in the S and C models. It is important to remember that in this investigation we are comparing a spherical atmospheric model and a cylindrical laboratory one so that in general $A_s \ll A_c$, where the subscripts s and c represent spherical and cylindrical geometries respectively.

To test the second hypothesis mentioned earlier, we inserted inhomogeneous terms into the modified C model (4.1)-(4.3) that mimic internal forcing similar to that in the simplified S model, and we obtained

$$\dot{y}_1 = -Py_1 + Py_2 - 8\sqrt{2} Ph/\pi^2, \quad (4.12)$$

$$\dot{y}_2 = -y_1y_3 + ry_1 - y_2 + q_{h,v}, \quad (4.13)$$

$$\dot{y}_3 = y_1y_2 - by_3 - 16\sqrt{2} h (3\pi^2)^{-1}y_1 - q_v. \quad (4.14)$$

In (4.12)-(4.14), if $r=h=0$, then we have a version of the C model that is internally forced only. As Fig. 7 shows, in this case no cusps appear in stable conditions, in agreement with the results obtained for the S model. Hence, when both models are internally forced only, unique solutions occur within the axisymmetric flow regime in each case. As a consequence, we would expect to observe smooth transitions from the Hadley regime to the Rossby regime in the atmosphere and the laboratory cylinder. It is important to note, however, that if a Hadley number of sufficient magnitude is reinserted into the internally forced C model (i.e., (4.12)-(4.14)) then the multiple solution regions that occur in a stably stratified fluid may be recovered.

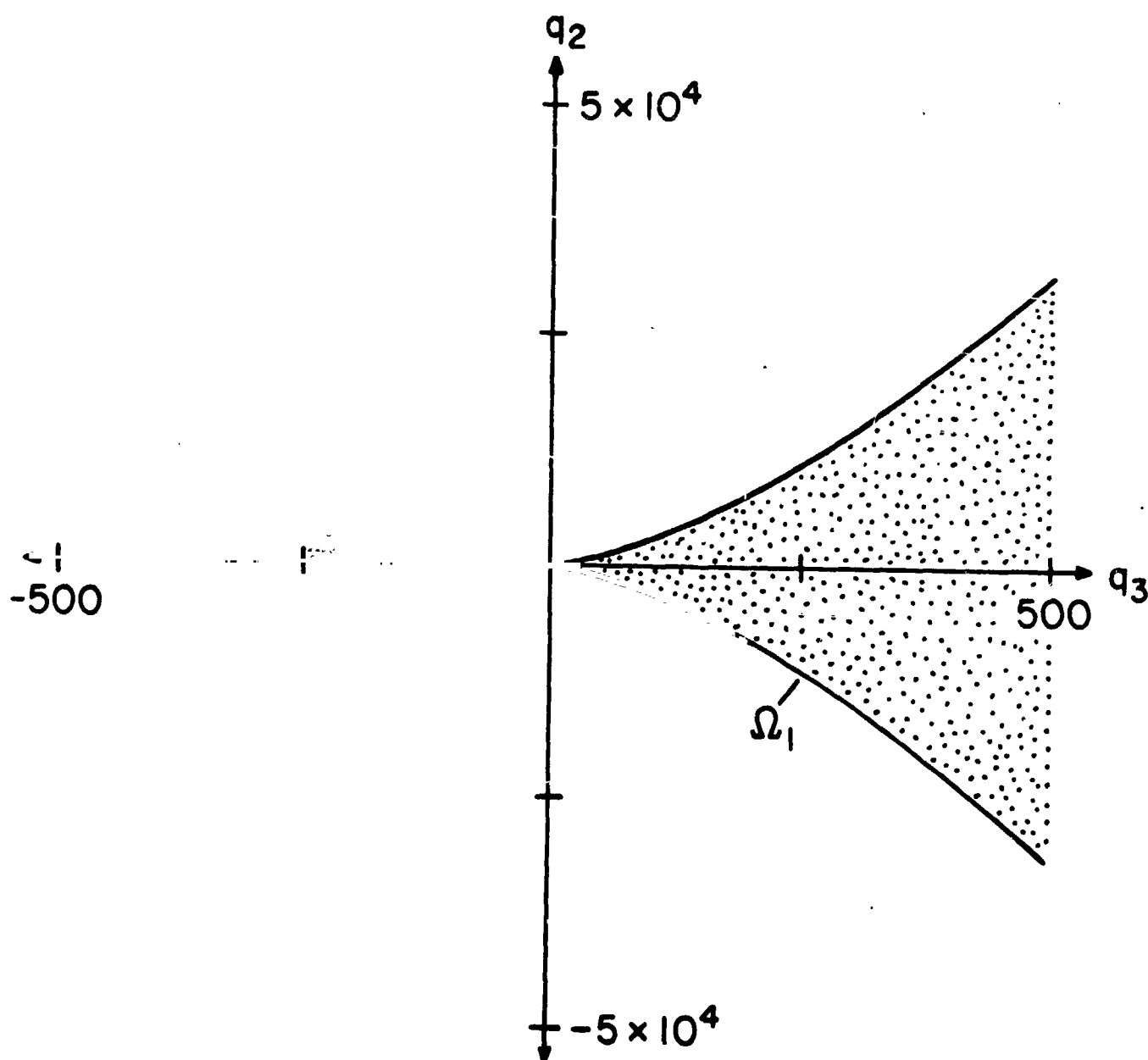


Fig. 7 Fold points in the thermal parameter plane of the modified C model with internal thermal forcing only. For values of $q_3 = q_v$ and $q_2 = q_{h,v}$ inside Ω_1 , (stippled region), three real roots of the steady state polynomial exist, but for values of q_2 and q_3 outside Ω_1 , only one real root exists. In this case, a set of parameters that typify a deep annulus were chosen: depth 13 cm, inner radius 2.5 cm, outer radius 4.95 cm, kinematic viscosity $9.6 \times 10^{-7} \text{ m}^2 \text{ s}^{-1}$, thermometric conductivity $1.4 \times 10^{-7} \text{ m}^2 \text{ s}^{-1}$.

These results are in agreement with those of Henderson (1982) who utilized an internal thermal forcing mechanism, that is based on the atmospheric net heating field, in a 23-coefficient spectral model of axisymmetric flow in the atmosphere. He found a smooth transition from the lower symmetric to wave flow regimes but he was not able to find an upper symmetric transition. We will discuss the significance of this result in the conclusion.

5. Discussion and conclusions

The question of greatest concern in this study is whether transitions, such as the one from the Hadley regime to the Rossby regime, occur catastrophically or smoothly. To begin to answer this question, we presented evidence that in an atmospheric model, but not in a laboratory one, the qualitative nature of the transitions within the symmetric flow regime itself is independent of the type of thermal forcing mechanism used. Significantly, when an internal thermal forcing mechanism was introduced into both models, we obtained qualitatively similar steady behavior; this result implied that the qualitative nature of the observed axisymmetric flows in both the atmosphere and appropriate laboratory vessels would be the same. Of primary importance then is to design laboratory experiments so that the type of thermal forcing is the same in the laboratory vessels and the atmosphere.

Because there is a lack of sensitivity of the steady axisymmetric behavior in the atmospheric model to different thermal forcing mechanisms, we are free to adopt a convenient view of representing thermal forcing in the atmosphere. One view, as discussed in Sec. 4, is that of Henderson (1982), who utilized an internal thermal forcing mechanism that was based on atmospheric observations, in a 23-coefficient model of axisymmetric flow in the atmosphere. He found that a smooth transition existed from the lower symmetric regime to the wave flow regime, but he was not able to locate an upper symmetric regime as was found for the annulus by Fultz *et al.* (1959).

In this study, an internal forcing mechanism in either model leads to unique steady solutions in stable stratification, so we should expect to observe unique solutions in axisymmetric flow regimes of both the atmosphere and the laboratory cylinder. In agreement with Henderson (1982), this implies

that the transitions between the lower symmetric and wave flow regimes will be smooth.

To demonstrate, theoretically, the effects of various combinations of internal and external thermal forcing on these physical systems, we compared the steady solutions of two axisymmetric low-order spectral models; these were the S model, which was a quasi-hydrostatic model based on the geometry of the atmosphere and the C model, which was a nonhydrostatic model based on the geometry of the laboratory cylinder. We found that the S model did not permit multiple solutions in statically stable conditions for any combinations of internal and external forcing parameters. In contrast, the C model permitted multiple solutions in a stably stratified fluid only when externally imposed horizontal heating of sufficient magnitude was incorporated.

When the modified C and S models were externally forced only, their differential systems appeared mathematically identical except for differences in the magnitudes of the constants in each system. The quantitative differences, which are responsible ultimately for the qualitative differences in steady behavior, were attributed to the hydrostatic approximation, which was used in the S model but not in the C model; this approximation restricted the choice of suitable basis functions and specified an appropriate range of aspect ratios in the S model. When both models were primarily internally forced (that is, there was either weak or no external forcing), no multiple solutions were found for either case in stable conditions, and the qualitative nature of the axisymmetric flows was the same.

The results above can be generalized to the atmosphere and to the corresponding cylindrical laboratory vessels. Since all combinations of forcing parameters in the S model led to unique solutions in the axisymmetric

flow regime in stable stratification, we infer that transitions between the Hadley and Rossby regimes in the atmosphere are likely to be smooth. In contrast, sufficient lateral lower boundary thermal forcing in the C model led to two regions of multiple solutions in a stably stratified fluid. Because of the proximity of the associated fold point curves to the upper portion of the symmetric flow-wave flow transition curve in Fultz et al. (1959), we expect to observe sudden transitions and hysteresis between the upper symmetric and wave flow regimes in the laboratory annulus. However, both the S and C models suggest smooth transitions between the lower symmetric regime, where the lateral lower boundary thermal forcing is relatively weak, and the wave flow regime in the atmosphere and the laboratory cylinder. It is important to note that, because we are not able to find the actual transition curve here, these results do not conflict with the conclusion of Miller and Gall (1983), who found no analog of the upper symmetric regime in their numerical model of a rotating hemispherical configuration.

The problem then is not the view of the forcing of the atmosphere that we adopt, but instead the adequacy of modeling its effects in the laboratory analogue. Indeed, we have noted that forcing a laboratory vessel primarily internally presents a technological problem because internal mechanisms are difficult to apply experimentally without also applying external forcing. But if internal forcing is crucial, then the results obtained from externally forced laboratory replicas might not explain properly the manner by which regime transitions occur in the internally forced atmosphere.

If we are interested in modeling the atmosphere, then based on the results obtained here (and those of Handerson (1982) and Miller and Gall (1983)), it appears that an upper symmetric transition may not be relevant. Indeed, both the S and C models suggest a smooth transition from the lower

symmetric to wave flow regimes when they are internally forced. In this case, laboratory vessels with adequate internal forcing mechanisms have the greatest utility for studying both the axisymmetric flows and the transitions from them to the wavy ones that would be expected in the atmosphere. However, if we are interested in modeling the upper symmetric transition, then as we saw in Sec. 3, an externally forced laboratory annulus is suitable.

Acknowledgments

We are indebted to Dr. Harry W. Henderson who provided many useful suggestions during the evolution of this study. The research reported here was partially funded by the National Science Foundation through Grants ATM79-08354 and ATM83-07213, and by the National Aeronautics and Space Administration through Grants NAS8-33794 and NAS8-36150.

Appendix A

Solutions to Linear Problems from (2.10)-(2.14).

Three suitable linear problems from (2.10)-(2.14) are

$$\nu \nabla^2 D - \nabla_H^2 w = -\gamma D, \quad (A.1.)$$

$$\nu \nabla^2 w - \frac{\partial \pi}{\partial z} = 0, \quad (A.1.2)$$

$$D = -\frac{\partial w}{\partial z}, \quad (A.1.3)$$

$$\nabla^2 \tau = -\Lambda \tau, \quad (A.2)$$

and

$$\nabla^2 \zeta = -\Gamma \zeta. \quad (A.3)$$

In problems (A.1) and (A.3), we have eliminated rotation to preserve the self-adjoint property and to minimize the difficulty of determining the basis functions. The problems (A.2) and (A.3) are merely the classical problems for Laplace's operator.

To facilitate the method used to solve (A.1), we combine (A.1.1)-(A.1.3) into a single fourth-order equation in the w -component, given by

$$\nabla^4 w + \frac{\gamma}{\nu} \frac{\partial^2 w}{\partial z^2} = 0. \quad (A.4)$$

The four no-slip boundary conditions that are necessary to solve (A.4) are given in (2.17)-(2.18).

We solve (A.4) by using separation of variables. The solution for w , given by $w(\mu, z) = P(\mu) \cdot W(z)$ in the axisymmetric model, is composed of the associated Legendre functions and a vertical function. We substitute this solution into (A.4) and utilize the orthonormality of the Legendre functions to obtain the characteristic equation

$$L_n W_n = -\lambda_n \frac{\partial^2 W_n}{\partial z^2}, \quad (A.5)$$

where L_n is the self-adjoint differential operator

$$L_n = \epsilon_n^2 - 2\epsilon_n \frac{\partial^2}{\partial z^2} + \frac{\partial^4}{\partial z^4}, \quad (A.6)$$

and $\lambda_n = \gamma_n / \nu$, $\epsilon_n = n(n+1)/a^2$.

From general knowledge of linear homogeneous differential equations with constant coefficients, we know that $W_n(z) \sim \exp(r_n z / Z_T)$ is a solution to (A.5) for suitable values of r . The associated characteristic equation is

$$\left(\left(\frac{r_n}{Z_T} \right)^4 + \frac{\epsilon_n}{Z_T^2} \left(\frac{r_n}{Z_T} \right)^2 + \epsilon_n^2 \right) \exp(r_n \frac{z}{Z_T}) = 0, \quad (A.7)$$

and its roots are

$$r_n^{(1)} = \pm i\alpha_n = \pm i \frac{Z_T}{\sqrt{2}} (\epsilon_n - (\epsilon_n^2 - 4\epsilon_n^2)^{1/2})^{1/2}, \quad (A.8)$$

and

$$r_n^{(2)} = -\pm i\beta_n = \pm i \frac{Z_T}{\sqrt{2}} (\epsilon_n + (\epsilon_n^2 - 4\epsilon_n^2)^{1/2})^{1/2}, \quad (A.9)$$

where $\Xi_n = \lambda_n - 2\epsilon_n$. In (A.8) and (A.9) we note that for $2s$ complex valued roots $(\pm \alpha_n, \pm \beta_n)$, there are s complex conjugate pairs denoted by $\{r_n^{(1)}, r_n^{(2)}\}$.

Since the eigenvalues λ_n are positive and real, it is easy to demonstrate that $\Xi_n > 0$ and that $(\pm \alpha_n, \pm \beta_n)$ are real (Higgins, 1983). The roots $r_n^{(1)}$ and $r_n^{(2)}$ become complex conjugate pairs $\pm i\alpha_n$ and $\pm i\beta_n$ so that the basis functions are combinations of trigonometric functions.

Because λ_n is positive, two different solutions to (A.5) are possible, depending on n . For $n=0$, the roots (A.8) and (A.9) are $\alpha_0=0$ and $\beta_0=Z_T(\lambda_0)^{1/2}$. This yields a general solution of the form

$$W_0(z) \sim A + B \frac{z}{Z_T} + C \exp(i \beta_0 \frac{z}{Z_T}) + D \exp(-i \beta_0 \frac{z}{Z_T}) \quad (A.10)$$

We apply the boundary conditions (2.17)-(2.18) to (A.10) and set the determinant of the matrix of coefficients to zero to obtain

$$\beta_0 \sin(\beta_0)/2 = 1 - \cos(\beta_0) \quad (A.11)$$

The solutions to (A.11) are obtained graphically by plotting $f(\beta_0) = \beta_0 \sin(\beta_0)/2$ and $g(\beta_0) = 1 - \cos(\beta_0)$ for $\beta_0 > 0$. The m^{th} vertical basis function $W_0^m(z)$, subject to the boundary conditions, is

$$W_0^m(z) = C_0^m \left(\left[\cos(\beta_0^m \frac{z}{Z_T}) - 1 \right] + K_0^m \left[\sin(\beta_0^m \frac{z}{Z_T}) - \beta_0^m \frac{z}{Z_T} \right] \right), \quad (A.12)$$

where

$$K_0^m = \frac{1 - \cos(\beta_0^m)}{\sin(\beta_0^m) - \beta_0^m}, \quad (A.13)$$

and the constant C_0^m remains arbitrary. The first two even and first two odd vertical modes of basis functions $W_0^m(z)$ and their orthogonal derivatives $d_0^m(z)$ are given in Fig. A.1. No attempt has been made to normalize the basis functions because determination of the analytical expression takes considerable effort.

When $n > 0$, the roots (A.8) and (A.9) satisfy the condition $\alpha_n \neq 0$, $\beta_n \neq 0$, $\alpha_n \neq \beta_n$, and the general solution becomes

$$\begin{aligned} W_n(z) \sim & A \exp(i\alpha_n \frac{z}{Z_T}) + B \exp(-i\alpha_n \frac{z}{Z_T}) \\ & + C \exp(i\beta_n \frac{z}{Z_T}) + D \exp(-i\beta_n \frac{z}{Z_T}). \end{aligned} \quad (A.14)$$

Proceeding as before, we find that α_n and β_n satisfy the equation

$$(\beta_n \tan(\frac{\beta_n}{2}) - \alpha_n \tan(\frac{\alpha_n}{2}))(\alpha_n \tan(\frac{\beta_n}{2}) - \beta_n \tan(\frac{\alpha_n}{2})) = 0, \quad (A.15)$$

I

II

in which term I produces the even functions and term II produces the odd functions. Graphical solutions are obtained, as in the previous case, and the n th vertical basis function W_n^m , subject to the boundary conditions, is

$$\begin{aligned} W_n^m(z) = & C_n^m (\cos(\beta_n^m \frac{z}{Z_T}) - \cos(\alpha_n^m \frac{z}{Z_T})) \\ & + K_n^m (\sin(\beta_n^m \frac{z}{Z_T}) - \frac{\beta_n^m}{\alpha_n^m} \sin(\alpha_n^m \frac{z}{Z_T})). \end{aligned} \quad (A.16)$$

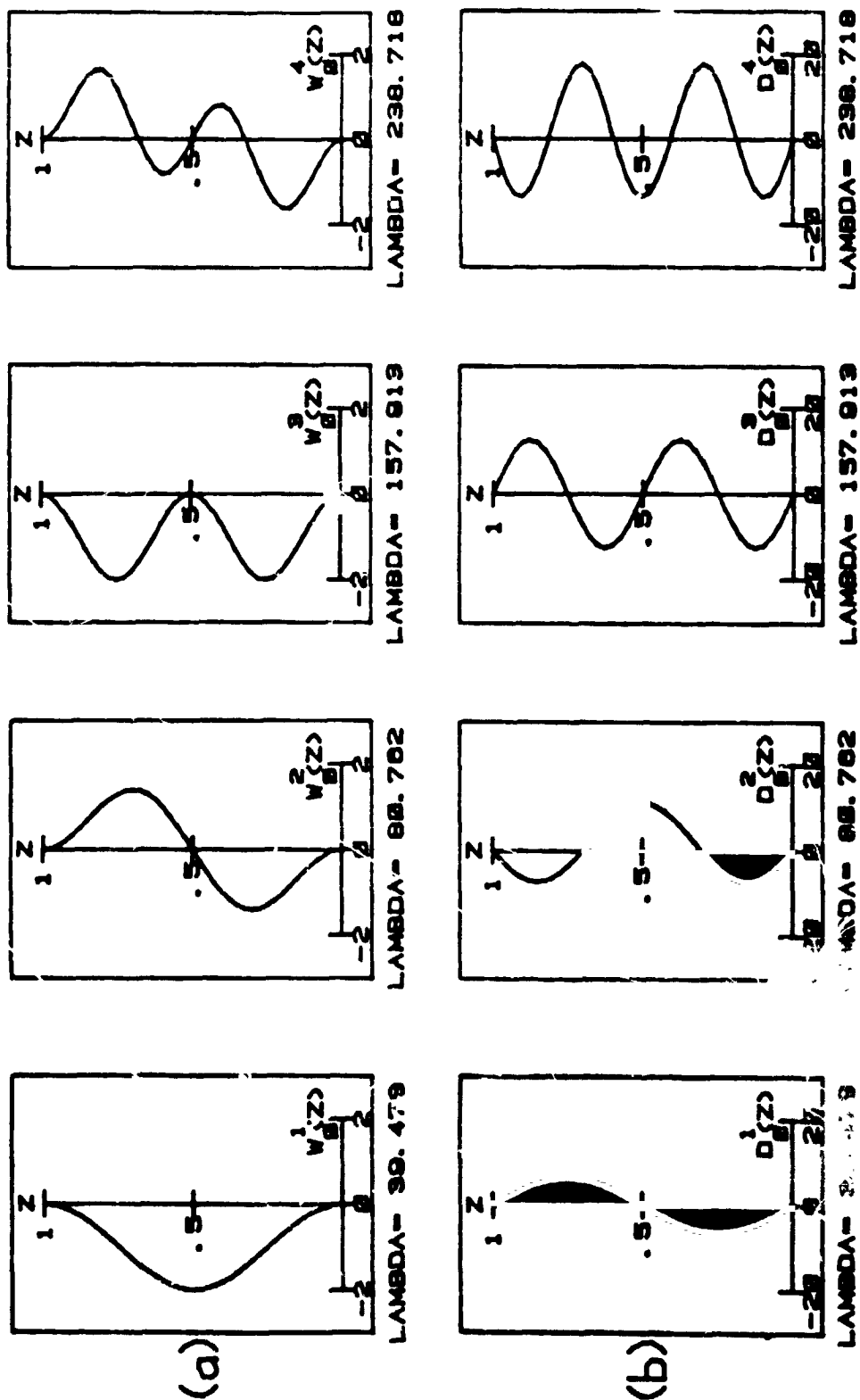


Fig. A.1 In (a), plots of the first four unnormalized vertical modes of basis functions $W_m(z)$. In (b), plots of the mutually orthogonal derivatives $D_m(z)$. Superscripts $m = 1, 3$ correspond to even modes whereas superscripts $m = 2, 4$ correspond to odd modes. Eigenvalues λ_0 (written "LAMBDA") are given below each plot and the upper horizontal boundary Z_T is scaled to one.

with

$$K_n^m = \frac{\cos(\alpha_n^m) - \cos(\beta_n^m)}{\sin(\beta_n^m) - \frac{\beta_n^m}{\alpha_n^m} \sin(\alpha_n^m)} ; \quad (A.17)$$

the constant C_n^m remains arbitrary.

Expressions (A.12) and (A.16) yield the functions $W_n^m(z)$ for all integer values of m and n . These results allow us to calculate the vertical basis functions $\sigma_n^m(z)$ for the scaled pressure variable π in the usual diagnostic way. If (A.1.3) is substituted into (A.1.1), then

$$\nabla_H^2 \pi = -(\nu \nabla^2 + \gamma) \frac{\partial w}{\partial z} \quad (A.18)$$

If a separable solution of the form $\pi(\mu, z) = P(\mu) \cdot \sigma(z)$ is used in conjunction with the solution for $w(\mu, z)$, then (A.18) becomes

$$\sigma_n^m(z) = \frac{\nu}{\epsilon_n} \left(\frac{\partial^2}{\partial z^2} - \epsilon_n \right) \frac{\partial W_n^m}{\partial z} + \frac{\gamma_n^m}{\epsilon_n} \frac{\partial W_n^m}{\partial z} \quad (A.19)$$

This expression describes the vertical dependence of the scaled pressure variable π .

The vertical basis functions for divergence D are determined directly from (A.1.3). We use a separable solution of the form $D(\mu, z) = P(\mu) \cdot \chi(z)$ along with the solution for $w(\mu, z)$ to obtain the vertical basis functions

$$\chi_n^m(z) = -\frac{\partial W_n^m}{\partial z} \quad (A.20)$$

The orthonormal, vertical basis functions in (A.12), (A.16), (A.19) and (A.20) for w, π and D respectively, have an associated ordered sequence of unique, real eigenvalues tending toward infinity (e.g., Ladyzhenskaya, 1969). Moreover, they complete a representation of the spectral expansions for w, D and π , that can be written as

$$\begin{bmatrix} W(\mu, z, t) \\ D(\mu, z, t) \\ \pi(\mu, z, t) \end{bmatrix} = \sum_m \sum_n a_n^m(t) \begin{bmatrix} P_n(\mu) W_n^m(z) \\ -P_n(\mu) \frac{\partial W_n^m}{\partial z}(z) \\ P_n(\mu) \sigma_n^m(z) \end{bmatrix} \quad (A.21)$$

$$(A.22)$$

$$(A.23)$$

To solve (A.2), we choose a separable solution of the form $\tau(\mu, z) = P(\mu) \cdot \phi(z)$. After substitution of this solution into (A.2), we find

$$\left(\frac{\partial^2}{\partial z^2} - \epsilon_n\right) \phi_n(z) = -\Gamma_n \phi_n(z) \quad (A.24)$$

where we have used the definition $\Gamma_n = \eta_n/\kappa$. With a solution for $\phi_n(z)$ of the form $\phi_n(z) \sim \exp(r_n z)$, we obtain

$$\phi_n(z) \sim A \exp(i(v_n)^{1/2} z) + B \exp(-i(v_n)^{1/2} z) \quad (A.25)$$

and $v_n = \Gamma_n - \epsilon_n$. The boundary conditions (2.20) are applied after differentiating (A.25) with respect to z ; this yields the equation

$$(\nu_n)^{1/2} (A+B, \pm i n (\nu_n)^{1/2} Z_T) = 0 \quad . \quad (A.26)$$

Equation (A.26) is satisfied if $(\nu_n)^{1/2} = 0$ or $(\nu_n)^{1/2} = -m\pi/Z_T$. In the first case, the eigenvalues are $\Gamma_n^0 = \epsilon_n$, and in the second case, the eigenvalues are $\Gamma_n^m = \epsilon_n + (m\pi/Z_T)^2$. The corresponding vertical basis function in the first case is

$$\phi_n^0 = d_n^0 \quad , \quad (A.27)$$

for $m=0$, where d_n^0 is a constant associated with each horizontal function Y_n^0 .

In the second case

$$\phi_n^m = d_n^m \cos(m\pi \frac{z}{Z_T}) \quad , \quad (A.28)$$

for $m>0$. The basis functions (A.27) and (A.28) specify the vertical dependence of the scaled potential temperature. The complete spectral expansion in the axisymmetric model is

$$\tau(\mu, z, t) = \sum_m \sum_n b_n^m(t) P_n(\mu) \phi_n^m(z) + \sum_n b_n^0 P_n \phi_n^0 \quad . \quad (A.29)$$

Finally, we solve the linear vorticity problem (A.3) via the same method that was used to obtain the basis functions for scaled potential temperature. With the boundary conditions (2.19) and a separable solution for ζ of the form $\zeta(\mu, z) = P(\mu) \cdot \psi(z)$, we find

and $v_n = \Gamma_n - \epsilon_n$. The boundary conditions (2.20) are applied after differentiating (A.25) with respect to z ; this yields the equation

$$(v_n)^{1/2} (A+B) \sin[(v_n)^{1/2} z_T] = 0 \quad . \quad (A.26)$$

Equation (A.26) is satisfied if $(v_n)^{1/2} = 0$ or $(v_n)^{1/2} = -m\pi/z_T$. In the first case, the eigenvalues are $\Gamma_n^0 = \epsilon_n$, and in the second case, the eigenvalues are $\Gamma_n^m = \epsilon_n + (m\pi/z_T)^2$. The corresponding vertical basis function in the first case is

$$\phi_n^0 = d_n^0 \quad , \quad (A.27)$$

for $m=0$, where d_n^0 is a constant associated with each horizontal function Y_n^0 .

In the second case

$$\phi_n^m = d_n^m \cos(m\pi \frac{z}{z_T}) \quad , \quad (A.28)$$

for $m>0$. The basis functions (A.27) and (A.28) specify the vertical dependence of the scaled potential temperature. The complete spectral expansion in the axisymmetric model is

$$\tau(\mu, z, t) = \sum_m \sum_n b_n^m(t) P_n(\mu) \phi_n^m(z) + \sum_n b_n^0 P_n \phi_n^0 \quad . \quad (A.29)$$

Finally, we solve the linear vorticity problem (A.3) via the same method that was used to obtain the basis functions for scaled potential temperature. With the boundary conditions (2.19) and a separable solution for ζ of the form $\zeta(\mu, z) = P(\mu) \cdot \phi(z)$, we find

$$\psi_n^m(z) = e_n^m \sin\left(m\pi \frac{z}{Z_T}\right) \quad , \quad (\text{A.30})$$

for $m > 0$; the constant e_n^m is arbitrary. The eigenvalues are

$$\lambda_n^m = e_n + \left(\frac{m\pi}{Z_T}\right)^2 \quad , \quad (\text{A.31})$$

and $\lambda_n^m = \gamma_n^m / \nu$. Equation (A.30) specifies the vertical dependence of vorticity ζ . The complete spectral expansion in the axisymmetric model is

$$\zeta(\mu, z, t) = \sum_n \sum_m c_n^m(t) P_n(\mu) \psi_n^m(z) \quad . \quad (\text{A.32})$$

Appendix B

Coefficients in (2.42)-(2.46).

Because the spectral components (2.41) are modified, the definitions of the interaction coefficients in the five-coefficient model (2.36)-(2.40) are modified. The new definitions are

$$B_1 = Z_T B_{211}^{121} = \frac{r}{2} \left(\frac{2}{5}\right)^{1/2}, \quad (B.1)$$

$$B_2 = Z_T B_{211}^{112} = \frac{3r}{2} \left(\frac{2}{5}\right)^{1/2}, \quad (B.2)$$

$$D_1 = \frac{D_{112}^{121}}{Z_T} = \frac{3r}{4\pi^2} \left(\frac{2}{5}\right)^{1/2}, \quad (B.3)$$

$$E_1 = E_{22}^{11} = \frac{Z_T^2}{a^4} \frac{27}{2} + \frac{6}{a^2}, \quad (B.4)$$

$$E_2 = \frac{E_{22}^{01}}{Z_T} = \frac{3}{a^2} \frac{Z_T}{\pi^2}, \quad (B.5)$$

$$F_1 = Z_T F_{202}^{110} = \frac{5}{4} r(2)^{-1/2}, \quad (B.6)$$

$$F_2 = Z_T F_{220}^{101} = \frac{5}{4} r(2)^{1/2}, \quad (B.7)$$

$$r = Z_T R, \quad (B.8)$$

$$J_1 = \frac{J_{12}^{21}}{Z_T} = \frac{3}{\pi} (15)^{-1/2}, \quad (B.9)$$

$$J_2 = Z_T J_{21}^{12} = 4\pi(15)^{-1/2} . \quad (B.10)$$

In the interaction coefficients above $\Gamma = 32/15$.

The definitions for the eigenvalues in (2.36)-(2.40) become $\lambda_1 = \lambda_2^1$, $\lambda_2 = \lambda_1^1$, $\lambda_3 = \lambda_1^2$, $\Gamma_1 = \Gamma_2^0$ and $\Gamma_2 = \Gamma_0^1$. We also note that the heating coefficients in (2.36)-(2.40) are given by

$$q_h = q_2^0 , \quad (B.11)$$

and

$$q_v = q_0^1 . \quad (B.12)$$

The expressions for d_i , $i=0-7$, in the steady polynomial (2.48) are

$$d_7 = -h_3 h_8^2 h_{10} , \quad (B.13)$$

$$d_6 = 0 , \quad (B.14)$$

$$d_5 = -h_1 h_{10} + h_2 h_8 h_{10} + h_3^2 h_5 - h_6 h_8^2 - 2h_3 h_7 h_8 h_{10} - h_3 h_8^2 h_9 , \quad (B.15)$$

$$d_4 = h_4 h_8^2 , \quad (B.16)$$

$$d_3 = -h_1 h_9 + h_2 h_7 h_{10} + h_2 h_8 h_9 + 2h_5 h_7 h_8 - 2h_6 h_7 h_8 - h_3 h_7^2 h_{10} - 2h_3 h_7 h_8 h_9 , \quad (B.17)$$

$$d_2 = 2h_4 h_7 h_8 , \quad (B.18)$$

$$d_1 = h_2 h_7 h_9 + h_5 h_7^2 - h_6 h_7^2 - h_3 h_7^2 h_9, \quad (B.19)$$

$$d_0 = h_4 h_7^2, \quad (B.20)$$

and

$$h_1 = D_1 B_1 \Omega^2 J_2^2 v \lambda_2, \quad (B.21)$$

$$h_2 = \Omega^2 J_1 J_2 v \lambda_2, \quad (B.22)$$

$$h_3 = v(E_1 + \lambda_1), \quad (B.23)$$

$$h_4 = g E_2 v P^{-1} \Gamma_2 q_h, \quad (B.24)$$

$$h_5 = g E_2 v P^{-1} \Gamma_2 r_s, \quad (B.25)$$

$$h_6 = g E_2 F_1 q_v, \quad (B.26)$$

$$h_7 = v^2 \lambda_2 \lambda_3, \quad (B.27)$$

$$h_8 = B_1 B_2, \quad (B.28)$$

$$h_9 = v^2 P^{-2} \Gamma_1 \Gamma_2, \quad (B.29)$$

$$h_{10} = F_1 F_2. \quad (B.30)$$

Appendix C

Coefficients of the Steady Polynomial (3.21).

The definitions for the coefficients j_i , $i = 1-9$, that appear in the steady polynomial (3.21) are

$$j_1 = 8(3\pi^2)^{-1}(2b)^{1/2} \quad , \quad (C.1)$$

$$j_2 = b(1+(P^*)^2) \quad , \quad (C.2)$$

$$j_3 = -b \quad , \quad (C.3)$$

$$j_4 = b \quad , \quad (C.4)$$

$$j_5 = 8 \cdot 2^{1/2} b^{3/2} (3+(P^*)^2) (3\pi^2)^{-1} \quad , \quad (C.5)$$

$$j_6 = (P^*b)^2 \quad , \quad (C.6)$$

$$j_7 = - (P^*b)^2 \quad , \quad (C.7)$$

$$j_8 = b^2 \quad , \quad (C.8)$$

$$j_9 = 8 \cdot 2^{1/2} (P^*)^2 b^{5/2} \pi^{-2} \quad , \quad (C.9)$$

where $b = 4(1+A^2)^{-1}$ and $P^* = P_A$.

References

- Byrnak, B.P., 1975: An operational spectral semi-implicit one layer model. The Danish Meteorological Institute, Meddelelser Nr. 25, 48 pp.
- Chang, H. and H.N. Shirer, 1984: Transitions in shallow convection: An explanation for lateral cell expansion. J. Atmos. Sci., 41, 2334-2346.
- Dutton, J.A., 1976: The Ceaseless Wind: An Introduction to the Theory of Atmospheric Motion. McGraw-Hill, 579 pp.
- Dutton, J.A., 1982: Fundamental theorems of climate theory - some proved, some conjectured. S.I.A.M. Review, 24, 1-33.
- Eliassen, E., B. Machenhauer and E. Rasmussen, 1970: On a numerical method for integration of the hydrodynamical equations with a spectral representation of the horizontal fields. Report No. 2, Institut for Teoretisk Meteorologi, University of Copenhagen.
- Fowles, W.W. and R. Hide, 1965: Thermal convection in a rotating annulus of liquid: effect of viscosity on the transition between axisymmetric and non-axisymmetric flow regimes. J. Atmos. Sci., 22, 541-558.
- Fultz, D., R.R. Long, G.V. Owens, W. Boham, R. Kaylor and J. Weil, 1959: Studies of thermal convection in a rotating cylinder with some implications for large-scale atmospheric motions, Meteor. Monogr., 4, No. 21, 104 pp.
- Hart, J., 1984: Alternative experiments using the geophysical fluid flow cell. NASA report CR-3766, 44 pp.
- Henderson, H.W., 1982: A numerical study of the global axisymmetric circulation with varying heating and rotation rates. Ph.D. dissertation, Department of Meteorology, The Pennsylvania State University, 254 pp.
- Higgins, R.W., 1983: Development of vector basis functions for representing global flows. M.S. thesis, Department of Meteorology, The Pennsylvania State University, 144 pp.
- Lacher, R.C., R. McArthur and G. Buzyna, 1977: Catastrophic changes in circulation flow patterns. Amer. Sci., 65, 614-621.
- Ladyzhenskaya, O.A., 1969: The Mathematical Theory of Viscous Incompressible Flow. Gordon and Breach, New York, Revised English Edition translated by R.A. Silverman, 45 pp.
- Langhaar, H.L., 1951: Dimensional Analysis and the Theory of Models. John Wiley and Sons, 166 pp.
- Lorenz, E.N., 1962: Simplified dynamic equations applied to the rotating basin experiments. J. Atmos. Sci., 19, 39-51.

- Lorenz, E.N., 1963: Deterministic nonperiodic flow. J. Atmos. Sci., 20, 130-141.
- Lorenz, E.N., 1984: Irregularity: A fundamental property of the atmosphere. Tellus, 36A, 98-110.
- Machenhauer, B., 1979: The spectral method. Numerical Methods Used in Atmospheric Models, Garp Publication Series, Publ. No. 17, 121-275.
- Miller, T.L. and R.L. Gall, 1983: Thermally driven flow in a rotating spherical shell: axisymmetric states. J. Atmos. Sci., 40, 856-867.
- Orszag, S.A., 1974: Fourier series on spheres. Mon. Wea. Rev., 102, 56-75.
- Panofsky, H.A. and J.A. Dutton, 1983: Atmospheric Turbulence: Models and Methods for Engineering Applications. John Wiley and Sons, 397 pp.
- Shirer, H.N. and R. Wells, 1982: Improving spectral models by unfolding their singularities. J. Atmos. Sci., 39, 610-621.
- Shirer, H.N. and R. Wells, 1983: Mathematical Structure of the Singularities at the Transitions Between Steady States in Hydrodynamic Systems. Lecture Notes in Physics, 185, Springer-Verlag, 276 pp.
- Veronis, G., 1966: Motions at subcritical values of the Rayleigh number in a rotating fluid. J. Fluid Mech., 24, 545-554.
- Vickroy, J.G. and J.A. Dutton, 1979: Bifurcation and catastrophe in a simple, forced, dissipative quasi-geostrophic flow. J. Atmos. Sci., 36, 42-52.
- Yost, D.A. and H.N. Shirer, 1982: Bifurcation and stability of low order steady flows in horizontally and vertically forced convection. J. Atmos. Sci., 39, 114-125.